Magnetic lab-on-a-chip for cell analysis

Magnetoresistive-based real-time monitoring of dynamic cell-environment interactions

PhD thesis in physics
by **Astrit Shoshi**
born Mai 10^{th}, 1979
in Gjakova, Kosova

University of Bielefeld
Department of Physics
Thin Films and Physics of Nanostructures
Germany

AIT Austrian Institute of Technology
Health & Environment Department
Molecular Diagnostics
Austria

Declaration

I wrote this thesis by myself and used none but the indicated resources.

Vienna, April 17^{th}, 2013

(Astrit Shoshi)

Reviewers:
Prof. Dr. Günter Reiss
PD Dr. Hubert Brückl

Date of submission: April 19^{th}, 2013

Preface

Nanotechnology is currently one of the most fascinating and challenging fields of research and development, providing a unique opportunity to discover the "nanoworld". The ability to fabricate structures with high reproducibility at micro- and nano-scale level is one of the biggest achievements in material-processing technologies towards miniaturized devices. An impressive increase in performance by scaling down the size of functional components of microelectronic devices has already demonstrated the great advantages engendered by miniaturization. Integrated circuits (ICs) or microchips have revolutionized the semiconductor industry, and are nowadays indispensable components of everyday electronic devices. Advancement in technology has the potential to decisively change the structure of a society, and the omnipresence of smart phones and computers have already proved their vast impact in the daily routine of modern life [Gibbons1991, Cantor2000, Curtis2001, Medina-Sanchez2012].
The trend in miniaturization still continues and similar down-scale technologies have been increasingly adapted to other disciplines, including the biological and chemical science. Exploiting the advantages of miniaturization, new instrumental platforms or microsytems offering novel functionalities have been designed that may affect biochemical analysis processes in a similar way as ICs have influenced the computer development [DeMello2006, Craighead2006]. Such micro-scale devices are referred to as "lab-on-a-chip" (LOC) or "Micro Total Analysis System" (μTAS) and represent microfluidic-based devices that perform in an integrated and automated fashion one or multiple laboratory functions on a single chip platform [Mark2010, Lim2010, Rios2012]. Miniaturization combined with integration, automation and parallelization of multiple laboratory tasks on a chip-like format can lead to the construction of micro-scale devices with superior performance compared to standard macro-scale devices [Chovan2002, Janasek2006].
The origin of the microfluidic technology dates back to the early 1950s, when first attempts have been made to produce small droplets in the nanoliter and picoliter range [Le1998, Haeberle2007]. In 1979, the first silicon-based miniaturized gas chromatograph has been realized, which is considered as a milestone in microfluidics [Terry1979]. Manz et al. published in 1990 the first high-pressure liquid chromatography column device and at the same time they introduced for the first time the μTAS concept [Manz1990a, Manz1990b]. In due time, the μTAS research field attracted a tremendous number of scientists from different disciplines, and the idea of μTAS technologies was transfered to biological systems, which finally led to the term "Lab-on-a-Chip". Due to their high degree of interdisciplinarity, LOC systems cover a broad spectrum of analytical biochemistry applications from clinical diagnostics to environmental monitoring and basic research [Rios2012]. One of the most striking future perspectives of LOC systems is their ability to provide point-of-need or point-of-care diagnostic tools. The consequences would be a decentralization of laboratories and, thus, medical testings, which has the potential to revolutionize medicine [Yager2006, Daw2006].

Typical lab-on-a-chip architectures consist of a series of basic components such as microfluidic pipes, valves, mixers, pumps and detection units. Each component addresses individual laboratory functions, including the injection of samples and reagents, sample preparations, chemical reactions, analytical separations, target analyte detection, and finally the data analysis [Lim2006, Whitesides2006, Mark2010, Rios2012]. In recent years, a very promising approach has attracted a lot of interest in the field of biomedical applications: magnetism and microfluidics [Pamme2006]. Magnetic lab-on-a-chip devices integrate as basic components microfluidic systems for sample injection and controlled fluid transport, magnetic particles for sample preparation, molecular reaction/recognition and separation, and magnetoresistive biosensors for analyte detection [Weddemann2010, Loureiro2011, Helou2013].

Microfluidics enable the controlled manipulation and transport of fluids within channels of tens to hundreds of micrometers in size [Whitesides2006]. On the one hand, using smaller volumes that are guided over predefined functional sites reduces the analysis time and allows an enhanced control of molecular concentrations and interactions [Daw2006]. On the other hand, the amount of the target analyte within the small volume is very low, which can be a major challenge for the sensing unit.

Magnetic particles (beads) are small, usually spherically shaped objects, that possess a magnetic component and, thus, a magnetic stray field. They can be manipulated by external inhomogeneous magnetic fields, and their surface area can be functionalized with a variety of receptors and drugs. Since they can be used both as markers and carriers, they are appealing for several medical applications such as magnetic resonance imaging, hyperthermia and targeted drug delivery [Llandro2010, Gupta2004, Plank2003]. In most of their applications, magnetic particles can be considered as the connecting link between biology and physics.

Magnetoresistive sensors are based on physical effects that lead to an electrical resistance change in presence of external magnetic fields and, thus, represent a suitable detection platform for magnetic particles [Reiss2005]. The discovery of this phenomenon, the GMR-effect, by Peter Grünberg and Albert Fert in 1988 has been awarded with the Nobel Prize in Physics in 2007. GMR sensors provide an electronic signal, show a high sensitivity, are scalable down to the sub-micrometer regime, and are compatible with standard CMOS (Complementary Metal-Oxide Semiconductor) technology. All of these features are promising properties for lab-on-a-chip and future point-of-need devices.

During the last two decades, GMR-sensors experienced incredible success as magnetic field sensors both in science and industrial applications. They are applied as read-out-heads in hard disk drives [Parkin1998], current testing units in ICs [Bae1998], rotary or steering-angle sensors in the automotive industry [Bosch] and domain wall displacement detectors [Gruenberg2000].

In recent years, the synergetic use of magnetoresistive sensors and magnetic markers has paved the way for magnetic biochips. The pioneering idea is to functionalize the surface area

of beads and the sensor surface with complementary receptors that exhibit a high binding affinity to a target analyte. Following specific binding, only beads carrying the target analytes attach to the sensor surface. The sensor embedded underneath the functional sites picks up the magnetic stray field of the beads and, thus, indirectly proves the presence of the target molecule. Funtionalizing different sensor surfaces and magnetic markers with distinct binding receptors enables the detection of several target analytes in parallel. In 1998, the first prototype of a magnetoresistive-based biosensor [Baselt1998] has been introduced, and this magnetic detection idea was rapidly adapted to a broad range of magnetoresistive sensor types encompassing GMR [Schotter2004b, Megens2005], spin valve (SV) [Graham2004] or tunneling magnetoresistive (TMR) [Brzeska2004a].

Apart from molecular recognition detection, magnetic biochips and LOC's recently have also been employed to the research field of cell biology. TMR-sensors have demonstrated their capability to detect single magnetotactic bacteria [Ionescu2010], SV- and GMR-sensors have been implemented in flow cytometry systems, and successful counting of magnetically labeled cells has been reported [Loureiro2011, Helou2013]. These studies basically focus on giving simple information about the presence of magnetically labeled cells, but do not exploit the full potential of magnetic biochips in terms of providing further relevant cell-specific properties.

The characteristics of a living cell can be explored, amongst others, by monitoring time-dependent cell interactions with their environment. Although human cells share a variety of common features, their basic nature is decisively affected by their immediate (micro-) environment. Cells continually interact with their neighboring cells and their extracellular matrix, at conditions which vary in space and time. On-chip investigations provide most reliable results when the chip environment resembles the cell's native microenvironment. In that regard, LOC's are a promising choice enabling a fast spatial and temporal control of external influences. In combination with an appropriate microfluidic design and surface biochemistry, they can provide a platform that mimics in-vivo microenvironmental conditions [El-Ali2006, Paguirigan2008].

Basic cell-environment interactions pertain the uptake (endocytosis) and release (exocytosis) of substances such as small molecules or particles that reach sizes of up to few micrometers. Concerning adherent cells, further relevant interactions are cell adhesion, spreading, migration and detachment. Such dynamic processes represent important aspects in biology, which accomplish numerous functions such as embryogenesis, cell differentiation, maintenance of tissue structure, wound healing, cancer metastasis or uptake of infectious agents as part of the immune response - all of them being of special interest for biomedical applications [Bardsley1983, Cretel2010, Mrksich2000].

Dynamic cell-environment interactions can be investigated by either end-point detection schemes or real-time monitoring techniques. In the former case, usually a series of measurements are carried out for separate cell cultures at different stages of the interaction process,

and they are assembled into an illustrating time lapse graph. This approach is associated with a lot of effort, is time-consuming, requires separate cell cultures, and is sensitive to preparation artifacts. In special cases such as electron microscopy, after analysis the cells are not alive anymore, thus making serial measurements impossible [Lundberg2003]. Real-time monitoring methods are capable of recording the entire interaction process in a long-term manner with high temporal resolution. Elucidating the total picture of dynamic cell-environment interactions leads to a better understanding of the complexity of such mechanisms and, in a wider sense, to treatment strategies of related diseases [Abraham2007].

Thesis outline

In this thesis, a magnetic lab-on-a-chip has been developed that serves as a multifunctinal platform for cell analysis. The detection unit consists of a GMR-biochip. In Chapter 1, a theoretical introduction to the giant magnetoresistance effect is given.
Subject of investigation are dynamic cell-environment processes including phagocytosis, adhesion/spreading, migration and enzymatic detachment. Phagocytosis refers to the uptake of particles or microorganisms with feature sizes larger than 0.5 μm [Swanson1995, Chavrier2001]. Phagocytosis is involved in all investigations. Eukaryotic cell cultures, namely human fibroblast cells from healthy tissue and mutated human prostate cancer cells, serve as model cells. Chapter 2 explains the basic structure of eukaryotic cells and highlights the cytoskeletal and molecular mechanisms underlaying adhesion/spreading, migration and phagocytosis.
In Chapter 3, an overview of the most common real-time monitoring techniques established for studying the above mentioned dynamic cell-environment interactions is given. Their application fields, advantages and disadvantages are pointed out. Finally, the magnetoresistive-based methodology for real-time monitoring of cell-environment investigations is presented. The detection principle is based on measuring changes of the local magnetic stray fields of beads within the embedded GMR-sensors. These stray field alterations are caused by distance changes of the beads relative to the sensor surface during cell-bead interactions. This purely magnetic approach enables reproducible, label- and background-free long-term monitoring without facing difficulties like photo-bleaching. Another unique feature is the ability to measure the average bead-to-sensor surface distance within living cells, which for example allows to monitor possible bead exocytosis.
In Chapter 4, a comprehensive introduction to the individual components of the developed magnetic lab-on-a-chip (MAGLab) is given. In order to cover a broad spectrum of cell-bead interactions, both the cells as well as the bead types are varied (Chapter 4.1 and 4.2). The biochip design and the magnetic characteristics of the GMR-sensors are discussed in Chapter 4.3 and 4.4, which includes energy minimization and micromagnetic simulations . The at-

tained results are implemented in the data analysis of the real-time monitoring experiments. The MAGLab setup is introduced in Chapter 4.5. The designed magnetic field configurations enabling basic laboratory functions such as a three-dimensional manipulation of beads and magnetically labeled cells are analyzed using finite element methods (Chapter 4.6) and proved experimentally in Chapter 4.7 and 4.8. Finally, a concept of the MAGLab system towards a magnetic total analysis system is described in Chapter 4.9.

In Chapter 5, basic cell-bead interactions that are relevant for the ensuing real-time monitoring experiments are examined in microtiter plates (off-chip). Differently functionalized growth surfaces are assessed (Chapter 5.1). Cells are exposed in two distinct manners (top-down and bottom-up approach) to beads differing in size and surface functionalization. The uptake capacity and cell viability of both cell types for the beads of choice for all real-time monitoring experiments are determined in Chapter 5.2 and 5.3, respectively.

Chapter 6 represents a cell adhesion/spreading analysis both by off-chip phase-contrast microscopy imaging (Chapter 6.1) and by the developed real-time monitoring methodology (bottom-up approach, Chapter 6.2). In either case, the cells are grown on bead-immobilized sensor surfaces and bead-free reference surfaces. In this approach, cell spreading and phagocytosis take place simultaneously. Cell spreading is associated with an increase of the overall cell plasma surface area. In contrast, bead uptake results in a loss of the cells plasma surface area. Due to this plasma membrane competing processes, an inhibition of cell spreading above bead-immobilized surfaces is predicted. Finally, the long-term stability of beads inside the cell is assessed.

Chapter 7 introduces the top-down approach. Here, the bead uptake behavior of cells is investigated excluding the factor of cell spreading. The cells are first grown above the sensor surface, to a cell monolayer (confluency), followed by subsequent bead incubation. The time required for the beads to complete sedimentation and, thus, to reach the cell monolayer is determined magnetically and optically (Chapter 7.2.1). Phagocytosis is investigates under physiological and metabolically inhibited conditions, while the latter case mimics disease related malfunctioning of phagocytosis (Chapter 7.2.2) and 7.2.3.

In the last Chapter 8, two more examples of nano-biointerface studies employing the MAGLab system are presented. A chip-based cell migration assay is established in Chapter 8.1, while the detachment kinetics of cells caused by enzymatic treatment are analyzed in Chapter 8.2. Finally, the results of this thesis are summarized, and an outlook on the future perspectives is given in Chapter 9.

Publications

A. Shoshi, J. Schotter, P. Schroeder, M. Milnera, P. Ertl, R. Heer, G. Reiss, H. Brueckl, *Contemporaneous cell spreading and phagocytosis: Magneto-resistive real-time monitoring of membrane competing processes.* Biosens. Bioelectron., 2013, 40 (1), 82-88
selected for Global Medical Discovery, ISSN 1929-8536, (February) 2013

A. Shoshi, J. Schotter, P. Schroeder, M. Milnera, P. Ertl, V. Charwat, M. Purtscher, R. Heer, M. Eggeling, G. Reiss, H. Brueckl. *Magnetoresistive-based real-time cell phagocytosis monitoring.* Biosens. Bioelectron., 2012, 36, 116-122

P. Schroeder, J. Schotter, **A. Shoshi**, M. Eggeling, O. Bethge, A. Hütten and H. Brückl. *Artificial cilia of magnetically tagged polymer nanowires for biomimetic mechanosensing.* Bioinspir. Biomim., 2011, 6 (4), 046007

J. Schotter, **A. Shoshi** and Hubert Brueckl. *Development of a magnetic lab-on-a-chip for point-of-care sepsis diagnosis*, JMMM, 2009, 321 (10), 1671-1675

N. Kataeva, J. Schotter, **A. Shoshi**, R. Heer, M. Eggeling, O. Bethge, C. Nöhammer and H. Brückl. *Progress in Using Magnetic Nanoobjects for Biomedical Diagnostics.* AIP Conf. Proc., 2008, 1025, 28-33

Letters in preparation

A. Shoshi, J. Schotter, P. Schroeder, M. Milnera, P. Ertl, R. Heer, H. Brueckl, *Magnetoresistive-based cell migration and enzymatic detachment assay.*

A. Shoshi, A. Keller, J. Schotter, P. Schroeder, M. Milnera, P. Ertl, R. Heer, H. Brueckl, *Magnetic cell-chip: Real-time monitoring of phagocytosis and spreading of prostate cancer cells.*

Conferences

Invited Talk, *Magnetic biochip platforms for biomolecular diagnosis and real-time cell analysis*, Nanosciences & Nanotechnologies, Thessaloniki, July 02^{th}-06^{th}, 2012

Keynote, *Magnetoresistive-based lab-on-a-chip devices for biomolecular detection and real-time cell analysis*, Biosensors, Cancun, Mai 15^{th}-18^{th}, 2012

Talk, *Magnetic lab-on-a-chip devices for biomolecular detection and real-time cell analysis*, BioNanoMed, Krems, March 01^{st}-02^{nd}, 2012

Talk, *GMR-based real-time cell endocytosis monitoring of magnetic particles*, DPG Frühjahrstagung, Dresden, March 14^{th}-18^{th}, 2011

Poster, *Real-time cell endocytosis monitoring of magnetic particles using GMR-Sensors*, Nanosens, Vienna, December 02^{nd}-03^{rd}, 2010

Poster, *GMR-based real-time cell endocytosis monitoring of magnetic Particles*, NanoBioTech, Montreux, November 15^{th}-17^{th}, 2010

Talk, *GMR-based real-time cell endocytosis monitoring of magnetic Particles*, Scientific and Clinical Applications of Magnetic Carriers, Rostock, Mai 25^{th}-29^{th}, 2010

Poster, *Magnetic Lab-on-a-Chip: Biochip integrating magnetic manipulation and magnetoresistive detection of labeled cells*, NanoBioTech, Montreux, November 16^{th}-18^{th}, 2009

Talk, *Magnetic Lab-on-a-Chip: Biochip integrating magnetic manipulation and detection of cells*, PhD Summit ARGE Sensorik, Vienna, July 1^{st}, 2009

Poster, *Magnetic lab-on-a-chip for point-of-care diagnostics*, Nanosens, Vienna, September 29^{th}-30^{th}, 2008

Talk, *Entwicklung eines magnetischen Lab-on-a-Chip für die Point-of-Care Diagnostik*, DPG Frühjahrstagung, Berlin, February 25^{th}-29^{th}, 2008

Contents

1. GMR theory **1**

1.1. Interlayer exchange coupling . . . 2

1.1.1. Quantum well model . . . 2

1.1.2. Phenomenological model . . . 6

1.2. Giant Magnetoresistance (GMR) . . . 6

2. Cell biology **11**

2.1. Structure of eukaryotic cells . . . 12

2.2. Dynamic cell-environment interactions . . . 15

2.2.1. Adhesion and spreading . . . 15

2.2.2. Migration . . . 18

2.2.3. Phagocytosis . . . 19

3. Real-time monitoring techniques **24**

3.1. Refractive optical microscopy . . . 25

3.1.1. Interference reflection microscopy (IRM) . . . 25

3.1.2. Total internal reflection fluorescence microscopy (TIRFM) . . . 26

3.1.3. Surface plasmon resonance microscopy (SPRM) . . . 28

3.1.4. Whispering gallery mode resonance (WGMR) . . . 30

3.2. Quartz crystal microbalance (QCM) . . . 31

3.3. Capacitive sensing . . . 33

3.4. Magnetoresistive sensing . . . 34

4. Magnetic lab-on-a-chip (MAGLab) **37**

4.1. Cell cultures . . . 38

4.1.1. Normal Human Dermal Fibroblasts (NHDF) . . . 38

4.1.2. Prostate cancer cells (DU145) . . . 39

4.2. Superparamagnetic particles (beads) . . . 41

4.2.1. Bead structure and magnetic cell-chip requirements . . . 41

4.2.2. Beads for on-chip real-time monitoring and off-chip phagocytosis . . . 43

4.3. Magnetoresistive biochip . . . 46

4.3.1. GMR-sensor layout and magnetic characteristics . . . 46

4.3.2. Magnetoresistive bead detection principle . . . 48

4.3.3. Dependence of the sensor signal on bead coverage . . . 50

4.4. Simulations . . . 53

4.4.1. Downhill simplex function minimization . . . 53

4.4.2. Micromagnetic simulations (OOMMF) . . . 55

4.5. MAGLab system . . . 58
4.5.1. Polydimethylsiloxane (PDMS) microfluidics . . . 59
4.5.2. Construction and setup . . . 62
4.5.3. Magneto-transport measurements . . . 64
4.5.4. LabView computer control . . . 65
4.6. FEMLAB simulation of magnetic forces in inhomogeneous fields . . . 66
4.6.1. Magnetic field design . . . 67
4.6.2. Magnetic forces . . . 70
4.7. 3D magnetic manipulation of beads . . . 72
4.8. 3D magnetic manipulation of bead-loaded cells . . . 76
4.9. MAGLab operation at molecular level: sample analysis principle . . . 79
4.10. Summary . . . 81

5. Basic cell-environment interactions **83**
5.1. Cell growth on functionalized surfaces . . . 83
5.2. Cell interactions with MagSense beads . . . 85
5.2.1. Uptake capacity . . . 86
5.2.2. Cell interactions with different bead types . . . 92
5.3. Cell viability . . . 93
5.4. Summary . . . 94

6. Real-time monitoring of bead phagocytosis during cell spreading **96**
6.1. Optical-based cell spreading analysis . . . 96
6.2. GMR-based real-time monitoring of cell spreading . . . 100
6.2.1. NHDF cells . . . 101
6.2.2. DU145 cells . . . 105
6.2.3. Long-term monitoring of internalized beads . . . 107
6.3. Summary . . . 108

7. GMR-based real-time cell phagocytosis monitoring **110**
7.1. Concept of GMR-based real-time cell phagocytosis monitoring . . . 110
7.2. Real-time cell phagocytosis monitoring . . . 111
7.2.1. Sample preparation and bead sedimentation . . . 111
7.2.2. NHDF cells . . . 112
7.2.3. DU145 cells . . . 117
7.3. Summary . . . 120

8. On-chip real-time monitoring of cell migration and detachment **122**
8.1. Chip-based cell migration assay . . . 122
8.2. Enzymatic cell detachment . . . 126

8.3. Summary 130

9. Summary and outlook **132**

A. Appendix **136**

A.1. Preparation and analytical tools 136

A.1.1. Thin film deposition 136

A.1.2. Optical UV-lithography 137

A.1.3. Etching techniques 138

A.1.4. Chip fabrication 138

A.1.5. Scanning electron microscopy 139

A.1.6. Zeta potential 139

A.1.7. Evaluation of the sensor bead-surface coverage 140

A.2. Cell biology 141

A.2.1. Culture medium 141

A.2.2. Cell passaging 142

A.2.3. Cell viability and staining 143

References **144**

Acknowledgments **164**

Curriculum vitae **165**

1. GMR theory

The coupling behavior of ferromagnetic layers separated by thin non-magnetic spacers was carried out extensively in the 60s and early 70s [Gruenberg1993]. In these investigations only a parallel alignment of the ferromagnetic layers could be observed and, thus, it was not clear whether the coupling was mediated via an interaction with the interlayer material. In 1986, Grünberg et al. [Gruenberg1986] observed for the first time in Fe/Cr (and rare earth metals) multilayers an antiparallel magnetization alignment of the Fe layers at a Cr interlayer thickness of about 1 nm. Parkin et al. [Parkin1990, Parkin1991] proved that the interlayer exchange coupling oscillates between the parallel and antiparallel configuration as a function of the spacer thickness. Furthermore, they showed that this damped oscillation behavior occurs with a variety of transition metals as spacer material. The interlayer exchange coupling is not restricted to non-magnetic metallic spacer layers as was shown by the pioneering work of Toscano et al. [Toscano1992]. One striking feature of the coupling of Fe layers separated by amorphous Si is that, in contrast to metallic spacer materials, the coupling strength increases with increasing temperature.

About two years after Grünberg's discovery, further investigations on Fe/Cr multilayer systems carried out by Baibich et al [Baibich1988] and Binasch et al [Binasch1989] revealed another surprising result: By applying external magnetic fields and, thus, forcing the magnetization orientation of the individual ferromagnetic layers from an antiparallel into a parallel configuration, leads to a significant drop of the electrical resistance. Due to the large magnitude of the resistance change, this magnetoresistive phenomenon was termed "**G**iant **M**agneto**r**esistance, (GMR)". Shortly afterwards, Barnas et al. [Barnas1990] demonstrated by reversing the magnetization of a multilayer system consisting of ferromagnetic layers with different coercivities (hysteresis), that an interlayer exchange coupling is not an essential requirement for the GMR effect. A more sophisticated system utilizing the hysteresis of multilayers is a *Spin Valve System*, where one ferromagnetic layer is exchange biased (pinned) representing the "hard" layer and the other one can freely rotate in a magnetic field representing the "soft" layer [Dieny1991].

However, in general the largest possible resistance change or GMR effect is obtained when ferromagnetic layers separated by a spacer are forced by an external magnetic field from an initial antiparallel into a final parallel configuration. The interlayer exchange coupling serves as a mechanism to create such an initial antiparallel configuration in alternating magnetic multilayers.

Both phenomenons, the interlayer exchange coupling as well as the GMR effect are based on spin-polarization of conduction electrons. The following discussion applies only to layer systems and not to granular alloys, which also exhibit the GMR effect [Berkowitz1992].

1.1. Interlayer exchange coupling

Multilayer systems consisting of alternating ferromagnetic layers separated by a non-magnetic, metallic spacer layer with layer thicknesses in the nano-meter regime, show an indirect interaction of the ferromagnetic layers across the spacer due to the interlayer exchange coupling. Depending on the spacer thickness and interface roughness, this coupling can result in an antiparallel, parallel or a 90° relative magnetization orientation of the ferromagnetic layers [Gruenberg1999]. In case of the parallel and antiparallel configuration, several oscillation periods have been found [Purcell1991].
There are essentially two different theoretical approaches to describe the physical origin of the interlayer exchange coupling, which rely on perturbative-based model calculations and total energy calculations [Bruno1995].
Numerous perturbative methods have been used to correctly depict the interlayer exchange coupling, which comprise the free-electron model, the hole confinement model, the Anderson (or sd-mixing) model and the Rudermann-Kittel-Kasuya-Yosida (RKKY) model [Bruno1995]. The previously known indirect RKKY-interaction between isolated magnetic impurities in non-magnetic host metals has been extended to magnetic multilayers by Yafet [Yafet1987]. This RKKY model succeeds in predicting correctly the oscillation period for most systems, but it fails in describing the phase and the coupling strength (amplitude). Nonetheless, the indirect RKKY interaction is generally accepted as the underlying mechanisms of the interlayer exchange coupling [Schotter2004].
The common idea in total energy calculations is to determine the magnetic coupling by calculating the total energy difference of the multilayer system for the parallel and antiparallel configuration. Besides semiempirical tight-binding models and *ab initio* schemes, the quantum well model is another theoretical tool of this method [Bruno1995]. The theoretical framework of the interlayer exchange coupling introduced in the following chapter relies on the quantum well model.

1.1.1. Quantum well model

This model is widely accepted and it is based on quantum interferences in the intermediate spacer due to spin-dependent reflections of the electrons at the spacer-ferromagnet interface. The multiple interferences induce a change in the density of states in the spacer layer as a result of constructive and destructive superposition. The interlayer exchange coupling is associated to the energy (-difference) of the system for the parallel and antiparallel configuration of the adjacent ferromagnetic layers as a function of the spacer thickness.
The quantum well model goes back to Edwards et al. [Edwards1991], and extended in great detail by Stiles [Stiles1993] and Bruno [Bruno1995]. The following presentation of the interlayer exchange coupling is based on the model introduced by Bruno.

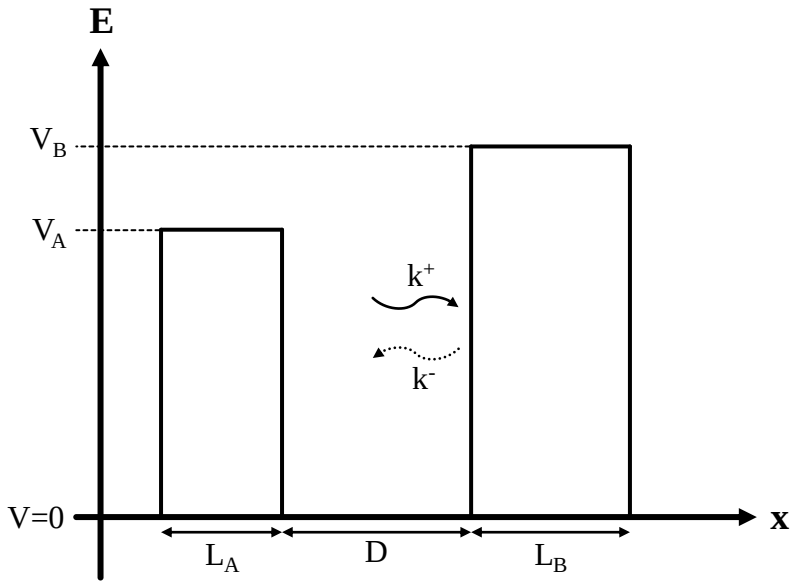

Figure 1.1: One-dimensional quantum confinement model.

As a first approach to the problem, a simple one-dimensional (1dim) model is considered as shown in Figure 1.1, which later on will be generalized to the more realistic case of a three-dimensional (3dim) multilayer system. The quantum well of length D and potential V=0 represents the spacer, which is sandwiched between two potential barriers A and B representing the spacer-ferromagnet interfaces. Their respective widths L_A and L_B can be infinite, whereas their respective potentials V_A and V_B can take either positive or negative values. An electron with wave vector k^+ traveling in the spacer to the right is reflected at barrier B. The reflected electron with wave vector k^- experiences the same reflection as it encounters barrier A. After one full reflection cycle the phase shift of the wavefunction is

$$\Delta\Phi = \alpha D + \Phi_A + \Phi_B. \tag{1.1}$$

whereat α indicates the difference of the wavevectors $k^+ - k^-$, Φ_A and Φ_B the phase shifts at the barrier reflections. The wavevector k represents the perpendicular component to the wavefunction, which is equal to the full wavevector for 1dim problems.
Depending on the energy of the electron, e.g. the reflection strength, the spacer width D and the Fermi surface, the multiple reflections lead to constructive $\Delta\Phi = 2n\pi$ or destructive $\Delta\Phi = (2n+1)\pi$ interferences with n being an integer. This results in a respective increase or decrease of density of state within the spacer. The change of density of states compared to a bulk metal is given by

$$\Delta n(\epsilon) = \frac{2}{\pi} Im\left(i\frac{d\alpha}{d\epsilon}\frac{r_A r_B e^{i\alpha D}}{1 - r_A r_B e^{i\alpha D}}\right) \tag{1.2}$$

with r_A and r_B as the respective reflection coefficients. By considering the integrated density of states

$$N(\epsilon) = \int_{-\infty}^{\epsilon} n(\epsilon^{'})d\epsilon^{'}, \tag{1.3}$$

the corresponding integrated modulation of the density of states has the following expression:

$$\Delta N(\epsilon) = -\frac{2}{\pi} Im\left(ln\left(1 - r_A r_B e^{i\alpha D}\right)\right) \tag{1.4}$$

The density of states changes as a function of the spacer width according to the confinement strength $|r_A r_B|$. In case of total confinement, $\epsilon < V_{A/B}$, the density of states is given by a set of δ-functions associated with bound states. For small confinement strength, $\epsilon > V_{A/B}$, one can observe the expected oscillatory contribution in the change of density of states. In case of positive values of $\Delta N(\epsilon)$, new states at energies below the Fermi level are generated, which have to be occupied by electrons taken from the Fermi level. For negative changes, electrons have to be added in at the Fermi level.
The associated energy change due to modifications of the density of states is calculated by means of the grand-canonical ensemble, which ensures the conservation of the number of particles. The energy change is considered at $T = 0$, which simplifies the Fermi-distribution to a sharp jump, and can be derived as follows:

$$\Delta E = \int_{-\infty}^{\infty} f(\epsilon)\Delta n(\epsilon)d\epsilon \overset{T=0}{=} \int_{-\infty}^{\epsilon_F} (\epsilon - \epsilon_F)\Delta n(\epsilon)d\epsilon \overset{part.integ.}{=} -\int_{-\infty}^{\epsilon_F} \Delta N(\epsilon)d\epsilon \tag{1.5}$$

The change in energy as a function of the layer thickness is dominated by a damped oscillation behavior.
The expressions received for the changes in density of states and the associated energy in 1.4 and 1.5 for the 1dim model, can be generalized to the 3dim problem by integrating over the in-plane component $k_\parallel$. Now both the reflection coefficient and the perpendicular component of the wavevector are functions of the energy ϵ and $k_\parallel$. The corresponding changes in the integrated density of state and coupling energy are:

$$\Delta N_\epsilon = -\frac{1}{2\pi^3} Im \int d^2k_\parallel ln\left(1 - r^A r^B e^{2i\alpha_\perp D}\right) \tag{1.6}$$

and

$$\Delta E = \frac{1}{2\pi^3} Im \int d^2k_\parallel \int_{-\infty}^{\epsilon_F} ln\left(1 - r^A r^B e^{2i\alpha_\perp D}\right) d\epsilon, \tag{1.7}$$

In general, the oscillatory changes in the total energy are related to the electron reflections at the barriers. In sandwich structures consisting of a non-magnetic spacer layer between two ferromagnetic layers, the reflections coefficient r at the ferromagnetic-spacer interface additionally depends on the relative orientation of the electron spin to the magnetization orientation of the adjacent magnetic layers. Each spin experiences different potentials and

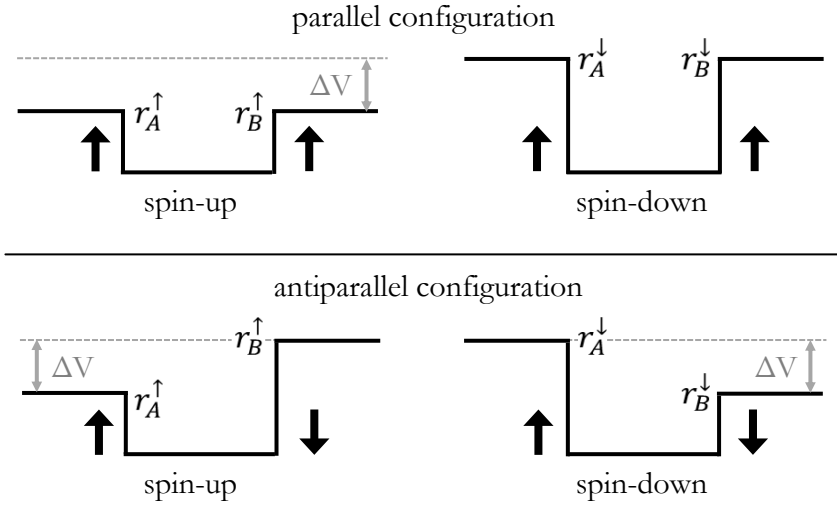

Figure 1.2: Spin-dependent potential barriers for the parallel and antiparallel configuration. The arrows indicate the magnetization vector of the magnetic layers.

this gives rise to spin asymmetry of the reflection coefficient. An electron with spin parallel (antiparallel) to the magnetization direction in the ferromagnetic layer experiences a smaller (higher) potential as shown schematically in Figure 1.2. The energy change in the parallel configuration is

$$\Delta E_p = \frac{1}{4\pi^3} Im \int d^2k_\parallel \int_{-\infty}^{\epsilon_F} d\epsilon \times \left[ln\left(1 - r_A^\uparrow r_B^\uparrow e^{2i\alpha_\perp D}\right) + ln\left(1 - r_A^\downarrow r_B^\downarrow e^{2i\alpha_\perp D}\right)\right], \tag{1.8}$$

while in the antiparallel configuration one has

$$\Delta E_{ap} = \frac{1}{4\pi^3} Im \int d^2k_\parallel \int_{-\infty}^{\epsilon_F} d\epsilon \times \left[ln\left(1 - r_A^\uparrow r_B^\downarrow e^{2i\alpha_\perp D}\right) + ln\left(1 - r_A^\downarrow r_B^\uparrow e^{2i\alpha_\perp D}\right)\right]. \tag{1.9}$$

The interlayer exchange coupling J is defined as the energy difference of these two configurations:

$$J = \Delta E_p - \Delta E_{ap} \tag{1.10}$$

Due to equation 1.10, the oscillatory energies as a function of spacer thickness D have the same period. The oscillation period is determined by the Fermi surface and solely depends on the spacer material. The phase and amplitude of the oscillatory coupling are different, which reflects the different spin asymmetry caused by different reflection probabilities at the spacer-ferromagnet interfaces and in a wider sense the geometry of the Fermi surface.
The presented quantum well model represents a simplified approach to provide a suitable mathematical framework of the interlayer exchange coupling. For instance, this model does not take into account the exact band structure of the materials involved, which in turn significantly influences the calculated period of the oscillating coupling. Furthermore, approximations are made regarding the reflection coefficients by assuming an infinite ferromagnetic layer

thickness, which in a realistic multilayer system would lead to modifications of the coupling strength. Bruno [Bruno1993] also showed a dependence of the interlayer exchange coupling on the ferromagnetic layer thickness due to resonant interferences within the ferromagnetic layers, which was previously observed experimentally by Barnas [Barnas1992].
Nevertheless, this model provides an intuitive picture about the mechanisms underlying the interlayer exchange coupling and is generally accepted. Furthermore, this theory has been applied to realistic systems such as $Co/Cu/Co$ multilayer systems and their predictions agree well with experimental results [Bruno1995, Stiles1993].

1.1.2. Phenomenological model

The interlayer exchange coupling can be described phenomenlogically by means of coupling energy terms. The relative magnetization orientation M_1 and M_2 of two ferromagnetic layers separated by a dia- or paramagnetic spacer layer is determined by the energy contribution of the bilinear J_L and biquadratic J_Q coupling term obtained by minimizing the interlayer exchange coupling energy:

$$E_i = -J_L \frac{\vec{M}_1 \cdot \vec{M}_2}{\left|\vec{M}_1\right| \cdot \left|\vec{M}_2\right|} - J_Q \left[\frac{\vec{M}_1 \cdot \vec{M}_2}{\left|\vec{M}_1\right| \cdot \left|\vec{M}_2\right|}\right]^2 = -J_L cos(\varphi) - J_Q cos^2(\varphi). \tag{1.11}$$

φ denotes the angle between the magnetization vectors of the ferromagnetic layers. Coupling type and coupling strength depend on the respective values of J_L and J_Q. In case of a dominant bilinear term, we obtain for positive (negative) J_L values a parallel (antiparallel) coupling. Under certain conditions, which are basically related to interface roughness and intermixing of free magnetic atoms in the spacer, the biquadratic term dominates and gives rise to a 90° coupling for negative J_Q values [Schotter2004].

1.2. Giant Magnetoresistance (GMR)

The GMR describes the resistance change of alternating ferromagnetic/spacer multilayers as a function of the angle between the magnetization vectors of adjacent ferromagnetic layers. The theoretical explanation of the GMR is given by a simple resistor network model, which is based on spin-dependent electron transport in magnetic multilayers.
The first spin-dependent theoretical approach relies on the Boltzmann transport equation and was worked out by Camley and Barnas [Camley1989] and Barnas [Barnas1990]. Starting from the same general formulation as Barnas, a resistor network theory with a simple analytical formula was developed by Edwards et al. [Edwards1991]. This model was introduced in a more detailed manner by his colleague Mathon [Mathon1991] and serves here as the basis for the following discussion.
The conductivity or the resistance of metals is basically determined by scattering processes.

In general, electron scattering events are elastic (energy is conserved) and in due consideration of the Pauli exclusion principle, the scattered electrons can only occupy free quantum states in the immediate vicinity of the Fermi level. The scattering probability depends on the number of states available at the Fermi level and is, therefore, proportional to the density of states. In a transition metal ferromagnet, the exchange interaction leads to a split of the d band for spin-up and spin-down electrons and the corresponding spin-dependent density of states at the Fermi level are very different. Due to the Mott's two-current model [Mott1964], spin flip scattering is negligible and the currents carried by spin-up and spin-down electrons can be considered as two independent parallel spin-channels. According to the shifted density of states for spin-up and spin-down electrons, the scattering probability and, thus, the resistance for the two spin channels are different.
In order to calculate the GMR, an interlayer exchange coupled multilayer system of alternating ferromagnetic and nonmagnetic layers in an initial antiparallel configuration is considered. The current is passed parallel in the direction of the layers and its respective resistivity is denoted by $R_{\uparrow\downarrow}$. The magnetization configuration is changed into a parallel one by applying an external saturation magnetic field and the total resistivity of the multilayer system is given by $R_{\uparrow\uparrow}$. The relative change in resistivity from one configuration into another is defined by the GMR-amplitude:

$$GMR = \frac{\Delta R}{R_{min}} = \frac{R_{\uparrow\downarrow} - R_{\uparrow\uparrow}}{R_{\uparrow\uparrow}} \tag{1.12}$$

The entire multilayer system is constructed by identical unit cells consisting of two ferromagnetic layers separated by a nonmagnetic layer. Thus, in order to calculate the total resistance in the parallel and antiparallel configuration, it is sufficient to determine the resistance of such a unit cell only.
The electrons transversing a multilayer unit cell experience different local resistivities depending on the orientation of their spins relative to the local magnetization orientation of the ferromagnetic layers. The distribution of the local resistivities ρ felt by spin-up and spin-down electrons for the parallel and antiparallel configuration are depicted in Figure 1.3. The resistivity ρ_s in the nonmagnetic spacer (NM) layer is the same for both spin orientations, whereas ρ_H and ρ_L denote the high and low resistivities which the electrons encounter in ferromagnetic layers for antiparallel and parallel orientation of their spins relative to the local magnetization vector. The aim is to find a rule for adding up the resistivities in each spin-channel, without the need of microscopic calculations. This is managed by introducing two physical limits regarding the mean free path of electrons in multilayer systems.

In the first assumption, the mean free path is much shorter than the thickness of each individual layer. In this limit there is no intermixing of electrons from different layers and all resistivities have to be added in parallel similar to a conventional resistor network. According to Figure 1.3, the eight individual resistivities lead to identical total resistivities for the parallel and antiparallel configuration and due to equation 1.12 there is no magnetoresistance.

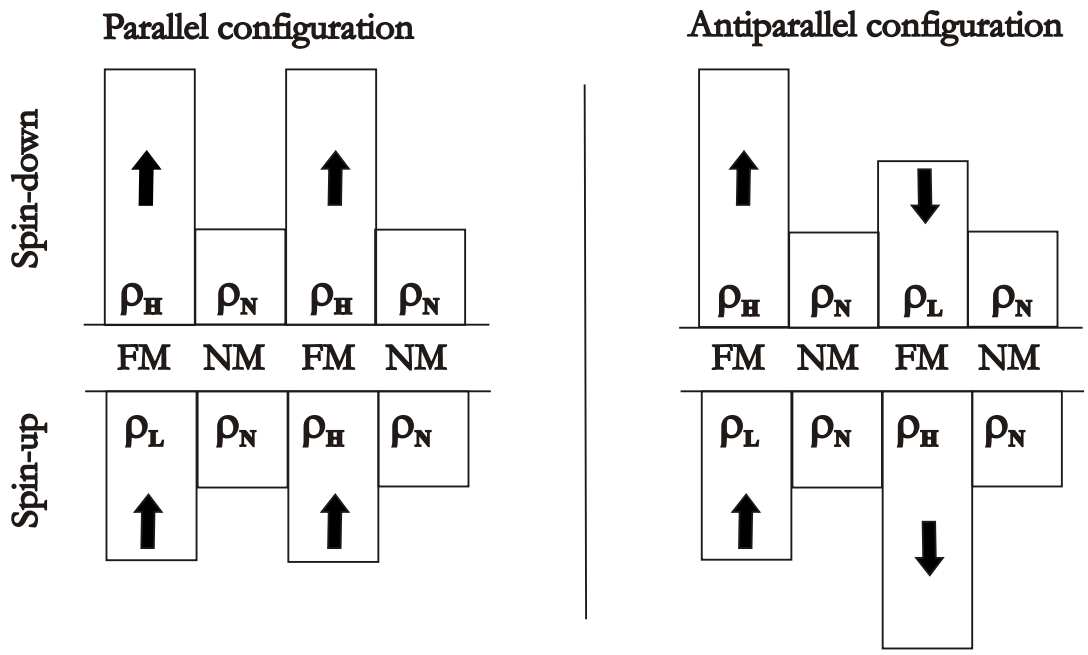

Figure 1.3: Schematic distribution of the local resistivities for spin-up and spin-down electrons transversing the superlattice unit cell in the parallel and antiparallel configuration.

In the second limit, a mean free path much longer than the thickness of the individual layers is assumed, which results in an uniform mixing of spin channels. This limiting case holds true for multilayer systems constructed by several nanometer thin layers, since typical mean free paths of electrons in metals are in the order of tens to hundreds of interatomic distances. Therefore, conduction electrons can reach neighboring layers with high and low resistivity before being scattered and experience an average resistivity $\overline{\rho}$. In the generalized case of an N component superlattice with individual resistivity ρ_n and layer thickness t_n, the following expression is valid

$$\overline{\rho} = \frac{t_1\rho_1 + t_2\rho_2 + ... + t_N\rho_N}{t_1 + t_2 + ... + t_N}, \tag{1.13}$$

and can be easily applied to the 4-component superlattice unit cell. Based on the result obtained in equation 1.13, a simple formula for the magnetoresistance can be derived. To that end, a unit cell of length L and width W with respective ferromagnetic and non-magnetic layer thicknesses t_M and t_N is considered. The two spin channels are treated independently and the corresponding total resistance of the unit cell in the parallel and antiparallel configuration is given by a parallel circuit model [Schotter2004]:

parallel configuration:

$$R_{\uparrow\uparrow} = \frac{(R_\uparrow)_{\uparrow\uparrow}\,(R_\downarrow)_{\uparrow\uparrow}}{(R_\uparrow)_{\uparrow\uparrow} + (R_\downarrow)_{\uparrow\uparrow}} = \frac{L}{2(t_M + t_N)^2 W}\,\frac{(t_M\rho_H + t_N\rho_N)(t_M\rho_L + t_N\rho_N)}{t_M\rho_L + t_M\rho_H + 2t_N\rho_N} \tag{1.14}$$

antiparallel configuration:

$$R_{\uparrow\downarrow} = \frac{1}{2}\left(R_{\uparrow}\right)_{\uparrow\downarrow} = \frac{1}{2}\left(R_{\downarrow}\right)_{\uparrow\downarrow} = \frac{L}{2(t_M + t_N)^2 W}(t_M\rho_L + t_M\rho_H + 2t_N\rho_N) \tag{1.15}$$

The substitution of these results in equation 1.12 leads to the GMR-effect:

$$\frac{\Delta R}{R_{min}} = \frac{R_{\uparrow\downarrow} - R_{\uparrow\uparrow}}{R_{\uparrow\uparrow}} = \frac{(\alpha - \beta)^2}{4\left(\alpha + \frac{t_N}{t_M}\right)\left(\beta + \frac{t_N}{t_M}\right)}, \tag{1.16}$$

with the parameters $\alpha := \frac{\rho_H}{\rho_N}$ und $\beta := \frac{\rho_L}{\rho_N}$.
The main result of this network resistor model is that for a high magnetoresistance a large spin asymmetry ratio $\alpha/\beta = \rho_H/\rho_L$ of the ferromagnetic layers is required. It predicts a monotonically decrease of the GMR and falls off as $1/t_N^2$ for large spacer layer thickness t_N. This monotonic decrease describes only the envelope of the experimentally observed damped oscillation as a function of the spacer layer thickness.
A comparison of this model to experimental results of different superlattice systems reported by Parkin et al. [Parkin1990] showed a good degree of agreement. Nevertheless, the giant magnetoresistance cannot be predicted correctly in all its properties due to the oversimplified assumptions of the presented model. It is known from experimental results, that the GMR effect decreases exponentially with increasing spacer layer thickness, whereas the model predicts an $1/t_N^2$ dependence. This discrepancy is attributed to the fact that for large spacer thicknesses the assumption of a much larger mean free path is no longer valid. Moreover, this assumption implies spin-dependent scattering in the ferromagnetic layer only and neglects the contribution of interface scattering at the magnetic and non-magnetic spacer barrier. In view of the resistor network model, for each interface in the superlattice unit cell one additional resistivity in each spin channel has to be included. Another problem arises when changing the measuring setup from the current in-plane (CIP) into the current perpendicular to plane (CPP) geometry. The model predicts the same GMR value independent of the measurement geometry, while the experiments confirm essentially larger GMR effects in the CPP-geometry [Holody1998].
In order to solve the discrepancies mentioned above, the network resistor model has to be extended or supplemented by new theoretical approaches as reviewed in [Gijs1997] and [Tsymbal2001]. In principle, the difference between the respective theoretical approaches lies in the assumption of the electronic band structure of the multilayer system and the electron transport in multilayers. The band structure in multilayers can be described within a free electron gas or a more accurate multi-band model. The electron transport is subject to ei-

ther the widely used semiclassical approach of the Boltzmann formalism [Ashcroft1976], or to a quantum-mechanical approach such as the Kubo formalism [Levy1990, Zhang1991] and Landauer-Büttiker formalism [Buettiker1988, Landauer1988].
The best theoretical approach for a quantitative description of the GMR effect is given by the combination of Kubo-/Landauer-Büttiker formalismus and the multi-band model [Tsymbal2001].

2. Cell biology

The first attempt to classify life was made 1735 by the two-kingdom system of Linnaeus [Linnaeus1735] and has led to several other scientific classification systems in biology. Currently, the three-domain and the six-kingdom classification systems introduced by Woese [Woese1977, Woese1990] and Cavalier-Smith [Cavalier-Smith2004], respectively, are used to elucidate the evolutionary tree of life. Within these systems, life forms on Earth can be divided into non-cellular (e.g. viruses) and cellular life. With regard to the more simplified three-domain system, cellular life is classified in eubacteria and archaea, which belong to prokaryotes (unicellular organisms), and eukaryotes representing multicellular organisms. The main differences that sets eukaryotic cells apart from prokaryotic cells are their nucleus, the carrier of the genetic material of cells, and their overall higher complexity.
The estimated number of living species on Earth is about 10 to 100 million and most of them make up single cell organisms [Alberts1989]. Unicellular organisms are able to replicate themselves by cell division. In multicellular organisms such as human beings, life always starts with one single cell. The whole organism is than generated by ongoing cell divisions and differentiations, which are assembled into groups and connected via a complex communication system in order to perform specific functions. Thus, individual cells represent the simplest living organisms and are considered as minimal self-reproducing units which carry the hereditary information that defines individual species. The life essential genetic information is stored in all cells in the same chemical form as a double stranded DNA (**D**eoxyribo**n**ucleic **A**cid) molecule and a complete new copy of the DNA is transmitted after each self-reproduction to their progeny [Alberts1989].
From genomic analysis it is known that all living organisms have one common ancestor [Doolittle2000]. Based on found microfossils of organisms, the current estimations revealed that the precursor cell or the last common ancestor (LCA) appeared about 3.0-3.8 billion years ago but the way it emerged is still controversially discussed [Brasier2006, Orgel1998]. There are basically two different theories trying to explain the appearance of the first cells, namely the prebiotic broth theory and the hydrothermal theory [Waechtershaeuser2000]. The first modern theory (heterotrophic hypothesis) was first published in 1924 by Oparin [Oparin1924] and five years later a related work was published by Haldane [Haldane1929]. The Oparin-Haldane hypothesis proposes a "broth or soup" of nutrient organic compounds available for organisms on the early Earth and assumes that their chemical reactions caused the synthesis of amino acids. This hypothesis was basically proven by experiments of Miller [Miller1997], who could demonstrate chemical reactions that synthesize many, but not all, amino acids and other precursors under presumed conditions of the early Earth. However, such key organic compounds could have been made on earth or simply delivered to it from outer space by meteorite or comet impacts, which illustrates the discrepancy of this hypothesis [Kvenvolden1970, Orgel1998]. The further evolution of life relies on spontaneously

formed phospholipid bilayers, which can self-assemble into bilayer vesicles and represent the basic compartments of the todays cell plasma membrane. The main challenge is to clarify whether the cytoplasm and, thus, life evolved within or outside the vesicle. Both scenarios of membrane evolution are treated by the "cytoplasm outside" model and "cytoplasm inside the vesicle" model and a comprehensive review is given by Griffiths [Griffiths2007]. The first model deals with the evolution of cytoplasmic compartments to a high degree of complexity outside the cell and their lipid vesicle envelopment based on known engulfment strategies from todays cells. In the latter model, one has to address the question on how precursors of key molecules responsible for life found their way inside the cell across the bilayer barrier of low permeability. The "cytoplasm outside" model is more plausible, but the "cytoplasm inside the vesicle" model is the more favored one [Griffiths2007].
The hydrothermal theory is based on synthesis on metal sulfides in deep-sea vents and goes back to experimental results of Wächtershäuser [Waechtershaeuser1988]. In deep-sea cracks of the earth, reactions between iron sulfide and hydrogen sulfide as a result of superheated water rich on minerals could have provided the energy needed for the reduction of carbon dioxide. This approach assumes that life started at the surface of iron sulfides and it never escaped, which is in contrast to the idea of a prebiotic soup assumed in the first theory. Life in its early two-dimensional stage is proposed to be autotrophic and it consists of an autocatalytic metabolism. Supported by the mineral surface, an autotrophically grown lipid membrane consisting of a broth of released compounds evolved to the second stage of a semi-cellular organism, consisting of a cytosol metabolism. In the final stage they detach from the surface to build true three-dimensional cellular organisms [Waechtershaeuser1988, Waechtershaeuser1992].
However, there is no scientific consensus yet and further experiments need to bring the decision about which, if any, of the described theories show the better agreement.
Despite the fact that the origin of the last common ancestor remains unsolved, the basic structure and properties of prokaryotic and eukaryotic cells are known. The first part of the following chapter will outline some universal features common in all eukaryotic cells and are based on the description given by Alberts et al. [Alberts1989]. The second part highlights specific cell features essential for the presented work here and gives a comprehensive description on the underlying mechanisms of dynamic cell-extracellular interactions such as phagocytosis, adhesion and migration.

2.1. Structure of eukaryotic cells

A human body is made of about 10^{13} eukaryotic cells of more than 200 different types with a typical size ranging from 5 to 50 microns. Despite their high diversity, they share some common features and their basic composition is illustrated in Figure 2.1 a). All cells are enveloped by a continuous asymmetric plasma membrane which defines its boundaries and confines the cells interior from the extracellular environment (Figure 2.1 b)). The main con-

stituent parts of a biological membrane are a thin lipid bilayer of about 5 nm and protein molecules. The lipid molecules are of amphiphilic nature and consist of a hydrophilic (polar) head group and a hydrophobic (nonpolar) tail. The most prominent membrane lipids are phospholipids, cholesterol and glycolipids. Characteristic for lipids is their spontaneous self-assembly in water-based environments leading not only to the formation of bilayers, but also to spherical vesicles (liposomes) and micelles. The individual lipids are able to diffuse rapidly in the plane of their own double layer construction and the membrane acts like a liquid structure. Even though the lipid bilayer is the backbone of the plasma membrane, its characteristic functional properties are basically determined by the way protein molecules are embedded into the membrane. Transmembrane proteins for instance are integrated into the membrane with domains of it being exposed to either side of the plasma membrane, so that they can perform different specific tasks on both sides, out- and inside of the cell. Peripheral or integral membrane proteins, in contrast, are attached to either face of the membrane to other proteins present in the membrane and are responsible for the membrane asymmetry. The function of membrane proteins is versatile. As transmembrane transport channels they regulate the entry and exit of ions and small hydrophobic molecules. They can serve as specific cell-surface receptors that bind molecules in the extracellular environment and induce intracellular signal cascades. In turn, binding signal molecules can activate a deformation of the plasma membrane leading to endocytosis or exocytosis processes (see phagocytosis). Similar to the lipid molecules, membrane proteins are amphiphilic and are able to diffuse in the plane of the membrane, but membranes also possess the ability to confine both proteins as well as lipid molecules into certain domains within the bilayer (e.g. lipid rafts). Overall, plasma membranes continuously rearrange their transmembrane proteins and their lipids and are, therefore, considered as dynamic or fluid structures.

The interior of eukaryotic cells is represented by the cytoplasm (excluding the cell nucleus) and it is composed of specific subunits, the organelles, which are closely packed in the cytosol (Figure 2.1 a)). These individually separated and membrane-enclosed intracellular compartments have specific functions and, similar to the plasma membrane, the involved proteins determine their characteristic structural and functional properties. They are categorized into discrete families and all eukaryotic cells possess an identical set of them. In different cell types they vary in abundance and are additionally equipped with other properties, in order to support the distinct functions of specific cells. The most prominent one is the nucleus, the organelle maintaining the genetic information. Mitochondria are responsible for the energy production by oxidizing glucose substances and the release of adenosine triphosphate (ATP), which mediates the energy transfer within the cell that is needed for metabolism. The serpentine shaped organelle is the endoplasmic reticulum (ER) and its membrane accounts for about half of the membrane of the total cell. It is basically involved in the synthesis of proteins (rough ER) and lipids (smooth ER) and, as it will be discussed later, it also contributes to

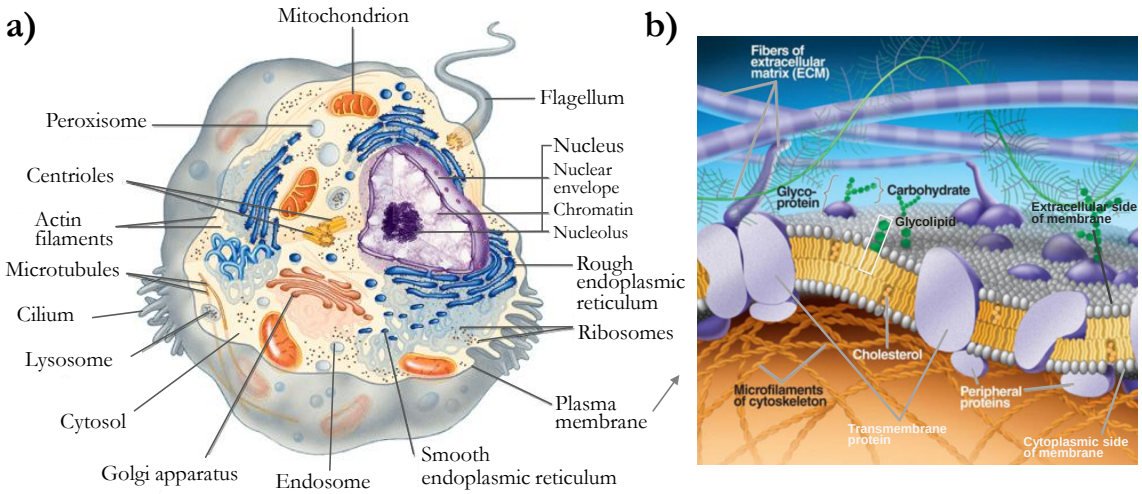

Figure 2.1: a) Common structure of eukaryotic cells including the intracellular compartments (modified from [ASCB]) and b) the plasma membrane (modified from [Meckel])

the phagocytosis process. The Golgi apparatus receives proteins and lipids from the ER and continues processing them in terms of sorting or modifying. The final protein synthesis step is the cytosol, an intracellular fluid, where beside organelle protein synthesis, also protein degradation takes place. With regard to endocytosis, other intracellular vesicular compartments such as endosomes and lysosomes play a significant role. After endocytosis, endosomes serve as transport vehicles for the encapsulated materials by the plasma membrane toward the digestive organelle, the lysosome. These compartments contain a variety of hydrolase enzymes that are active only at ambient solutions of pH 4.5-5 and degrade the ingested material. The cytosol itself has a pH of 7.2, which would protect intracellular compartments from auto-degradation by enzymes which might be released from the lysosome.

The intracellular organization of organelles is determined by their interaction with the cytoskeleton, which represents the (dynamic) scaffold of the cell. The cytoskeleton is also anchored at specific receptors integrated into the plasma membrane. The combination of both, the plasma membrane and cytoskeleton, determines the structure and shape of each cell. The basic structure of the cytoskeleton is composed of "long chain proteins" called filaments, which can be classified into three groups of complex bundled networks, namely microtubules (20-25 nm diameter), actin filaments or microfilaments (5-6 nm diameter) and intermediate filaments (6-11 nm diameter) [Franke1978]. Microtubules are hollow, cylindrical shaped polymerizations of tubulin proteins and form cilia and flagella being part of cell's extracellular sensing and locomotion. In addition, they build the fundamental machinery responsible for cell devision, the mitotic and meiotic spindle apparatus and are also involved in intracellular organelle movement. Intermediate filaments have a high tensile strength and are, therefore, predominantly found in cells such as epithelial cells of the skin, where a high cell-cell connection strength is required to withstand stretching or pressure stress. From the view of endocytosis,

the actin filament is the most significant part of the cytoskeleton, which triggers the uptake process. The actin cytoskeleton is constructed by double-stranded, helical polymers of actin proteins building flexible and strong structures throughout the cell with its highest density in vicinity of the plasma membrane. These filament networks can be assembled in long bundles, as a meshwork or as a combination of bundles and attachment plaques. Consequently, this leads to finger-like, sheet-like protrusions of plasma membrane forming the known filopodia, lamellipodia and "stress fibers". This is done by a rearrangement of the individual filament-filament and filament-organelle connections [Zigmond1996]. The assembly (disassembly) of actin polymerization is controlled by accessory proteins, such as actin-binding, capping and the actin depolymerizing factor/cofilin family (AC family). The filament length is controlled by acceleration (inhibition) of the polymerization rate by profilin ($\beta-$thymosin), the filament destabilization by tropomyosin and the stabilization of the filament network by filamin and $\alpha-$actinin. Thus, the actin cytoskeleton controls the degree of cell-surface attachment, plays an important rule in cell phagocytosis, motility, division and intracellular transport processes and provides a tensile platform in muscle contraction [Chen2000, Ridley2003].

2.2. Dynamic cell-environment interactions

Dynamic interactions between cells and their extracellular environment represent important aspects in biology and are of special interest for biomedical applications. In our case, the extracellular environment is either a two dimensional surface, a three dimensional spherically shaped particle with sizes in the micrometer regime or a combination of both. Basically, adherent cells need to attach to and spread on an underlying surface in order to perform numerous biological functions such as embryogenesis, maintenance of tissue structure, proliferation, differentiation, wound healing, metastasis or uptake of infectious agents as part of the immune response [Bardsley1983, Cretel2010, Mrksich2000]. A decisive parameter for immediate and long-term cell behavior is the surface characteristic of the extracellular environment. This comprises, on the one hand, the biomolecular and chemical nature of the substrate and, on the other hand, its physical properties such as stiffness, roughness and topography [Cavalcanti-Adam2007, Cretel2010]. Following the first contact between the cell and its environment, all further cellular processes such as cell spreading, phagocytosis or migration are mediated and triggered by bidirectional adhesion signals.

2.2.1. Adhesion and spreading

The cellular decision making to either adhere/spread on a surface or to remain rounded is determined by adhesion receptors. These adhesion (transmembrane) proteins are located at the intracellular and extracellular side of the plasma membrane. There are two main cell surface receptor families, the integrins and syndecans [Morgan2007](Figure 2.2(a)). Integrins are composed of two subunits (α and β) and each $\alpha\beta$ combination represents receptors with specific

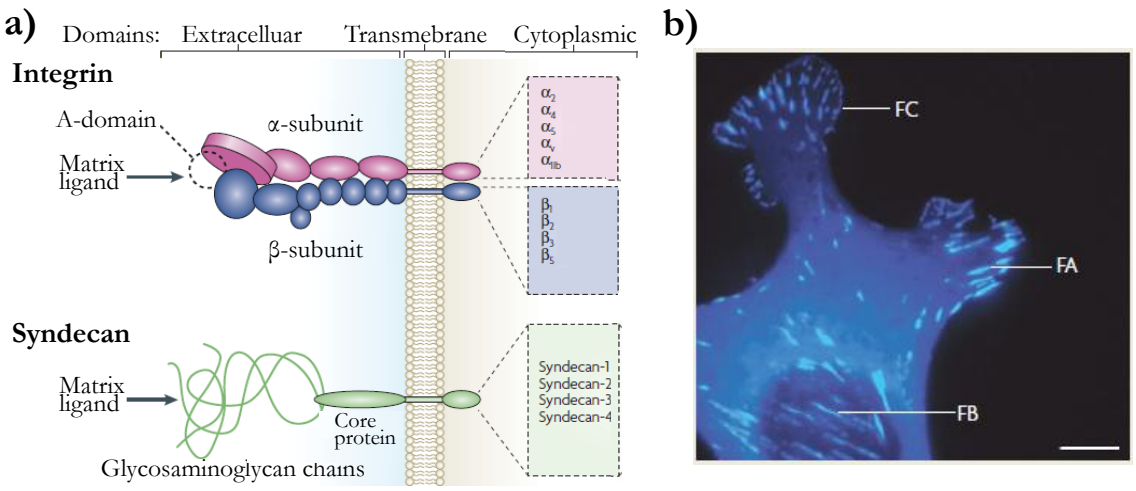

Figure 2.2: a) Schematic of extracellular, transmembrane and cytoplasmic domain structure of integrins and syndocans (modified from [Morgan2007]). b) Image showing the three major adhesion contact forms (from [Morgan2007]).

binding and signaling properties. Syndecans belong to the proteoglycan family and consist of a core protein carrying covalently bound heparan sulphate or chondroitin sulphate glycosaminoglycan chains, which bind to the extracellular environment [Morgan2007, Giancotti1999].

Adhesion receptors activate and transfer signals in both directions of the plasma membrane. The "inside-out signaling" comprises the regulation of the extracellular binding activity of the integrins/syndecans. The "outside-in signaling" are the feedback signals transfered inside the cell as a result of binding to the extracellular environment [Giancotti1999]. Adhesion receptors are connected to the cytoskeleton, cytoplasmic kinases, and transmembrane growth factors by adapter proteins. Hence, the interplay of this complex signaling network regulates the basic cellular interaction processes, including cell adhesion and spreading, phagocytosis and migration.

Cells in suspension display an almost spherical shape. Once attached to a (quasi-two-dimensional) surface they initially adapt a cap-like shape and immediately start interacting and adhering to the surface by integrin binding events. In case of unfavorable feedback interaction signals, the cell remains in a rounded, frustrated state followed by the initiation of a programmed cell death (apoptosis). In case of favorable feedback interaction signals, the cell continuous flattening until a final disk-like state with maximum cell area is reached, denominated as cell spreading. Experiments on fibroblasts and epithelial cells carried out by Sheetz and co-workers ([Doebereiner2004, Doebereiner2005, Doebereiner2006, Dubin-Thaler2008]), showed that there are three sequential spreading phases with dynamic inter-phase transitions, i.e. velocity patterns, throughout the entire spreading process. The spreading starts with its basal or early spreading phase [Doebereiner2004, Loosli2010], and within this phase, the cell-surface contact area is about the cross-sectional area of the round cell (Figure 2.3 a)). In the

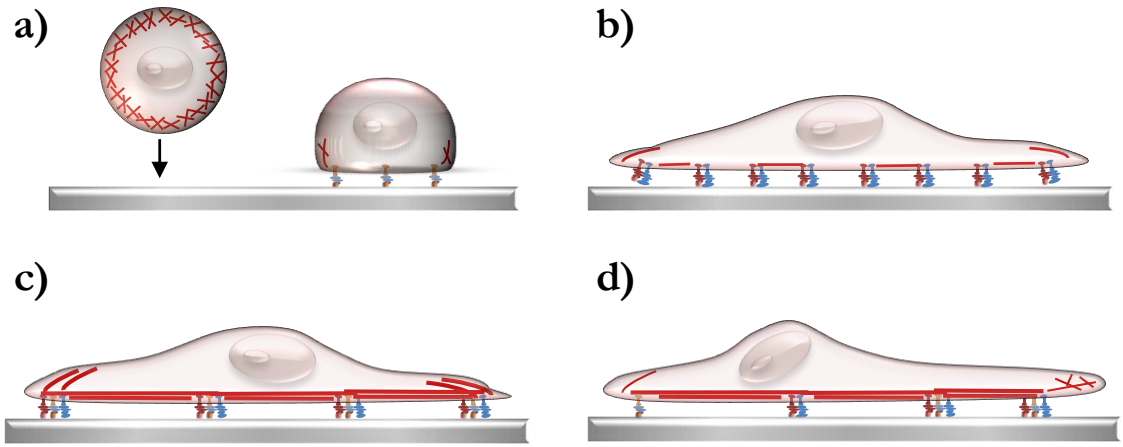

Figure 2.3: Illustration of cell flattening in the a) early, b) intermediate, c) late spreading phase and d) possible post-spreading activity such as cell migration (after [Loosli2010]).

continuous or intermediate spreading phase, the cell extends about 200 nm thin protrusion (lamellipodium and filopodia) as a consequence of cytoskeletal forces originating from actin polymerization at the leading edge of the cell plasma membrane [Doebereiner2004]. As a result, the cell-substrate contact area increases rapidly and the initiation of contractile forces begins (Figure 2.3 b)). The final phase is denoted as contractile or late spreading phase within which the spreading slows down, the cell-surface adhesion is optimized and periodic contractions (cytoskeletal pre-tensions) occur [Doebereiner2004, Loosli2010]. The cell adhesion is accomplished by building diverse integrin clusters, known as adhesion contacts or adhesion signaling complexes, which are distributed focally rather than uniformly over the ventral surface membrane (Figure 2.3 c)). The major cluster units are focal complexes (FCs), focal adhesions (FAs) and fibrillar adhesions (FBs), which can be manifested as pathes, flecks and stripes [Morgan2007] (Figure 2.3). In early spreading, FCs form underneath the lamellipodial protrusion, which transform into FAs in the continuous phase and they evolve into FBs in the late phase. These adhesion contacts are dynamic and depend on the actual cell activity. They can be formed, transformed into each other and completely disrupted in order to allow cell migration or phagocytosis, for instance (Figure 2.3 d)).

Numerous analytical and numeric models have been introduced to correctly predict the kinetics of the different stages of cell spreading. Due to Loosli et al. [Loosli2010], these models can be categorized in kinetics of spreading, cell reinforcement, cytoskeleton reorganization and discrete spreading models using divided medium. Basically, there are two main theoretical approaches to the problem. Numerical models, such as the finite element model of Guilak and Mow [Guilak2000], primarily focus on the description of the cell rheology, i.e. the "cell flow" under specific boundary conditions, where the cell is treated as a biphasic fluid. A comprehensive review of numerical models can be found in Lim et al [Lim2006] and Vaziri and Gopinath [Vaziri2008]. Other analytical models take into consideration the cellular na-

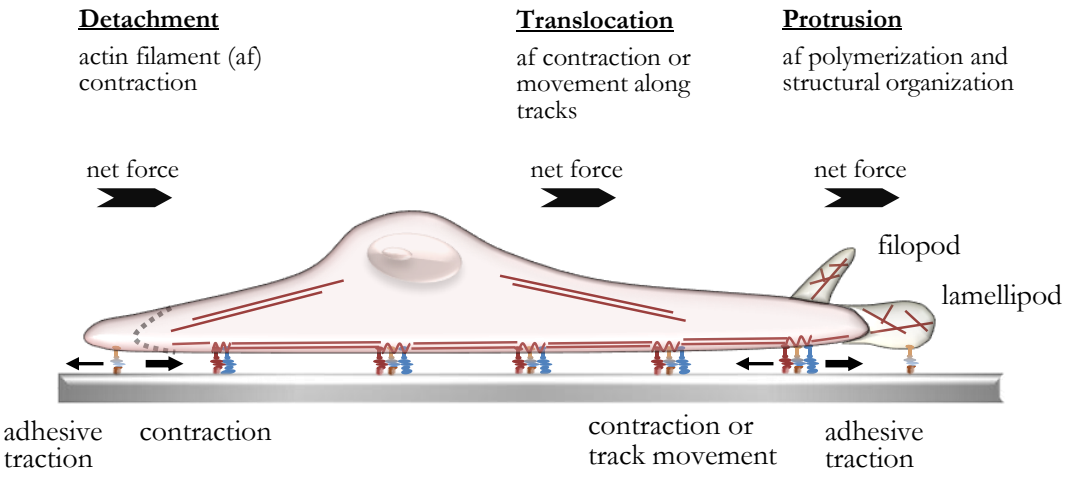

Figure 2.4: Illustration of the cyclic process of cell migration including forces involved in cell body translocation (after [Lauffenburger1996]).

ture and focus in the early cell-surface molecular interaction and cytoskeletal organization [Loosli2010]. The attempt to incorporate key cellular features such as biological membrane adhesion complexes, the cytoskeletal organization and their interaction with proteins of the extracellular environment [Shenoy2005, Li2010, Cuvelier2007, Chamaraux2005, Zemel2010] or even the extracellular properties such as the substrate stiffness in the mechano-chemical coupling model of Huang et al. [Huang2011] is the more promising theoretical approach.

2.2.2. Migration

As illustrated in Figure 2.3 d), migration is one possible cell activity after the cell adhesion and spreading process is completed and plays a crucial role in a variety of biological functions. In embryonic development, groups of cells collectively migrate long distances to reach their target destination, where they differentiate into specialized cells and enable the formation of different tissues and organs [Ridley2003]. In wound healing the migration of fibroblast and vascular epithelial cells is essential in the remodeling of the extracellular matrix [Lauffenburger1996]. In the inflammatory immune response, leukocytes migrate from their circulatory system into the infected tissue to uptake and destroy invading pathogens [Huttenlocher1995, Ridley2003]. From the pathological point of view, migration contributes to vascular diseases, osteoporosis, multiple sclerosis, mental retardation and especially to metastasis of tumor cells by their migration into the circulatory system [Ridley2003]. In biotechnological applications such as tissue engineering, migration plays a significant role in the colonization of biomaterial scaffolds used for implants [Pierres2003, Sengers2007].

Cell migration is considered as a dynamic multistep process of cyclic nature, and the following description is based on the publications of Horwitz and co-workers [Lauffenburger1996, Ridley2003]. The migratory cycle starts with the initiation of a spatial asymmetry leading

to a morphological polarization of the cell (Figure 2.4). This includes different molecular processes at the front and rear of a cell, and the consequences of polarization are directional membrane protrusions at the leading cell front. The formed broad lamellipodia and spike-like filopidia protrusions are basically driven by actin polymerization based on the "elastic Brownian ratchet" and cortical expansion mechanism. Subsequently, the protrusions build new adhesion contacts to the substratum by activated integrins localized at the leading front in order to stabilize them. After their stabilization, the focal complexes connecting the substratum with the cytoskeleton serve as traction and force generating sites required for cell locomotion. The contractile force moving the cell body forward originates from the interaction of actin filaments with myosin motor proteins. The underlying mechanism of cell translocation is either a contraction of filaments that connect the intracellular cytoskeleton to cell-substratum focal adhesions or a relative movement of adhesion contacts along actin filament tracks. The final stage of cell migration is the detachment of the cell rear by disrupting the adhesion contacts, accompanied by contraction pulling that contributes to the cells rear release.
In general, the migration speed depends on the rates of membrane protrusions and rear release. Experimental data demonstrate that the migration velocity correlates inversely with the contractile force and the cell-substratum adhesion strength. In case of fibroblast cells, maximum migration speeds in the range of 1 μm/min can be observed. Another parameter influencing the migration speed is the degree of spatial asymmetry in adhesive strength.
The cell migration picture presented describes the migration cycle of a variety of different cell types, but the individual migration stages of this model are primary found in slow-moving cells such as fibroblasts. The migration behavior of fast-moving cells, in contrast, resembles a gliding or floating over the substratum. However, the migration behavior of all cell types strongly depends on the present extracellular environment.

2.2.3. Phagocytosis

Phagocytosis was discovered by Ilya Metchnikoff during his research on a starfish larva in 1883 and together with Paul Ehrlich, he is considered as the pioneer of immunology [Tauber2003, Stuart2005]. Phagocytosis is an ancient, evolutionary conserved mechanism by which cells uptake large particles and microorganisms [Chavrier2001]. The two main functions of phagocytosis include food uptake in unicellular organisms, while in multicellular organisms it is responsible for the clearance of infectious agents, apoptotic, senescent and damaged cells and contributes essentially to the immune and inflammatory response of the host defense [Greenberg2002]. Invading pathogens are phagocytosed by scavenger cells followed by the initiation of their degradation and the activation of the adaptive immune system to effectively combat the pathogenic threat [Aderem1999]. Another prominent example elucidating the importance of phagocytosis in multicellular organisms is the development

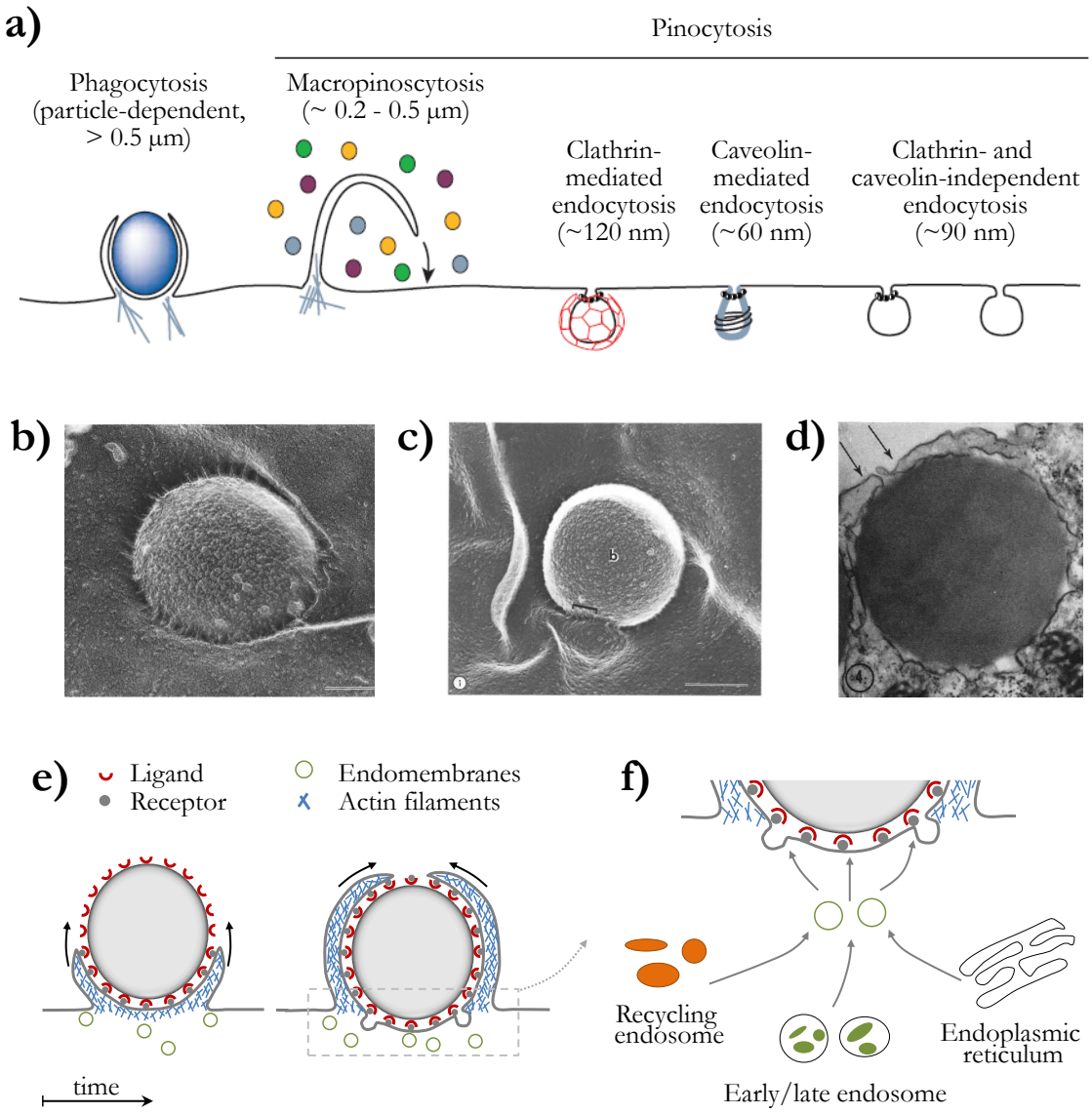

Figure 2.5: a) Endocytosis comprising all regulated pathways into the cell (modified from [Conner2003]). SEM analysis showing particle phagocytosis by invagination b) and protrusive membrane engulfment c) (from [Aggeler1982]). d) SEM image of phagocytic vesicle just before complete closing around a 2.68 μm particle (from [Korn1967]). e) Zipper-like mechanism in phagocytosis (after [Tollis2010]) and f) focal exocytosis at phagosome formation (after [Groves2008]).

of an embryo into a fetus (embryogenesis) or a tadpole to an adult frog (metamorphosis). During embryonic development, specific cells undergo a programmed cell death denominated as apoptosis. Their clearance, without causing any inflammatory reaction, is carried out by specialized phagocytes and subsequently enables, among other functions, the formation of extremities. Thus, phagocytosis is an important factor in cell biology and plays a major role in biomedical applications [Allen1996, Swanson2008].

Cells utilize two basic mechanisms to internalize small molecules and large particles or organisms, namely pinocytosis and phagocytosis (Figure 2.5 a)). These two cell "eating" and "drinking" mechanisms, respectively, describe all regulated portals into the cell and are comprised as endocytosis. Pinocytosis is subdivided into macropinocytosis, which includes particle uptake in the range between $0.2-0.5\ \mu m$, and fluid uptake via vesicle formation mediated by clathrin, coveolin and those independent of both of them. Phagocytosis refers to the uptake of particles/organisms larger than $0.5\ \mu m$ in diameter and is, in contrast to pinocytosis, conducted to specialized cells [Swanson1995, Chavrier2001]. These cells are categorized into professional, paraprofessional and non-professional phagocytes, and the main difference between them lies in limitations regarding the range of particles they can uptake [Rabinovitch1995]. Professional phagocytes include macrophages/monocytes, dendritic cells and neutrophils, and their phagocytic capability is determined by a variety of appropriate phagocytic receptors. These receptors enable the recognition of target particles by specific binding. Paraprofessional and non-professional phagocytes such as fibroblast, epithelial, Hela and Vero cell lines lack the efficient phagocytic receptors. In this case, the phagocytic process is mediated by fibronectin, laminin or other receptors [Rabinovitch1995].
Phagocytic receptors of the plasma membrane initiate phagocytosis by recognizing ligands or certain molecular configurations ("molecular patterns") expressed on the surface of particles. In general, particle recognition occurs either directly or via opsonising molecules [Stuart2005]. In professional phagocytes, the internalization of particles is mediated by opsonic receptors including Fc (Fcγ) and complement receptors, oligosaccharide mannose or fibronectin receptors [Aderem1999]. The most intensively studied receptors are opsonic receptors [Chavrier2001]. For instance, the phagocytic receptor FcγRIIa recognizes the Fc part of immunoglobulin G [Tollis2010]. Lateral receptor clustering by multiple receptor-ligand bindings activate intracellular phagocytic signals through signal transducers including PI-3 kinase, rho family of GTPases, protein kinase C and motor proteins [Aderem1999]. In turn, the focal accumulation of diverse signaling enzymes and adaptors trigger the polymerization of actin filaments and the remodeling of plasma membrane at the site of particle ingestion. Depending on the receptor-ligand recognition, the membrane forms either invaginations (Figure 2.5 b)) or pseudopod extensions surrounding the particle (Figure 2.5 c) and d)). Invagination, i.e. sinking of particles into the cell without protrusive cup formation, is primary observed in phagocytosis mediated by complement receptors such as CR3 [Allen1996]. The engulfment or cup formation by pseudopod extension occurs by a zipper-like receptor-ligand binding mechanism as illustrated in Figure 2.5 e) [Swanson1995]. The leading edges creeping tightly along the particle surface finally meet and enclose the particle into a membrane-bound vesicle (phagosome). The membrane utilized for vesicle formation is supplied by the plasma membrane and endomembranes [Desjardins2003]. For instance, macrophages are capable to internalize within 30 minutes the equivalent of $> 100\%$ of their macroscopic plasma membrane area [Greenberg2002].

Professional phagocytes store excess membrane area in terms of folds and villi, which is recruited during the uptake process by plasma membrane unfolding [Herant2005]. An additional membrane source are endomembranes including recycling endosomes, early/late endosomes and endoplasmic reticulum (Figure 2.5 f)). Endomembrane compartments are translocated by the cytoskeleton to the site of phagosome formation and inserted at the plasma membrane by a "focal exocytosis" fusion mechanism [Groves2008, Niedergang2004]. Shortly after the particle internalization is completed, the early phagosome matures by a series of interaction events. On their endocytic maturation pathway, phagosomes migrate from the cell periphery to a perinuclear location [Niedergang2004]. It starts with the depolymerization of actin filaments making the phagosome accessible to (early and late) endosomes and especially to lysosomes. These endosomal compartments contain degradation agents including enzymes, acids and oxygen radicals. Through multiple fusion and fission based on tethering and docking mechanisms, a hybrid-like organelle termed as phagolysosome is formed with the primary goal to digest the phagocytosed particle [Luzio2007, Tollis2010]. The fusion/fission rate as well as the final immune response, in terms of antigen presentation, depends strongly on the nature of the phagocytosed particle [Aderem1999, Niedergang2004].
The mechanism underlying phagocytosis is of high complexity and its biophysical and biochemical understanding remains still incomplete. The presented zippering mechanism of phagocytosis goes back to Griffin et al. [Griffin1975] and is generally accepted. Nevertheless, it has two main weaknesses. The first discrepancy addresses the unsolved problem of the energetic source associated with actin polymerization during the receptor-ligand zippering, which is required to drive membrane protrusions around the particle. The second lack of clarity is whether the zippering mechanisms is capable of explaining the experimentally observed particle-shape dependency of phagocytosis [Tollis2010]. In order to face these discrepancies, other models including the contractile shear-rigidity gradient model of Hartwig et al. [Hartwig1980] and the cortical cytoskeleton expansion model of Southwick and Stossel [Southwick1983] have been proposed. A rather new approach is the ratchet-like mechanism based on experimental results of Dembo and co-workers [Herant2005, Herant2006]. In contrast to the zipper-like model, the membrane progression is unidirectional and irreversible at the onset of phagocytosis. Actin polymerization at the leading edge does not directly apply forces (energy) to form membrane protrusions rather than filling gaps originating from membrane fluctuations and, thus, preventing the backward movement of the membrane similar to a ratchet. Recently, a three dimensional stochastic ratchet model for the zipper mechanism has been introduced by Tollis et al. [Tollis2010]. They investigated phagocytosis by a active and passive zipper mechanism. The active (passive) model describes an actin-dependent (actin-independent) uptake process, i.e. actin polymerization being involved in the cup formation (active) and a reversible engulfment process that is driven solely by receptor-ligand binding events (passive). The active model was able to explain the experimentally observed

shape-dependent uptake, whereas the passive model seems to give more insights into the, so far, unanswered question of energy sources during the cup formation.

3. Real-time monitoring techniques

The most common techniques established for studying dynamic interactions between cells and particles or surfaces are based on optical observation methods, e.g. flow cytometry, fluorescence confocal microscopy imaging, confocal laser scanning microscopy, conventional fluorescence microscopy and phase contrast microscopy ([Shoshi2012a] and references therein). Also non-optical methods such as scanning and transmission electron microscopy (SEM and TEM, respectively) are utilized, for instance to visualize the initial events of cell-particle engulfment [Aggeler1982] or (post-) phagocytosis cell morphology and to determine intracellular particle localization and/or quantity [Berry2004, Chithrani2006, Gupta2004, Olivier2004].
Long-term observations of the entire process of cell-environment interaction with high temporal resolution are very challenging by using the analytical tools listed above. To elucidate the kinetics or dynamics of interaction processes, generally several end-point measurements at different stages are carried out and assembled into an illustrating time lapse graph. These time-dependent snap-shots can be accomplished in different ways such as staining the cells with a diversity of fluorophores followed by optical excitation and image recording or by "freezing" the as-is cell state by means of common fixation procedures (for example by means of crosslinking or precipitating fixatives such as aldehydes or alcohols, respectively) [Moloney2004]. In order not to run into the risk of missing important information, the measuring time interval should be chosen as short as possible. However, the preparation steps are in most cases irreversible and the investigation of dynamic interactions automatically implies separate cell cultures. In view of reproducibility of results, this fact can lead to additional errors. Another important aspect is that the fixation of cells can result in artifacts representing an uncontrollable source of error [Lundberg2003]. Moreover, usually further cell analysis is not possible due to the fact that in most cases the cells are not alive anymore. For example, this is always true after cell analysis by SEM or TEM imaging.
In order to explore cell-environment interactions with higher time resolution and to better understand the complexity of dynamic cell interaction processes, real-time monitoring techniques are required. Emphasis is placed on chip-based real-time monitoring techniques, which have the potential to provide a multifunctional platform for sequential cell analysis. Furthermore, they enable the study of distinguished cell cultures over time, allow parallelization for high throughput analysis and save time as well as effort compared to end-point detection schemes.
This chapter highlights the versatility of real-time monitoring techniques with special focus on dynamic cell interactions including spreading, phagocytosis and migration. Excluded from this overview are online monitoring techniques, which might have the potential for cell analysis, but still operate at a molecular detection level. The same applies to techniques that represent simply a slight modification or improvement of already existing ones. For instance, fluorescence interference contrast microscopy applies features that resemble interference reflec-

tion microscopy and total internal reflection fluorescence microscopy. Finally, the detection concept of our magnetic lab-on-a-chip system based on magnetoresistive biochips as a real-time monitoring tool is presented.
Research on real-time cell-surface interactions at a nano-scale level driven by new physical techniques is of high importance in cellular biophysics and material science and the development of future biomaterials for biomedical applications (Gardel and Schwarz, 2010).

3.1. Refractive optical microscopy

Apart from conventional phase contrast and confocal microscopy, other novel optical imaging techniques such as internal reflection microscopy (IRM), total internal reflection fluorescence microscopy (TRIFM) or surface plasmon resonance microscopy (SPRM) are employed to follow dynamic cell-surface interactions with high spatial and temporal resolution [Burmeister1998, Schneckenburger2005, Cretel2010, Ryzhkov2010]. Basically, these techniques are suitable for studying biochemical processes that occur in the vicinity of interfaces. This includes molecular binding kinetics or simple protein adsorption at a liquid/solid interface as well as receptor-ligand binging events which are essential in cell-surface interactions [Axelrod1984, Schneckenburger2005].

3.1.1. Interference reflection microscopy (IRM)

IR microscopy is an optical technique commonly employed to measure the thickness of thin transparent layers and has been adapted by Curtis [Curtis1964] to study the interfacial structure of cells adhering/spreading to glass substrates. In particular, the cell to substrate separation distance is determined by means of interferometry as depicted in Figure 3.1(a). An incident monochromatic beam, usually in the red to near-infrared regime, illuminates a cell adhering on a glass substrate. Cells are almost optically transparent and approximately 1% of the incident light intensity is reflected, which occurs basically at four interfaces. The reflectivity is a function of the refractive indices n_0 and n_1 of the incident media and transmitted media, respectively, which build the interface. In case of incident light propagating normal to the interface, the reflectivity is given by the square of the Fresnel coefficient $R=[(n_1 - n_0)/(n_1 + n_0)]^2$ [Burmeister1998]. The light reflected at the distinct interfaces interact with each other and lead to interference effects. In the IRM image, constructive interferences are noticeable as bright regions whereas destructive interferences or interfaces of low reflectivity result in dark regions. Reflectivity minima represent regions at which the plasma membrane is closest to the surface and relative intensities can be assigned to changes in the separation distance (Figure 3.1(b),(d)). IRM is basically sensitive to changes in the separation distance above a total membrane-substrate distance of 30 nm. For values between 0 and 30 nm, which is an important range for bond interaction analysis, the relative intensity changes are not sufficient to accurately resolve the separation distances and, thus, other techniques

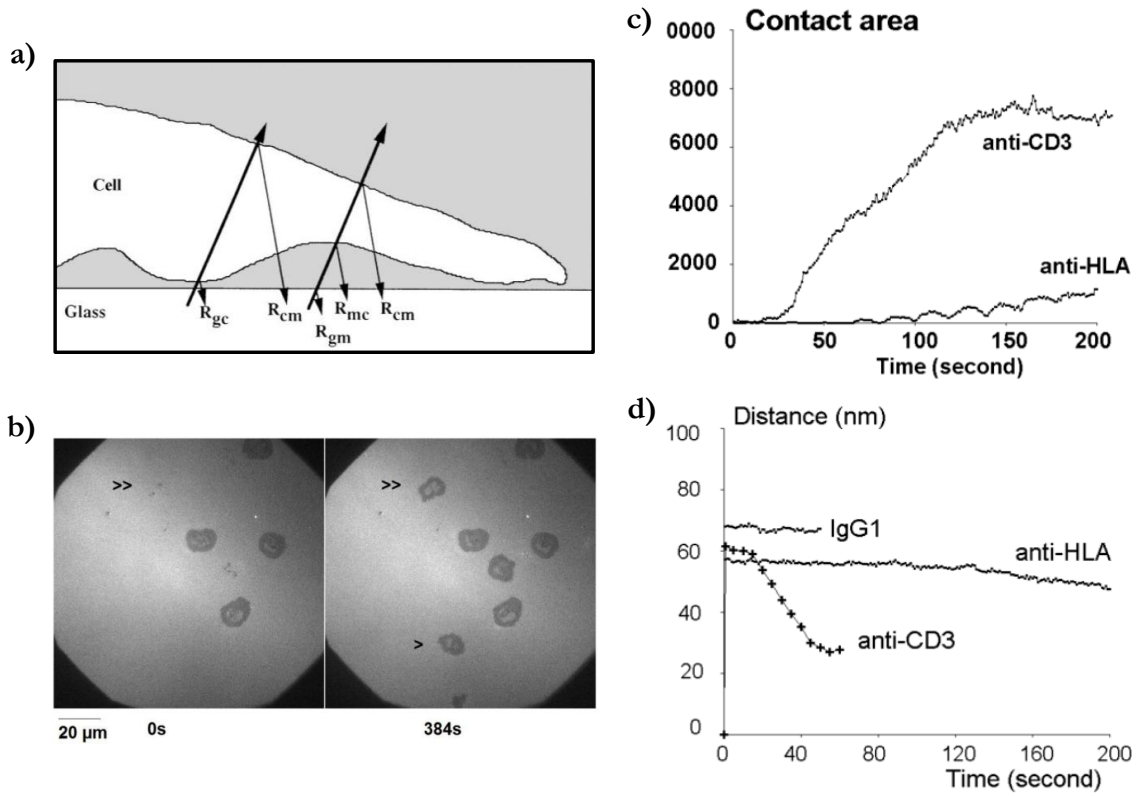

Figure 3.1: a) Schematic illustration of interfaces involved in reflection of the incident light (thin arrows), where R_{gc} is the glass/cytosplasm, R_{gm} is the glass/medium, R_{mc} is the medium/cytoplasm and R_{cm} is the cytoplasm/medium reflectivity (taken from [Burmeister1998]). b) IRM imaging of cells adhering/spreading (see arrows). c) Calculated contact area and d) average cell-substrate separation distance representing different features of cell spreading kinetics (taken from [Cretel2010]).

with an improved spatial sensitivity such as total internal reflection fluorescence microscope have to be applied (see Chapter3.1.2). However, the distinct advantage of this technique is that there is no need of fluorescence labeling to follow cell-surface interactions and, hence, it excludes photobleaching problems or possible damaging of cells in presence of fluorescent dyes [Burmeister1998]. In view of cell applications, this technique has been basically used to study in real-time cell adhesion (Figure 3.1(d)), migration as well as detachment from the surface by employing proteolytic enzymes, for instance [Gingell1979, Burmeister1998].

3.1.2. Total internal reflection fluorescence microscopy (TIRFM)

TIRFM is a more sensitive technique compared to IRM, and even small fluctuation in the membrane-substrate contour can be monitored [Burmeister1998]. The detection principle is schematically depicted in Figure 3.2(a). A light beam propagates through a glass substrate and an adjacent liquid solution including cells, and these two media have different refractive indices n_g and n_l, respectively. Total internal reflection occurs at the solid-liquid interface

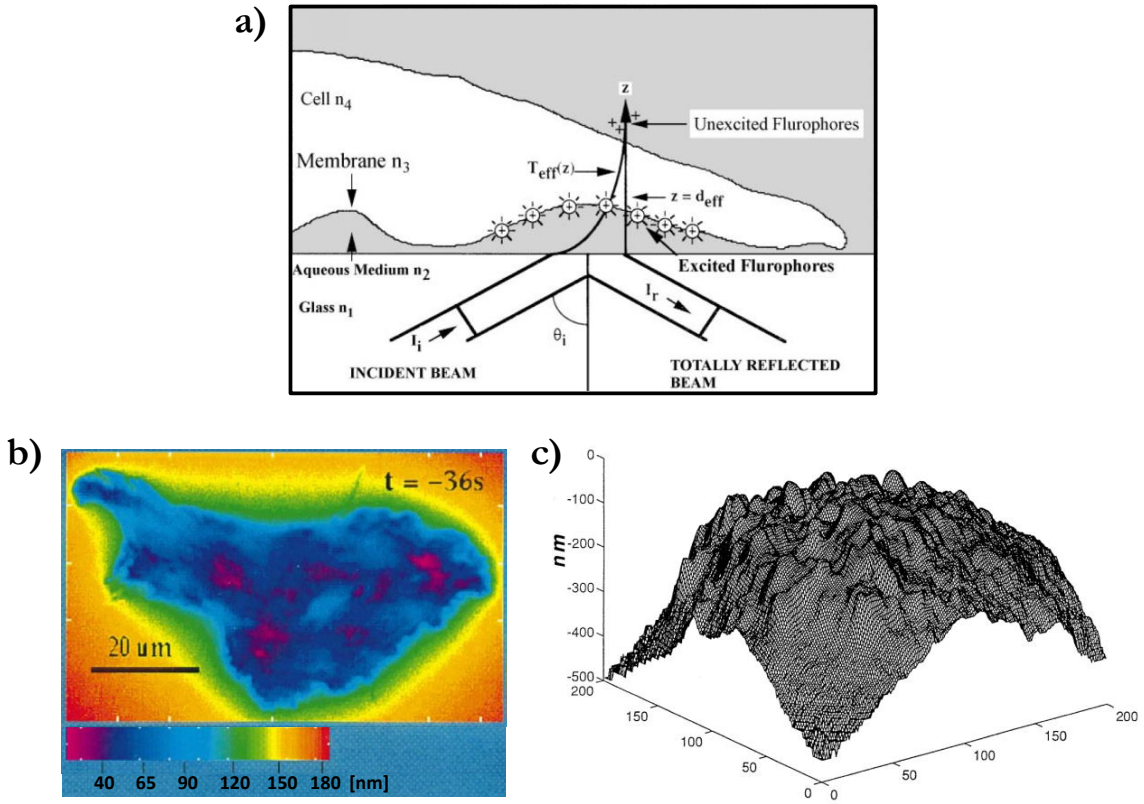

Figure 3.2: a) Schematic of TIRF illumination in the four-phase model of a cell with corresponding exponential decay of the evanescent intensity. b) Typical TIRFM image visualizing a confluently grown endothelial cell and c) shows an example of a fluorescence image transformed into cell-separation distances (taken from [Burmeister1998]).

when the incident light angle θ_i is larger than a critical angle θ_c=$arcsin(n_l/n_g)$ and the condition $n_l < n_g$ applies. During total internal reflection, an evanescent wave field that penetrates the liquid is formed near the interface in terms of a standing wave. Its intensity decays exponentially with distance to the interface and depends on the incident angle θ_i. The penetration depth, instead, is a function of both, the incident angle and the wavelength of the incident light, and is adjustable within the range between 70 nm and 300 nm, which is a fraction of the incident beam wavelength [Axelrod1984, Burmeister1998, Schneckenburger2005]. In the TIRF microscopy, the evanescent field is used for excitation of fluorescence dyes within this limited range of illumination, while dyes farther out in the liquid solution or cell body remain unexcited. In contrast, the lateral illumination area can account for several hundred microns in each dimension [Kobitski2004].

In case of dynamic cell-surface interactions, the simplified solid-liquid light transmission model has to be substituted by a 4-phase system consisting of a glass substrate (phase 1), a water-filled gap (phase 2), the lipid membrane (phase 3) and the cell cytoplasm (phase 4) as illustrated in Figure 3.2(a) [Burmeister1998]. The cells adhere at the glass substrate and

their plasma membrane is labeled with fluorescent dyes. Dyes within the limited evanescent field range at the vicinity of the interface are selectively excited and detected by capturing the corresponding fluorescence emission (Figure 3.2(b)). In comparison to conventional microscopy, where the entire cell body is illuminated, the selective excitation reduces significantly the fluorescence background signal [Kobitski2004]. The separation distance between the cell membrane and the substrate and, thus, the corresponding cell contour or topography can be determined by varying the angle of incidence (Figure 3.2(c)) [Cretel2010, Burmeister1998]. In general, this method is suitable for single-molecule imaging [Tokunaga1997] and has also been applied to detect cell adhesion/spreading, migration as well as endocytosis and exocytosis in living cells [Thompson1997, Schneckenburger2005, Betz1996]. The main difficulties of TIRF microscopy can be of either intrinsic or extrinsic nature. Intrinsic errors include local variations in the refractive index, a light scattering by intracellular compartments, and intensity modulations by unspecific absorption and dye aggregation can distort the results when fluorescence images are transformed into cell-separation distances. Extrinsic errors comprise sensitivity improvement or the reduction of background signal arising from other intrinsic/extrinsic fluorophores, their limitation to transparent substrates, the alignment of the optical system and, as in all fluorescence-based techniques, photobleaching by repeated imaging with high light intensity remains an issue [Burmeister1998].
With regard to the lifetime of organic fluorophores, an interesting alternative of cell labeling is offered by colloidal metallic particles and quantum dots [Parak2005]. Quantum dots are semiconductor nanocrystals that show size dependent fluorescence emission wavelength and reduced tendency to photobleach. They are used in a similar manner as their organic counterparts in several in vivo or in vitro biolabeling studies and are especially promising in optical real-time monitoring with high time resolution [Parak2005, Kobitski2004].

3.1.3. Surface plasmon resonance microscopy (SPRM)

A surface plasmon is an electromagnetic wave associated with charge density oscillations at the surface of a conductor, e.g. a gold or silver layer [Yeatman1996]. Surface plasmon resonances can be excited by optical means at the interface of a metal and a dielectric layer under the condition that their dielectric constants have opposing signs [Homola1999]. The electromagnetic wave or the surface plasmon wave travels along the interface, and due to energy and momentum boundary conditions, it is distributed perpendicular to the interface in an asymmetric manner in both layers. The majority of the field is concentrated in the dielectric with an exponential (evanescent) decay from the interface, and the typical decay length is in the range of some hundreds of nanometers [Giebel1999]. Most of the experimental configurations used to generate surface plasmons are based on opitcal prisms-coupling, grating-coupling and optical waveguide-coupling systems [Homola1999]. Prisms-based coupling of photons into the metallic layer relies on the attenuated total reflection (ATR) method, usually realized by the

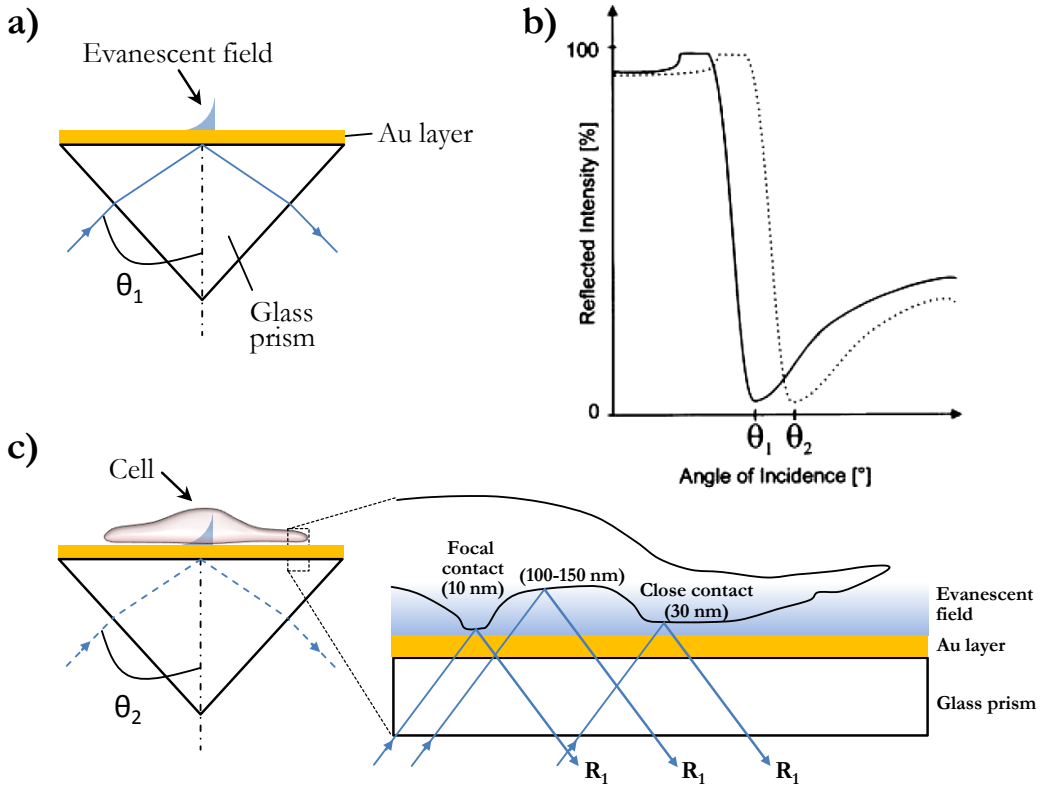

Figure 3.3: a) ATR method of surface plasmon excitation at resonance angel θ_1 b) Cells within the range of the evanescent field lead to a shift of the resonance excitation angle to larger values $\theta_2 > \theta_1$. Undulations at the cell membrane-metal interface are visible as changes in the reflected intensity R ((a) & (b) after [Giebel1999]) c) Reflectivity curves without (solid line) and with a dielectric material in the region of the evanescent field (dotted line) (taken from [Giebel1999]).

Kretschmann configuration, which is similar to that of the TIRFM. Plasmon resonance is excited by an incident light beam being totally reflected at the interface between the prism and a thin metallic layer of about 50 nm thickness (Figure 3.3). Consequently, the reflectivity shows a pronounced dip at the resonance angle θ_1 (Figure 3.3 (c), solid line). The evanescent field at the outer metal surface depends on the refractive indices and thicknesses of the involved materials. When a dielectric material with a higher refractive index, a cell for instance, approaches the metal surface and enters the evanescent field region, it modifies the propagation of the field, resulting in a shift of the angle of resonance to higher angles (Figure 3.3 (c), dashed line). Once the dielectric constant of the cell is known, the degree of the angle-shift can be transformed into corresponding separation-distances. Usually, a fixed angle of incidence is chosen and possible spatial variations between membrane and metal surface are recorded as relative intensities of the reflectivity [Giebel1999].
The application of SPR microscopy in biology are predominantly focused in biosensing at the molecular level or adsorbed thin layers of nanometer thickness [Homola1999, Yeatman1996].

Giebel et al. used a prism-based configuration to monitor in real-time cell-surface interactions, with rather low spatial resolution due to distortions comparable to TIRFM [Giebel1999]. An improvement was achieved by optical microscopy objective-based systems, which can be applied for continuous monitoring of single-cell-surface adhesion and this seems to be a suitable tool for investigating related dynamic processes including migration and detachment [Wang2012].

3.1.4. Whispering gallery mode resonance (WGMR)

This optical technique is based on whispering gallery modes (WGMs) in micro resonators (or cavities) of different shapes including spheres, cylinders, toroides, rings and disks [Vollmer2008a]. Whispering gallery modes (WGM) are types of waves that travel inside the resonator in a plane along the resonator-ambient interface by total internal reflections (Figure 3.4a)). WGMs can be characterized by their polarization and three quantum numbers associated to field maxima numbers in radial, azimuthal and polar orientation. A commonly utilized method to excite WGMs in resonators with a laser beam is the evanescent field coupling from a tapered optical fiber [Vollmer2008b] or the exploitation of fluorescent dielectric particles [Himmelhaus2009]. The most important factor is the geometry of the resonator. The bandwidth and the wavelength position of the modes depend on the shape and size of the particle and as long as the spherical symmetry is maintained, the modes are degenerated and, thus, can freely travel in any plane. During the uptake process, the shape of the particle is changed due to applied cytoskeletal stress and this deformation lifts the degeneracy leading to a corresponding broadening into bands of modes (Figure 3.4b)). Band broadening is additionally accompanied by a red-shift of the modes caused by the higher refractive index of the cell body enclosing the particle compared to the pre-endocytosed state of the particle being surrounded by the liquid cell medium. As soon as the endocytosis process is completed, the cell's cytoskeleton relaxes again and the band broadening vanishes [Himmelhaus2009].

Micro resonators or cavities have sizes up to 100 μm in diameter and are suitable to detect molecules, DNA, membranes, viruses or even cells by simple adsorption or binding at the resonator surface [Vollmer2008a]. Challenging in the evanescent field coupling scheme is the control of the nanometer-gap between the resonator and optical fiber. This requires a lot of effort on the mechanical precision setup and represents a limiting factor in regard of the resonator size. This disadvantages are eliminated by exploiting fluorescence particles for WGM excitation and practicable particle sizes down to about 6 μm in diameter can be applied, which qualifies them for endocytosis analysis experiments [Himmelhaus2009]. Emphasis has to be placed on the associated restrictions in utilizing fluorescent dyes as resonators. Despite standard problems such as photo bleaching or permanent illumination of cells with laser light also reproducibility or comparability of results is an important subject. This is attributed to the large shape and size dependence of the WGMs and, thus, a high quality with low particle-to-

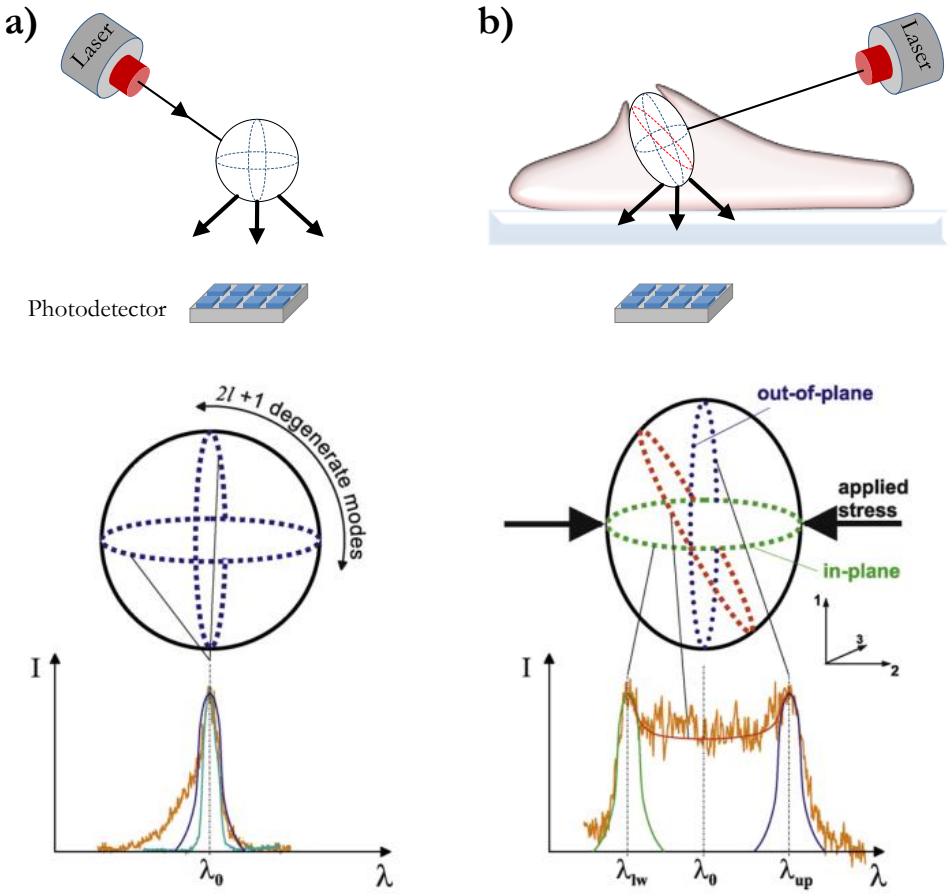

Figure 3.4: Sensing principle utilizing whispering gallery modes a) Laser beam excitation with the respective WGM spectrum of fluorescence particles suspended in cell medium (after [Himmelhaus2009]). b) Mode broadening during the uptake process due to induced cell stress leading to particle deformation and loss of mode degeneracy (taken from [Himmelhaus2009]).

particle deviations is required. Furthermore, this technique is less suited to analyze multiple cell experiments simultaneously required for statistic or high throughput analysis.

3.2. Quartz crystal microbalance (QCM)

The piezoelectric quartz crystal microbalance is an acoustic resonator technique, which is sensitive to mass changes during binding events or film deposition at the quartz surface [O'Sullivan1999, Wegener2001]. Typically, a QCM consists of a thin piezoelectric quartz crystal disk embedded between two metal electrodes (Figure 3.5(a)). The application of an alternating electrical potential across the quartz disk induces crystal oscillations (acoustic waves) at a characteristic resonance frequency f_0. The resonance frequency is directly proportional to the mass attached at the surface of the quartz disk and any mass changes lead to a respective frequency shift $\Delta f \propto K f_0 \Delta m$ [O'Sullivan1999, Gryte1993]. Beside material/setup

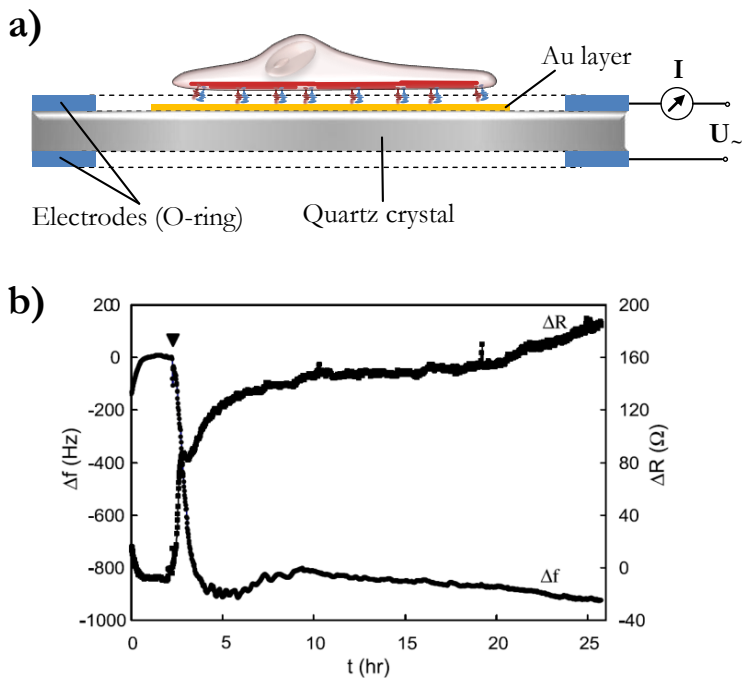

Figure 3.5: a) Basic configuration of a QCM system used to measure cell-surface interactions (after [Marx2005]). b) Typical resonance frequency and resistance shift due to sedimentation (arrow) and spreading of epithelial cells to the Au-coated crystal surface (from [Marx2005]).

specific properties including the active area, shape and thickness or mass of the crystal, the initial resonance frequency f_0 also depends on the operating environment, which can basically be vacuum, air or liquid. Cell experiments automatically imply a liquid solution and its viscosity and density are parameters of high impact to f_0 [Marx2005]. In addition to mass detection, also energy dissipation processes (energy loss of the oscillator) can be measured by analyzing the bandwidth w or the frequency-to-bandwidth-ratio as well as the resistance R of the resonator [Marx2003].

Cells adhering or spreading on the crystal(-coated) surface reveal a time-dependent, reversible QCM frequency shift as shown in Figure 3.5(b), which was demonstrated by subsequent detachment of cells [Marx2005]. The attached cell mass and, thus, their number is extracted from the evaluation of Δf and ΔR. The interpretation of both shifts strongly depend on the material properties attaching the crystal. Cells are usually treated as a non-rigid viscoelastic film, which do not obey the Sauerbray equation supposed to describe rigid behavior of attached layers. The calibration and data interpretation represent a decisive aspect of this detection technique. An additional crucial question, undiscussed so far, is to what extent the crystal oscillations affect and possibly distort the natural cell attachment/spreading behavior during the measurements. However, this method was successfully applied to monitor in real-time cell adhesion/spreading, detachment and stimulated exocytosis of biomolecules [Fredriksson1998, Marx2005, Cans2001].

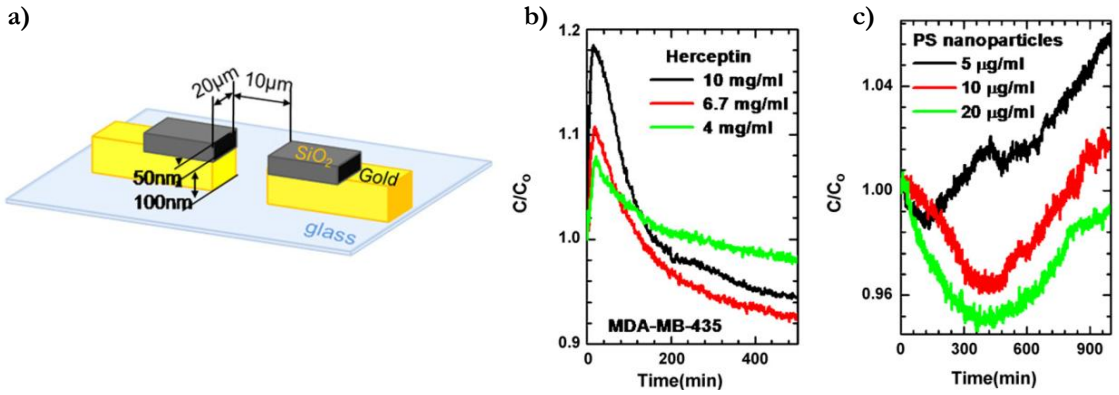

Figure 3.6: a) Graphic illustration of a chip-based capacitor sensor. Real-time monitoring of receptor-mediated endocytosis (b)) and non-specific pinocytosis (c)) (taken from [Lee2010]).

3.3. Capacitive sensing

Capacitance is associated with the storage of an electrical charge, and the structure of the capacitor can be arbitrary. A conventional capacitor consists of two parallel plate electrodes, and its capacitance, which is the ratio of charge to applied voltage, is a function of the dielectric constant (k) between the plates, the area (A) and the distance (d) of the plates, and they relate to each other as $C = \epsilon_0 \epsilon_r kA/d$, with ϵ_0 and ϵ_r as the vacuum and relative permittivity constant, respectively. In capacitance-based monitoring techniques, usually the main parameters remain constant except for one variable, which can be the plate distance, area or the dielectric property. Pertaining cell monitoring analysis, the cell body or its membrane is considered as a capacitor structure that can be charged. This is realized by applying external electrical fields that leads to a cell polarization by accumulating surface charges at the cell membrane. This membrane polarization or capacitance is, therefore, proportional in magnitude to the overall cell membrane area. Hence, changes in cell morphology that are associated to cell-particle interactions lead to immediate capacitance changes [Holevinsky1998]. Holevinsky et al. [Holevinsky1998] introduced an invasive voltage clamp method where one electrode is placed inside and the other one outside the cell. Depending on the size and composition of particles being exposed to the cells, they observed critical membrane capacitance decreases during cell phagocytosis experiments. Lee at al. (2010) presented a capacitance-based sensor for real-time monitoring of cell polarization in an external AC electric field as shown in Figure 3.6 a), and they were able to distinguish between receptor-mediated endocytosis (Figure 3.6 b)) and non-specific pinocytosis (Figure 3.6 c)). Another chip-based approach employs high-density interdigitated electrode systems (μIDES) to monitor in real-time cellular stress responses as a toxic reaction to nanoparticle exposure [Richter2007, Richter2011]. A similar technique based on impedance sensing was also employed for online monitoring of cell migration [Wang2008].

One of the challenges using such dielectric methods as cell analysis tools is, first of all, to be

able to distinguish between the cell and the surrounding cell medium, and in a further step to determine precisely cell morphology changes [Lee2010]. To achieve this, a precise control of size, shape and passivation of the sensor structures is required [Richter2007]. Furthermore, it is difficult to distinguish between resembling processes such as endocytosis and exocytosis [Holevinsky1998].

3.4. Magnetoresistive sensing

In cases where the target cell or molecule of interest is inherently non-magnetic, the magnetic detection schemes is exclusively based on magnetic particles that serve as labels. Magnetic labels are associated with a variety of advantages. First of all, their magnetic properties remain stable over a long period of time. They can be arbitrary in size and additionally, their surface can be functionalized with distinct receptors allowing targeted investigation of specific molecular recognition events, exploring for instance the versatility of cells endocytic pathways. Furthermore, the sample of interest or other components in the surrounding liquid solution are basically of non-magnetic nature, which excludes any magnetic interferences and helps to improve the detection limit. Another unique feature is the ability to manipulate and guide particles by means of magnetic gradient fields generated by external coils or micro fabricated on-chip conduction lines [Manteca2011, Megens2005]. This enables the acceleration of molecular binding processes compared to usual thermally activated diffusion [Heer2007] and the precise on-chip positioning of magnetically labeled species at predetermined sensing zones [Panhorst2005a, Graham2002, Lagae2002].
Magnetic particles in combination with a detection unit that is sensitive to magnetic fields constitute a functional architecture which is capable to act as a real-time monitoring tool. The magnetic stray field of these particles is transformed into electronic signals by a variety of magnetic transducers including Hall probes, giant magnetoimpedance devices or sensors, atomic force microscopes, superconducting quantum interference devices (SQUIDs) or magnetoresistive sensors [Grossman2004, Megens2005]. However, to date only the last two techniques have been employed for cell analysis. SQUID magnetometers are able to detect not only magnetically labeled bacteria but also binding rates between functionalized magnetic particles and bacteria cells by discriminating the relaxation times of bound (Néel relaxation) from unbound (Brownian relaxation) particles in a pulsed magnetic field [Grossman2004]. SQUIDs operate in a cryogenic environment and the close distance between sensor and sample holder exacerbates the temperature control of the investigated sample, which is usually not crucial for robust cell types such as bacteria [Carr2007]. Still, SQUID-based studies with environmentally sensitive organisms such as adherent cells are missing. In contrast, sensors operating at room temperature based on magnetoresistance have already demonstrated their ability to detect both static as well as dynamic cell-surface interactions with adherent and non-adherent cell types [Shoshi2012a, Shoshi2013, Ionescu2010, Loureiro2011].

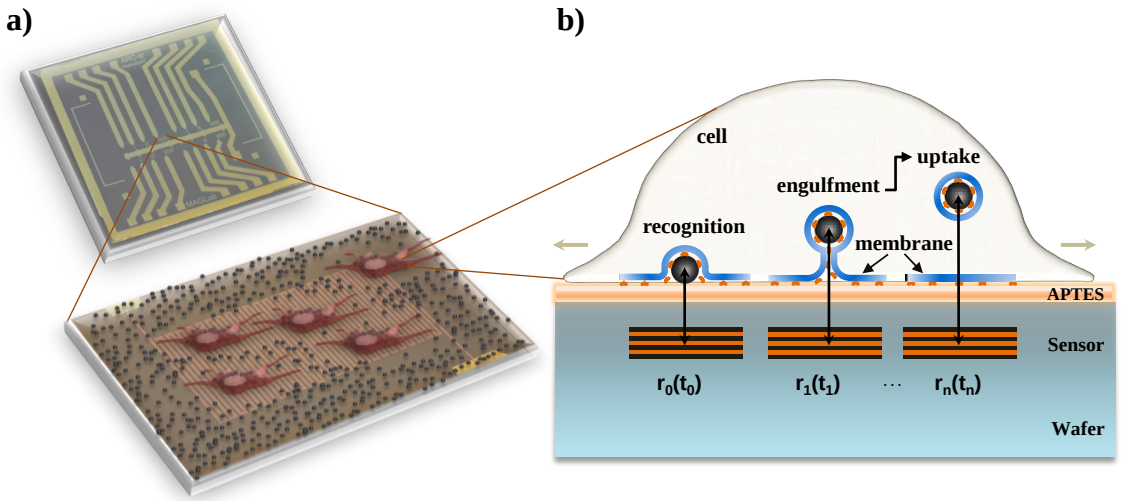

Figure 3.7: (a) Sketch of spread cells on top of a magnetoresistive sensor surface covered by pre-immobilized magnetic particles.(b)Cross-section sketch of phagocytosis stages: After particle recognition, the cell starts engulfing and finally internalizing the particle in phagosomes,leading to an increase of the particle-to-sensor distance r(t).

The first prototype of a magnetoresistive-based biosensor called Bead Array Counter was developed by scientists of the Naval Research Laboratory [Baselt1998]. The individual sensing elements were designed to detect even single micron-sized magnetic particles and this multi-analyte sensor showed good selectivity and sensitivity in DNA hybridization arrays [Edelstein2000, Miller2001]. The magnetic detection idea was rapidly adapted by a number of other research groups as reviewed by Megens et al. [Megens2005] with a variety of sensor configurations and designs focusing from single-bead to high bead-concentration detections. A broad range of magnetoresistive sensor types has been employed comprising giant magnetoresistive (GMR), spin valve (SV), tunneling magnetoresistive (TMR), or anisotropic magnetoresistance (AMR) sensors, but the most common biosensors are GMR and SV sensors. Although the magnetoresistive detection approach can now be considered as firmly established biochip principle [Megens2005], its application in the research field of cell biology with special focus on dynamic cell-environment interactions is rather new [Shoshi2012a, Shoshi2013]. Ionescu et al. ([Ionescu2010]) developed a TMR-based biosensor enabling the detection of single magnetotactic bacteria (*Magnetospirillum* sp.), and they succeeded to additionally characterize their endogenous magnetic nanoparticle properties within magnetosomes. Freitas and co-workers presented a flow cytometry system based on a magnetoresistive (SV) chip, and they succeeded in counting magnetically labelled cells that flow within integrated microfluidic channels above SV sensors [Loureiro2011]. More recently, Helou et al. reported on a GMR-based flow cytometry workflow with integrated sample preparation and they were able to detect cancer cells in whole blood [Helou2013]. Even though these studies essentially confine themselves on giving simple informations about the presence or absence of magnetically labeled cells,

they still demonstrate the potential of the magnetic approach in cell biology. By means of the magnetoresistive methodology, a variety of biologically more relevant nano-biointerface studies including dynamic cell-environment interactions can be realized.
Next, the concept of magnetoresistive-based monitoring of cell phagocytosis (uptake) during their spreading process is presented as an example. The idea of all other real-time monitoring experiments performed within this thesis is basically similar and is briefly discussed in the relevant sections. The detection principle is based on measuring changes of the local magnetic stray field of superparamagnetic particles (beads) within embedded magnetoresistive sensors. These stray field variations are induced by distance changes of the beads relative to the sensor during dynamic cell-bead interactions. The approach is sketched in Figure 3.7. Initially, beads are immobilized onto various sensors of the biochip surface. The bead-induced response of the underlying sensor depends on the magnetic moment, the number of immobilized beads as well as the mean vertical separation distance r(t) to the sensor layer. When cells attach to and spread on the chip surface, they start to internalize the beads, which results in an increase of their mean vertical distance (Figure 3.7b)). With the increasing distance, the stray field strength of a bead at a point within the sensor region decreases approximately by r^{-3}, which results in a lower sensor signal. As long as all other parameters are fixed, the sensor output decreases proportionally to the time dependent progress of cell spreading and phagocytosis, which allows continuous monitoring in real-time.
In contrast to fluorescent-based methods, this purely magnetic approach enables long-term monitoring without facing difficulties like photo-bleaching or background noise from tissue in terms of autofluorescence [Megens2005]. Another unique feature is the capability of measuring the average post-phagocytosis bead-to-sensor separation distance within living cells. In view of drug delivery applications, this information could be used not only to study phagocytosis, but also to monitor possible subsequent exocytosis behavior. By tailoring the surface bio-chemistry and/or physical characteristics of the magnetic drug carriers, this methodology might be used to analyze and tune the drug dwell time in cancerous cells/tissue, thus improving their efficiency.
In order to realize a real-time monitoring technique for investigating cell-environment interactions, a magnetic lab-on-a-chip system has been developed, and a detailed description of its components and advantages is given in the following chapter.

4. Magnetic lab-on-a-chip (MAGLab)

Adherent cells such as fibroblast continually probe their (micro-)environment, and a crucial parameter for immediate and long-term cell behavior are external influences that vary in time and space and finally trigger cellular responses that determine their phenotype. The main influences in-vivo or in-vitro are simply cell-cell interactions or interactions with their extracellular environment [Paguirigan2008]. Thus, in order to reproducibly investigate such kind of interactions, one needs a precise control of the environmental conditions. Most standard methods represent macroscale techniques based on culture flasks, Petri dishes or microtiter plates with dimensions in the centimeter regime or even larger. The control of the surrounding environment with such methods is only possible to a limited degree [Paguirigan2008]. Especially, a fast control of changes in the environment is difficult to achieve. In this regard, superior technical possibilities are offered by microscale methods including microfluidic or lab-on-a-chip technologies, which can be considered as down-scaled versions of macroscale devices that additionally exploit the advantages of miniaturization (laminar flow etc.) [El-Ali2006, Paguirigan2008].

In microfluidic labs on chip, the size of microfluidic channels can be down-scaled to few micrometers, which enable the controlled transport of fluids with volumes in the range of 10^{-9} - 10^{-18} liter [Whitesides2006, Blazej2006]. The most significant advantages of miniaturizing devices include, first of all, improved analytical performance in terms of faster and parallel measurements with higher sensitivity and selectivity. Second, also the consumption of reagents is minimized, the automative integration is increased and, as a result, the total costs including manufacturing are significantly reduced [Kuswandi2007].

Employing LOCs for cell biology assays offer a variety of new opportunities compared to standard laboratory bench-scale methods. Due to the miniaturization (extremely low volumes) and the integrated passive or active pumping systems, LOCs provide a suitable platform for temporal and spatial control of the cellular environment. Furthermore, by appropriate designing of microfluidic systems, e.g. its dimensions, geometry and physiochemical surface properties, it is possible to accomplish microenvironments that mimic for instance the extracellular matrix and allow to study interactions close to those found under in vivo conditions [El-Ali2006].

In chip-based techniques also the detection system has to be miniaturized, and their integration is basically limited by the sensors sensitivity and scalability [Kuswandi2007]. Using small sample volumes for analysis automatically implies a small amount of the targeted analyte to be detected and, therefore, a high sensor sensitivity is required. One successful approach is to scale down the size of the sensing unit, which is not compatible to all kinds of detection methods (for example to those based on conductivity or potential measurements) [Kuswandi2007]. In contrast, as already mentioned in Chapter 3.4, magnetoresistive sensors show an excellent sensitivity and their scalability goes down to the sub-micrometer regime enabling even single-

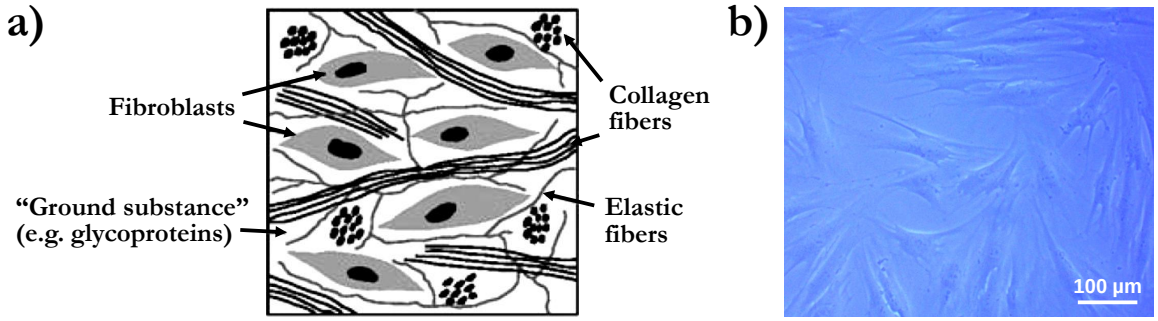

Figure 4.1: (a) Basic components of the extracellular matrix in dermal connective tissue (from [Williams1998]). (b) Optical phase contrast image of fibroblasts 24 hours after seeding. Cell confluency is reached after about 72 hours.

bead detection.

The magnetic lab-on-a-chip or MAGLab system developed during this thesis integrates superparamagnetic particles, microfluidics and magnetoresistive sensors, which are subsequently discussed in the following sections. In addition, two different types of human cells involved in the experimental studies are described. Also, the MAGLab-Setup itself is presented and its basic functions are described in terms of magnetoresistive detection, three-dimensional particle manipulation by applying magnetic forces and on-chip sample preparation/analysis.

4.1. Cell cultures

The interaction between cells and particles depend´s on both the type of cells as well as the type of particles employed. The scope of the presented work includes both types of variations. Next, the cells involved in this study are described and their biological functions are highlighted.

4.1.1. Normal Human Dermal Fibroblasts (NHDF)

Fibroblasts are present in all kinds of connective tissue and are considered as its basic cellular component [Grinnell1994, Williams1998]. Fibroblasts in mammals are widely distributed, and cells isolated from different sites of the body show a high degree of heterogeneity [Kalluri2006]. This topographic diversity simply reflects influences due to local micro-environmental factors [Kalluri2006, Williams1998]. The human skin consists of three distinct layers, namely the epidermis, dermis and subcutis, wherein the first layer is the outermost. NHDFs are cells from the dermal connective tissue and exhibit, especially in a confluent state (highest cell population grown on a two-dimensional surface), an elongated shape (Figure 4.1 b)).

Fibroblasts are primarily responsible for the synthesis of the extracellular matrix (ECM), e.g. the production of proteins and polysaccharides such as collagen (Figure 4.1 a)). At the same time, they also contribute to the ECM degradation and regulate its turnover by means

of phagocytosis. Thus, fibroblasts actively influence the physical and chemical structure of each form of connective tissue and play a crucial role in maintaining the ECM homeostasis [Kalluri2006]. Another important function of fibroblasts is their involvement in the inflammatory and immune response by producing cytokines that mediate the interplay between fibroblasts and leukocytes. They also contribute to antigen-presentation or regulate the epithelial differentiation by releasing growth factors [Kalluri2006, Williams1998].
Apart from their general functions under normal healthy conditions, they also play an important rule in cases of injury by actively driving the wound healing process. They rapidly migrate to the injured location in order to substitute the damaged dermis by new deposition of ECM or to close the margin of open wounds by applying contractile forces. In most cases, injuries pertain the skin and, therefore, skin fibroblasts (NHDFs) are the cells of choice in common wound healing assays [Grinnell1994]. Principally, also tumors can be described as wounds that do not heal and, thus, fibroblasts contribute significantly in the progression, growth and spread of cancers [Kalluri2006]. In summery, the functions of fibroblasts are versatile and they are the most abundant cells in human bodies. Thus, the chance to be exposed to particles is high, and this qualifies them as candidates for model cell systems investigating cell-particle interactions at a nanometer level.

4.1.2. Prostate cancer cells (DU145)

DU145 cancer cells belong to the epithelial family and were originally isolated from metastasis of the nervous system of a Caucasian man [vanBokhoven2001]. Epithelium together with connective, muscle and nervous tissue comprise all types of tissue in mammals [Alberts1989]. A common characteristic feature of all epithelial cells is their cell polarity. As depicted in Figure 4.2 d), they possess two different surfaces, namely the apical and basal side. This enables them to form oriented colonies, whereas the inner (outer) side of the colony represents the basal (apical) surface. Epithelial cells grow on a basement membrane, e.g. a specialized extracellular matrix located at the basolateral side of cells, and line, for instance, the interior surface of blood vessels [Kalluri2006]. The migration of healthy epithelial cells is a crucial mechanisms during embryogenesis and wound healing. They also play an essential role in tumor invasion and metastasis due to the fact that most of metastatic human tumors originate from epithelial-cell tissue [Wells2005].

The most striking feature of cancer cells compared to their healthy counterparts is their unregulated cell proliferation (growth). The reasons are different mutation events and epigenetic changes that lead to the creation of cancer (carcinogenesis). In the early tumor stage, cancer cells are usually embedded in the epithelium and build a lesion (none healing wound) within the respective tissue (Figure 4.2 b)). As long as the mutated cancer cells are located inside the basal lamina, the cancer is considered as benign and is easily removable by surgery. Once they break through the basal lamina and surrounding blood vessel walls, the

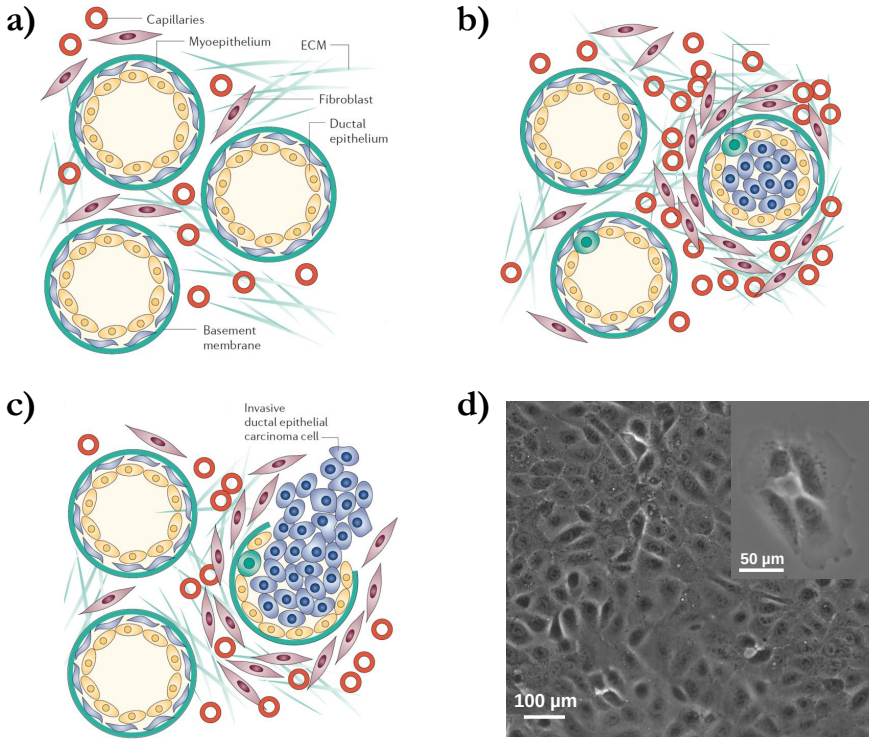

Figure 4.2: Progressive stages in cancer development. a) Normal tissue with intact ductal epithelial cells and basement membrane. b) Lumen containing carcinoma cells still confined by the basement membrane inside the duct (benign tumor). c) Breakthrough and invasion of ductal carcinoma cells leading to metastasis (maligning tumor) (all from [Kalluri2006]). d) Phase contrast images of DU145, whereas the inset shows characteristic formation of polar colonies.

cancer cells enter the blood stream and are dispersed over the entire body (Figure 4.2 c)). Usually, about one per million of the escaped cells survive and subsequently invade other tissue areas, preferably lymphoid tissue and bone marrow. The embedded cells continue their uncontrollable growth in their new tissue environment allowing the formation of metastases [Kalluri2006, Alberts1989].

The formation of metastasis is the most crucial stage of cancer development and its complexity is still poorly understood. Metastases are responsible in 90 % of all deaths caused by prostate cancer [Alberts1989]. They dramatically impede the therapeutic treatment, and the potential of conventional methods including surgery or radiotherapy is maxed out. In order to push the limits of therapeutic treatment, new superior diagnosis methods have to be developed. Very promising are approaches based on magnetic particles, which already are established in biomedical applications. For instance, they serve in magnetic resonance imaging (MRI) as contrast agents [Babes1999]. In view of cancer treatment, they can be used as carriers for targeted drug delivery, e.g. they can be guided or accumulated by applying magnetic gradient forces at locations where the cancer is situated. Compared to standard chemotherapies, where

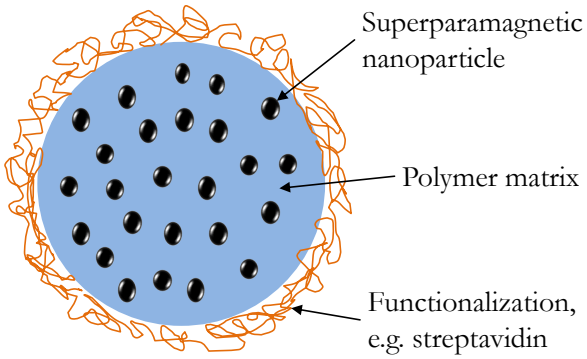

Figure 4.3: Typical structure of magnetic beads.

the drugs are distributed intravenously throughout the entire body, drug-targeting enables a more specific treatment with significantly reduced side-effects [Plank2003]. Once the particles are located close to the carcinoma, they can additionally be heated up by applying alternating magnetic fields (magnetic hyperthermia). The local temperature increase above 42°C leads to the death of all cells exposed to it. In combination with drug-targeting, this approach can lead to improved cancer treatment therapies [Meyer2001].

4.2. Superparamagnetic particles (beads)

Magnetic particles were initially developed by Dynal Biotech [Dynal] for magnetic separation or selection of biomolecules and cells out of a given solution. The surface area of the particles is functionaliazed with complementary receptors that specifically bind to the target analyte. The bound analytes are then segregated by applying magnetic gradient forces. By now, they are used not only as markers but also as carriers that can be guided by external magnetic fields under in-vivo or in-vitro conditions. Thus, a huge variety of applications emerged especially in biomedicine ranging from magnetic resonance imaging, tissue repair, hyperthermia and targeted drug delivery (magnetofection) [Gupta2004, Plank2003, Shoshi2005]. Here, they are employed both for on-chip cell manipulation and the detection of cellular interactions. The main technical advantages using magnetic markers compared to standard fluorescent dyes have already been highlighted previously (see Chapter 3.4). This chapter emphasizes their general structure, the requirements associated with their application in cell biology and especially their magnetic properties that are important for the magnetoresistive detection.

4.2.1. Bead structure and magnetic cell-chip requirements

In most biological applications the efficiency of magnetic particles is highest when they act as individually separated objects. In order to prevent magnetic agglomerations in solution, they should display either paramagnetic or superparamagnetic behavior. Thus, the common structure of most commercially available beads consists of small magnetite (Fe_3O_4) or maghemite

($\gamma-Fe_2O_3$) particles of few nanometers (< 20 nm) in size that are homogeneously embedded into a polymer matrix (Figure 4.3). These nanoparticles are superparamagnetic, e.g. the thermal energy at room temperature is greater compared to the magnetic anisotropy energy, which leads to a fast magnetization switching and time averaged zero net moment. Individual nanoparticles within the bead can be considered as magnetically isolated from each other. In absence of external magnetic fields, the beads act as non-magnetic objects. After applying an external magnetizing field, the magnetite nanoparticles develop a net magnetization in field direction and the beads are magnetized [Rife2003, Ali-Zade2004, Bergmann1992].
In general, there are four variables that determine the final characteristic properties of beads, namely the size, shape, surface biochemistry and magnetic content. These properties are tunable according to the targeted application. Commercially available bead sizes range from the tens of nanometer to micrometer regime, and their "aimed" shape is spherical [MagSense] or ellipsoidic [Bioclone]. Their surface functionalization is versatile and covers a broad area of application-specific surface groups including streptavidin, amine, carboxy, aldehyde, epoxy and more [Bioclone].
The uniformity pertaining the size and shape of beads is important both from the cell biological and magnetoresistive detection point of view. The entire interaction process strongly depends on the size and shape of beads exposed to living cells, which significantly influences the activation of mechanisms involved in the uptake process or the uptake rate itself (see Chapter 2.2.3). For instance, the engulfment rate of spheroidal-shaped particles is higher when they are presented with their tip rather than their long side first [Tollis2010]. Irregularities in size and shape also lead to respective distributions of the magnetic moment, which accordingly results in less reproducible measurements. One way to counteract this effect is to increase the number of measurement repetitions, thus averaging out possible deviations.
The functionalization of the bead surface with proper receptors is a standard method in biology to enable specific binding events at predefined areas. This selective binding method allows for example to capture or confine target analytes on top of functionalized sensor surfaces. Moreover, the biochemical properties of beads is are a decisive factor in interaction studies. Beads of same size and shape but different surface characteristics can lead to completely different results, i.e. from rapid to total refusal of phagocytosis (see Chapter 5.2.1).
Another crucial requirement particularly in long term monitoring investigations with living cells is the stability of the magnetic markers. Usually, commercial particles are dispersed in aqueous buffer solutions (pH 7.4) stabilized by surfactants that show excellent stability for several years [Dynal]. In contrast, particles within phagolysosomes are exposed to an acidic ambient (pH ~4.5) with a variety of hydrolase enzymes. As already discussed in Chapter 2.2.3, the main purpose of phagocytosis is the degradation of the internalized particles.
The size of the particles involved is decisive in activating the uptake mechanism to be investigated. Particles larger (smaller) than 0.5 μm are usually internalized by phagocytosis

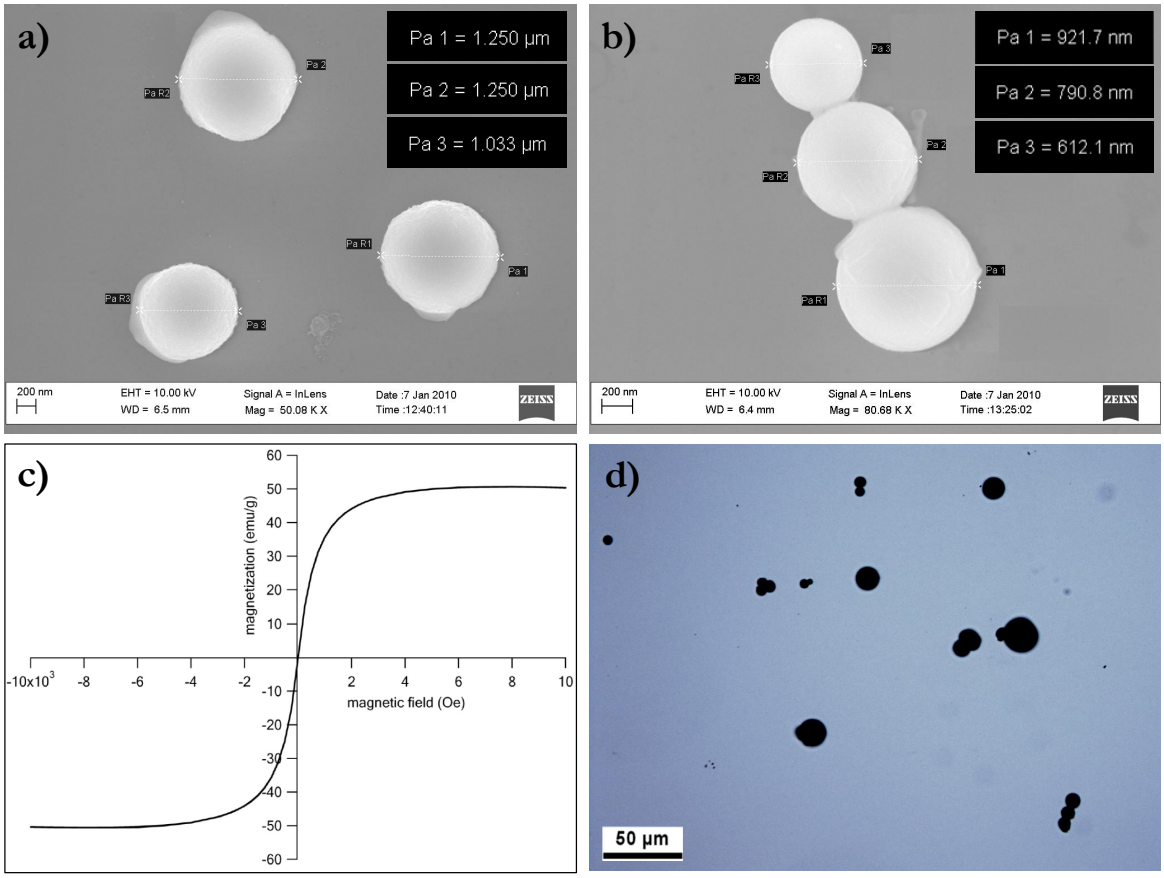

Figure 4.4: (a) and (b) show SEM images of nominally 1.0 μm and 0.5 μm MagSense beads, respectively, and (c) shows their magnetization behavior (from [MagSense]). d) Optical microscopy image of Chemagen beads demonstrating their high size dispersion.

(pinocytosis).
Another factor of fundamental importance is the biocompatibility and non-toxicity of magnetic beads. With regard to a multifunctional cell analytical platform, bead toxicity does not only limit the number of on-chip analytical steps but also has a significant impact on the cells natural behavior.
Finally, from the view of the magnetoresistive bead detection, a high magnetic moment with low variations in magnetic content among beads is of particular interest. To that end, a high and uniform magnetic component concentration is requested [Rife2003].

4.2.2. Beads for on-chip real-time monitoring and off-chip phagocytosis

There are diverse types of commercially available beads and the selection criteria are defined according to the cell-chip requirements. Table 4.1 gives an overview of selected beads, not only for real-time monitoring purposes but also to study the uptake capability and capacity of cells. The bead type that fulfills most of the biosensor demands listed above are MagSense

Table 4.1: Properties of the selected superparamagnetic bead types.

	MagSense		Micromod			Chemagen
Product name/number	MS 0401, Lot SPMA200802		Sicastar –M COOH	Nanomag-CLD-greenF		M-PVA 013
Polymer matrix	Not specified		Silica	Dextran		Polyvinyl alcohol
Surface Functionalization	Streptavidin		Carboxy	Green dye		plain
Magnetic material	Fe_3O_4 nanoparticles					
Nominal diameter [µm]	0.5	1.0	1.5	0.5	1.0	6
Measured diameter [µm]	0.896±0.150	1.192±0.154	-			~2.0-25
Mono-disperse	Yes		Yes			No
Magnetic content (weight %)	> 90		-	80-90		50 – 60
Sat. moment/bead [fAm²]	50	133	39	7	52	-
Moment/bead at 36 kA/m [fAm²]	23	60	-			

particles from the company MagSense Life Sciences, Inc. [MagSense], and they represent the beads of choice for all real-time monitoring experiments. MagSense beads are characterized by uniformity in shape and size (Figure 4.4 a), b)) and possess a magnetic oxide content of over 90 % (per weight), which results in high bead magnetization (Figure 4.4 c)) compared to other bead types with magnetic contents usually in the range between 40 and 90 % [Bioclone, Micromod]. Their surface can be functionalized with streptavidin, carboxyl and antibodies. In all cell studies, streptavidin coated beads were employed.
The uptake strongly depends on the bead shape and size, and this information is usually not given accurately by the manufacturers. Therefore, additional investigations based on scanning electron microscopy (SEM) and dynamic light scattering (DLS) measurements are established to assess the shape, mean bead size and size distribution. Furthermore, the surface charge of the beads is analyzed, which is another important parameter of physicochemical bead properties relevant to cell phagocytosis (Zhang et. al., 2009, Lu et. al., 2009). To that end, both MagSense bead types with nominal size 0.5 μm and 1.0 μm were dispersed in all kinds of solutions used during the uptake experiments. SEM imaging reveals bead diameters of 0.896±0.150 μm and 1.192±0.154 μm, respectively, while the hydrodynamic diameter obtained by DLS depends on the specific buffer solution (Table 4.2 and Figure 4.4 a), b)). According to expectations, the buffer with the lowest salt concentration (dH_2O) shows the largest hydrodynamic diameter, while in buffers with high salt concentration (PBS and DMEM), the particle charge is screened, which leads to smaller hydrodynamic diameters. In general, the beads show a good uniformity with reasonable size dispersion.

According to the manufacturer, the MagSense beads show a pH and temperature stability of 2-10 and 2-120 °C, respectively. They are coated with a dense layer of the protein streptavidin, which has a high binding affinity to the vitamin biotin [MagSense]. The modification of the bead surface serves two purposes: bead uptake by the cells and binding to the silanized sensor surface (see Chapter 4.3.3). Several tests on APTES modified Si-substrates and microtiter plates indicate that both functions are fulfilled by MagSense beads (see Chapter 5.2.1).

Table 4.2: Zeta potential and DLS size measurements of MagSense beads with nominal diameters of 0.5 and 1.0 μm in dH_2O, PBS and DMEM. The pH was measured while stirring at 300 rpm with a bar magnet.

	Zeta potential $[mV]$		Size distribution $[\mu m]$		pH
Nominal size $[\mu m]$	1.0	0.5	1.0	0.5	
dH_2O	-44.2±4.3	-41.7±4.4	1.412±0.234	1.042±0.170	5.6
PBS	-28.3±23.3	-25.9±15.2	1.184±0.119	0.931±0.098	7.2
DMEM (no FCS)	-19.3±36.4	-19.8±14.2	1.260±0.134	0.991±0.132	7.8

Moreover, the zeta potential is determined by measuring the electrophoretic mobility of the particles dissolved in three different buffers (Table 4.2). In addition, the pH of the solutions was also measured. In all buffer solutions, the beads display a negative surface charge ranging from -19 mV to -45 mV. In general, particles suspended in solutions are considered stable when the absolute value of the zeta potential is beyond about 30 mV (Malvern Instruments, 2003). Therefore, beads dissolved in water can be considered as stable, while those dispersed in PBS and particularly in cell medium show a higher tendency of agglomeration. However, in cell experiments the beads are only dispersed in cell medium during a short time period less than 2 hours for preparation and sedimentation to the cell monolayer (see Chapter 7), and we do not observe significant aggregation during real-time monitoring of phagocytosis.

In conclusion, with the specification of the size distribution, surface biochemistry and the zeta potential, the most relevant factors affecting cell uptake are characterized.

In addition to the MagSense beads, we also examined the interaction between cells and other bead types (Table 4.1). The main focus in that regard is to explore to what extent the uptake mechanisms can be influenced by the bead properties. In this case, the magnetic properties have less priority and the selection is focused to spherical beads differing in size and surface functionalization. The first choice are two different kinds of particles from Micromod, which have about the same size as the MagSense particles, but strongly differ in their surface functionalization. This enables to directly compare the cells phagocytic behavior depending on beads provided from the same as well as different manufacturers. The selection criteria of the second choice of beads is simply determined by their size. Chemagen beads are employed to investigate the maximum possible size of a single bead that can be internalized by a human cell. A striking feature of these beads is their high size dispersion ranging from approx. $2 - 25$ μm (Figure 4.4 d)).

The next chapter focuses on the magnetoresistive biochip and the detection of the magnetic dipole stray field of magnetic particles.

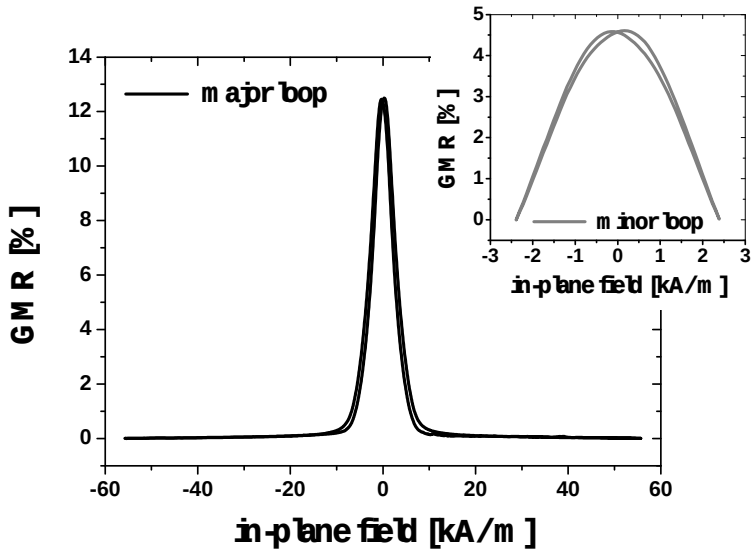

Figure 4.5: Major and minor loop magnetoresistive response of a GMR multilayer system.

4.3. Magnetoresistive biochip

4.3.1. GMR-sensor layout and magnetic characteristics

The fabrication of our magnetoresistive biochips starts with the deposition of a continuous stack of ten permalloy/copper ($Py = Ni_{80}Fe_{20}$/Cu) double layers in the second antiferromagnetic coupling maximum (AFCM) onto a 20 mm × 20 mm piece of a <100> silicon wafer with 50 nm thermal oxide. The complete multilayer system further consists of MgO/CoFe-buffer and tantalum capping layers and has the following composition:

$$Si - wafer/MgO_{4nm}/CoFe_{2nm}/10x[Cu_{1.7-2.4nm}/Py_{3nm}]/Ta_{2nm}.$$

The buffer layers serve as seed layers in order to ensure enhanced growth, whereas the capping layer acts as a primer for the Si_3N_4-passivation layer and protects the stack from oxidation prior to passivation. Figure 4.5 shows the major and minor loop response of an as-deposited and unpatterned GMR stack to external in-plane magnetic fields. The resistivity decreases almost linearly with increasing applied field and goes into saturation at 4.4 kA/m with only minimal hysteresis. The hysteresis is determined by the shift of the GMR-amplitude from zero in-plane field observed in the major loop magnetoresistive response. The average GMR effect is 12 % (maximum measured value of 13.2 %) and results in an average sensor sensitivity of 2.7 % per kA/m. This multilayer system represents a suitable sensor with good sensitivity for detecting the magnetic stray field of magnetic particles.

The continuous layer stack is patterned into individual meander-shaped sensor elements by

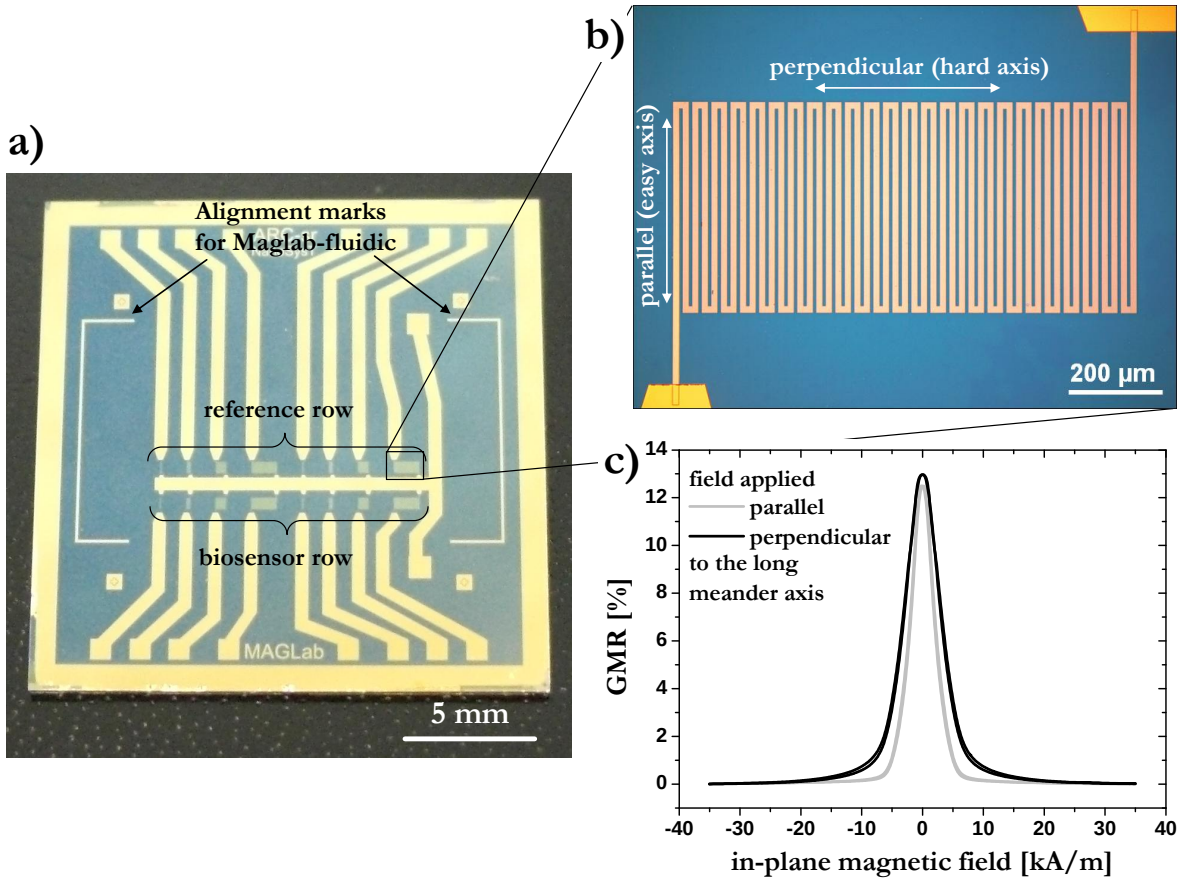

Figure 4.6: a) Magnetic biochip layout. b) Optical micrograph of the meander-shaped sensor of type D and c) its magnetoresistive response to in-plane magnetic applied along the easy/hard meander axis.

positive photolithography and subsequent tantalum or titanium hard mask argon ion etching (a detailed sensor processing is given in Appendix A.1.4). Each chip consists of 16 sensors of four different sizes arranged in two identical rows, representing reference and magnetic particle detection sensors (ref- and biosensors, Figure 4.6 a)). The sensors are designed in a way that the resistance of each of them at zero magnetic field is about 6-8 $k\Omega$. The conductive paths and contact pads consist of $Ta_{10nm}Au_{250nm}Ta_{5nm}$ trilayers and are processed by positive photolithography, sputter deposition as well as etching and lift-off techniques. Finally, the entire chip surface, except for the contact pads, is protected by a 230 nm thick Si_3N_4 passivation layer to screen interactions with cells and fluids including cell medium, buffer and DI water. The dimensions and magnetic characteristics of the individual sensor elements as well as an optical micrograph of sensor type D are displayed in Table 4.3 and Figure 4.6 b), respectively. In Figure 4.6 c) the magnetoresistive response of a D-type sensor to in-plane magnetic fields parallel (easy axis) and perpendicular (hard axis) to the meander lines is shown. Due to the non-isotropic layout of the meander-sensors, there is a shape anisotropy

Table 4.3: Dimensions and characteristics of the different sensor element types.

Sensor	A	B	C	D
line width [μm]	3	5	8.5	13.5
total line length [μm]	48	142	396	988
surface area [$\times 10^3 \mu m^2$]	21.6	63.9	178.2	444.6
H_S perp. to hard meander axis [kA/m]	13.2	10.8	8.8	7.5
Resistance [kΩ]	6-8	6-8	6-8	6-8

present forcing the magnetization along the long axis of the meander lines. Thus, the increasing shape anisotropy leads to higher hard axis saturation fields (H_S) for smaller sensors (Table 4.3), while the easy axis saturation field of 5.2 kA/m is almost identical for all sensor types. Beside shape anisotropy, also contour imperfections at the meander line edges lead to additional domain wall pinning, which contribute to a slightly increased hysteresis from 330 A/m to 540 A/m compared to the magnetoresistive response of the continuous stack (Figure 4.5)[Schotter2004].

4.3.2. Magnetoresistive bead detection principle

In order to prevent particle agglomeration in solutions, we employ types of beads that are of superparamagnetic nature. Therefore, an external magnetic field has to be applied in order to magnetize the beads and to induce stray fields that can be detected by the embedded magnetoresistive sensors. Basically, there are two bead detection principles possible, namely the out-of-plane and the in-plane approach. In the out-of-plane (in-plane) approach, the magnetizing external magnetic field is applied perpendicular (parallel) to the film plane of the sensing layers. Challenging in both approaches is to keep the influence of the external field to the sensor minimal, in order not to affect its sensitivity, while at the same time to maximally magnetize the beads for the highest possible magnetic stray field strength.

The out-of-plane approach was originally introduced by Baselt et al. [Baselt1998] and has gained acceptance by several other groups. The key advantage of this approach is the exploitation of the shape anisotropy of nanometer-thin sensing layers, which allows the application of high external magnetic fields without a significant influence on their magnetization configuration. In our case, the GMR sensor is composed of Py sensing layers of 3 nm thickness. Compared to the lateral dimensions of about 3 μm to 13.5 μm (Table 4.3), their thickness can be considered as infinitely thin. In homogeneously magnetized layers, there is a demagnetizing field H_d and its components can be expressed by the tensor N and the layer magnetization $\vec{M}$: $\vec{H}_d = -N \cdot \vec{M}$. The demagnetizing factor N strongly depends on the shape of the layer and, thus, additionally influences the strength and direction of the demagnetizing field. For layers of infinite thinness, the component of the perpendicular (parallel) demagnetizing factor reduces to $N_\perp = 1$ ($N_\parallel = 0$) [Shoshi2005]. Considering the saturation magnetization

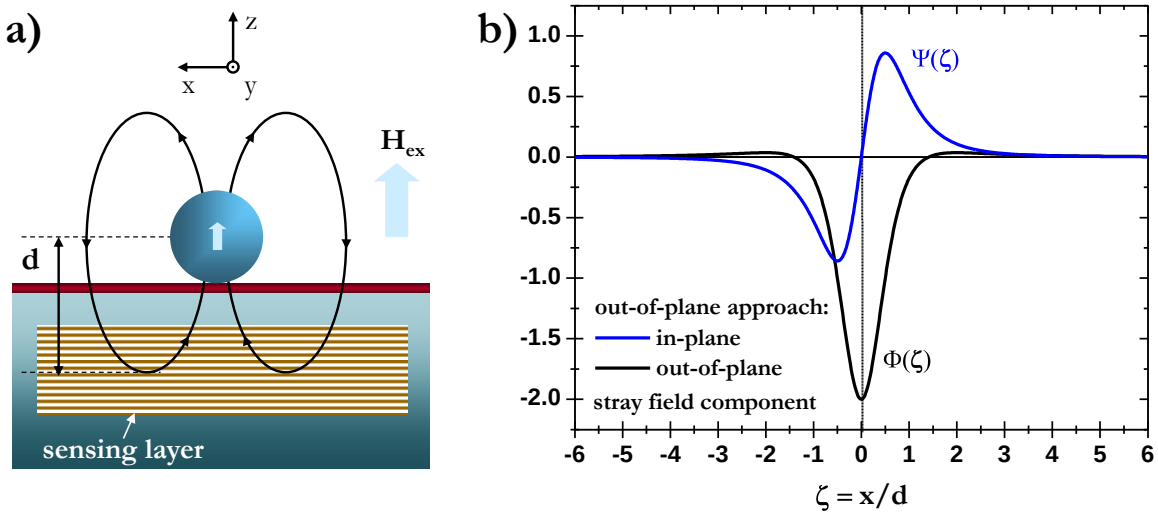

Figure 4.7: Magnetic stray field of a single bead in the out-of-plane magnetization approach. a) Schematic of the out-of-plane approach configuration and b) the corresponding amplitude of the in-plane and out-of-plane stray field component along a straight line with abscissa x for y=0 (after [Schotter2004]).

of the Py ferromagnetic layer of 860 kA/m [Bozorth1993], this results in a demagnetizing field of about the same magnitude, which counteracts the magnetization of the Py layer to align perpendicular to its plane [Schotter2004]. Thus, a large magnetic bead moment can be induced by applying a high magnetizing field perpendicular to the sensor plane without directly affecting the sensor. In contrast, there is no strong demagnetizing field counteracting the magnetization to align parallel to the Py layer plane and consequently, the sensor is highly sensitive to in-plane fields.

Although the sensing layer is sensitive to in-plane fields, principally also the in-plane approach is possible. Here, the external in-plane field superposes the magnetic stray field of the beads and one has to make sure, that the sensitive region of the sensor lies at larger in-plane fields. This is essential, because low magnetizing fields would result in a low bead moment and, thus, unmeasurable low bead stray fields. On the other hand, applying high magnetizing fields leads unavoidably to sensor saturation [Schotter2004].

However, our sensors are sensitive to low in-plane fields and, thus, all measurements are performed at external fields perpendicular to the sensing layer. In the following, the resulting magnetic stray field of a single bead acting on the sensing layer is discussed. The magnetic moment of a homogeneously magnetized sphere is given by its magnetization M and its volume V: $m = VM$. Magnetic beads are composed of nanometer sized superparamagnetic particles, which are dispersed homogeneously within a polymer matrix. Consequently, their effective magnetic moment is proportional to the total volume and magnetization of their magnetic content. A single magnetized bead idealized is a magnetic dipole with its origin at the bead

center and the related magnetic stray field at a distance $\vec{x}$ can be expressed as [Jackson1999]:

$$\vec{B}(\vec{x}) = \frac{\mu_0}{4\pi} \frac{3\vec{n}(\vec{n} \cdot \vec{m}) - \vec{m}}{|\vec{x}|^3} \quad with \quad \vec{n} = \frac{\vec{x}}{|\vec{x}|} \tag{4.1}$$

The magnetic moment $\vec{m}$ depends on the magnetizing field and becomes maximal for saturated bead magnetization, e.g. $M = M_S$. The respective in-plane and out-of-plane component of the bead's magnetic stray field in the out-of-plane magnetization approach is depicted in Figure 4.7 b) and they are calculated according to the following equations [Schotter2004]:
in-plane stray field component:

$$B_{ip}(\zeta) = \frac{\mu_0}{4\pi} \frac{m}{d^3} \underbrace{\frac{3\zeta}{[1+\zeta^2]^{5/2}}}_{\Psi(\zeta)} \tag{4.2}$$

out-of-plane stray field component:

$$B_{op}(\zeta) = \frac{\mu_0}{4\pi} \frac{m}{d^3} \underbrace{\frac{2-\zeta^2}{[1+\zeta^2]^{5/2}}}_{\Phi(\zeta)} \tag{4.3}$$

with $\zeta = x/d$ and d being the vertical distance between the bead center and sensing layer center (Figure 4.7 a)). The in-plane stray field component displays a radial symmetry around the bead's center and reaches maximum magnitude at $d/2$. In comparison, the out-of-plane stray field component is clearly stronger but its influence to the sensing layer is negligible due to the present demagnetizing field in this direction. Only the in-plane component effectively contributes to local magnetization (re-)configuration of the sensing layer [Schotter2004]. Therefore, from the experimental point of view, prior to each experiment the out-of-plane magnetizing field has to be adjusted perpendicular to the chip plane.

4.3.3. Dependence of the sensor signal on bead coverage

In a further step, the local effect of the afore discussed in-plane components of the bead's magnetic stray field to the sensor resistance is investigated. In the experiment, the magnetic particles need to be immobilized on top of the sensor surface, which is the Si_3N_4 passivation layer. Therefore, the sensor surface is functionalized with a 2 % APTES solution (from Aldrich, Inc.) by dissolving APTES in a buffer solution consisting of 99.2 % (v/v) methanol and 0.8 % (v/v) acetic acid. According to AFM measurements, this APTES layer is less than 10 nm thin (data not shown) and ensures both cell growth to the chip-surface as well as immobilization of surface-modified beads, e.g. strepavidin coated MagSense particles of 1.2 μm in diameter. Aminosilane layers are positively charged and, as a consequence, negatively charged streptavidin-modified beads self-assemble due to electrostatic forces [Sivagnanam2008]. This

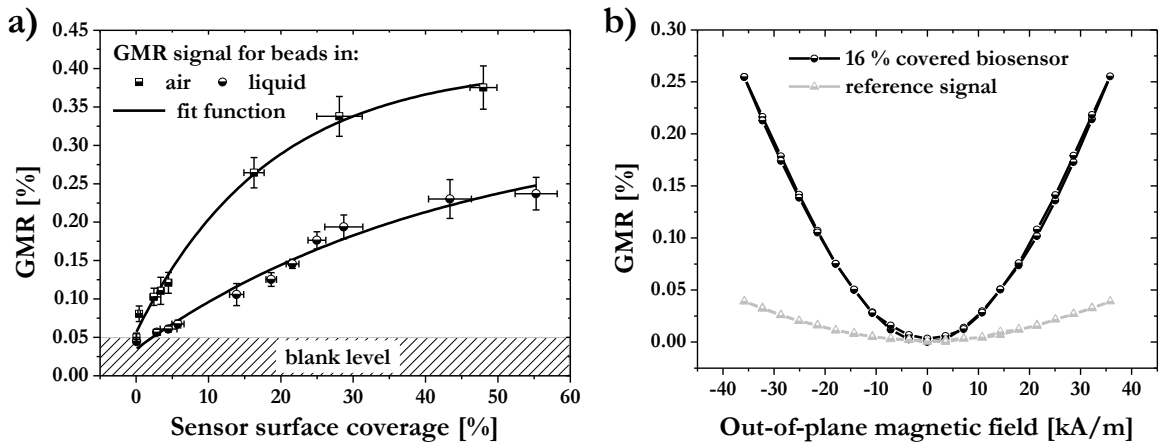

Figure 4.8: a) Dependency of the GMR sensor signal on the bead surface coverage. b) Typical magnetoresistive response of a bead covered biosensor and an uncovered reference-sensor.

ensures, on the one hand, a close bead-to-sensor distance and, at the other hand, a fixed stationary bead arrangement at the sensor surface. A defined bead position is, amongst others, crucial for sensor signal reproducibility for example for buffer exchanges during the cell experiments without bead repositioning.

According to equation 4.2, the maximum in-plane magnetic field of a single 1.2 μm Magsense bead is calculated at the maximum magnetizing field H_{ex}^{max} applied during the experiments. If the bead is in direct contact to the sensor surface, a minimum bead-to-sensor distance of $d_{min} = 860\ nm$ is reached, which is the sum of the bead radius (600 nm), the total thickness of the passivation layer (230 nm) and half the sensor thickness (30 nm). In this case, the induced in plane stray field is maximal along a circle around the bead with radius $r_{max} = d_{min}/2 = 430\ nm$ and reaches a value of $H_{max} = 3.5\ kA/m$. Here, a magnetic moment of $m = 33 fAm^2$ per particle is employed, which is extracted from the magnetization curve supplied by MagSense (Figure 4.4) at a magnetizing field H_{ex}^{max} of 36 kA/m.

However, the GMR-sensor is influenced by the average magnetic stray field of an ensemble of beads immobilized on top of the sensor surface. Their total in-plane components cause local reconfigurations of the magnetization vectors of the sensing layers. At zero magnetizing field, the ferromagnetic layers are aligned antiparallel (2. AFCM) and each reconfiguration results in a more parallel alignment of their magnetization vectors and, thus, in a decrease of the total resistivity. In order to investigate the dependence of the sensor signal on the bead surface coverage, successively increasing concentrations of beads are immobilized on the same chip. The corresponding surface coverage denotes the x-axis in Figure 4.8 a). The determination of the bead-surface coverage is carried out by means of a homemade image analysis program and

the evaluation procedure is explained in Appendix A.1.7. After each immobilization step, the homogeneous out-of-plane magnetizing field is applied and the sensor signal is recorded. The relative signal change obtained at zero and maximum magnetizing field denotes the y-axis in Figure 4.8 a). This kind of sensor calibration is performed in two different manners. In the one case, the complete chip is dried after each bead immobilization step ("air-calibration"), while for the other case ("liquid-calibration"), the sensors are read out without any drying step in between. The GMR-sensor calibration in an aqueous environment represents similar sensor conditions as encountered during cell monitoring experiments.
Exemplary, a typical GMR response of a bead covered biosensor and a blank reference-sensor are shown in Figure 4.8 b). The reference-sensor shows a slight response (GMR $\approx$ 0.05 %) to the magnetizing field, which is considered as the blank level for further signal analysis. This minimal sensor response can be explained by a slight out-of-plane tilt, despite the present demagnetizing field (shape anisotropy), of the magnetic moments of the ferromagnetic layers by the applied magnetizing field [Schotter2004]. The signal of the biosensor shown belongs to a 16 % bead surface coverage (air-calibration). With increasing magnetizing field, the induced magnetic moment and, consequently, the bead's in-plane stray field becomes stronger, which results in a higher GMR signal. The sensor response is symmetric and reaches its maximum signal amplitude of ˜0.25 % at the maximum magnetizing field applied of $\pm$36 kA/m.
A quantitative evaluation of the GMR signal is plotted in Figure 4.8 a). Each data point corresponds to the amplitude of the GMR signal obtained from a sensor element with a specific bead surface coverage. The data points are fitted by an exponential growth function (solid line) according to

$$y = \alpha - \beta * exp(-x/\delta) \tag{4.4}$$

The fitting results are $\alpha = 0.329$ % and 0.405 % (saturation GMR amplitude), $\alpha - \beta = 0.04$ % and 0.05 % (blank level) and δ = 43 % and 18 % (bead coverage at which the saturation GMR amplitude decreases by β/e) for the liquid- and air-calibrations, respectively. As more and more of the total sensor area is affected by the local stray fields of immobilized beads, the output signal initially increases linearly with the surface coverage. As the beads are getting closer to each other, their dipolar stray fields start to overlap and the sensor response saturates. Since the beads experience a buoyant force in liquid and can move within the constraint of their molecular binding length to the surface both by thermal agitation and mutual magnetic interaction, the average vertical distance of the beads to the sensor is larger in the liquid case, thus resulting in smaller sensor response for the same bead coverage. Within the window between depletion and saturation, the output signal of such magnetoresistive sensors is a direct measure of the density of magnetic particles bound on the sensor surface.
The optimal operating point of our sensor is at half the saturation level, which is reached at about 25 % and 10 % bead coverage, respectively. Since for the uptake experiments during cell spreading the sensor area is always in liquid, we aim at an initial bead surface coverage

of about 25 % (see Chapter 6).

4.4. Simulations

The magnetization characteristics of the sensor's ferromagnetic layers in an external magnetic field is simulated by the simplex energy minimization method. The goal of this simulation is to determine the interlayer exchange coupling constants of a continuous GMR stack, which are important parameters for the micromagnetic simulations performed in the ensuing chapter (see Chapter 4.4.2). Here, the OOMMF sofware is used to investigate the interaction of magnetic sensor moments at a microscale level with external magnetic fields arising from beads. This model serves as a qualitative picture of the real-time monitoring detection principle of beads followed in this thesis.

4.4.1. Downhill simplex function minimization

Applying external magnetic fields to the multilayer system causes changes in the relative magnetization orientation of the adjacent FM layers. Consequently, the FM layers align in a way that leads to a final state of minimal total energy. Thus, the magnetization configuration of our GMR-stack at a given external in-plane magnetic field can be simulated by minimizing its total energy function.

To that end, we employ the downhill simplex method introduced by Nelder and Mead [Nelder1965], which is a robust method for finding minima of a function depending on numerous independent variables [Hoeink2008]. In case of n variables, the respective "simplex" describes a geometrical figure in a n-dimensional space with $(n + 1)$ vertices or points. For instance, the simplex of a function with two (three) variables is in a two(three)-dimensional space a triangle (tetrahedron). The minimization of a function of n variables starts with the definition of an origin, from which all other points span an n-dimensional place. At the next stage, the values of the function are calculated for all points of the simplex and the point with maximal value is replaced by another point with lower value. This continual forming of new simplices by creating new points of lower function values is carried out by three basic operations, namely reflection, contraction and expansion. Finally, a criterion has to be defined indicating the final minimum state, which terminates the optimization procedure. A more detailed description of the simplex method can be found in the following literature [Nelder1965, Press1988, Press1992, Hoeink2008].
The energy minima of our GMR multilayer system is calculated by means of the amoeba implementation, which is the program implementing the minimization method. The corresponding amoeba code was provided by Dr. Volker Höink.
We consider an infinite repetition of unit-cells of the type Py(1)/Cu/Py(2) with spatially homogeneous magnetization of each of the two Py layers of 3 nm thickness. Their energy per

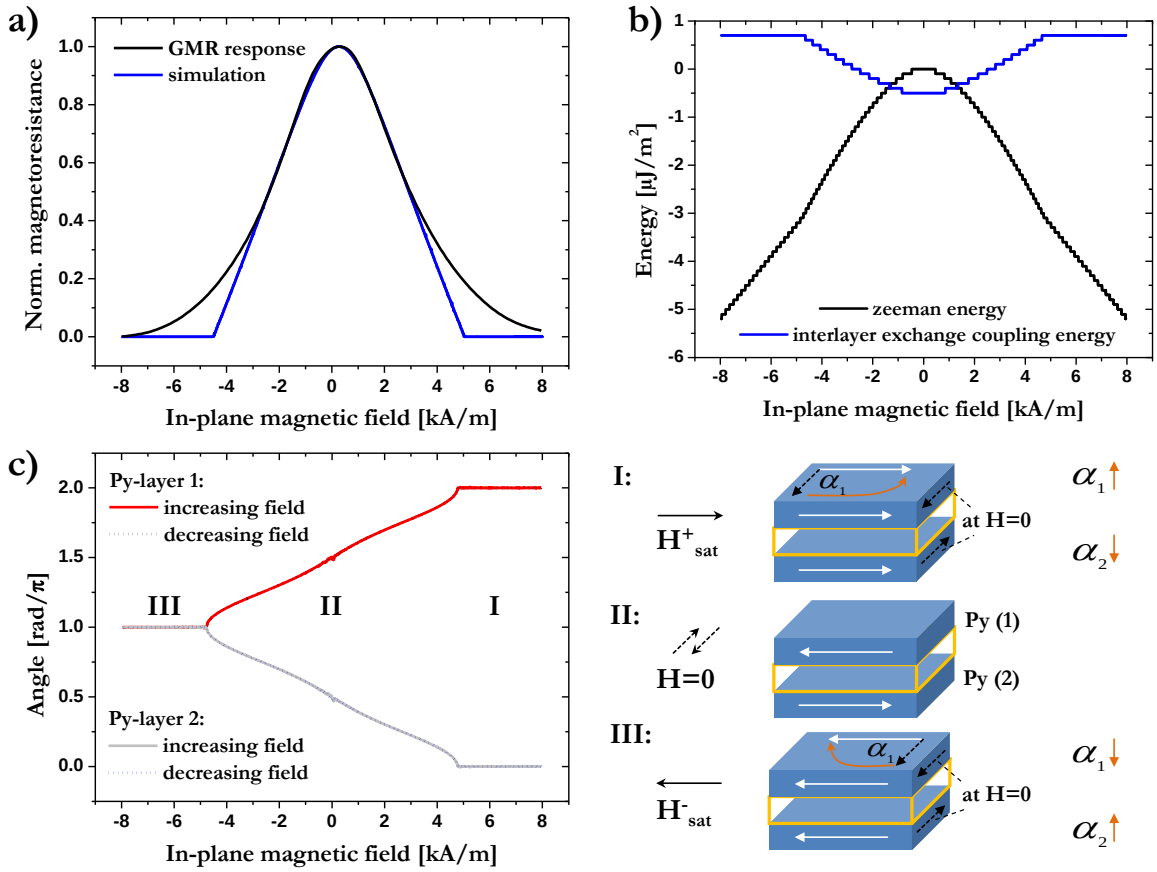

Figure 4.9: a) Normalized magnetoresistive response of a continuous multilayer stack and the corresponding energy minimization simulation fit. b) In-plane field dependent interlayer exchange coupling and zeeman energy. c) Magnetization orientation of the Py-layers relative to the axis of the external magnetic field. The white arrows represent the layers final magnetization configuration. The black lined (dashed) arrows in stage I and III denote the direction of the external field (magnetization orientation of the Py-layers at H=0). The dashed arrows in stage II show the external field axis relative to the initial (H=0) magnetization configuration of the Py-layers.

unit area (E) in an external magnetic field (H) of interest is given by [Hoeink2008]:

$$E = -\mu_0 M_s t_{Py} H\,[cos(\alpha_1) + cos(\alpha_2)]\; - 2J_L cos(\alpha_1 - \alpha_2) - 2J_Q cos^2(\alpha_1 - \alpha_2), \qquad (4.5)$$

whereas other energy terms, e.g. due to anisotropy, are excluded. In this case, the two Py layers are identical in saturation magnetization (M_S) and thickness (t_{Py}). The angles α_1 and α_2 of their magnetizations relative to the external magnetic field are different due to the initial antiferromagnetic coupling. The bilinear and biquadratic interlayer exchange coupling constants are denoted by J_L and J_Q, respectively. The first term is the sum of the field-dependent Zeeman energy of both Py layers, while the last two terms represent the bilinear and biquadratic interlayer exchange coupling energy. In a multilayer stack, each Py layer ex-

periences coupling from both adjacent unit-cells, so a factor of two is included in the coupling terms. Thus, the resulting values of J_L and J_Q resemble the coupling strength per unit cell. In equation 4.5, no anisotropy contribution is considered, since no significant magnetoresistive hysteresis is observed in the as-deposited GMR multilayer response characteristics (see Figure 4.5).

In Figure 4.9 a), a normalized GMR response of a continuous layer stack is plotted along with its corresponding downhill simplex fit, which is obtained by the amoeba minimization procedure. In equation 4.5 there are two fixed parameters, which are the values of the ferromagnetic layer thicknesses t_{Py}=3 nm and their bulk saturation magnetizations M_S=860 kA/m. At a given external magnetic field H, the coupling constants have to be adjusted for the best agreement of the fit function with the measured GMR response. The best match is obtained for linear and biquadratic coupling strengths of 2.85 $\mu J/m^2$ and 0.51 $\mu J/m^2$, resulting in an effective exchange coupling of $J^* = 2J_Q + J_L = 3.87\mu J/m^2$, which agrees well to literature values of similar systems [Huetten1999]. This value is further employed in the micromagnetic simulations of the GMR response to magnetized beads (see Chapter 4.4.2).
The energy minimization procedure also reveals the magnetization orientation of the two ferromagnetic layers Py(1) and Py(2) relative to the orientation of the applied magnetic field H. For the given situation, their orientation is indicated in each case by the angles α_1 and α_2 (Figure 4.9 c)). At the initial state, e.g. at H=0, the interlayer exchange coupling energy is dominant, and the magnetization orientation of the Py-layers is aligned antiparallel (Figure 4.9 b)). The direction of the external in-plane magnetic field H is orthogonal to the magnetization orientation of both Py-layers. Thus, at initial state, the relative angles α_1 and α_2 are 90° or odd multiples of $\pi/2$ (Figure 4.9 c) II). By increasing the field strength H in positive (negative) direction, the Zeeman energy becomes more and more dominant, which induces a sheering of both Py-magnetizations in opposite direction as shown in Figure 4.9 c)I and c)III, respectively. At saturating fields, the magnetization of the Py-layers is forced into a parallel orientation (Figure 4.9 b)). This configuration is reflected by even (odd) multiples of π for positive (negative) external saturation fields (Figure 4.9 c) I&III).

4.4.2. Micromagnetic simulations (OOMMF)

The Object Oriented MicroMagnetic Framework (OOMMF) is a public domain micromagnetics program developed by scientists of the National Institute of Standards and Technology (NIST) to determine the equilibrium configuration of the magnetization in ferromagnets or the dynamic response of magnetic moments that are brought into an external magnetic field [OOMMF2008]. The magnetization configuration of a ferromagnetic layer is divided into individual cells, whereas each cell is always magnetized to saturation M_S. Thus, the magnetization of a single cell at any time is given by $\vec{M} = M_S\vec{\hat{m}}$, with $\vec{\hat{m}}$ being a unit vector. The

presence of an external magnetic field results in a non-equilibrium magnetic configuration, and the magnetic moment vector precesses around the axis of a local effective field $\vec{H}_{eff}$. The precessional motion is restricted by damping phenomena at microscale, which eventually causes the moment vector to align along the effective field direction. In the OOMMF simulation, this time dependent relaxation process can be described by solving the Landau-Lifshitz-Gilbert ordinary differential equation [Gilbert2004, Ralph2008]:

$$\frac{\partial \vec{M}}{\partial t} = -\gamma_0 \vec{M} \times \vec{H}_{eff} + \frac{\alpha}{M_S} \vec{M} \times \frac{\partial \vec{M}}{\partial t}, \tag{4.6}$$

where γ_0 is the gyromagnetic ratio and α the Gilbert damping parameter. The effective field $\vec{H_{eff}}$ represents a collection of four distinct contributions that arise from the magnetocrystalline anisotropy, micromagnetic exchange coupling between neighboring atoms, the demagnetizing field and the externally applied magnetic field (Zeeman), which in our case is the sum of the magnetizing external out-of-plane field and bead's stray field [Ralph2008, Weddemann2010].
Next, the influence of the magnetic stray field of beads on the magnetic configuration of a GMR-type sensor in the second antiferromagnetic coupling maximum is simulated. First of all, the direct sensor response to an increasing or decreasing number of beads immobilized on top of the sensor surface is analyzed. Second, the change of the sensor signal is simulated when the vertical distance between the beads and the sensor surface increases or decreases, while the number of immobilized beads is kept constant. This case mimics the phagocytosis process and is especially relevant for the later discussion of the cell uptake experiments.

The sensor dimensions are too large to allow micromagnetic simulations of the entire meander-shaped sensor element within acceptable runtimes and, hence, the GMR-sensor dimensions have to be reduced. The entire multilayer system is modeled by a $Py/Cu/Py$ trilayer, where each layer has a thickness of 2 nm (also equals unit cell size in z-direction). The total lateral sensor area included in the simulation equals the average area per bead at the mean surface coverage encountered during the experiments. In case of the "phagocytosis during cell spreading (bottom-up, Chapter 6)" and "phagocytosis excluding cell spreading (top-down, Chapter 7)" experiments, the mean surface coverage is 23 % and 60 %, which lead to lateral dimensions of the modeled sensor areas of 2.26 μm x 2.26 μm and 1.38 μm x 1.38 μm, respectively (Figure 4.10 c) and d)). The total sensor area is subdivided into unit-cells of 20 nm x 20 nm x 2 nm. Here, the lateral cell dimensions are in the range of typical grain sizes for sputter-deposited permalloy layers [Schotter2004]. The bilinear and biquadratic exchange coupling constants and the associated effective exchange coupling $J^* = 2J_Q + J_L$ are taken from the previous simplex simulations. Due to the simplified modeling of our multilayer system by a trilayer, this single layer to layer coupling is doubled to 7.74 μJ/m^2 as effective antiferromagnetic exchange coupling strength for the OOMMF model. As material parame-

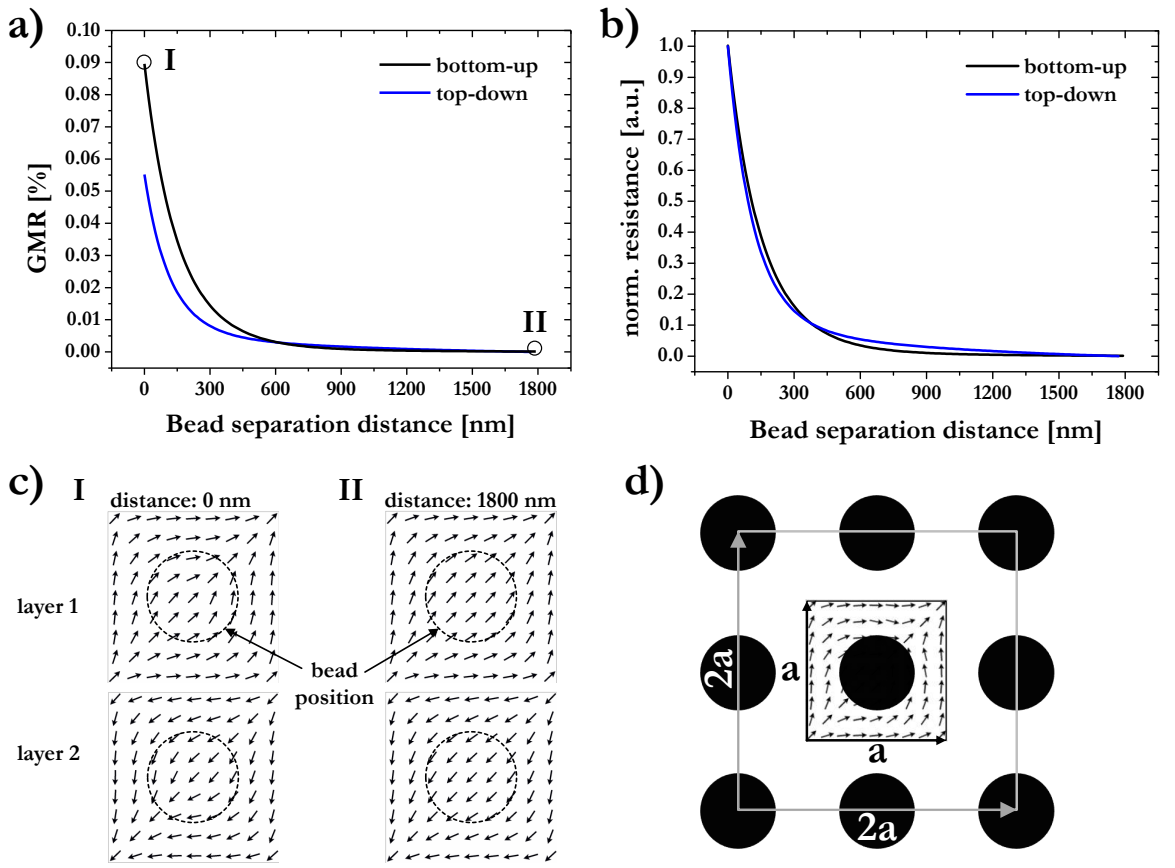

Figure 4.10: a) Simulated dependence of the magnetoresistance on the vertical bead-to-sensor separation of both approaches and b) the respective normalized sensor resistances. c) Magnetization configuration of both sensor layers at different separation distances for the bottom-up case. The magnetization pattern of the top-down approach is similar. d) Arrangement of the 9-bead array together with the simulated sensor element with side length a=2.26 μm or a=1.38 μm.

ters for permalloy, we use the bulk saturation magnetization M_S=860 kA/m [Bozorth1993] at room temperature, the exchange stiffness constant A=13 pJ/m [Bozorth1993] and no magnetocrystalline anisotropy due to the almost hysteresis-free sensor response. A single bead of radius 600 nm is positioned laterally at the center of the modeled sensor region, while its vertical separation from the top of the trilayer is varied from the thickness of the passivation layer (200 nm) to 1.8 μm in 10 nm steps. In addition to the stray field originating from the bead positioned at the center of the unit-cell, also the stray fields of the eight nearest neighboring beads is considered in the simulation. These beads are arranged equidistantly along a quadratic frame of side length 2x2.26 μm or 2x1.38 μm with the sensor element at its center (Figure 4.10 d)). According to the experimental setup, an external bead-magnetizing out-of-plane field of 36 kA/m is applied, which results in a bead moment $m = 33fAm^2$.
The OOMMF program calculates the magnetic stray field of an ensemble of nine beads at

a constant magnetizing field and its influence to the local magnetization vector of both Py-layers in dependence to the bead-to-sensor vertical distance. For each vertical distance step, an output file is generated that possesses the information about the magnetization vector of each unit-cell of both layers (Figure 4.10 c)). By summing up the magnetization vectors of the unit cells, the total magnetization configuration of both layers is obtained and the respective magnetoresistance effect can be calculated. To that end, the GMR-amplitude of 12 % measured on real meander-sensor elements is implemented into the converting EXE-file. A more detailed version of the conversion procedure can be found in [Schotter2004].

Figure 4.10 a) and b) display the simulated uptake process for both phagocytosis cases. Here, the x-axis values describe the vertical distance between the sensors passivation layer surface and the bead surface. In order to obtain the vertical separation distance from sensor-to bead-center, the passivation layer thickness (230 nm) and the bead radius must be added to the x-values. The simulated results reveal in both cases for successively increasing vertical bead-array distances, a decrease of the sensor signal due to the diminishing effect of the bead's stray fields. Common in both simulations is that for distances larger than about 650 nm, the beads's stray field effectively vanishes and does not influence the sensor anymore. Remarkable is the higher GMR amplitude for lower bead-surface coverage, which is counterintuitive. This phenomenon is due to additional edge effects, which become an issue with decreasing effective sensor sizes. The simulated sensor size area is represented by the average area per bead, which decreases with increasing bead-surface coverages. However, the OOMMF code utilized for the simulations does not apply periodic boundary conditions and, consequently, no stray fields and diverted magnetization patterns at the sensor borders are considered [Schotter2004, Mu2010]. Normalizing the simulated sensor resistances to the value of one demonstrates that both simulated approaches reveal comparable qualitative results (Figure 4.10 b)). Although the simulated results cannot predict the measured sensor signal quantitatively, they still help to understand the sensors behavior in a qualitative manner. Therefore, this sensor model is used to assess the average bead distance change from the magnetoresistive measurements observed during cell phagocytosis experiments.

One of the most challenging tasks was the realization of the platform for all cell experiments. The next chapter will give a detailed technical overview of the entire MAGLab system.

4.5. MAGLab system

This chapter gives a comprehensive introduction to the most relevant constituent parts of our magnetic lab-on-a-chip (MAGLab) setup. The microfluidic fixtures, the settings of the magneto-transport measurements and the LabView program controlling the MAGLab features are described.

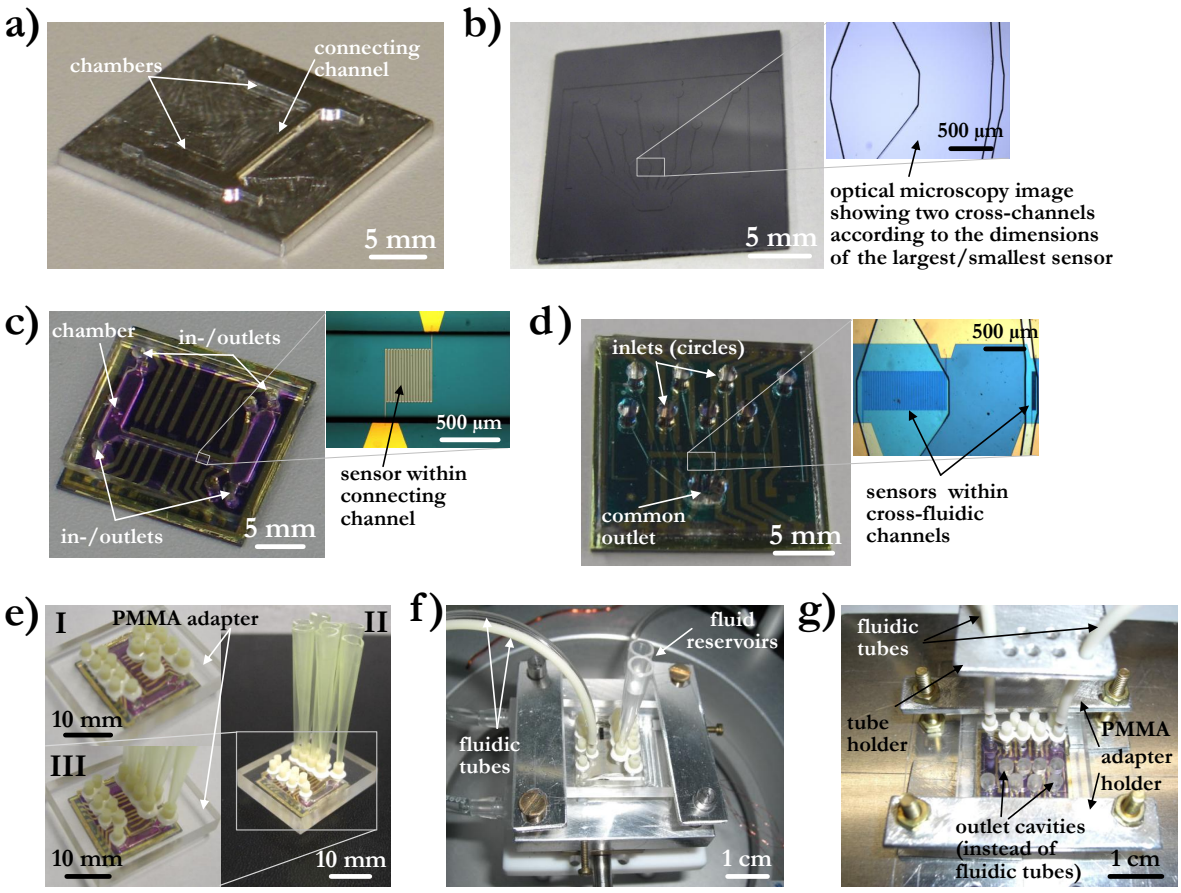

Figure 4.11: a) Aluminum and b) silicon master mold of the Maglab- and cross-fluidic, respectively. c) and d) show the corresponding PDMS replica mounted onto the biochip. The insets are optical microscopy images demonstrating the alignment of biosensors within the fluidical channels. e) Examples of PMMA adapters for the cross-fluidics and their assembly f) in the Maglab-setup and g) cross-fluidic-setup for functionalization purposes.

4.5.1. Polydimethylsiloxane (PDMS) microfluidics

Active microfluidic systems based on the polymer PDMS are established to precisely control fluids that contain living cells and magnetic beads over predefined areas of the magnetoresistive biochip. PDMS as a material can be described as a soft elastomer, optically transparent, gas permeable and absorptive to small molecules [Toepke2006, McDonald2000, Merkel2000]. Its elasticity, e.g. its low Young's modulus, is a useful feature in building active microfluidics with a diversity of integrated valves or pumps [Whitesides2006]. Optical transparency is desired due to the fact that most observation methods rely on optical microscopy. The permeation or diffusion of gases and the adsorption of hydrophobic molecules can significantly change for instance the pH or concentration of solutions within PDMS microfluidics [Toepke2006].

In microfluidics, small volumes of liquids (or gases) are guided through channels that have

cross-sectional dimensions ranging from a few tens to hundreds of micrometers [Whitesides2006]. The fabrication technique of PDMS fluidic systems used in this thesis is based on soft lithography, particularly on replica master molding, which is a non-photolithographic method. The fabrication starts with the creation of a master mold containing the microfluidic design and geometry in terms of a bas-relief on its surface (Figure 4.11 a) and b)). The patterns are transfered into microfluidic systems by casting the liquid PDMS polymer against the master. After polymer curing, a negative replica of the master mold in PDMS is generated that forms the microfluidic channels (Figure 4.11 c) and d)). This is indeed a very easy, fast and cost efficient method to fabricate microfluidic fixtures without the need of cleanroom microprocessing (except the fabrication of the bas-relief). Therefore, PDMS is a suitable material choice, especially at early development stages of microfluidic devices, where a plethora of concepts and ideas have to be tested and evaluated rapidly with less effort [McDonald2000].
Figure 4.11 shows two distinct PDMS fixtures and the corresponding masters employed for cell experiments. The cross-sectional dimensions of the Maglab-fluidic are in the order of $0.65 - 16.5$ mm with a common depth of 500 μm. The design consists of two separated symmetrical chambers connected by a fluid channel. The lateral dimensions of the middle part of the chamber are 2.0 x 9.35 mm and the tapered ends (in- and outlets) are of 0.5 x 1.95 mm in size. The width and length of the connecting channel is 0.65 mm and 12.5 mm, respectively. In total, the intake capacity is about 24 μl.
The geometrical dimensions of the connecting channel and the fluid chambers are adjusted according to the dimensions and locations of the biosensors on the chip as well as to the position of small coils integrated into the sample holder of the MAGLab setup, which will be discussed in the next sections. The biosensors are aligned underneath the microfluidic channel and a second row of reference sensors is situated outside the fluidic system in order to enable reference measurements (Figure 4.11 & 4.6). However, this PDMS fixture is especially suited to monitor migrations of magnetically labeled cells that move, for instance, from the left chamber through the channel across the biosensors, where their detection takes place towards the right chamber (see Chapter 8.1).
The purpose of the second type of microfluidic fixtures is the individual surface functionalization of all biosensors, which facilitates the parallel investigation of cellular responses to differently modified surfaces. To that end, two different finger-like PDMS fixtures are designed (Figure 4.11 d) and e)). They are basically similar but simply differ in having either a common outlet or eight individual outlets (circle areas). Again, the geometry of the middle part of the microfluidic fits the size of the corresponding sensors, and their widths account for 136 μm, 230 μm, 480 μm and 1075 μm. Beyond this area, the channel width is 100 μm, their total length varies between 0.9 mm and 11.8 mm, and their overall height is 20 μm. Compared to the first fluidic fixture, the volume capacity of each channel is in the range between 80 nl and 130 nl and, thus, less than one microliter is sufficient to fill the entire microfluidic system.

The fluid flow rate in the Maglab-fluidic and the cross-fluidic fixture can be actively controlled by means of a peristaltic pump (Watson Marlow 205 U). Its rotation per minute (rpm) is adjustable in 0.1 rpm steps between 0.5 rpm and 90 rpm and the fluids are piped through tubes of inner diameters (ID) ranging from 63.5 μm - 510 μm (purchased from [VWR]). The pump calibration, e.g. flow rate versus rpm, with a tube of ID 250 μm reveals a linear behavior and its linear fit function leads to a flow rate of 5.106$\pm$0.115 μl/m. Fluids arriving from the tubes are first guided through a connecting interface to the PDMS microfluidics, the PMMA adapter (Figure 4.11 e)), and finally enter (exit) the channels of the fluidic system via inlets (outlets). The corresponding PMMA adapter of the Maglab-fluidic is the Maglab-lid with integrated channel connections of 2 mm in diameter (see Chapter 4.5.2). In total, it includes six channels and the position of four of them is congruent to the position of the in-/outlets of the fluidic system (Figure 4.11 c)). During experiments, the biochip with mounted PDMS fluidic is assembled into the Maglab-setup and the lid is positioned on top of it sealing up the lid-fluidic interface by applying moderate mechanical forces. The flow velocity in the channel of the MAGLab-fluidic is calculated and also measured by optical bead tracking. The calculated and measured speeds of 640 μm/s and 650 μm/s, respectively, agree very well.
In case of the cross-fluidic, according to different cross-fluidic designs there are four slightly different PMMA adapters of comparable features. The basic adapter dimensions (3.0 cm x 2.5 cm x 0.5 cm) and the inner diameters of the inlets (outlets) of 1.14 mm (0.51 mm) are identical. They simply differ from each other in the position of the in-/outlets, and two of them are shown exemplary in Figure 4.11 e)I and e)II. For the functionalization experiments, they can be either assembled into the Maglab-setup (Figure 4.11 f)) or into another separate cross-fluidic-setup (Figure 4.11 g)). The calculated flow velocity in the cross-fluidic channel at 0.5 rpm accounts for 9800 μm/s.

In addition to the mentioned fluidic systems, also more simple non-active PDMS fluidic fixtures are employed. Usually they are 2 mm thick, with overall lateral dimensions of 18 mm x 18 mm, and consist of a window of 2.5 mm x 15 mm. The window is adjusted in a way that the PDMS fixture covers the entire biochip, except of the biosensor row. This enables a direct access to the biosensors for magnetic particle immobilization and cell seeding. The ref-sensors remain completely covered throughout the whole experiment and are protected against interactions with fluids or cells. These kinds of fluidic fixtures turned out to be very useful in all kinds of cell phagocytosis and spreading experiments. In combination, all three types of fluidic fixtures allow handling of volumes at the nanoscale as well as macroscale level.

4.5.2. Construction and setup

The entire MAGLab system was designed by means of ProE2000i2 (Version 2001), which is a parametric, integrated 3D CAD modeling program created by Parametric Technology Corporation [PTC]. A sequence of ProE construction images is displayed in Figure 4.12 a)-e) illustrating the heart of the MAGLab system. Their fabricated counterparts along with most of the peripheral instruments are depicted in the image sequence Figure 4.12 f)-l).

Two decoupled pairs of Helmholtz (HH) coils are connected to two distinct power supplies (Kepco BOP 50-20 MG) with their centers sharing the same geometrical position. They generate at their common center position homogeneous magnetic fields parallel (1132 A/m per A) and perpendicular (1959 A/m per A) to the chip plane, with maximum values of 23 kA/m and 39 kA/m, respectively (Figure 4.12 b), c), g)). The in-plane HH-coil is employed to measure the magnetoresistive characteristics of the sensor, while the out-of plane HH-coil is required to magnetize the beads during the magnetoresistive measurements. The out-of plane coil is mounted on a plate, which is in turn assembled on a tripod consisting of two screws with fine pitch thread and a sphere (Figure 4.12 c), f)). The adjusting screws help to achieve the required perpendicular orientation of the HH-coil relative to the chip plane.
In the middle of both HH-coils, a base construction consisting of three distinct parts is positioned: the chip holder, which is positioned exactly in the center of both HH-coils, a linear moving system underneath and a connecting lid on top of the chip holder. The linear moving system contains four fixed small coils, while a fifth one is linearly moveable (Figure 4.12 e), k), l)). The core-wound coils, denoted as millicoils, with dimensions on the mm-scale, consist of 600 windings of Cu-wires ($\oslash$= 100 μm) and an iron core with 1 mm diameter and 10 mm length. They are connected to a bipolar power supply (Traco Power, $\pm$15 VDC/1.3 A) and generate inhomogeneous magnetic fields of 45.7 A/m per mA in direct vicinity of the core tip (Figure 4.13). In a continuous (pulsed) operating mode, fields up to $\pm$16 kA/m ($\pm$22 kA/m) are produced. However, the continuous operating mode is limited by the Joule heat generation. Within a time interval of about 300 sec, the millicoil can operate at currents up to 300 mA without reaching crucial heat values (higher than 150 °C). At 300 mA, smoke development and subsequent short-circuit of the coil occurs after about 11 minutes. For currents higher than 300 mA, the Joule heat generation within 60 seconds becomes already a limiting factor as temperatures up to 250 °C are reached. Thus, a pulsed operating mode is more practical (Figure 4.13). The moveable millicoil is mounted on a carriage, which in turn is driven by a microstepping motor (MDRIVE 23 Plus) by means of a rotating spindle. Each rotating step of the motor moves the millicoil about 156 nm linearly along a groove in the chip holder with a maximal velocity of 1560 μm/s. The other four millicoils remain at fixed positions within the chip holder. For the sensor measurements, a lifting and lowering of the entire linear system including the millicois towards and away from the chip holder is required,

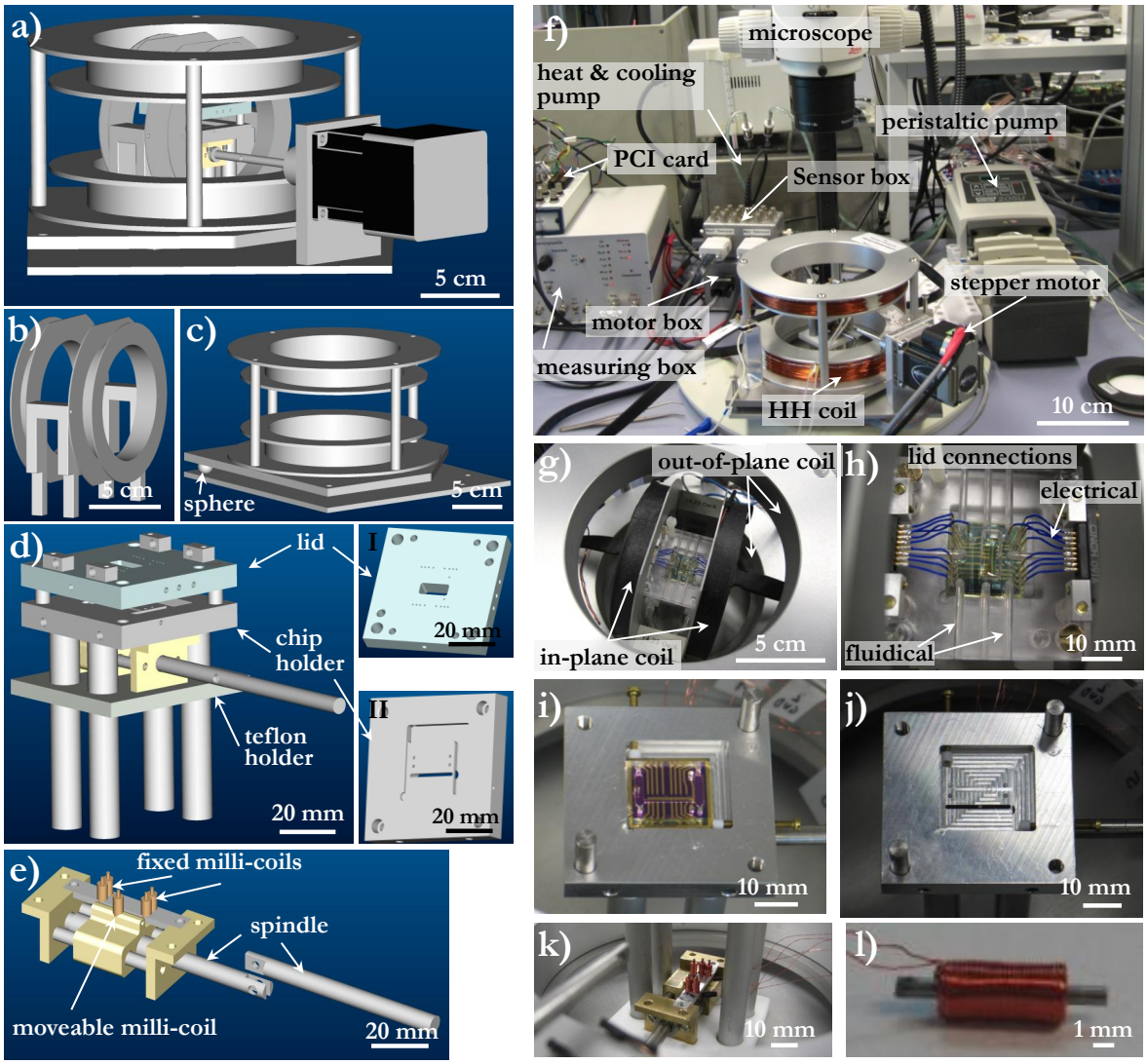

Figure 4.12: Introduction of the MAGLab system. a) ProE overview of the MAGLab construction. In-plane (b) and out-of-plane (c) Helmholtz (HH) coils. d) Basis construction including (d)I)the lid for the electrical and fluidical connections, (d)II) the temperature controlled chip holder and e) the linear moving system with mounted millicoils. f) Overview of the entire MAGlab-setup including peripheral instruments. g) Assembled in-plane and out-of-plane HH-coils. h) Connector lid. i) Chip holder with assembled PDMS-loaded GMR-Chip. j) Chip holder with lifted linear moving system showing the groove and hole cut-outs with visible core tips of the millicoils. k) Lowered linear moving system with assembled (l) millicoils.

which is accomplished by means of a screw underneath the teflon holder (Figure 4.12 d), k)). This is due to the fact that the out-of-plane field magnetizes, besides the beads, also the cores of the millicoils, and they would strongly affect the sensor's performance. At a lifted position, only the core tips are visible, which are planar to the area of the chip holder on which the sensor-chip is placed (Figure 4.12 i), j)). This ensures closest possible distance to

the chip and highest possible magnetic gradient fields, which are needed for effective on-chip bead manipulation.

The chip holder additionally consists of an internal U-shaped drilled hole labyrinth, through which liquids can be pumped in order to control its temperature. To that end, a cooling and heating system (Jubalo F12) is used, which can operate in the range between -30°C...100°C and serves several purposes. In order to avoid bubble formation, the incubation of beads on top of the sensor surface is performed at about 6 °C. Furthermore, low temperature measurements represent an effective method to influence and study the uptake behavior of cells under none-physiological conditions. In contrast, temperatures at physiological conditions (37°C) are indispensable when working with cellular organisms and especially when performing long-term experiments. By further increasing the temperature, also disease-related circumstances can be mimicked, such as the elevated body temperature during fever and the associated increased expression of heat shock proteins [Lindquist1988].
Once the PDMS-fluidic loaded chip is mounted on the chip holder, a lid placed on top of the chip establishes the electrical and fluidical connections (Figure 4.12 h)). In order to ensure a soft contact to the sensor pads, spring-loaded pin contacts (Duraseal Series S, from www.uweeelctronics.de) have been assembled into the lid. The position of the pin contacts exactly matches that of the contact pads, which makes any alignment steps unnecessary. The fluidic flow is controlled by four independent channels of 2 mm in diameter, which are accurately adjusted to the in-/outlets of the PDMS-fluidic. In general, fluids are pumped through biochemically inert tubes (PharMed BPT; ID: 0.51 mm, wall: 0.85 mm; purchased from www.vwr.at), which build the interface between peristaltic pump and connector lid. Furthermore, in case a direct access to the chip is required, the lid consists of a window (dimensions 5 mm x 12 mm) large enough to encompass the entire set of bio- and ref-sensors. In all cell and bead incubation experiments, the best homogeneous distribution over the sensor area is achieved by a sedimentation process. For this purpose, the cell/bead solutions is directly pipetted into the connector lid window, which is afterwards sealed by a cover glass.

Additionally, our MAGLab setup is equipped with a long-range microscope (Leica MZ 16) and a CCD camera (Leica DFC 320) for on-chip optical observations (Figure 4.12 f)).

4.5.3. Magneto-transport measurements

All electrical magneto-transport measurements comprising the in-plane magnetoresistive characteristics and the out-of-plane read-out of the sensors are carried out in a 2-point measurement geometry. The electronic system (Figure 4.12 f), measuring box) employed is a homemade 4-pole voltage supply source that is also suitable for 4-point measurements. The electronic circuit regulates the voltage drop across the sample, which can be set in the range

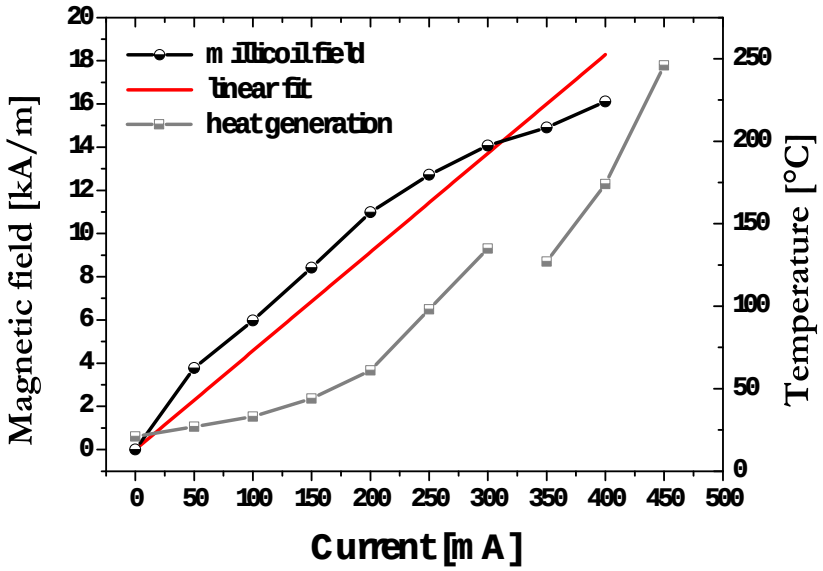

Figure 4.13: Magnetic field dependence on the applied DC current and the corresponding Joule heat generation in the continuous mode. The time duration for current intervals between 0 mA and 300 mA accounts for 300 seconds. For currents between 350 mA and 450 mA, the time duration was reduced to 60 seconds due to the rapid Joule heat generation followed by coil destruction.

from 0...2 V. The corresponding current is measured by an electrometer with seven different amplifier settings ranging from 1 nA to 1 mA and is an integrated part of the electronic system [Justus2003]. Usually, for the GMR-sensor measurements a voltage of 100-400 mV is applied and the electrometer amplifier is set to 1-10 μA. The entire measuring procedure is computer controlled.

4.5.4. LabView computer control

Our magnetic Lab-on-a-Chip is basically controlled by two different homemade LabView (www.ni.com) programs, which will be briefly presented. The first LabView code is designed by Dr. Thomas Uhrmann and controls all source settings relevant for the read-out of the sensors and the parameters of the magnetic fields of both HH-coils (Figure 4.14 a)). Furthermore, it displays the measured resistance change over the applied in-/-out-of-plane magnetic field. The second LabView code has been developed within the MAGLab project by Dr. Jörg Schotter and focuses on the entire sample preparation and analysis procedure (Figure 4.14 b)). For instance, it determines the characteristics of the fluidic system by controlling the direction and rotating speed of the peristaltic pump (Watson Marlow 205U). It regulates the interplay of the magnetic fields generated by the millicoils, and the in-plane as well as out-of-plane HH-coils by controlling the field amplitude and polarity/direction. As will be demonstrated in Chapter 4.7, the appropriate superposition of inhomogeneous and homogeneous magnetic fields allows computer controlled manipulation of beads/cells in all three dimensions. Fi-

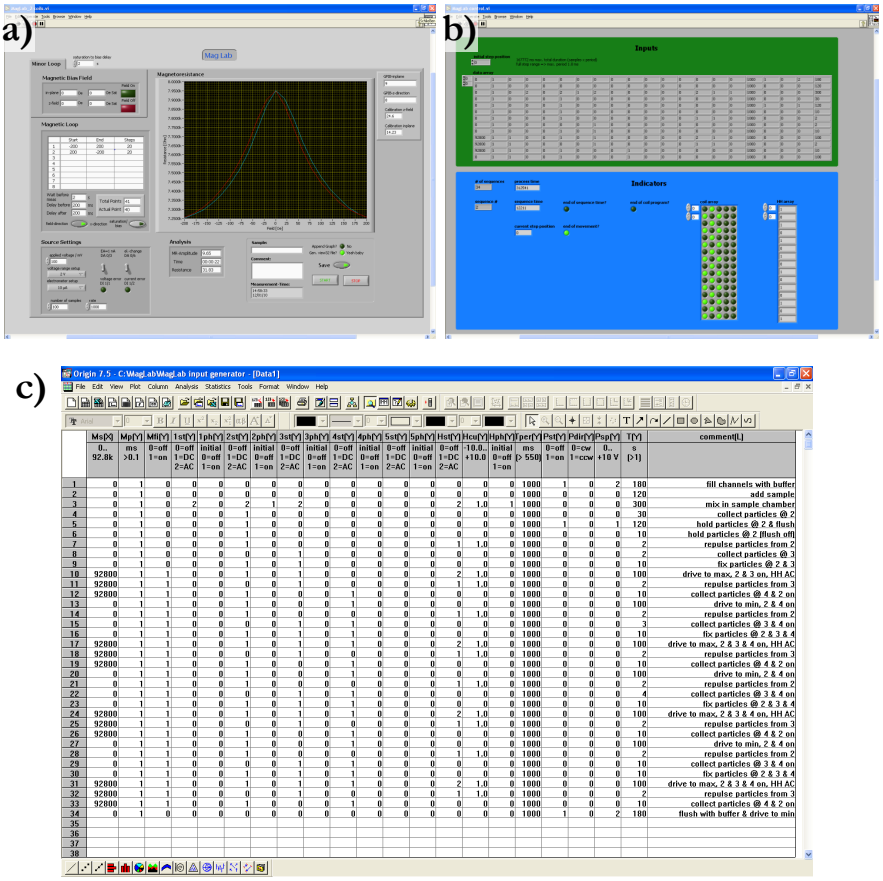

Figure 4.14: LabView program for a) the read-out of the magnetoresistive sensors and b) controlling and timing of the millicoil fields, the settings of the stepper motor (the position of the moveable millicoil) and the flow rate as well as direction of the peristaltic pump. c) Example of an Origin-file containing commands in the desired chronological order that initiate several subsequent process steps.

nally, also the moving direction and final position of the moveable millicoil along the groove is controllable by specifying the stepper motor settings. The chronological sequence of the individual steps necessary for the sample preparation and subsequent analysis are defined in an Origin-table, which is uploaded in the LabView code as a TXT-file (Figure 4.14 c)).

The next chapter focuses on the simulation of inhomogeneous and homogeneous magnetic fields and the magnetic forces applied to magnetic particles.

4.6. FEMLAB simulation of magnetic forces in inhomogeneous fields

The coil geometries of the MAGLab-system are chosen in such a way that by superposing their magnetic fields both attractive and repulsive forces can be applied on magnetic particles. In the following, the design of the magnetic fields, the magnetization of superparamagnetic beads being exposed to such fields and the associated exerted magnetic forces are analyzed

with the aid of numerical methods, particularly by finite element methods (FEM) using the software tool FEMLAB 3.1i from COMSOL Multiphysics [Comsol].
A variety of physical problems can be mathematically described by ordinary or partial differential equations. By solving these equations, a set of dependent variables, e.g. the function values and the partial derivatives of a certain order, can be determined. Depending on the complexity of the problem, an exact mathematical solution without oversimplifying the situation is nontrivial. There are many approaches to solve differential equations, and very popular are finite element methods. In a first step, the original equation is reformulated into the so-called weak or variational formulation, which can be considered as a more generalized version. Then, the reformulated equation is discretized in a finite dimensional subspace (finite elements) which represent an approximation of the original solution space. Taking boundary conditions into account, this leads to a corresponding linear equation system $Ax = b$ that can be solved by standard methods of numerical linear algebra. The key advantage of the finite element method is that most entries of the system matrix A are equal to zero and only the non-zero entries are considered [Zienkiewicz2005, Weddemann2009].

4.6.1. Magnetic field design

Figure 4.15 a) displays a cross-section along the r-z-plane of our designed magnetic field arrangement. It exemplary illustrates the distribution of the superposed magnetic fields of the out-of-plane HH-coil and the millicoil sourced with $I = 5$ A and $I = 500$ mA, respectively. The coil geometries chosen are identical to the real geometries found in our MAGLab-setup. The center of the HH-coil is the origin of the MAGLab-construction ($r = z = 0$). The squares represent a cross-section of the HH-coil bodies of 529 windings each, while the inset shows the millicoil consisting of the core and the winding body (600 windings) illustrated by rectangular areas. The position of the millicoil-center is $r = 0$ and $z = -5.5$ mm. The setup configuration presented in Figure 4.15 a) is rotationally symmetric around the z-axis. Material specific properties such as the electric conductivity of copper (windings), the magnetic permeability or saturation magnetization of soft iron (millicoil-core) are included in the simulation.

As a first approach, the core of the millicoil is excluded from the simulation and only the superposed magnetic fields produced by the windings of the millicoil and the HH-coil are studied. For the field generation, we assume a constant current density through the cross-sectional area of the winding bodies:

$$j_i = \frac{I_i \cdot N_i}{a_i \cdot b_i}, \tag{4.7}$$

where N denotes the number of windings sourced by a current I, and a and b are the side lengths of the cross-sectional area. In case of the millicoil and HH-coil this area accounts for

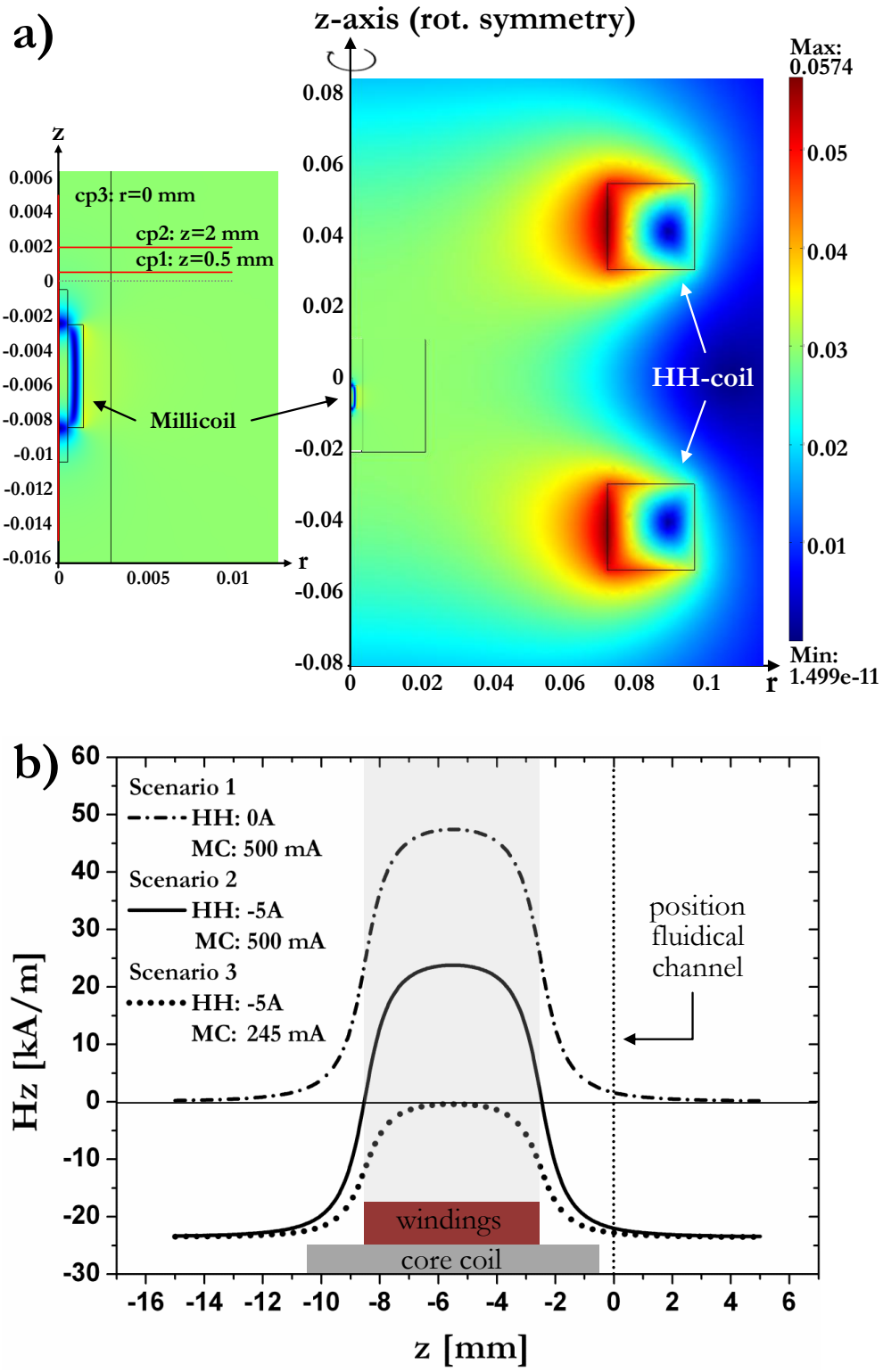

Figure 4.15: Femlab-Simulation of magnetic fields. a) Cross-section of the field distribution of our MAGLab-setup. Bz field along the z-axis at r=0 for different current scenarios.

a_1 = 0.00095 m x b_1 = 0.006 m and a_2 = 0.023 m x b_2 = 0.023 m, respectively. Positive currents result in a HH-field in positive z-direction, and this holds true also for the magnetic field produced inside the millicoil. In the shown examples, the currents j_1 and j_2 have always opposing signs and only the current amplitudes are varied. Moreover, attention is put on the z-component of the magnetic field in the region where the core is situated. Figure 4.15 b) shows the calculated Bz field along the direction of the rotationally symmetric z-axis (Figure 4.15 a) cp3 cutting plane) for three different current scenarios. Scenario 1 demonstrates the case where the magnetic field produced by the millicoil-windings is dominant and the directions of the magnetic fields are unidirectional. The field of about 25 kA/m inside the millicoil is strong enough to magnetize and saturate the iron core (saturation field of iron ∼1.714 kA/m [Bozorth1993]). A similar constellation is represented in scenario 3, where the HH-field is dominating over the entire range of the core coil, which would result in its complete magnetization in HH-field direction. As will be discussed later, this kind of scenario leads to attractive forces only. In scenario 2, we can observe both negative as wells as positive field directions of Bz within the range of the core coil. The millicoil-field dominates the core magnetization within the range interval of z=-9...-3 mm with a core magnetization $M_z = +M_s$. However, this range of influence can be further increased by shifting the Bz-curve toward positive values until the entire iron core is dominated by the millicoil field. In case the core is situated outside this range, the HH-field is determinative and we assume a core magnetization of $M_z = -M_s$. This is indeed a very simplified view of the core magnetization. In a realistic system, the ferromagnetic core is divided into a multiplicity of domains with different magnetization orientations [Eggeling2006]. Nevertheless, it represents a good approximation of the core magnetization along the z-axis.

As a second approach, the magnetization of the iron core is considered and the superposed magnetic fields originating from the HH-coil and the millicoil are calculated. The magnetization of the iron core is assumed to be saturated by the millicoil-field according to the previous discussion. In total, the magnetic field of three different cases is analyzed:

1. core-coil only ($j_1 = 0.5$ A, $j_2 = 0$ A)
2. core-coil and HH-coil parallel field direction ($j_1 = 0.5$ A, $j_2 = 7.5$ A)
3. core-coil and HH-coil antiparallel field direction ($j_1 = 0.5$ A, $j_2 = -7.5$ A)

In Figure 4.16, the radial and z component of the superposed field B along the cutting planes 1 & 2, as indicated in Figure 4.15, are illustrated. The cutting plane 1 & 2, in the following denoted as cp1 and cp2, are set at $z = 0.5$ mm and $z = 2$ mm, respectively (Figure 4.15 a)). Their values correspond to the height of the MAGlab-fluidic channel (500 μm) and the average height of fluidic fixtures used for the most cell experiments. The surface of the chip itself has the vertical position $z = 0$ mm. The magnetic field course of both components shows a

non-linear dependence on the radial distance r. Since the homogeneous out-of-plane HH-field lacks the radial component, B_r is identical in all three cases. For cp1 (cp2), B_r reaches its maximal value of 3.8 kA/m (1.6 kA/m) at a radial distance of about 2 mm (3 mm) from the origin, and it drops to zero at distances of about 25 mm (25 mm). The B_z component has its maximum value directly above the core-center at $r = 0$ and it levels off (or diminishes in the case of "core coil only") at distances of about 5 mm in all three cases. The maximum value is reached for the parallel case, which accounts for 37 kA/m and 32 kA/m for cp1 and cp2, respectively. In general, the radial component of the superposed field has a much larger range of influence, while the strength of the z-field component is clearly higher.

4.6.2. Magnetic forces

By means of the calculated magnetic field we calculate the forces that are exerted to magnetic particles when they are brought into such fields:

$$\vec{F} = \nabla(\vec{m} \cdot \vec{B}) \tag{4.8}$$

The employed MagSense particles of 1.2 μm in diameter display superparamagnetic behavior, and an external magnetic field $\vec{B}$ induces a magnetic moment $\vec{m}$. In the following, an instantaneous magnetization alignment of the particle along the direction of the external magnetic field is assumed. By doing so, its magnetization is described by the classical Langevin function, which can be approximated for the components in z- and r-direction as follows [Eggeling2006]:

$$m_{r,z}(B_{r,z}) = S_2 \cdot (coth(S_1 \cdot B_{r,z}) - \frac{1}{S_1 \cdot B_{r,z}}), \tag{4.9}$$

with $S_1 = 55.91\ T^{-1}$ and $S_2 = 65 \cdot 10^{-15}\ Am^2$ as factors that specify the course of the Langevin function. S_1 corresponds to the saturation field of the particle, which is taken from a Langevin fit of a magnetization curve of similar particles. The second factor S_2 represents the saturation magnetic moment taken from the data sheet of the MagSense particles. The magnetic potential of a particle in a magnetic field $\vec{B}$ is given by [Eggeling2006]:

$$U_{pot}(r, z) = -\vec{m} \cdot \vec{B} = -(m_r \cdot B_r + m_z \cdot B_z). \tag{4.10}$$

The partial derivative of the magnetic potential with respect to r and z leads to the desired magnetic force components [Eggeling2006]:

$$F_{r,z} = \frac{\partial U_{pot}(r, z)}{\partial_{r,z}}. \tag{4.11}$$

Figure 4.16 c) and d) display the calculated force components depending on the distance r to the origin according to the previously defined three cases. Negative or positive force values

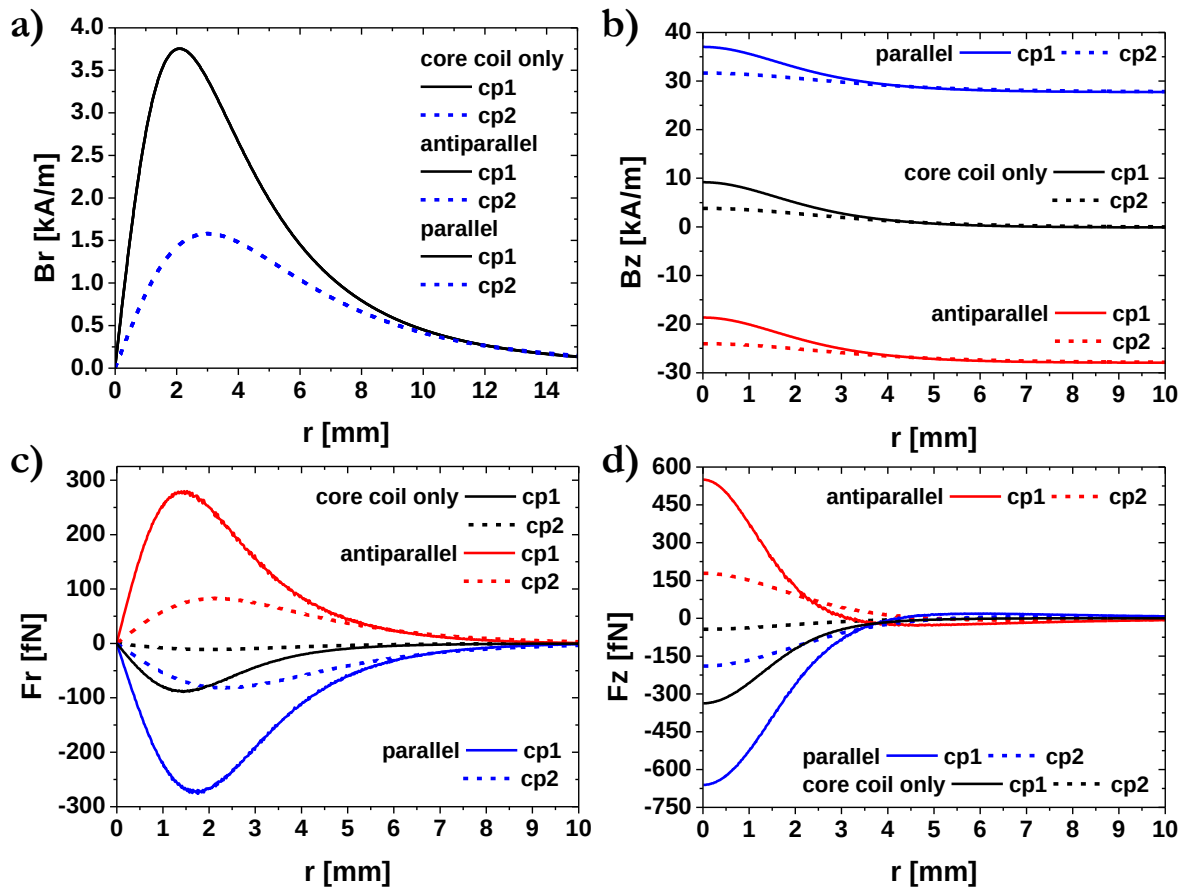

Figure 4.16: Femlab-Simulation of magnetic fields and forces. a) and b) display the radial and z-component of the superposed magnetic fields generated by the millicoil and HH-coil sourced with 0.5 A and 7.5 A, respectively. c) and d) represent the forces acting on MagSens beads of 1.2 μm when exposed to such a magnetic field.

result in particle attraction or repulsion, respectively. Concerning the component F_r and F_z, maximum attractive (repulsive) forces of about -272 fN (279 fN) and -660 fN (550 fN) can be applied, respectively. The F_r (F_z) magnetic forces become negligible at r-values about 8 mm (3.5 mm), which determines the operating range of our designed magnetic field arrangement. As expected, the force values at cp2 are lower and give a good indication on how fast the forces decrease from the center along the z-axis.

Next, the calculated forces need to be evaluated with regard to whether they are strong enough to move or manipulate the particles. To that end, the gravitational F_g and buoyancy F_b forces acting on a MagSense particle are calculated, while the net force $F_n = F_g - F_b$ serves as reference value. The net force is given by:

$$F_n = M_p \cdot g = \frac{4}{3}\pi \cdot r^3 \cdot (\rho_p - \rho_l) \cdot g. \tag{4.12}$$

The density of liquid (water) and MagSense particle are $\rho_l = 1.0 \cdot 10^3\ kg/m^3$ and $\rho_p = 2.5 \cdot 10^3\ kg/m^3$, respectively, and the particle radius is $r = 0.6 \cdot 10^{-6}$ m. With $g = 9.81$ kgm/s^2 we attain a net force of about 13 fN, which is up to a factor of 50 smaller compared to the simulated repulsive force acting on the particle.

In addition, particles moving in a liquid feel a drag force which is given by the Stokes drag law:

$$F_{stokes} = 6\pi \cdot \eta \cdot r \cdot v, \tag{4.13}$$

with the radius of the particle $r = 0.6$ μm, the viscosity of water $\eta = 1$ mPa·s and v the particle velocity. When no magnetic forces or fluidical flow is present, the particle velocity can be considered as zero (the contribution of the Brownian motion and fluid convection is vanishingly small). At this initial stage of bead manipulation, the drag force can be neglected. Consequently, the only requirement for an "up and down" bead movement is a higher repulsive and attractive magnetic force than the beads net-gravitational force, respectively. However, the drag force becomes important when the beads start moving. Beads entering the magnetic field range experience an acceleration according to the field gradient. With increasing bead velocity, also the drag force increases and the acceleration reaches a saturation value when the drag force equals the magnetic force.

Similar calculations can also be made for magnetic manipulation of bead-labeled cells. Fibroblasts have an average size of 21 μm in diameter and the density of living cells is about 1.35 g/cm^3 [Lindner2008]. Due to equation 4.12, the calculated net force is $F_n = 17$ pN. This force exceeds the simulated magnetic force value by a factor of 26. Consequently, a labeling of at least 26 beads per cell is required in order to achieve a repellent cell movement.

According to this results, both particle as well as cell manipulation in all three space dimensions are possible by the designed magnetic fields of our MAGLab-setup. Their experimental validation is demonstrated in the next chapter.

4.7. 3D magnetic manipulation of beads

Magnetic particles suspended in a liquid can be moved or manipulated by applying magnetic forces originating from gradient fields. These are usually generated in two different manners. In the on-chip approach, a current is passed through microfabricated conduction lines of appropriate geometries that enables nanometer precise positioning of magnetic particles [Lagae2002, Graham2002, Megens2005, Panhorst2005a, Pamme2006]. When a typical current of 15 mA is passed through a gold conductor with a cross-section area of 2 μm x 200 nm, a gradient magnetic field is generated, and the maximum field values in immediate vicinity of the conductor are ~2000 A/m. With increasing distance from the conductor, the gradi-

ent field decreases and vanishes at about 20 μm [Shoshi2005]. Since the dimensions of our microfluidic fixtures are in the submillimeter range, the on-chip generation of gradient fields becomes impractical. In order to increase the operation range of the gradient field and, thus, to enable bead manipulation in the submillimeter regime, we follow the off-chip approach by employing core-wound coils with mm-dimensions (see Chapter 4.5.2). In comparison, the area of influence of a gradient magnetic field generated by the coil sourced with a current of 350 mA reaches distances relative to the coil core tip up to 6 mm (Figure 4.16 c), d)). Another unique feature of using a combination of coils is the ability to apply both attractive as well as repulsive forces, which enable the three-dimensional (3D) movement of magnetic particles.

In the following, several distinct bead manipulation processes are demonstrated, which are used to perform single or multiple laboratory tasks on a chip according to Chapter 4.9. Moreover, the magnetic manipulation methodology is extended to living organisms such as magnetically labeled cells.
In each experiment, if not otherwise stated, the surface of the used Si-wafer or biochip is saturated with a 1mg/ml BSA-dH_2O solution (Bovine Serum Albumin, [Sigmaaldrich]), which prevents unspecific bead binding. The magnetic beads involved are either MagSense Strepavidin of 0.9 μm or Dynabeads MyOne Strepavidin of 1.2 μm in diameter [MagSense, Dynal]. The corresponding movies of all presented bead manipulation examples can be found in the attached DVD.

Bead (re-)collection

Here, a bead collection and recollection process is demonstrated (Figure 4.17 a)) which combines both fluid flow and magnetic manipulation within the MAGLab-fluidic fixture. As a first step, the entire fluidic is filled with PBS buffer. Then, an amount of 0.5 μl of a 1 mg/ml bead solution is injected into the left chamber. The moveable millicoil is positioned by means of the stepper motor directly underneath of a C-type GMR-sensor and is sourced with a current of 130 mA. This results in a magnetic field strength within the coil of about 12 kA/m, which is about 7 fold larger than the field required to saturate the magnetization of the iron core (Chapter 4.6). The magnetized core leads to a dipolar magnetic gradient field perpendicular to the chip plane, resulting in attractive magnetic forces. When the the peristaltic pump is turned on, the buffer including the beads flows from left to the right along the fluidic channel. Beads approaching the millicoil are magnetically attracted and collected above the sensor surface as shown in Figure 4.17 a) at 0 s. Subsequently, the current of the millicoil is turned off and the buffer flow is launched for 30 seconds at a flow rate of 2 μl/min. The average flow speed in the channel accounts for 110 μm/s. As a result, the collected beads are carried away by the buffer according to the flow profile evolving after 15 s and 30 s (Figure 4.17 a)). Immediately following the 30 seconds, the millicoil current of 130 mA is switched on again,

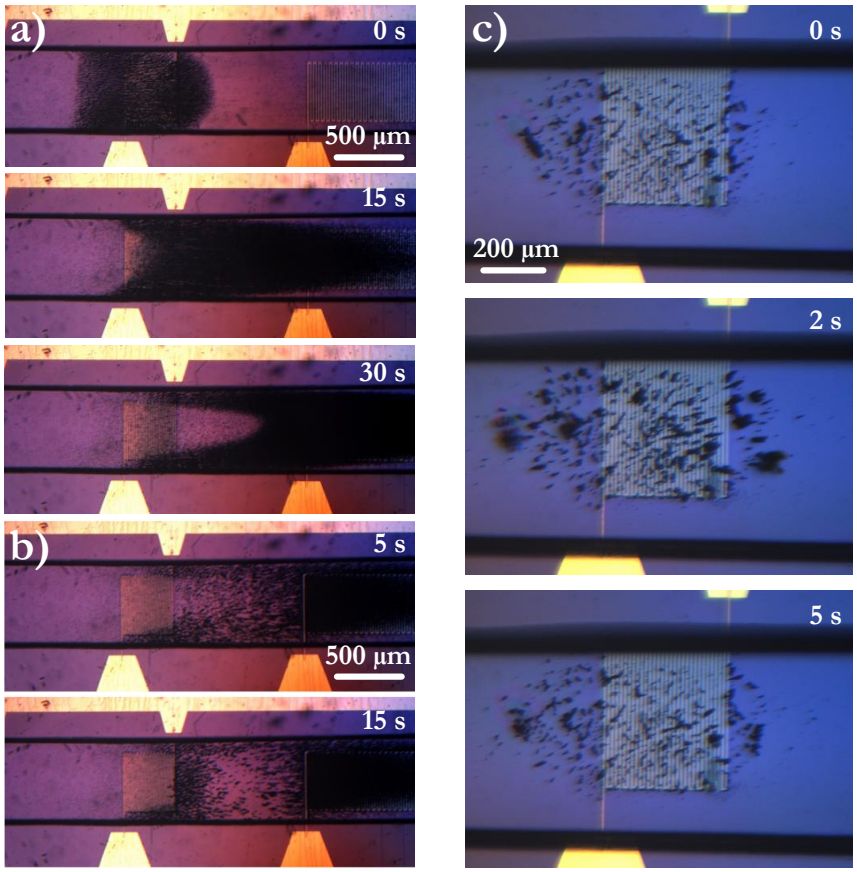

Figure 4.17: a) Magnetic bead collection. At time 0 s, the beads are collected above the iron core position. Switching the millicoil off and initiating a fluid flow for 30 s results in dragging of beads according to the flow profile. b) Magnetic bead recollection. After flow initiation, the millicoil is turned on and bead recollection after an elapsed time of 5 s and 15 s is displayed. c) Bead mixing by applying attractive (0 s and 5 s) and repulsive forces (2 s). The condition for the later case is fulfilled when the HH-coil and millicoil are sourced with currents of -3 A and 130 mA, respectively.

and the beads which are within the gradient field range are recollected at the millicoil position as illustrated in Figure 4.17 b) after a time period of 5 s and 15 s (see movie "Bead (re-)collection").

Bead mixing

Another analytical step is a three-dimensional (3D) bead mixing process, which enables an accelerated specific binding of target molecules in solutions. To that end, magnetic repulsive and attractive forces are applied according to the simulations in Chapter 4.6. Initially, the millicoil is sourced with 130 mA, and the upwards magnetized iron core produces a magnetic field of 5.9 kA/m in direct vicinity of its tip. The millicoil operates during the entire experiment in a continuous mode at a constant current. Once the beads are collected (Figure 4.17

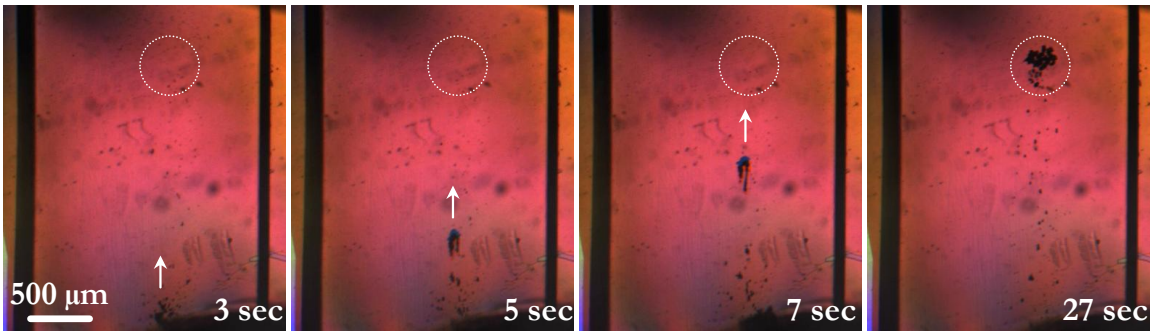

Figure 4.18: Bead transfer between two neighboring millicoils. The dashed circle and the arrow indicate the position of the upper millicoil core and the bead transport direction, respectively.

c) at 0 s), the out-of-plane HH-coil is turned on, which is sourced with a repetitious triangular current of ±5 A amplitude, e.g. ±9.8 kA/m field strength, of 1 Hz. The frequency determines the slope of the applied triangular voltage and, thus, the time evolution of the mixing cycle. For positive HH-coil currents, the magnetic field direction is parallel to the core magnetization, leading to a increased total field strength. In this configuration, the magnetization direction of the beads is also parallel and, therefore, an attractive force is exerted leading to downward bead movement (Figure 4.17 c) at 0 s). A successive decrease of the current from the positive to the negative regime results in an opposing HH-field direction relative to the core magnetization direction. At current values of about -3 A, the HH-field strength is sufficient to magnetize the beads in parallel direction, while the core magnetization exhibits an antiparallel orientation. As a consequence, this constellation leads to repulsive forces and a star-like upward bead movement (Figure 4.17 c) at 2 sec). However, currents beyond the window around -3 A represent conditions that favor attractive force exertion (Figure 4.17 c) at 0 s and 5 s; see movie "Bead mixing").

Coil-to-Coil bead transfer

The bead mixing procedure has to be repeated with all three millicoils in the mixing fluidic chamber, which ensures the capture of all possible target analytes in the sample solution. This, however, implies the transfer of beads between neighboring millicoils as depicted in Figure 4.18. The dashed circle indicates the position of the iron core of the outer fixed millicoil, and its center is 3 mm apart from the next neighboring core center of the second fixed millicoil. The position of the later one is directly under the integrated lid fluidic channel and, therefore, not visible through the microscope. The arrows indicate the bead transfer direction from the second to the outer coil. First, the beads are collected above the second coil as described in the "Bead (re-) collection" part, and the outer coil is initially turned off. Then, a homogeneous field is produced by sourcing the out-of-plane HH-coil with -3 A. Simultane-

ously, the outer and the second millicoil are sourced with -130 mA and 130 mA, respectively. Similar to "bead mixing", the outer coil exerts attractive and the second coil repulsive forces. Consequently, the previously collected beads are pushed away from the second coil and at the same time collected by the outer one, which results in the desired inter-coil bead transfer (see movie "Coil-to-Coil bead transfer"). The amount of beads transfered from one coil to another is adjustable by varying the time duration which they operate either in a repulsive or attractive mode. The coil settings are basically a combination of the previously described bead (re-)collection and mixing examples.

Lateral bead transport

The lateral transport of beads is realized by means of the magnetic forces from the moveable millicoil with similar coil settings as described in the "Bead (re-)collection" chapter. After the coil-to-coil bead movement, a portion of beads is transfered to the moveable coil (Figure 4.19). While from now on the fixed coils are turned off, the moveable coil is sourced permanently with 130 mA and starts moving linearly with a speed of 156 μm/s along the fluidic channel. Consequently, the beads are dragged along the channel according to the predefined stepper motor settings from the right to the left or vise versa (see movie "Lateral bead transport"). Each of the functionalized sensor surfaces is precisely addressable and allows beads that carry target analytes to bind specifically. Unbound beads, ideally those who do not carry target molecules, are transfered to the fixed millicoils in the right "waste" chamber and can be washed out by flushing the fluidic with buffer solution.

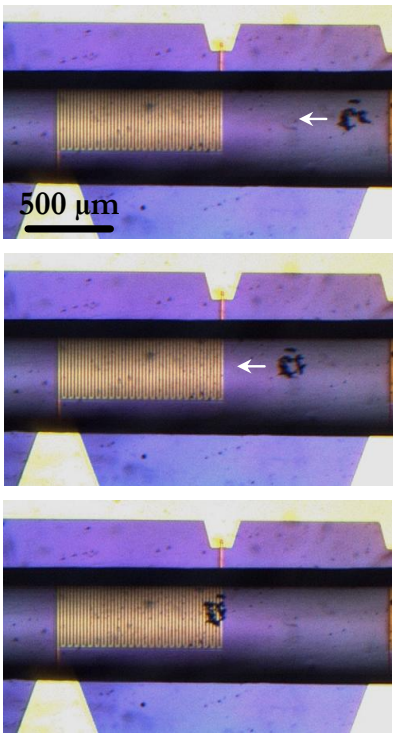

Figure 4.19: Lateral bead transport within the MAGLab-fluidic channel.

4.8. 3D magnetic manipulation of bead-loaded cells

The fibroblasts employed in the following experiment first need to be magnetically labeled in order to be able to manipulate them. In general, living cells can be labeled by either specifically binding magnetic beads at plasma membrane proteins that are situated outside the cell or by bringing beads inside the cell body [Safarik1999]. Here, the later method is followed and the beads enter the cell by utilizing the phagocytic uptake mechanism. A detailed description of the uptake procedure is given in Chapter 5. Here, only basic data relevant for the magnetic manipulation is provided. In this study, MagSense particles of 1.2 μm in diameter with a Streptavidin coating are used. Moreover, the surface of the Si-wafer or

glass slide is not saturated with BSA-protein.
The magnetic labelling starts with confluent cell growth in 6-fold Multiwells followed by adding a bead-solution of 2.5 μg/ml. Assuming a homogeneous distribution, each cell should be approximately covered by 100 beads. After the over-night incubation, all beads are internalized by phagocytosis. For further processing, the bead-loaded cells are harvested by means of Trypsin-EDTA and transfered into a 1.5 ml Eppendorf tube.
Figure 4.20 a) displays a schematic cross-sectional view of a fluidic fixture with an integrated window sandwiched between two glass slides of 150 μm thickness or between a glass slide and a Si-wafer. The PDMS fluidic has a thickness of about 2.5 mm and is placed on a glass slide or Si-wafer. Next, the window of 10x10 mm^2 is filled by adding 300 μl cell-buffer solution containing about 6700 bead-loaded cells. Then, the window is closed by the second glass slide and the whole complex is assembled into the chip holder of the MAGLab-setup.

Cell collection

As a first example, magnetically labeled cells within the fluidic are collected above the moveable coil. To that end, identical coil settings are used compared to the case of bead collection presented in Chapter 4.7. The image sequence in Figure 4.20 b) illustrates the time laps of cell collection. In the first image, at time 0 sec, there are no magnetic fields present and the cells are homogeneously suspended in the buffer solution. Moreover, the position of the iron core and the groove of the chip holder is visible. Once the magnetic field is turned on, the bead-loaded cells are attracted toward the region of highest magnetic force, which is predominantly the edge of the iron core (Figure 4.20 b) 25 sec). The operating range of the magnetic gradient field is about 3 mm, and all cells within this distance are collected in less than 30 seconds. Since the dimension of the PDMS window is larger, more and more cells randomly enter the operating range due to thermally induced fluid dynamics due to convection. However, the fluidic can be considered as cell-depleted after a time period of about 80 sec. The collecting time period can be modified by varying the applied millicoil currents and the magnetic labeling of the cells (see movie "Cell collection").

Cell mixing

This example pertains the mixing of bead-loaded cells by applying attractive and repulsive forces. The coil setting parameters and the magnetic manipulation procedure are similar to those used in Chapter 4.7. Compared to the cell collection case, the PDMS fluidic is mounted on a Si-wafer of 500 μm thickness instead of the glass slide, which improves the visibility of the transparent cells under the microscope (Figure 4.20 a), c)). First, the cells are collected by means of the millicoil, and in a second step, the HH-coil is sourced with a triangular current. The resulting attractive and repulsive forces lead to slight up- and downwards movement of

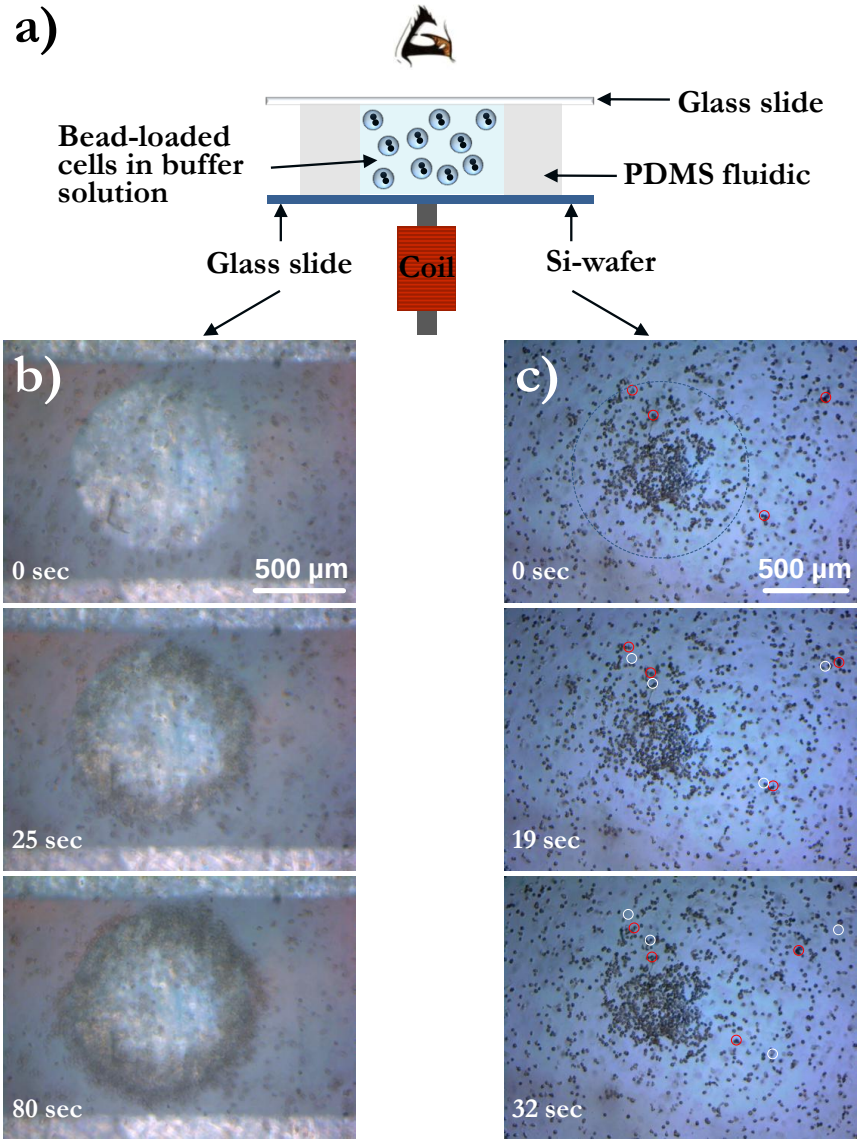

Figure 4.20: Magnetic manipulation of bead-loaded cells. a) Cross-sectional sketch of the setup. b) Cell collection within microfluidics by means of attractive forces. c) 3D cell manipulation by applying repulsive (19 sec) and attractive forces (32 sec). The dashed blue circle indicates the core-tip position. The red circles mark the current position of some selected cells and the white circles the position of the same cells in the respective previous image.

the cells (see movie "Cell mixing"). The observation shows that employing similar coil settings lead to a less pronounced manipulation of the bead-loaded cells compared to the mixing of magnetic beads only. The main reason is attributed to the fact that cells have a significantly higher surface adhesion affinity to the Si-wafer than magnetic particles. Fibroblasts are adherent cells, and they immediately start anchoring at the surface. However, an enhanced cell manipulation performance could be achieved by further optimizing the coil settings and the bead-loading. In this case, higher gradient fields and an increased number of beads inside the

cell are advantageous.
Noticeable is also the location of the collected beads which under these conditions is the center of the iron core. Thus, by adjusting the coil setting parameters and the setup configurations, one can realize a cyclic bead movement from the core edge to the core center. This manipulation mode has been demonstrated with beads only and can be seen in the movie "Bead-Movement-Up-Down".

4.9. MAGLab operation at molecular level: sample analysis principle

Apart from experiments with cellular organisms, the MAGLab setup is also capable to operate at the molecular level, representing a magnetic-based total analysis system [Weddemann2010, Pamme2006]. In the following example, the conceptual separation and detection of target analytes in fluid samples, such as blood, by appropriately functionalized beads and functional sites of the chip is described. The underlying idea behind the analysis procedure, which includes the sampling, sample preparation, reaction, detection and data analysis, has been published in [Schotter2009], and the description given here is based on it.
Figure 4.21 illustrates the chronological sequence of fundamental steps for on-chip sample preparation and analysis. The upper part in the image sequence displays the top view design of our biochip together with the relative position of the five millicoils underneath the chip and the MAGLab-fluidic fixture (true to scale). The downer part shows a schematic cross-sectional view which is indicated by the dashed line (not to scale). The magnetization direction of the out-of-plane homogeneous field remains constant at every stage of sample analysis and induces a downward magnetization of the magnetic particles. Accordingly, each of the millicoils is marked by a white arrow that indicates its magnetization direction. The moveable millicoil is labbeled by the letter "m" and is initially positioned in line with the left two fixed millicoils.

The actual analysis starts with the injection of the sample fluid and the functionalized beads into the left fluidic chamber. Then, the remaining volume of the left fluidic chamber is filled with buffer solution. The next step concerns the binding of the target analytes to the bead surface by means of an active mixing process as described before. In order to capture as many target molecules as possible, this mixing step is repeated with all three millicoils in the left chamber. As a result, the capture and, thus, the separation of the target analytes out of the fluid sample happens in a much faster fashion compared to non-active mixing devices, which simply rely on passive transport by diffusion [Heer2007]. In a further step, beads are magnetically fixed by using one of the millicoils and the remaining fluid sample is washed out of the fluidic and replaced with buffer solution (Figure 4.21 b)). This removes non-specifically bound molecules, which ideally comprise all non-target analytes and as a result, unspecific binding events at the functionalized sensor surface are reduced. Subsequently, an adequate portion of beads is transferred to the moveable millicoil that magnetically transports them

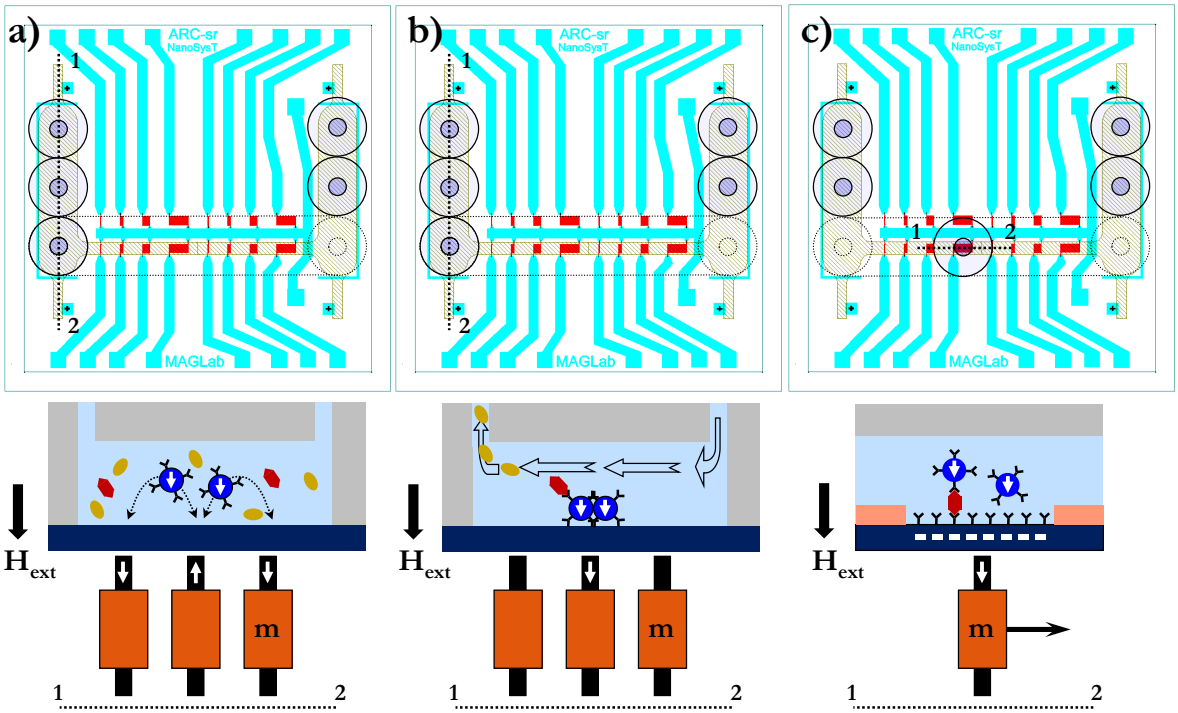

Figure 4.21: Illustration of the on-chip sample analysis procedure by our MAGLab system. The upper images show the top view design of our chip, the relative position of the five millicoils underneath and the fluidic fixture on top of the chip (true to scale). The cross-sectional view in the bottom images is indicated by the dashed line and displays the PDMS-loaded chip, the actual arrangement and operation mode of the millicoils (not to scale). a) Analyte binding by a bead mixing process. b) Analyte separation from other substances by fixating the beads and flushing the fluidic with buffer. c) Magnetic transfer of beads to the functionalized sensor areas enabling specific binding of beads that carry target analytes (after [Schotter2009]).

along the channel where the sensors are located. The sensor surface is functionalized with complementary molecules, which allow beads that carry target analytes to bind specifically (Figure 4.21 c)). Beads without bound target analytes are transported through the channel without binding, and are finally transferred to the right (waste) chamber. This transport procedure is continued until all beads are transferred from the left to the right chamber. In case that beads adsorb non-specifically on the sensor area a washing procedure can be initiated. Here, the moveable millicoil is driven along the channel in a repulsive mode while simultaneously flushing the fluidic channel with buffer towards the waste chamber. One has to make sure that the chosen repulsive force is strong enough to lift non-specifically adsorbed beads, but too weak to rupture the specific bounds. After the sample preparation process is finished, the analysis starts with the read-out of the sensors. To that end, the millicoils are moved away from the chip holder in order not to disturb the sensors by the stray fields of their magnetized iron cores. Finally, the sensor signal is evaluated, which represents a direct measure of the number of specifically bound beads and, thus, the target analyte to be

detected.

4.10. Summary

A magnetic lab-on-a-chip system consisting of several distinct components has been realized. In the ensuing chapters, the application of this system as a multifunctional platform for on-chip cell analysis is demonstrated. The mammalian cell cultures involved in this research study were human fibroblast cells from healthy tissue and mutated or epigenetically changed human prostate cancer cells. Their phenotype along with their biological function in a human being has been highlighted. A variety of cell features can be analyzed by monitoring their interaction with magnetic particles. These particles must meet a vast number of demands associated with their application in cell biology, and their characteristic nature decisively influences the interaction process. The particles of choice for all real-time monitoring experiments of the following sections are MagSense beads. Therefore, all their cell-relevant physical and biochemical properties have been characterized (see Chapter 4.2). The cell-bead interaction monitoring is carried out by giant-magnetoresistive sensors and, thus, the magnetic characteristics of both the beads as well as the sensor has been discussed (see Chapter 4.3). The configuration of the sensor's ferromagnetic multilayers exposed to external magnetic fields has been simulated by minimizing its total energy function. The employed amoeba minimization procedure has revealed an effective interlayer exchange coupling constant of a continuous GMR-stack of $J^* = 3.87\ \mu J/m^2$ (see Chapter 4.4.1). This parameter has been further implemented in micromagnetic simulations, by which the local effect of the bead's magnetic dipole field to the magnetic moments of the sensor's ferromagnetic layers has been investigated (see Chapter 4.4.2). Basically, two different examples have been simulated, which resemble the conditions encountered during the cell uptake experiments. Both cases have shown a decreasing sensor response by increasing the vertical distance between the bead- to sensor-center. The signal has vanished for distances larger than 650 nm. Furthermore, the sensor has been calibrated by successively immobilizing beads on the sensor surface, and a 25 % coverage has been identified as the best operating range.
The beads and cells have been precisely controlled over predefined sensor areas of the biochip by means of active and passive PDMS microfluidics fabricated by replica master molding (see Chapter 4.5.1). The active fluid flow has been driven by a peristaltic pump and volumes from 24 μl down to 80 nl have been handled. The volume capacity of the passive fluidic fixtures has been up to 50 μl. The fluidic fixtures have been mounted on top of the biochip, and the whole complex was assembled in the MAGLab setup. The entire MAGLab setup has been designed by a 3D CAD modeling program and it consists of two decoupled pairs of Helmholtz coils generating homogeneous magnetic fields parallel and perpendicular to the chip plane. At its center, a chip holder with integrated cooling and heating system is situated. On top of the chip holder, a connector lid with integrated fluidical and electrical connections is posi-

tioned, which enables the fluid transfer and the read-out of the sensors. Underneath the chip holder, further millimeter-scale core-coils are integrated, while one of them is linearly moveable. Finite element simulations have revealed that by superposing the homogeneous and inhomogeneous magnetic fields from the HH-coil and core-coil, respectively, both attractive as well as repulsive forces can be applied to magnetic beads within the microfluidic channel (see Chapter 4.6). The calculated forces are about 50 times higher compared to the net gravitational force acting on MagSense beads in aqueous solution. Equivalent calculations for magnetic manipulation of fibroblast cells showed that a labeling of at least 26 beads is required to exceed the cell's net gravitational force. The simulated results have been verified experimentally by demonstrating magnetic bead and cell manipulation in all three space dimensions (see Chapter 4.7 and 4.8). All magnetic fields, the read-out of the sensor, the peristaltic pump and the stepper motor driving the moveable core-coil are computer controlled by a LabView program. Finally, a sample analysis procedure has been presented illustrating the potential of this MAGLab system to operate at the molecular level aiming towards a magnetic-based total analysis system.

5. Basic cell-environment interactions

Some fundamental questions concerning the interaction between cells and their environment carried out in multiwells (off-chip) are discussed. Emphasis is put on both the way the cells influence their immediate environment as well as the way the environment changes the nature of the cell. Despite the fact that cells tend to adapt to their external environment, it cannot be presumed that they grow on any chip surface independent of its biochemical properties or interact with particles of arbitrary size and surface functionalization. A clear understanding about the cell uptake capacity by varying not only the bead features but also the cell type is required. Of further significance is the beads potential (cyto-)toxicity as an important part of this bidirectional cell-environment interaction.
All off-chip experiments are carried out under conditions similar to those found during the real-time monitoring experiments. The interpretation of the cell spreading and phagocytosis results of the next chapters is partly based on the results obtained here. The general procedure of cell culturing and handling under controlled sterile conditions is described in the Appendix A.2.1.

5.1. Cell growth on functionalized surfaces

As a first task, the surface properties suitable for long-term cell growth are studied. Usually, the cultivation of all kind of adherent cells is realized in standard culturing flasks. In our case, flasks from "greiner bio-one" [Greiner] are utilized and possess a growth area of 25 cm^2. In a confluent state, the density of fibroblast cells is about 20 000 cells/cm^2. When working with a smaller number of cells is required, we employ microwell plates (Becton Dickinson, purchased from [VWR]). In most cases, a 12-multiwell is used with a maximum number of about 41 600 fibroblasts in each well. Culturing flasks and multiwells are made of polystyrene. Their cell growth area is treated by vacuum gas plasma but its exact nature is a corporate secret. Independent of the cell type, they ensure a homogeneous growth and are considered as "reference surfaces" in the following discussion. Figure 5.1 a) displays exemplary the distribution of fibroblasts 20 hours after growing on a multiwell reference surface. Each well was seeded by about 20 800 NHDF cells and immediately after cell spreading, they occupy about 50 % of the multiwell growth area. Cell confluency (100 % surface coverage) is reached after 3 days, which is in the following denoted as cell doubling time. A good cell adhesion and growth is characterized by a homogeneous cell distribution and a pronounced flattening of the cells, i.e. the cells-substrate contact area is largest. In contrast, in case the surface is unfavorable for spreading, the cell remains in a rounded, frustrated state as described in Chapter 2.2.1.
In total, five distinct surface modifications are tested, namely Si_3N_4, APTES, SU-8, PEG-Biotin and Poly-L-Lysine. All samples are prepared on Si/SiO_2(50nm)/Si_3N_4(230nm)-wafer pieces of 1 cm x 1 cm in size. The plain and functionalized wafer pieces are placed in micro-

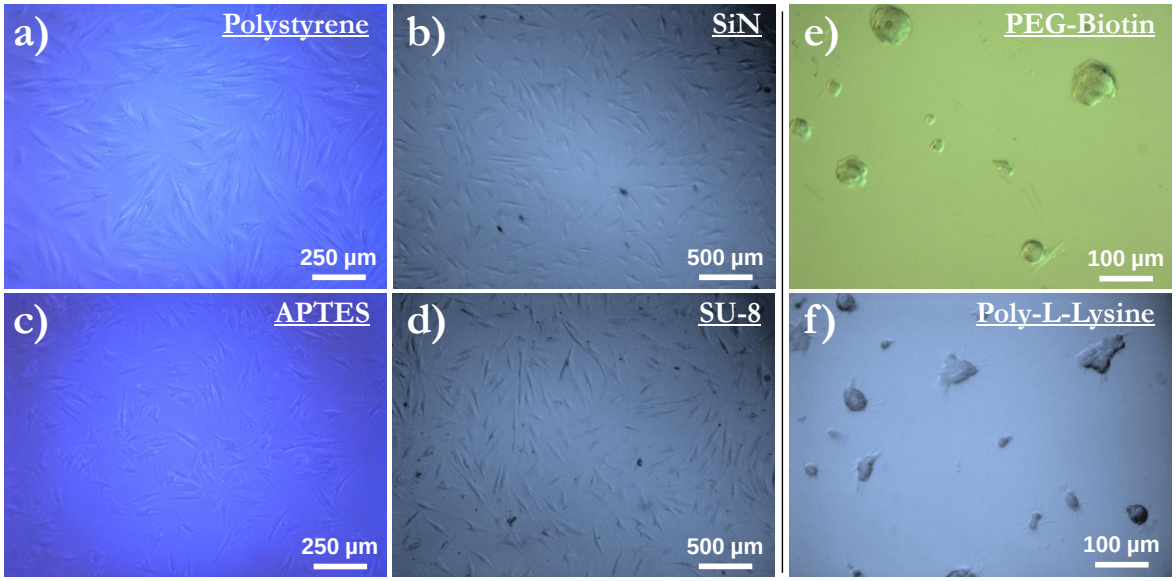

Figure 5.1: Examination of surface functionalizations for cell cultivation. Fibroblasts 20 hours after cell seeding, which are grown on a) the reference polystyrene surface, b) a plain chip-like Si_3N_4 layer, c) an positively charged aminosilane modified surface, d) a spin-coated photoresist layer of 500 nm thickness, e) a biotinylated layer enabling conjugation of streptavidin coated beads and f) a Poly-L-Lysine functionalization as an example from the literature (e.g. [Nakagawa2000]).

wells followed by cell seeding under sterile conditions. All surface modifications are primarily studied with fibroblast cells.

The first surface to be investigated equals the unmodified chip surface, i.e. a plain chemical-vapor-deposited Si_3N_4 passivation layer of 230 nm thickness. As a next surface, the Si_3N_4 passivation layer is modified by an aminosilane (APTES) layer according to the description given in Chapter 4.3.3. The silane molecules react with the surface forming either covalent "-Si-N-O-Si-" or thermally induced bonds [Melnik] leaving reactive amino groups available at the surface for further cell growth. In order to increase the quality of the silane layer, the passivation layer might be additionally treated by an oxygen plasma that creates new reactive groups at the surface. The subsequent heat treatment at 60 °C leads to a higher cross-linking and polymerization of the APTES molecules. The SU-8 2000.5 is an epoxy based photoresist (from [Microchem]), which is spin-coated over the Si_3N_4 passivation layer and has a final thickness of 500 nm (more details in Appendix A.1.2). It is chemically and thermally stable and the advantage of this approach is that the resist can further be patterned by standard photolithography processing. This would enable the controlled cell growth over predefined chip areas. The NHS-PEG_4-Biotin modified surfaces are realized on APTES functionalized wafer pieces. This biotin compound contains a polyethylene glycol (PEG) that serves as a spacer arm and is a chemical compound composed of repeating ethylene glycol (O-CH_2-CH_2)

units (from Thermo Scientific, [Piercenet]). The NHS-ester reacts with amino groups of the aminosilane layer, while the vitamin biotin represents the new functional group at the surface. From the bead immobilization point of view, the biotinylation represents an attractive surface for the streptavidin coated MagSense beads due to the high binding affinity between biotin and streptavidin [Panhorst2005]. The last surface to be studied is a Poly-L-Lysine modification of the Si_3N_4 passivation layer. This kind of surface functionalizations are commonly used in the literature as attachment factors for cell cultures such as HeLa cells [Nakagawa2000]. According to the data sheet provided by SIGMA, the Si-wafer is incubated for 5 min in a 0.01 % (w/v) Poly-L-Lysine solution.

The obtained results are displayed in Figure 5.1, and they represent different interaction possibilities. The plain chip surface (Figure 5.1 b)) and the SU-8 modified surface (Figure 5.1 d)) lead to similar results, where cell distribution and flattening is well pronounced. Thus, both surfaces would be an acceptable choice for cell culturing. This is not the case for PEG-Biotin and Poly-L-Lysine functionalized surfaces, where cells show typical frustration behavior (Figure 5.1 e), f)). Beside remaining in a rounded state, they additionally agglomerate to multicellular clusters. This is a common way utilized by cells to minimize the cell-surface contact area when the environment is unfavorable. Remarkable are also stress fibres build around the cell clusters (Figure 5.1 f)). The best cell growth results are obtained for APTES surfaces showing a cell spreading behavior similar to that of the reference polystyrene surface (Figure 5.1 a), c)).

Beyond providing a suitable basis for cell growth, the functional groups available at the surface are utilized for conjugation and, thus, immobilization of the negatively charged streptavidin coated beads. Tests performed on the positively charged APTES surfaces revealed that the electrostatic forces are strong enough to immobilize beads. From the detection point of view, the functionalization layer should be as thin as possible, since a close bead-to-sensor distance results in a maximum sensor signal. The APTES functionalion layer of less than 10 nm thickness (AFM data not shown) is the surface of choice for all cell experiments. This includes also experiments established with prostate cancer cells. For cancer cells, only the APTES modified surface was tested and the growth results were again comparable to the results achieved on polystyrene surfaces (see e.g. Chapter 5.2.1).

5.2. Cell interactions with MagSense beads

Phagocytosis of particles strongly depends on both the bead as well as cell type involved. Here, the interaction of two cell types with beads from various manufacturers varying in size and surface functionalization is investigated. First to be determined is which particles can be internalized by cells and, if so, to which extent. Most of the presented experiments

are carried out with fibroblasts, and the surface offered to the cells is an APTES coated $Si/SiO_2/Si_3N_4$-wafer.

5.2.1. Uptake capacity

At first, the interaction between MagSense beads and fibroblasts is studied, which represent the cells and beads of choice for most real-time monitoring experiments. The second part focuses on the interactions with prostate cancer cells. From the real-time phagocytosis monitoring point of view, the highest signal change can be generated if all the immobilized beads on top of the sensor surface can be internalized by cells. As described in Chapter 4.3.3, a good operating point of our biosensor is reached when 25 % of its surface is covered by beads. Thus, one has to make sure that all immobilized beads can be incorporated by the cells. To that end, more information about the average uptake capacity of a single NHDF and cancer cell especially for MagSense particles of 0.9 μm and 1.2 μm in size is required.

NHDF cells

Different amounts of beads are immobilized onto the sensor-like plain surfaces (Figure 5.2 a)). Each sample is placed into 12-well microtiter plates followed by a six hours incubation in 2 ml of bead-dH_2O solution with distinct bead concentrations (μg/ml): 1.0, 2.5, 5.0, 10.0, 20.0, 40.0, 60.0, 120.0. The highest bead concentration leads to a bead surface coverage of almost 100 %. After replacing the dH_2O by cell medium, approx. 80 000 cells are seeded in each well, which is sufficient to reach almost 100 % cell confluency. Subsequent to an overnight incubation, the cells are fixated by a simple drying procedure at room temperature. Then, the total number of internalized beads per cell is ascertained semiquantitatively by counting beads inside individual cells. To that end, images were taken by optical- and scanning electron-microscopy (SEM), while for SEM imaging an additional 100 nm thick Au-layer is sputter-deposited to ensure surface conductivity (Figure 5.2 e), f)). Following the image analysis, only cells with maximal bead loading at each bead immobilization concentration are choosen, and the results are displayed in Figure 5.2 e).

Once the cells sediment on top of the bead immobilized surfaces, they immediately start growing and internalizing particles. A common cell behavior observed immediately after ingestion into the cytoplasm is a further directional bead transfer towards the cell nucleus, at the border of which the beads accumulate [Wang2010]. As the cells continuously spread with increasing time, all particles in direct vicinity are ingested and transfered toward the cell center. Consequently, a circular bead-free area around the cells emerges, termed as forecourt (Figure 5.2 b), c)). Beads entering the cell nucleus is not observed. Their arrangement surrounding the nucleus proves that the beads are inside the cell rather than adhering to the

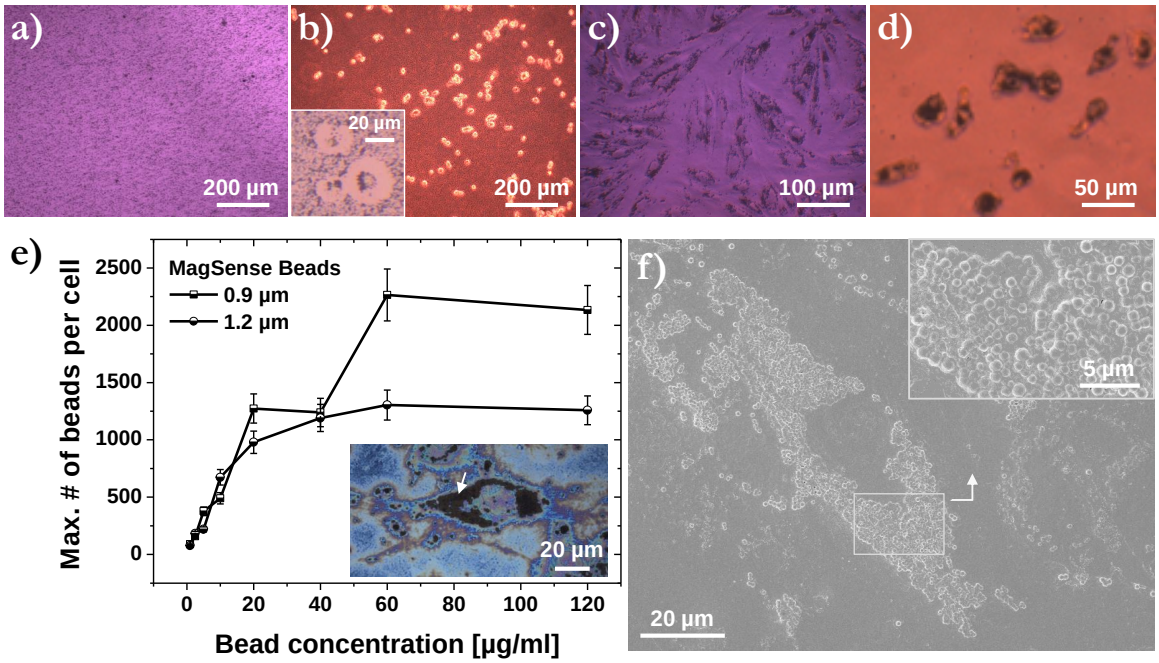

Figure 5.2: NHDF uptake capacity assay based on phase contrast and SEM imaging. a) 1.2 μm beads immobilized on APTES surface (40 μg/ml). b) Cell distribution 10 min after seeding, while the inset shows the formation of a "forecourt" after 30 min indicating bead internalization during spreading. c) Following phagocytosis and complete cell spreading, the initially homogeneously immobilized beads are rearranged within the cell cytoplasm around the cell nucleus (12 hours after seeding). d) Rounded cells after Trypsin-EDTA treatment demonstrating bead phagocytosis rather than attachment at the plasma membrane. e) Uptake capacity in dependence of the immobilized bead concentration; the inset optical micrograph shows a dried-out cell loaded with beads indicated by the arrow. f) High resolution SEM image of a heavily loaded cell at 60 μg/ml concentration demonstrating a close packaging of beads surrounding the nucleus.

cells' outer plasma surface (Figure 5.2 d) and f)).

The uptake behavior at low concentrations up to 20 (60) μg/ml shows a linear dependence of the uptake capacity with increasing bead concentration for the 1.2 μm (0.9 μm) beads. Continuous bead concentration increase leads to saturation, indicating a threshold value of the cellular uptake capacity. The saturation value conforms to the maximum internalized number of beads per cell and amounts to 1270 and 2265 for the 1.2 μm and 0.9 μm beads, respectively. As long as the bead concentration is low, i.e. up to 20 μg/ml, the bead counting procedure may be considered as accurate. When the bead number inside the cells increases, bead agglomerations occur and the counting becomes inaccurate, which leads to an average error of 10 %.

Each of the given concentrations results in a certain mean bead surface coverage and, thus,

Table 5.1: Comparison of the total volume and surface-area of phagocytosed beads to the average cell volume and surface-area (BCV and BCS ratios in %). *The average bead loading values as well as amoeba size were taken from [Weisman1967].

Bead/Cell type	MagSense [μm]		NHDF [μm]	Latex beads* [μm]		Amoeba* [μm]
	0.9	1.2	21	1.3	2.68	20
$\#_{tot}$ Beads	2260	1270	-	270	63	-
Volume [μm^3]	860	1220	4850	310	635	4190
BCV-Ratio [%]	18	25	-	7	15	-
Surface [μm^2]	5725	5968	1385	1430	1420	1250
BCS-Ratio [%]	413	431	-	114	114	-

an occupied average area per bead. Therefore, additional information regarding the uptake capacity can be obtained when the maximum number of beads that are situated underneath a confluently grown cell is determined. We calculate the limit of hexagonally close packed surface coverage reached at the maximum bead concentration, while the average cell-surface contact area of a spread cell is taken from the SEM (Figure 5.2 f)) and cell spreading analysis (see Chapter 6.1). Confluently grown fibroblasts display an elongated elliptical shape with measured mean major and minor axes of about 113 μm and 37 μm, respectively. According to their spreading area, a single confluent cell can cover about 2630 (4690) close-packed 1.2 μm (0.9 μm) beads. Compared to the experimental results, the theoretical estimations reveal a difference in the maximum uptake capacity of about 50 %. This leads to the conclusion that the cell uptake capacity is limited to a certain amount of beads. Moreover, optical microscope observations of uptake experiments at high bead concentrations (> 60 μg/ml) showed remaining beads present after cell detachment/replacement, which is a further indicator supporting the saturation effect of bead endocytosis.

The engulfment and uptake process depends, amongst others, on the bead size. Electron microscopy studies on size dependent phagocytosis confirm that beads of 1.3 μm and larger are ingested individually, being tightly enveloped by the plasma membrane. The average gap between the bead-surface and the enclosing vesicle is less than 120 nm [Korn1967]. Beads in the range of 0.5 μm in diameter can be internalized both by phagocytosis [Aggeler1982] and by micropinocytosis [Korn1967]. Aggeler et al. investigated by means of electron microscopy the initial events during the uptake process by macrophages and proved the individual engulfment of 0.45 μm latex particles. Whereas in the later case, beads of 0.557 μm diameter are first accumulated at the outer cell membrane by a substance secreted by the amoeba and then collectively internalized, with many beads tightly packed inside one phagosome. Uptake inhibition experiments performed at low temperatures showed that there is no radical discontinuity between the pinocytosis and phagocytosis process [Pratten1986]. Phagocytosis is the more likely uptake mechanism when the particle size becomes increasingly larger. In all

our real-time monitoring experiments presented in the next chapters, solely beads of 1.2 μm in diameter are used, suggesting phagocytosis as the prime uptake mechanism. In contrast, beads with 0.9 μm in diameter are located in the transition zone between phagocytosis and micropinocytosis. In this case, both uptake mechanisms have to be taken into consideration. However, their size is closer to the bead size internalized by phagocytosis and, thus, for the calculations in Table 5.1 we assume an individual bead uptake. In general, each bead transfer into the cytoplasm via membrane-bound vesicles (phagosomes) goes along with a loss of the cell surface membrane. Therefore, the total surface area of internalized particles corresponds in good approximation to the plasma membrane interiorized during phagocytosis [Korn1967, Herant2006, Tsan1971]. Table 5.1 compares both the total volume as well as surface-area of internalized beads to the average cell volume and surface-area, denoted as the bead-cell-volume ratio (BCV-ratio) and bead-cell-surface-area ratio (BCS-ratio), respectively. According to phase contrast images taken after cell detachment, we attain for non-adherent fibroblast cells with an almost spherical shape a measured average diameter of 21 μm. The BCV ratio demonstrates that the total volume of MagSense beads taken up is comparable for both bead sizes. They occupy about 18 % and 25 % of the cell volume for the 0.9 μm and 1.2 μm large particles, respectively. Our findings agree with results from the literature. Weisman et al. demonstrated that the total volume or mass of inert latex particles internalized by neutrophils and acanthamoeba is identical within a variation of factor two for all particle sizes in the range between 0.126 μm and 2.68 μm [Weisman1967].

Prostate cancer cells (DU145)

MagSense beads of 1.2 μm in size are immobilized at a concentration of 40 μg/ml. This amount of beads results in an average surface coverage of about 30 %, which is slightly higher compared to the optimal operating sensor coverage value of 25 % (see Chapter 4.3.3). Figure 5.3 displays the time dependent progress of bead phagocytosis starting from cell seeding until complete cell spreading. Again, with elapsing time a forecourt around the cells is formed, suggesting bead uptake. In the cell detachment experiments no free beads could be observed, which proves that their uptake capacity is sufficient to incorporate all immobilized beads. According to the image analysis, the diameter of a rounded DU145 cell is 16 μm and its cell-surface contact area is 790 μm^2. In case of a maximum bead concentration, i.e. 100 % hexagonally closed packed surface coverage, each cell can cover a maximum calculated number of about 630 beads. In this experiment, the estimated total amount of beads internalized by each cell is 190, which corresponds to a 30 % bead surface coverage.

In a living multicellular system such as a human body, adherent cells are commonly found in a spread, confluently grown state. In this regard and in view of potential in vivo applications, the uptake behavior of already grown cells is of high interest. The sample preparation

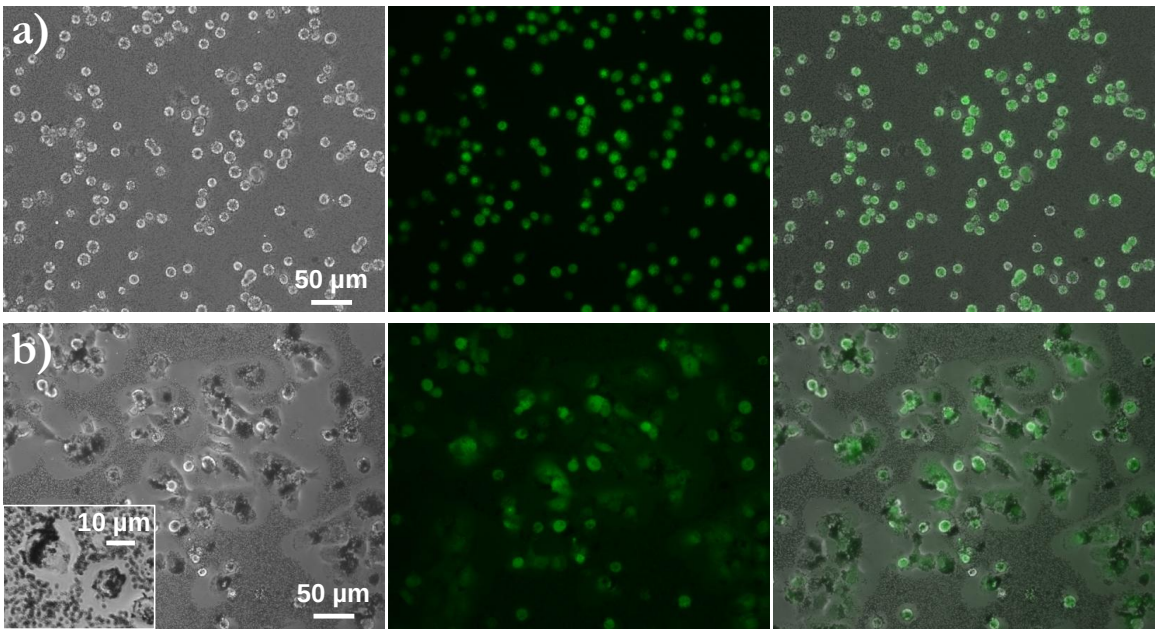

Figure 5.3: Phase-contrast, fluorescent (Calcein-AM) and overlay images of a) as seeded (15 min) prostate cancer cells on bead-modified surfaces and b) bead uptake within an elapsed cell growth time of 6 hours; the inset image demonstrating the forecourt formation is taken after 60 min.

procedure remains almost the same except of the reversed chronological order of cell and bead incubation, i.e. the cells are first grown on sensor-like surfaces building a cell monolayer and then the beads are added. This kind of uptake experiments are denoted as "top-down" approach. In contrast, the previously described experiments of immobilized beads followed by cell growth are denoted as "bottom-up" approach. In the experiments carried out with fibroblast, no significant differences between the bottom-up and top-down uptake behavior could be observed. The cancer cells instead display a strongly reduced top-down uptake capability (Figure 5.4). Incubating the same amount of beads (40 μg/ml) results in occasional phagocytosis, while the majority of cells is free of any beads, suggesting no phagocytosis.
Characteristic to all top-down experiments involving cancer cells are local accumulations of beads forming isolated bead-islands (Figure 5.4 b)). Though this kind of phenomenon is observed by other groups too, the driving force behind it remains unknown [Plank2010].
In some top-down experiments, an amount of cancer cells is chosen that is too low to totally cover the substrate surface and to build a confluent monolayer. This constellation allows to study the uptake behavior of already completely spread cells that still can migrate in non-occupied areas of the surface. Following incubation, the beads sediment upon the cells and the cell-free surface area. Figure 5.4 c) shows bead accumulations at the border, where the cells subsequently migrate into the cell-free area immobilized by beads. This behavior was partially observed and gives the impression as if the beads are being pushed away by the

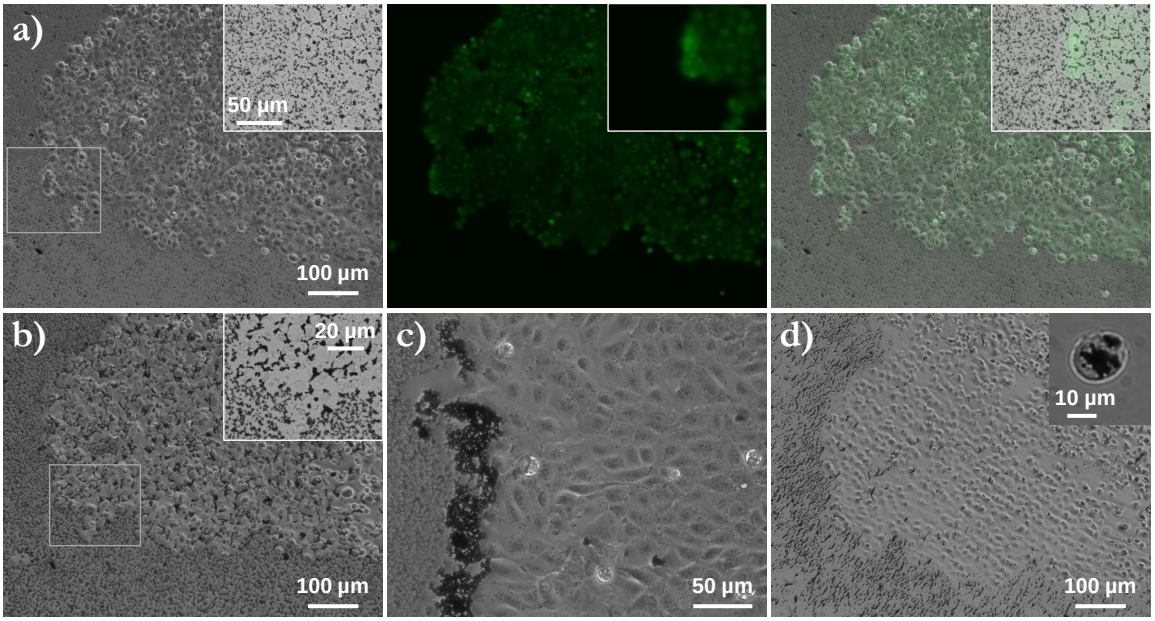

Figure 5.4: Phase-contrast, fluorescent (Calcein-AM) and overlay images taken during the uptake experiment. a) Prostate cancer cells are first grown on APTES surfaces and then incubated with beads (40 μg/ml); image taken after 15 min. b) After an overnight incubation, the beads laying on top of the cell monolayer agglomerate to randomly distributed bead-islands, while those laying outside the cell monolayer remain homogeneously distributed. c) Bead accumulations at the border, where cells subsequently migrate into the cell-free area immobilized by beads. d) Removing non-adherent or non-internalized beads by dipping a magnet close to the cell surface; the inset shows a bead-loaded cell after its detachment by Trypsin-EDTA.

invading cell front, instead of being incorporated. In a further step, a magnet was dipped in the cell medium close to the cell monolayer. By slow lateral movements, most of the non-attached beads could be removed, while those which are internalized or attached to the cells surface remained (Figure5.4 d)). Finally, the cells are detached by Trypsin-EDTA according to the description in previous Chapter 5.2.1 (see Figure 5.2 d)). The cells containing beads are magnetically separated from the bead-free cells and transferred into a new multiwell. Despite the fact that some of them contain beads, the majority of the cells is bead-free (Figure 5.4 d)).

The phagocytic behavior of fibroblasts is similar for the bottom-up and top-down approach, while cancer cells show a tremendous difference in the uptake capacity depending on the applied approach. The pronounced uptake behavior of cancer cells in the bottom-up approach is possibly attributed to the fact that the surface including the immobilized beads is considered by the cells as one growth surface. During the cell spreading process, thin lamellipodial protrusions creep onto the substrate surface. In case that an immobilized bead is encountered, the cells plasma membrane flows outward the bead surface progressively surrounding it. Due to their spherical shape, eventually the leading membrane edges meet, fuse

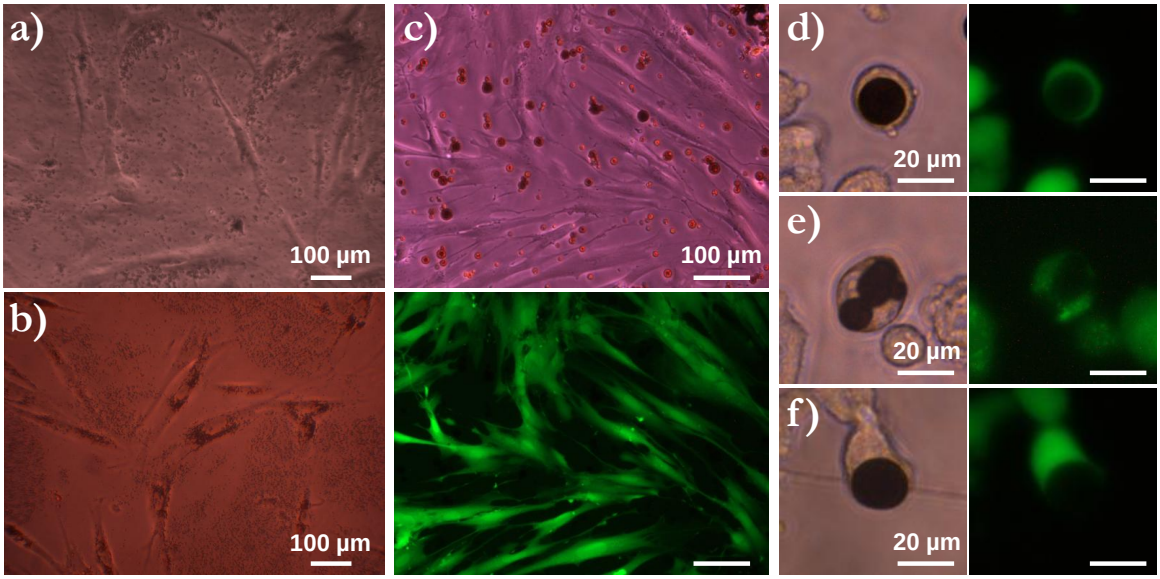

Figure 5.5: Phase-contrast images of a) non-internalized Nanomag-CLD-greenF and b) internalized Sicastar-M beads from Micromod. c) Phase-contrast and fluorescent images of Chemagen beads added on top of grown cells. Fibroblasts with single (17 μm) d) and multiple e) phagocytosed Chemagen beads. f) Cell attached to a 20 μm sized bead that is to large for phagocytosis.

with each other forming an membrane-bound vesicle containing the bead [Weisman1967]. In general, the complete cell spreading process can be considered as the attempt of a cell to internalize a particle that is too large for phagocytosis. Experiments on phagocytosis of yeast pathogens by granulocytes have demonstrated that both processes obey similar characteristics [Evans1993, Herant2006, Stewart1989]. In both cases, the sequential cell spreading and cell body contraction exhibited abrupt start and stop kinetics [Evans1993].

5.2.2. Cell interactions with different bead types

Beside MagSense particles, also the uptake of particles from other companies with varying functional properties and particle diameters is investigated. First, attention is put on Sicastar-M (~1.5 μm - COOH modified) and Nanomag-CLD-greenF (0.5 & 1.0 μm - fluorescence labeled, FITC) particles from Micromod (see Chapter 4.2). The chosen bead sizes are in the range of the MagSense beads, while all of their surface functional groups differ from each other. Here, all bottom-up uptake experiments are performed with fibroblasts (60 % confluency) and the bead concentration used is 30 μg/ml. Optical microscopy images are taken 10 hours after cell incubation, thus allowing their complete spreading.
Regarding the fluorescence labeled Nanomag particles, no cell-bead interactions could be observed. There are no typical bead rearrangements around the cell nucleus and no significant bead accumulations inside the cells after Trypsin-EDTA cell detachment (Figure 5.5 a)). The

particular differences are not clear at this stage. Additional experiments are required to clarify whether the cells lack the appropriate complementary receptors to recognize the modified beads or whether the beads are considered as toxic.
In contrast, the carboxyl modified beads show a good interaction affinity. Fibroblasts are grown on an APTES-modified surface covered by 20 μg/ml Sicastar bead concentration. After the initial forecourt formation, the cells continue spreading which finally assume an elongated shape (Figure 5.5 b)). Three days after, the entire surface is covered by cells and all beads are incorporated.

The main purpose of the next experiment is to identify the maximum possible size of a single bead a human fibroblast cell can uptake. The concentration used for the Chemagen particles with sizes within ~2-25 μm is 200 μg/ml. Figure 5.5 c) displays the distribution of cells after an overnight bead incubation. As long as the cells are in a spread state, no clear conclusion can be drawn whether the particles are inside the cell or attached on top of them. In order to better distinguish these two cases from each other, we treated the cells with Trypsine-EDTA, which transforms them from a spread flat to a spherically shaped state. In Figure 5.5 d) and e) Calcein-AM stained cells with single and multiple incorporated beads are displayed, respectively. After an incubation time of 24 hours, the largest bead size found inside a cell accounts for ~18 μm in diameter. This results in an equivalent BCV ratio of about 63 %, which is approximately by a factor of three higher compared to the BCV ratio of MagSense particles. However, in case the bead size is too large for phagocytosis, the cell remains attached at the bead surface trying to engulf it (Figure 5.5 f)).

5.3. Cell viability

For all in vivo or in vitro applications, the magnetic carriers must be biocompatible and non-toxic. Hence, the objective of this investigation is to assess the (cyto-)toxic effects of MagSense particles. A standard method to study the cells viability is based on a fluorescence assay using the vital dye acetoxymethyl ester of calcein (Calcein-AM). This initially nonfluorescent dye crosses passively the cell membrane and is converted after removing the acetoxymethyl group by cytosolic esterases into green fluorescent calcein. This calcein molecule is retained inside the cell and, thus, leads to its labeling or staining. In contrast, dead cells lack the cytosolic esterases and, therefore, no fluorescence signal occurs [Bratosin2005]. Typical cytotoxic indicators are for instance changes in the mitochondrial function, permeability of the plasma membrane, cellular morphology resulting in abnormal cell sizes (shrinking/swelling), detachment and apoptosis [Jeng2006].

The sample preparation resembles the top-down approach described above. First, fibroblasts are grown (confluently) in multiwells followed by bead incubation (1.2 μm MagSense of

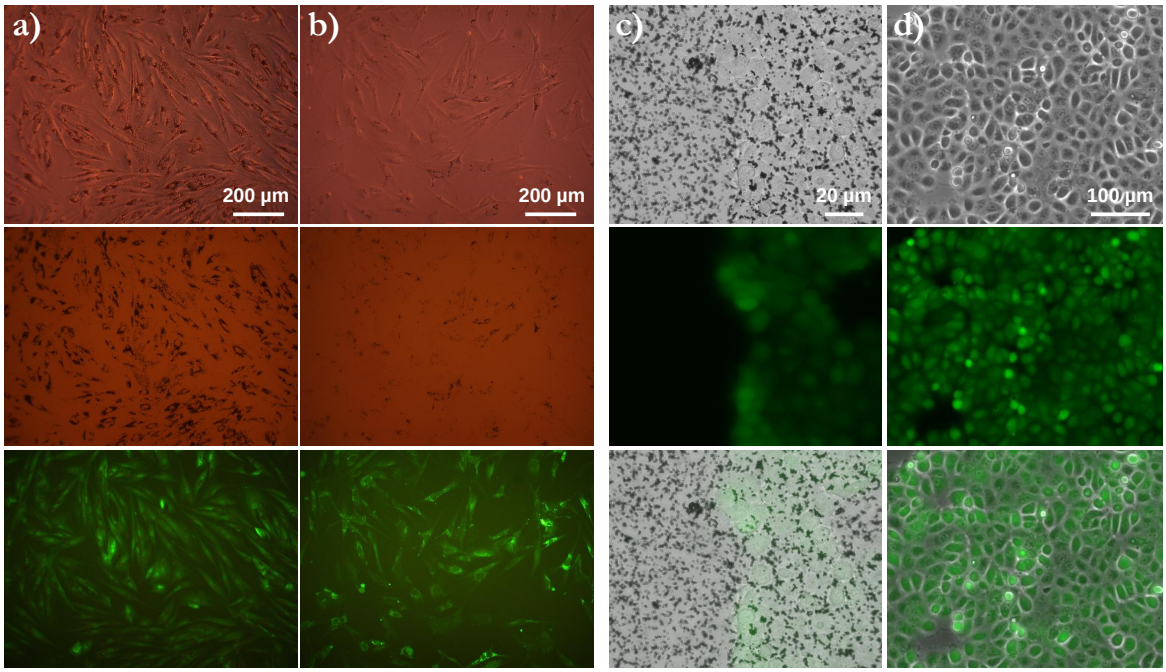

Figure 5.6: Cell viability assay based on fluorescence using the vital dye Calcein-AM. Phase-contrast, disabled phase-contrast and fluorescent images of fibroblasts a) seven days and b) 14 days and of DU145 cells c) one and three days after bead incubation.

60 μg/ml concentration). Cell vitality is tested by Calcein-AM staining after 7 and 14 days. During this time period the cells are passaged every 72 hours, indicating the cell doubling time.

Figure 5.6 demonstrates the strong green fluorescence observed after one and two weeks following bead incubation. The results obtained for both cell types are similar. Independent of the incubation time, no cytotoxic effects could be observed. However, we could ascertain a slight delay in the cell doubling time (fibroblasts ~80 hours) compared to reference cells. Noticeable is the decreasing number of beads inside the cells after each cell division cycle (Figure 5.6 a), b); see disabled phase-contrast images). The expected bead-loading per cell after four cycles of doubling is about 6 % of the initial bead-loading value. In general, the fact that the cells continue to proliferate or replicate themselves by cell devision represents another indicator for the non-toxicity of the investigated particles. However, the viability experiment with the DU145 was terminated after 3 days since almost no cells with internalized beads could be observed.

5.4. Summary

Subject of this chapter has been the off-chip investigation of basic cell-environment interactions and their reciprocal interferences. In order to cover a broad range of interaction possibilities, we have varied the type of cells, beads and surface functionality. In a first step,

the influence of five different surface functionalizations was assessed. APTES was identified as the most suitable surface functionalization for all cell experiments allowing not only fibroblast and cancer cell growth, but also bead immobilization. In a further step, the bead uptake capability and capacity was examined in two different approaches, namely bottom-up and top-down, involving five different bead types from three distinct companies. Except for the Nanomag-CLD-greenF beads from Micromod, fibroblast cells internalized all other bead types independent of the uptake approach. The maximum number of 1.2 μm MagSense beads inside the cell accounts for 1270, which corresponds to the equivalent of 25 % (> 400 %) of the cells overall volume (macroscopic surface area). Fibroblast are able to internalize Chemagen beads up to 18 μm in diameter constituting the equivalent of about 63 % of the cells volume. The uptake behavior of the prostate cancer cells was examined solely with MagSense beads, which are the particle of choice for the real-time monitoring experiments. In the bottom-up approach, a slightly higher bead-surface coverage (30 %) was employed compared to the coverage (25 %) at which the sensor shows best performance. The phagocytic capacity of at least 200 beads per cells is sufficient to internalize all the immobilized beads. This is essential in view of the real-time phagocytosis monitoring experiments, which results in the highest signal change. In contrast to the fibroblasts, the uptake behavior of cancer cells is very different for the top-down and bottom-up approach. In the bottom-up approach cells consider the surface including the beads as one growth surface and, thus, spreading on spherically shaped particles leads unavoidably to their successive engulfment. Although the cell detachment experiments demonstrated partial bead phagocytosis, the phagocytic property becomes minor once they are completely spread at the surface (top-down approach). Finally, the biocompatibility assay based on the Calcein-AM fluorescence revealed no cytotoxicity of MagSense particles for both types of cells. Independent of their bead-loading, cells continue to proliferate with a slight delay in the doubling time, which is another indicator of the non-toxicity of the MagSense beads.

6. Real-time monitoring of bead phagocytosis during cell spreading

In this chapter we investigate the interactions between living cells and immobilized beads based on monitoring the time evolution of the sensor-signal in real-time (bottom-up approach). The concept underlying the bottom-up approach has already been introduced in Chapter 3.4. Once the cells are added, they sediment and attach to the sensor surface followed by cell spreading. The respective time evolution of the GMR-response is highly dependent on the spreading progress and, thus, reflects the actual stages the cells undergo during spreading. Associated with the cell's shape transformation, i.e. from an initial spherical to a final flattened state, are two relevant morphological changes. First of all, with elapsing time the cell-surface contact area increases and, consequently, the cell-bead interaction range. Due to bead phagocytosis, the overall distance between the immobilized beads and the sensor-surface is altered, which represents a time-dependent parameter. Secondly, with proceeding spreading stage also the surface-to-volume ratio increases. For instance, the macroscopic surface area of a flat fibroblast exceeds that of a spherical one by a factor of 5.6. We have demonstrated in the last chapter (Chapter 5.2.1) that phagocytosis can lead to a cell surface area loss of up to about 400 %. Thus, cell spreading rivals the surplus plasma membrane area required for vesicle formation during bead phagocytosis. Due to these competing events, one could expect a delayed or inhibited cell spreading progress on bead-immobilized surfaces compared to plain reference surfaces. To that end, the first part of this chapter concerns the analysis of the spreading behavior of both cell types on bead-covered and bead-free surfaces by means of optical phase-contrast and fluorescence microscopy. The obtained results serve as reference values for the real-time magnetoresistive phagocytosis monitoring experiments presented in the second part. In addition, the stability of internalized beads has been examined by a long-term monitoring experiment.

6.1. Optical-based cell spreading analysis

The spreading of fibroblast and cancer cells is studied on sensor-like plain ($Si/SiO_2/Si_3N_4$/-APTES) as well as bead modified ($Si/SiO_2/Si_3N_4$/APTES-Beads) surfaces. In the later case, the plain APTES surface is immobilized with 1.2 μm MagSense particles resulting in an average surface coverage of ~23 %, which is identical to those used during the GMR-based monitoring experiments. Both types of surfaces are transfered into a 6-multiwell. To better identify the spreading stage of the cell and to enhance the contrast of the microscopic imaging, we additionally stain the cells with Calcein-AM (see cell staining protocol Appendix A.2.3). After harvesting the cells from culturing flasks with Trypsin-EDTA (or Accutase), they are suspended in cell medium and about 41 000 fibroblast and 85 000 cancer cells are added in each well corresponding to about 50 % surface coverage. The seeded cells start to sediment and attach to the underlying surface. The initial attachment process is characterized by a

first lag time of about 10 min for both cell types, during which no cell morphological changes could be observed. Immediately thereafter, membrane protrusions are formed initiating cell spreading at a certain rate until a final flattened, disk-like shape is reached. This shape transformation stage denotes the cell state with maximum cell-surface contact spreading area.
Figure 6.1 a) and c) display the total time evolution of the cellular top view projection area, which is in good approximation to the cell-surface contact area. The corresponding phase-contrast and fluorescent time-lapse images are shown in Figure 6.1 b) and d). The projection area is determined by means of the software ImageJ 1.41o and the evaluation procedure is exemplary described in [RSB]. Each data point in Figure 6.1 a) and c) represents the average value of about 30 unsynchronized cells. Synchronizing the cell cycle would result in a more homogeneous distribution of the measured projection area and, thus, a decrease of the standard deviation. The reason lies in the fact that cells close to division possess about double the size than those immediately after division. The advantage of using unsynchronized cells is that independent of their harvesting point of time, their projection area analysis would always approximately lead to similar results.

According to Figure 6.1 a), the first 2.2 h of fibroblast spreading may be considered as quasi-linear with similar spreading rates of 700 $\mu m^2/h$ for both investigated surfaces. In the further course of time, the spreading process displays for both growing surfaces an asymptotic behavior. In addition, we can observe a divergence with a clear inhibition in the spreading rate for the bead immobilized surface. However, at equilibrium state the projection area reaches a maximum average value of 3900 μm^2 for the reference surface, which is comparable to values from the literature. Woods at al. investigated surfaces coated by intact fibronectin, a glycoprotein of the extracellular matrix that promotes complete fibroblast adhesion, as well as those modified by several fragments of fibronectin [Woods1986]. They observed spreading areas in the range between 1733 μm^2 and 4904 μm^2, while the intact fibronectin coated substrate revealed the maximum projection area of 4173 μm^2. In contrast, the cell projection area of the bead-modified sample accounts for 3250 μm^2, which is 17 % less compared to the reference case.

The expected delay in spreading rate due to the contemporaneous plasma membrane loss and volume increase caused by ongoing phagocytosis appeared for fibroblast cells after an elapsed time of about 2.2 h. Within this time frame, there is no remarkable spreading delay between the involved surfaces. This, in turn, implies that the additional plasma membrane surface utilized for internalizing beads in membrane-enveloped vesicles is supplied by rapid membrane recycling through focal endomembrane exocytosis. For later times beyond 2.2 h, the projection area of fibroblasts spreading upon bead-immobilized surfaces shows a very slow increase, while the projection area of reference cells continues to grow. Therefore, a

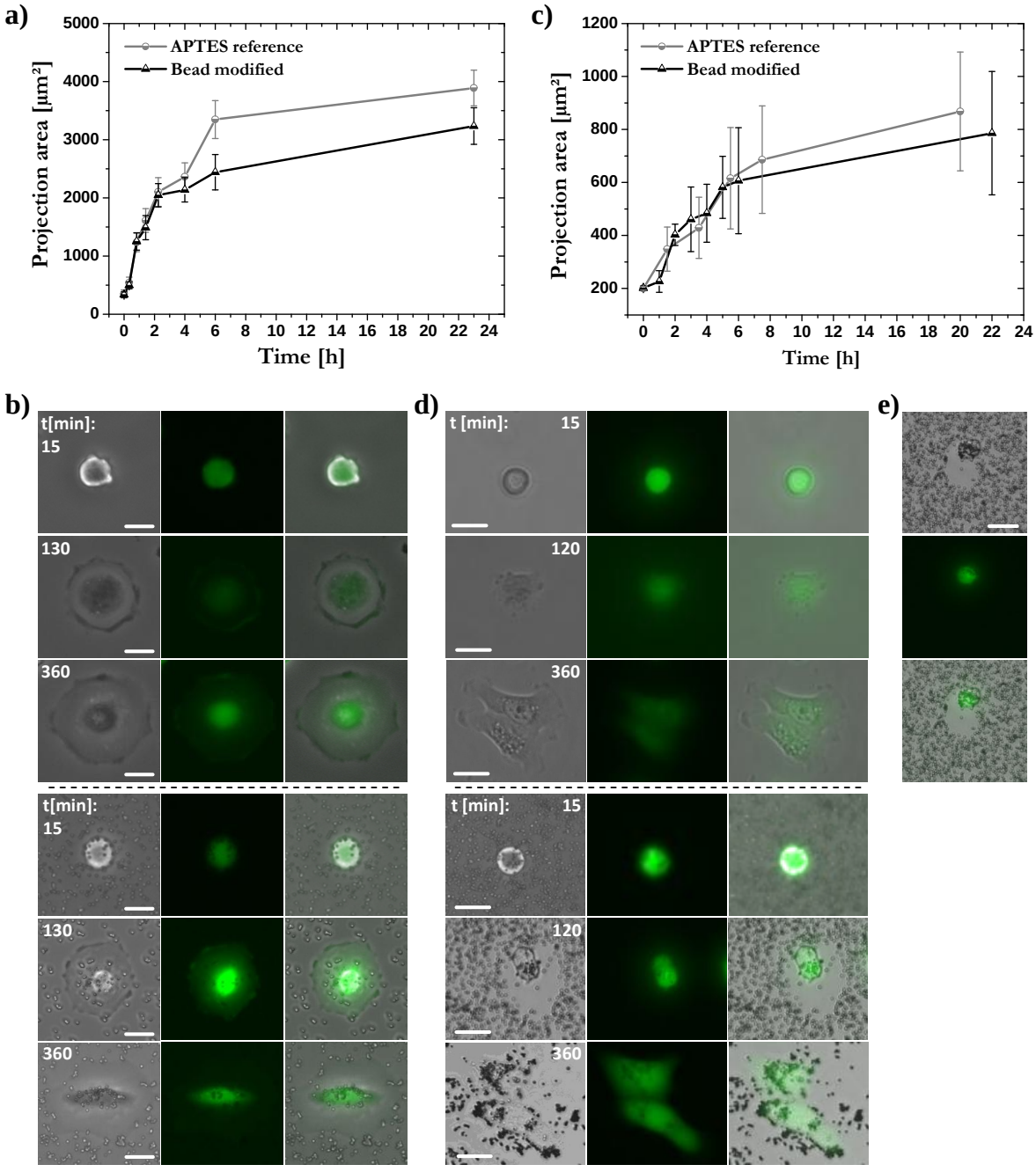

Figure 6.1: Cell spreading analysis on bead-free and bead-modified surfaces. a) and c) display the time evolution of the cellular spreading area, while b) and d) represent the corresponding phase-contrast and fluorescent time-laps images for fibroblast and DU145 cells, respectively. e) DU145 cell leaving a particle-free trace along their migration route prior to the spreading process; scale bar 20 μm.

time ≤2.2 h can be considered as spreading saturation time for the case of a bead-modified surface. After 6 h of cell spreading, the maximum difference in projection area of ~900 μm^2 is reached. Taking into account the dorsal and ventral membrane, this area has to be doubled. The total projection area difference corresponds to a membrane area utilized for vesicle formation sufficient for about 400 phagocytosed beads. At time 6 h, the cells' projection area on bead-modified surfaces amounts to 2440 μm^2. Considering the known bead surface coverage of ~23 %, the calculated number of beads covered by each cell at this spreading stage is about 500. The approximate agreement of these two values suggests that spreading and phagocytosis are membrane competing processes limited by the capacity of endomembranes. The total plasma membrane required to engulf 500 beads is 2260 μm^2, which is equivalent to 163 % of the macroscopic surface area of a spherically shaped fibroblast cell. As discussed in Chapter 2.2.3, in addition to the macroscopic plasma membrane also intracellular compartments contribute to the phagosome formation. These recycling endomembranes are limited and continuous cell spreading accompanied by phagocytosis eventually leads to their successive depletion [Cannon1992, Desjardins2003]. In contrast, professional phagocytes such as macrophages or neutrophils store additional plasma membrane area in folds and villi. The unwrinkling of the plasma membrane is another membrane source utilized by cells to increase their macroscopic surface area enabling the huge plasma membrane turnover during phagocytosis. Macrophages are capable to internalize the equivalent of up to 145 % of their overall surface area within 30 min [Herant2005, Cox2000]. The last data set determined at time 23 h suggests a slight increase in projection area, which could be attributed to further membrane supply originating from different sources. The recruitment of the different plasma membrane sources, i.e. endosomes, lysosomes, endplasmic reticulum or plasma membrane unwrinkling, happens at different stages of phagocytosis [Booth2001, Braun2006].

In case of cancer cells, the spreading behavior is almost similar for the reference as well as bead-modified surface with a quasi-linear spreading rate within the first 6 h of about 70 μm^2/h (Figure 6.1 c)). For the bead modified and reference surface a time ≤5 h and ≤6 h can be considered as spreading saturation time, respectively. For later times, we can observe an asymptotic behavior for both growing surfaces reaching at equilibrium a maximum projection area of 790 μm^2 (870 μm^2) for bead-modified (reference) samples. Depending on the underlying substratum, their maximal spreading area can vary between 580 μm^2 and 875 μm^2 [Wells2005]. In contrast, there is only a slight divergence between the two investigated surfaces visible and, thus, the expected delay in spreading rate caused by simultaneous phagocytosis is less pronounced compared to the fibroblasts. For times beyond 6 h, the projection area of reference cells lies always above that of the bead-modified surface with a maximum area difference of 83 μm^2 after 22 h of spreading. The excess plasma membrane of twice the projection area is sufficient to envelop about 37 beads. At time 5 h, the cells reach a spreading

area of 580 μm^2, which is enough to cover about 123 beads. These two values showed a good agreement for the studies carried out with fibroblasts, whereas here a difference by the factor of three is observed. The possible reasons leading to this result and its consequences are discussed below.

Besides the common lag time of about 10 min, the spreading behavior of the investigated cell types show also different characteristics. A common spreading feature that all fibroblasts share is their continual spreading until a maximum area is reached. Once the spreading process is completed, they start migrating and proliferating on the substrate without a tendency to build cell clusters. Cancer cells instead exhibit two different spreading patterns, while one of them resembles that of fibroblasts. In the other spreading pattern, we could observe an additional cell migration immediately after the lag time without any noticeable indication of cell spreading. This behavior was particularly eye-catching in case of bead-modified samples due to the fact that moving cells continually uptake beads and leave a particle-free trace along their migration route (Figure 6.1 e)). Moreover, DU145 cells exhibit a high cluster formation affinity that is partly visible even for almost confluently grown cells (see Figure 4.2 d)). Cells migrating on the surface increase their likelihood to meet other cells and, thus, the cell migration before complete cell spreading might contribute to an enhanced cluster formation. In case of a confluent cell monolayer, fibroblasts show a very pronounced spreading with homogeneously distributed cells, while the cancer cells show more irregularities with an overall hilly profile. The final spreading area of fibroblasts grown on reference and bead-modified surfaces is by a factor of about five and four times higher compared to that of DU145 cells, respectively. The projection area of completely spread fibroblast and cancer cells is by a factor of about eleven and four higher, respectively, compared to the as-seeded cells. The macroscopic plasma membrane surface area after spreading is for fibroblasts and cancer cells higher by a factor of 5.6 and 2.0, respectively, compared to the as-seeded cells. Due to their low projection area change during spreading and their less uniform spreading characteristics, DU145 cells are not an ideal choice for cell spreading inhibition studies.

6.2. GMR-based real-time monitoring of cell spreading

Independent of the cell type involved, the procedure of the real-time monitoring experiments concerning phagocytosis during cell spreading remains the same. The preparation of the chip consists of an APTES surface modification and a PDMS fixture mounting. After assembling into the MAGLab setup, 1.2 μm MagSense particles are immobilized on the biosensor surfaces by incubating 400 μl of a 25 μg/ml bead-dH_2O suspension. In a further step, the water is replaced by cell medium and approximately 6000 NHDF or 21000 DU145 cells are seeded onto the bead modified biosensor surface. This moment indicates the initiation of cell spreading and phagocytosis. For the magnetoresistive-based real-time monitoring, both the signal of

the bead-covered biosensors as well as the bead-free ref-sensors are measured in appropriate time intervals at every stage of the experiment. Each data point represents the average value of 2-3 measurements, and the respective standard deviation is displayed as error bar. In parallel, optical microscopy images are recorded visualizing the cell/bead distribution during the different stages of the experiment. From the moment of cell seeding, a daily cell medium exchange is accomplished. At the end of the experiment, all cells are detached by using trypsin-EDTA and finally removed by several PBS and dH_2O washing steps. The results attained for fibroblasts and DU145 cells are presented consecutively.

Another fundamental question concerning the long-term stability of internalized beads is addressed in the last part of this chapter. Most of our magnetically monitored phagocytosis/spreading experiments last for several days. Especially with regard to such long-time experiments, digestion or degradation of beads would result in a systematic error in the data interpretation. The stability of internalized beads for times beyond the maximum time required for the real-time monitoring experiment is confirmed.

6.2.1. NHDF cells

The GMR-signal trace of a single biosensor comprising the entire experiment is exemplarily displayed in Figure 6.2 a) and b), while the respective time-lapse optical microscopy images are depicted in Figure 6.2 c). A set of biosensors is analyzed and the data is summarized in Table 6.1. The real-time monitoring course of each experiment is divided into different stages indicated by the letters I - VI. The sensor response in air and dH_2O (I, II) is identical and corresponds to the blank signal level of the GMR-sensor (see Chapter 4.3.3). In stage III, beads suspended in dH_2O are immobilized, resulting in a biosensor surface coverage of about 23 %. Consequently, the bead's stray fields lead to a GMR-signal increase of the biosensors, while the non-covered ref-sensors remain at blank level. To ensure long-term cell growth and proliferation, a suitable environment has to be provided. To that end, the DI water is carefully exchanged by DMEM cell medium without significantly distorting the bead positions, thus retaining the previous GMR-responses of the biosensors (IV). The time-dependent cell-bead interactions are initiated in stage V by adding about 6000 fibroblasts into the fluidic chamber at time zero. In a spread-out state, this amount of cells would be sufficient to form a confluent monolayer across the exposed chip-area defined by the fluidic chamber dimensions. Table 6.1 shows the number of cells on each sensor counted from the optical images taken immediately after complete sedimentation of the cells (~5-10 min). The shape of the cells at this as-attached state is still spherical, and at this point only about 16 % of the chip surface area is covered by cells. The last step in each experiment pertains the cell detachment and removal indicated by stage VI.

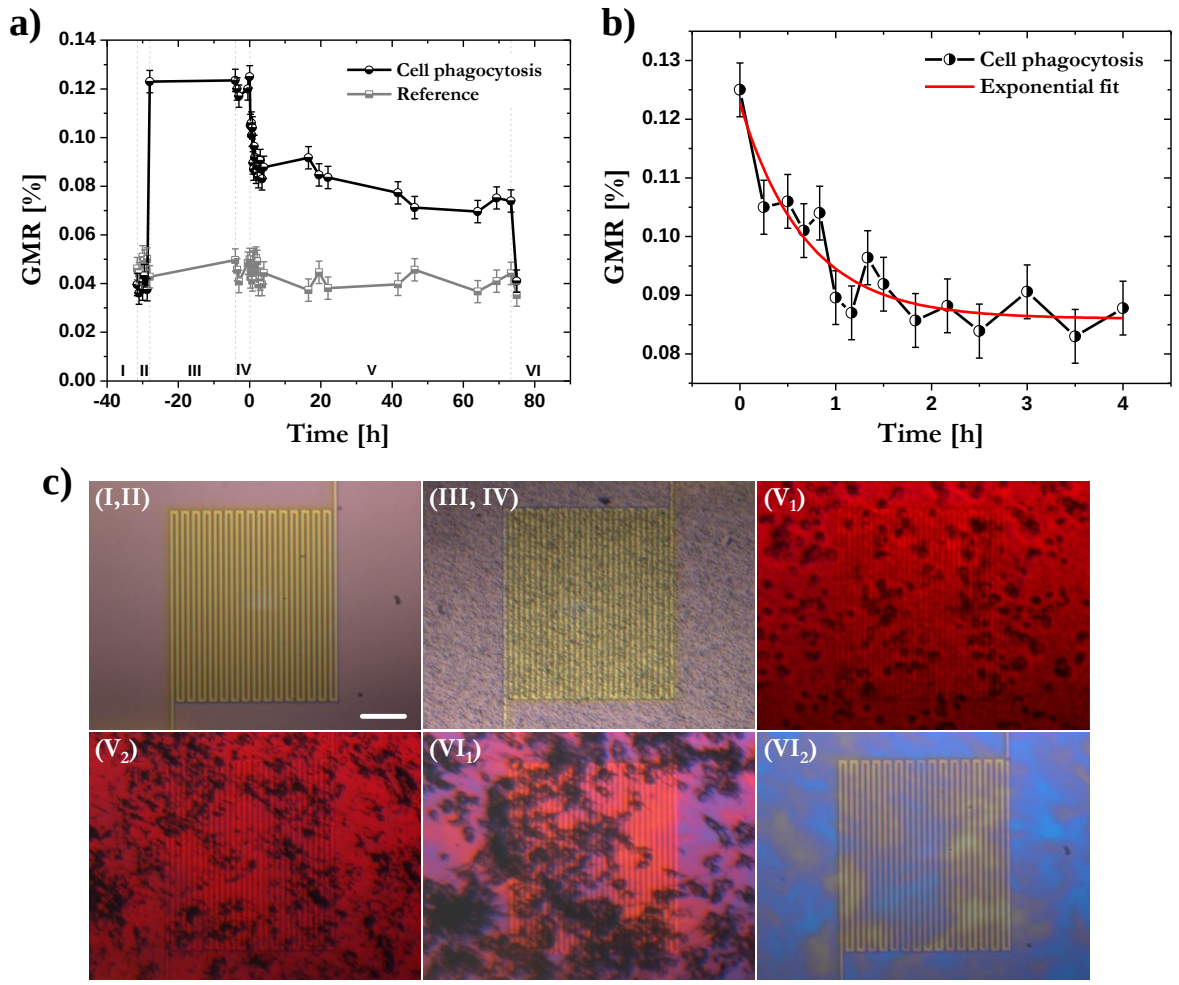

Figure 6.2: a) GMR-signal time evolution of the entire bead phagocytosis experiment during cell spreading and b) zoom-in of the early stage of bead uptake kinetics. c) Time-lapse optical micrographs in air/dH_2O (I/II), after bead immobilization in dH_2O (III) and after adding cell medium into the fluidic (IV), 20 min (V_1) and 1100 min (V_2) following cell incubation, during Trypsin-EDTA detachment (VI_1) and after complete cell replacement by several washing steps (VI_2).

The highest GMR-signal decrease associated to cell-bead interactions was observed within the first four hours after cell incubation. This time period of the signal trace is analyzed by an exponential fit function according to Figure 6.2 b). In Table 6.1 the time required for the fit function to decay to 5 % of its initial value is defined as saturation time during the cell spreading process. This 5 % threshold value corresponds to the average standard deviation of the GMR-amplitude within the monitoring time interval of 2-4 h. In the following, the average values obtained from the GMR-trace analysis of a set of biosensors are presented. The first rapid decrease of the GMR-signal levels off after an average saturation time of 97±32 min. Within this time, the GMR-amplitude drops on average by 39 % relative to the full signal above blank. This signal drop reflects cell spreading and the associated decreased

Table 6.1: Real-time monitoring data analysis of bead phagocytosis during NHDF cell spreading.

Sensor	Cell		GMR drop [%] due to			Saturation time
	Number	Surface cov.	Uptake	Confl. growth	Replacement	[min]
B1	26	14	57	-10	53	55
C1	77	15	23	23	54	81
D1	178	14	21	12	67	70
A3	12	19	52	18	30	115
B3	27	15	37	30	33	135
C3	88	17	45	16	39	125
Average values	-	16±2	39±15	15±13	46±14	97±32

stray field strength of the magnetized beads due to their phagocytosis. Taking into account the standard deviation of 32 min, this saturation time agrees to the optically determined spreading saturation time (Figure 6.1 a)). The total number of phagocytosed beads per cell within the saturation time of 97 min is about 320. This calculation is based on the known initial bead surface coverage of 23 % and the spreading area of about 1600 μm^2 reached after 97 min, which is extracted from the spreading analysis data examined in Chapter 6.1 (Figure 6.1 a)). The uptake rate of each cell within this quasi-linear spreading regime accounts for 3 beads per minute. As will be discussed in the next chapter, this value is about four times higher compared to the uptake rate of already confluently grown cells (top-down approach). For times beyond the average saturation, cell spreading and bead phagocytosis continues until a confluent cell monolayer is reached, leading to another slower average signal drop of about 16 %, denoted as confluent growth drop. This value corresponds to the relative signal change from the level after uptake time given by the fit function curve to the level before removal; the pre-removal signal level is determined by averaging the values of the last three data points prior to cell detachment. Typically, the signal drop reaches a plateau-like level (~45 h) well before the cells are detached by Trypsin-EDTA (~73 h), which is in addition coherent to the average time fibroblasts take to complete their spreading process (Figure 6.1 a)). The observed statistical variations in sensor signal evolution at times beyond formation of a confluent monolayer can be, on the one hand, subject to migration of cells with different bead loadings in and out of the sensor range. On the other hand, also intracellular bead movements might alter the average bead-to-sensor distance.

Besides determining time scales, another unique feature of this magnetic monitoring approach is its ability to estimate the average vertical distance the magnetic beads were lifted from the sensor surface during phagocytosis. To that end, the results obtained from our micromagnetic simulations performed in Chapter 4.4.2 are compared to the experimentally observed signal drops. The simulations have revealed that lifting beads vertically from the sensor surface

results in a respective GMR-signal decrease. During the real-time monitoring experiments (Figure 6.2), we could observe signal drops caused by an increase of the vertical bead-to-sensor surface distance as a result of phagocytosis. In order to directly compare measured (Figure 6.2) and simulated (Figure 4.10) data, both results are normalized to 1, thus eliminating any bead concentration dependent effects. The evaluation of both normalized data leads to the wanted bead-to-sensor distance changes. In a first step, the experimentally obtained relative GMR-signal drops between cell incubation (t=0 h) and just before cell removal (~70 h) are averaged. Taking the difference of their values results in a relative signal level change of 54±14 % from the highest level at t=0 (excluding the blank level). According to the normalized simulated distance-dependence (Figure 4.10), the same relative GMR signal drop can be obtained by lifting the beads vertically from their initial (0 nm) to their final bead-to-sensor surface distance of 120±45 nm. For comparison, the thickness of the plasma membrane surrounding the particles is less than t_p=10 nm. Its thickness, however, can slightly differ from the lipid double layer membrane of other intracellular compartments such as lysosomes or even phagosomes being around 6-7 nm [Tilney2001]. Based on the as-attached cell size of 21 μm and the final spreading projection area on bead-modified surfaces of 3250 μm^2, the calculated average height of a confluent cell body under the assumption of constant cell volume is about t_c=1.5 μm. Here, a simplified view of an uniform average height of a cell is assumed. SEM cross-sectional analysis showed instead highest thickness values around 3 μm directly above the cell nucleus, while outer ranges of the cell body can measure about 0.5 μm [Gimbrone1974]. Considering the average cell height, the approximate range of possible distances of a phagocytosed bead with $d_b = 1.2$ μm diameter to the sensor surface is 20-280 nm, while the lower and upper range values correspond to $2 \times t_p$ and $t_c - d_b - 2 \times t_p$, respectively. The average bead-to-sensor distance results obtained from our real-time monitoring agree well to the average value of this range (150 nm). Moreover, the phagocytic membrane successively engulfing the bead forming a phagosome has a thickness about 200 nm, which lies within the estimated range [Korn1967].

The final step in each experiment is the cell detachment followed by their complete removal. After applying Trypsin-EDTA, the cells detach and their shape changes from a spread state to a rounded state. From the corresponding optical microscope images (Figure 6.2) c) VI_1) it can be seen that no beads remain at the sensor surface, suggesting that all beads are internalized by the cells during the preceding phagocytosis monitoring experiment. This observation is consistent to the previously determined maximum cell uptake capacity of 1270 beads of 1.2 μm in size. Subsequent to cell removal, the GMR-signal drops again to the blank level, which demonstrates the sensors' long-term stability and proves that this method is reproducible and background-free.

Table 6.2: Real-time monitoring data analysis of bead phagocytosis during DU145 cell spreading.

Sensor	Cell		GMR drop [%] due to			Saturation time
	Number	Surface cov.	Uptake	Confl. growth	Replacement	[min]
A2	35	33	62	9	29	282
B2	86	27	69	3	28	339
C2	202	23	46	-1	53	360
D2	636	29	77	2	21	235
A4	33	31	67	5	28	194
B4	79	25	64	12	24	243
A1	31	29	41	23	36	341
B1	82	26	66	18	16	110
Average values	-	28±4	62±12	9±8	29±11	263±85

6.2.2. DU145 cells

Exemplarily, the GMR-signal time evolution of a selected biosensor over the entire monitoring experiment along with its corresponding time-lapse optical micrographs are displayed in Figure 6.3 a) & b) and c), respectively. The gained data from signal trace analysis of a set of biosensors is shown in Table 6.2. We follow the same procedure as previously described in the NHDF cell experiments and all indicated stages from I to VI describe identical operational steps. In the first two stages, the GMR-response of the biosensors remains at the blank level and reaches a certain GMR-signal level after bead immobilization (III). Following cell medium exchange (IV), at time zero in stage V about 21000 cancer cells are added and the counted number of cells sedimented on each biosensor is summarized in Table 6.2. At this early as-attached state, on average about 28 % of the sensor surface is covered by cells. Stage VI corresponds to cell detachment and removal.

The exponential fit function analysis of the first rapid signal drop after cell incubation reveals an average signal decrease above blank of 62±12 % within an average saturation time of 263±85 min (Figure 6.3 b) and Table 6.2). The signal drop mirrors the successive uptake of beads during the cell spreading process. The magnetically and optically determined spreading saturation times of around 263 min and 300 min (Figure 6.1 c)), respectively, agree within the standard deviation of 85 min. At saturation time, the cells projection area is 515 μm^2, and considering the known bead surface coverage of 23 %, the total number of beads covered by each cancer cell is 103. Assuming an instantaneous bead phagocytosis, this results in an uptake rate of 0.4 beads per minute, which is by a factor of eight smaller compared to fibroblasts. Following the saturation time, a further confluent growth drop of 9 % is observed. The experimentally obtained relative GMR-signal drop between cell seeding (t=0 h) and just before cell removal (t $\approx$ 22 h) accounts for 70±12 %. Based on the normalized

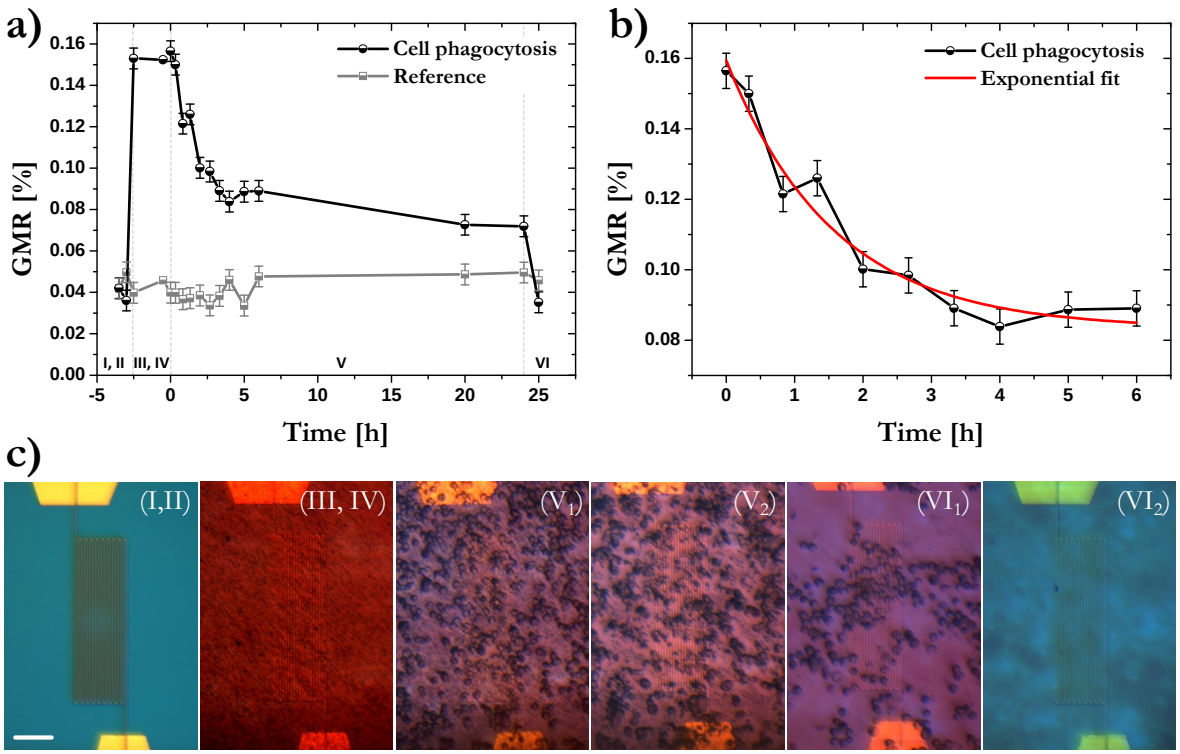

Figure 6.3: a) GMR-signal time-lapse of the entire bead uptake experiment during cell spreading and b) zoom in of the early stage of bead phagocytosis kinetics. c) Time-lapse optical microscope images taken in air/dH_2O (I/II), after bead immobilization in dH_2O (III) and filling the fluidic with cell medium (IV), 30 min (V_1) and 360 min (V_2) after cell incubation, during Trypsin-EDTA detachment (VI_1) and after complete cell removal (VI_2).

simulated distance-dependence of the magnetoresistance, this signal change is equivalent to an average vertical bead lifting of 175±60 nm from to the sensor surface, which is close to the distance value obtained for fibroblasts. The estimated body height of a 16 μm large cancer cell with a final projection area of 790 μm^2 is t_c=2.715 μm. Despite their smaller size, their cell body height is about twice thicker compared to that of a confluently grown fibroblast cell, which demonstrates the pronounced spreading affinity of fibroblasts. As a consequence, the approximate range of possible distances of an internalized 1.2 μm bead to the sensor surface is clearly larger and accounts for 40-1475 nm. Though there is enough space for further intracellular bead transfer in the vertical direction, their average bead-to-sensor surface distance suggests a final bead position close to the ventral plasma membrane, which is common for both cell types. Finally, in stage VI all cells are detached without remaining beads present and the GMR-signal drops back to the blank level after complete cell removal (Figure 6.3).

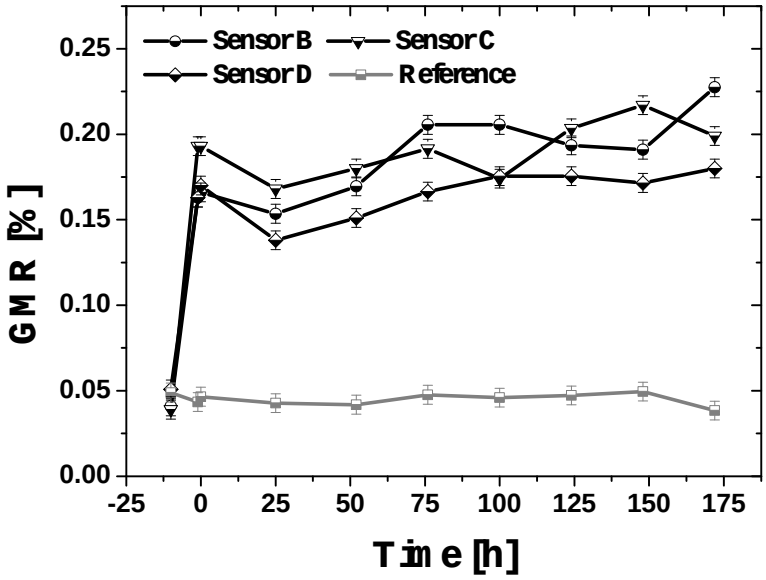

Figure 6.4: Long term monitoring of the sensor signal induced by confluently grown bead-loaded fibroblast cells.

6.2.3. Long-term monitoring of internalized beads

In the previous experiments we have assumed that the bead nature before and after phagocytosis remains the same and that the number of beads internalized remains constant. Beside this, there are two additional scenarios possible following bead phagocytosis, namely degradation and exocytosis. After bead phagocytosis, phagosomes "mature" to phagolysosomes by fusion and fission with lysosomes. They transfer their contents into phagolysosomes providing digestive enzymes and an acidic environment by decreasing the pH (4.6-5.0), with the primary function to digest the internalized particles [Luzio2007]. Exocytosis describes the process by which already internalized particles are released from the cell by fusion of phagosome-membranes with the outer plasma membrane. For instance, fundamental functions such as secretion of neurotransmitters or the expulsion of cellular waste are based on exocytosis [Betz1996].

According to the manufacturer, the employed MagSense particles are stable in a pH range of 2-10. Here, we study their long-term stability in an enzymatic, acidic environment by monitoring the magnetic response of bead-loaded fibroblast cells. In a first step, the cells were incubated with 1.2 μm beads by adding 2 ml of 100 μg/ml bead-DMEM solution. The incubation procedure is similar to the cell uptake capacity experiments described previously (see Chapter 5.2.1). After bead-loading, the cells are transferred to the chip where they are grown confluently to cover the entire sensor area. In general, any bead degradation or exocytosis would lead to changes in the total bead magnetic stray field. In order to detect possible changes, the GMR-signals of cell covered biosensors and uncovered reference sensors are mon-

itored over seven days, a period well beyond the maximum time duration of our phagocytosis experiments. In addition, we exchange the cell medium daily before each magnetoresistive measurement series. At the same time, any exocytosed beads that do not remain attached to the cell monolayer would be removed, too. Figure 6.4 displays the time-course of three selected sensor elements over the entire monitoring experiment. Before cell seeding (t=-12 h), all sensor elements are free of any bead-loaded cells and their GMR-response corresponds to the blank level. Twelve hours after cell seeding and growth (t=0 h), the signal of cell-covered sensors significantly increases, while the signal values of reference sensors remains at blank level. Apart from a slight oscillatory behavior, the signal level of the cell-covered sensors remains constant in the next seven days. In case of successive bead degradation and/or bead exocytosis, we would expect a monotonic signal decrease. According to this result, bead degradation and exocytosis can be excluded for our NHDF cell experiments.

Basically, the period of the observed oscillatory behavior would correspond well to the 72 h cell replication cycle of fibroblasts. However, these oscillations are also observed for confluently grown cells, where no further cell division takes place. More likely are rearrangements of cells over the sensor surface by cell migration. It is known from uptake capacity experiments that the number of beads internalized differs slightly from cell to cell. Therefore, variations in the cell distribution over time could result in slight changes of the magnetoresistive signals. One also cannot rule out the possibility of intra-cellular bead movements in the vertical direction due to digestive path ways, which would lead to ever-changing bead-to-sensor distances and, thus, to persistent signal changes. The mentioned possibilities are speculative. To clarify this behavior in detail, additional investigations are necessary.

6.3. Summary

The phagocytic behavior of human fibroblast and prostate cancer cells during their spreading process on bead-immobilized (sensor-)surfaces has been investigated by means of standard optical microscopy and by monitoring in real-time the magnetoresistive sensor signal evolution. The optical-based reference measurements revealed a general spreading characteristic consisting of an initial lag time of 10 min without significant spreading, a fast quasi-linear spreading phase for early times followed by a slow asymptotic behavior reaching an equilibrium with maximum cell-surface contact area. Cell spreading measurements, particularly those carried out with fibroblasts grown on bead-modified and bead-free APTES surfaces, demonstrated that simultaneous cell spreading and phagocytosis are competing events that rival the surplus plasma membrane area required for both processes. Fibroblasts grown on bead-modified surfaces showed a clear spreading inhibition after 2.2 h and the difference in saturation spreading area agreed well to the total membrane area required to envelop the respective number of internalized beads. The saturation spreading area of fibroblasts

grown on reference (bead-modified) surfaces was by a factor of five (four) higher compared to DU145 cells. Despite their larger size, the calculated cell body height of a confluently grown fibroblast is about twice smaller compared to DU145 cells, demonstrating the pronounced spreading affinity of fibroblasts. The GMR-based real-time magnetoresistive measurements revealed that the bead uptake rate and, thus, cell spreading is not a linear function with time. We could observe a higher rate at early stages which decreased steadily until it reached saturation after an average saturation time of 97±32 min and 263±85 min for fibroblast and cancer cells, respectively. The optically and magnetically determined saturation times agreed within the standard deviation, thus reflecting the cell spreading kinetics. The associated bead uptake rate of fibroblasts accounts for three beads per minute, which is by a factor of eight higher than for DU145 cells. The uptake efficiency is significantly higher compared to the uptake rate of already confluently grown cells (see Chapter 7). In addition to determining time scales, the magnetic monitoring approach also allows to estimate the average vertical distance of phagocytosed beads from the sensor surface, which is around 120±45 nm and 175±60 nm for fibroblast and cancer cells, respectively. Each of the real-time monitoring experiment ended with the complete cell removal, and the GMR-signal dropped back to the blank level, demonstrating that our magnetic approach is reproducible and background-free. Finally, the stability of beads in phagolysosomes has been investigated by long-term monitoring measurements of internalized beads suggesting no noticeable bead degradation and exocytosis in fibroblast cells.

7. GMR-based real-time cell phagocytosis monitoring

In the previous chapter 6 we have discussed the topic concerning contemporaneous membrane competing processes such as cell spreading and phagocytosis. In a living multicellular system such as a human body, adherent cells are usually found in a complete spread and confluently grown state anchored at the extracellular matrix (ECM). Therefore, the aim of this chapter is to investigate the phagocytic kinetics of cells under conditions as close as possible to their natural in vivo state. In a confluent state, the phagocytosis is accomplished by the cell's dorsal plasma membrane and the cell spreading process is excluded from the measurements (top-down approach). Of particular interest is also the cells phagocytic property under different physiological conditions, which might promote or inhibit bead uptake. By regulating the particle entry into the cell, we can mimic disease related phagocytosis inhibition/promotion. After introducing the concept underlying the cell phagocytosis monitoring of the top-down approach, we present the sample preparation procedure, a bead sedimentation analysis, and a comprehensive analysis of the results obtained for both cell types involved.

7.1. Concept of GMR-based real-time cell phagocytosis monitoring

The principle of this approach is basically similar to the previously introduced bottom-up approach and relies on the monitoring of the GMR-signal induced by beads in embedded sensors, which changes during the phagocytosis process. The basic idea is illustrated in Figure 7.1. First of all, the cells are seeded on top of the sensor surface, where they start spreading

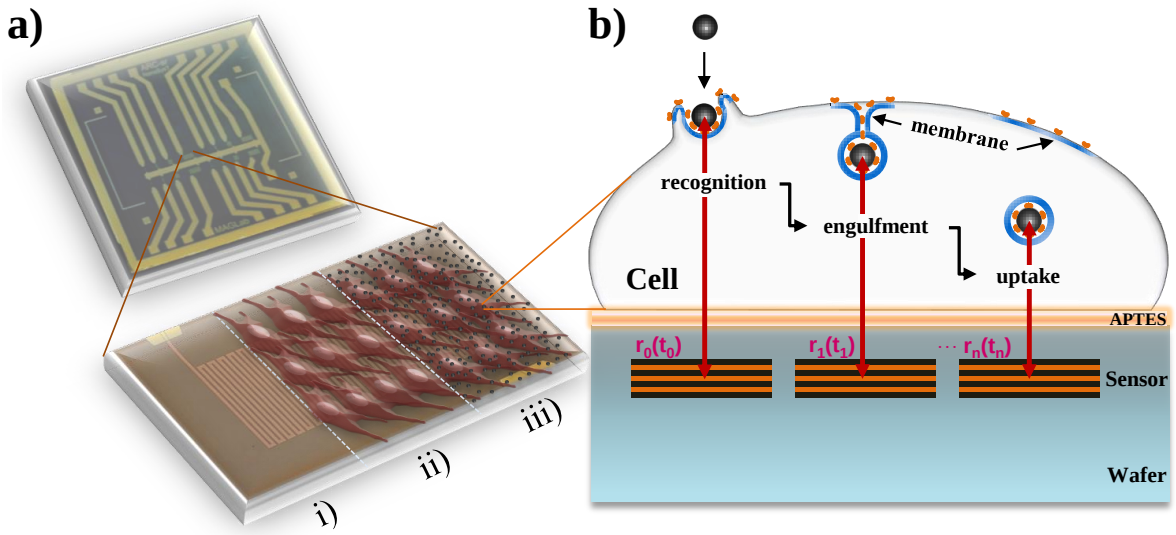

Figure 7.1: a) Sketch of the magnetic phagocytosis monitoring methodology: i) plain sensor surface, ii) confluent cell monolayer, iii) bead incubation. b) Cross-sectional sketch of different stages during phagocytosis. Following bead recognition, the cells envelop and internalize the particles in phagosomes, resulting in steady decrease of the bead-to-sensor surface distance.

and growing until a confluent monolayer is formed. Thereafter, the beads are added into the fluidic chamber, and they reach the cell monolayer passively due to gravity. The signal that the sedimented beads produce in the underlying sensor depends on their overall density (bead surface coverage) and the average vertical distance from the sensor surface. The stray field strength of the beads within the sensor region increases with decreasing vertical distance, while all other parameters are fixed. Thus, immediately after bead recognition, the sensor output increases proportionally to the progress of phagocytosis, which allows real-time monitoring.

7.2. Real-time cell phagocytosis monitoring

The sample preparation procedure introduced in the following is identical for all experiments. Prior to the real-time monitoring experiments, the time required for bead sedimentation is analyzed both optically and magnetically. Concerning the real-time monitoring experiments, we first commence NHDF cell standard uptake experiments at physiological conditions (37 °C) and then turn our focus to the metabolically inhibited uptake carried out at 4 °C. Finally, the cancer cell monitoring experiments carried out at 37 °C are presented.

7.2.1. Sample preparation and bead sedimentation

Following APTES functionalization and PDMS fluidic mounting, each experiment starts with the incubation of approximately 6000 NHDF and 22000 cancer cells, which are grown to a confluent monolayer covering the entire biosensor area defined by the fluidic dimensions. Non-specifically adsorbed cells on peripheral PDMS surfaces around the biosensors show no adhesion or spreading and are usually removed by the next cell medium exchange. On top of the cell monolayer, about 400-450 μl of MagSense 1.2 μm beads dissolved in cell-medium (65 μg/ml) are added. The amount of beads added results in a surface coverage of about 60 %, which is slightly higher compared to the upper uptake limit of fibroblast cells (Chapter 5.2.1). Though the maximum uptake limit of cancer cells is significantly lower, the same amount of beads is used in order to allow a direct comparison of experiments carried out with both cell types. The beads suspended in cell medium start to settle down immediately after incubation and homogeneously cover the cell monolayer grown on top of the chip surface. The time required for all beads in solution to sediment at the chip surface is analyzed both by optical microscopy and GMR-sensor signal readout. To that end, we use an APTES functionalized sensor chip mounted with a PDMS-fluidic and apply the same amount and concentration of beads in DMEM cell medium to the fluidic chamber. During bead sedimentation, the GMR-response and optical images are recorded in appropriate time intervals. The bead-surface coverage degree of the sensor is determined by a homemade image analysis program (Appendix A.1.7). The obtained results from both approaches are normalized to 1 and are featured in Figure 7.2. As expected from the largely linear dependence of the sensor signal on bead coverage (Figure 4.8), the two curves agree well and reveal a sedimentation time of

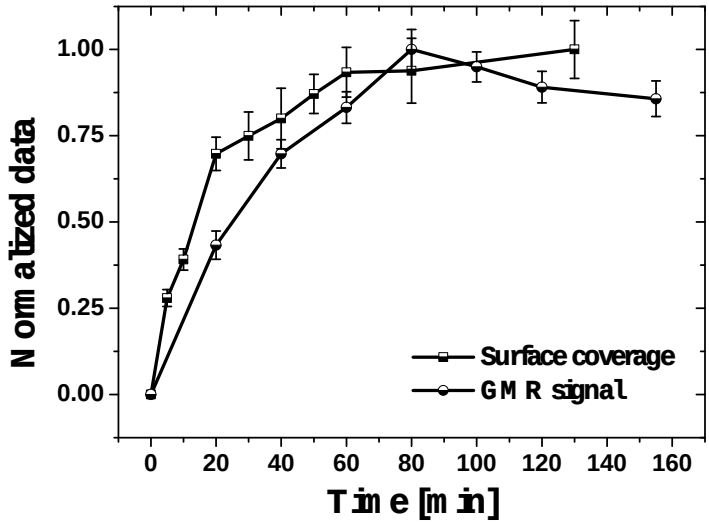

Figure 7.2: Bead sedimentation profiles obtained by GMR-sensor signal and optical bead surface coverage measurements.

about 80 min (average time required to rise to about 95 % of the full signal amplitude, while the 5 % threshold value corresponds to the mean standard deviation of the last three data points of each curve).

7.2.2. NHDF cells

During the top-down experiment, both the magnetoresistive response of the biosensors/ref-sensors as well as accompanying optical microscopy images are recorded. Exemplary, the time-dependent GMR-signal and a micrograph sequence of a single sensor comprising the entire top-down phagocytosis experiment are depicted in Figure 7.3 a) and c), respectively. In total, a set of ten sensors from two separate experiments are considered for data analysis. Since for times t $<$ 0 h all biosensors are situated either in air, cell medium or covered by a confluent cell monolayer, their GMR-response corresponds to the blank level. Immediately after bead incubation at t=0 h, we observe a steady increase of the GMR-response leveling off at a certain value. Following signal saturation, an oscillatory signal behavior similar to the long-term monitoring experiments discussed in Chapter 6.2.3 is measured. In the early uptake phase up to 2.4±0.8 h, a first rapid signal increase followed by a kink in the phagocytosis monitoring curve is observed, which is common for all measurements (Figure 7.3 b)). For times beyond the kink, the GMR-signal increases gradually but in a much slower fashion. The initial slope of the first rapid signal increase is about 8.5±3.9 times larger than the later increase. A direct comparison of the early stage increase to the bead sedimentation characteristic (Figure 7.2) shows that there is a good conformity in their time dependence. Hence, we conclude that the main contribution to the initial signal increase is due to bead sedimentation on top of the cell monolayer, with phagocytosis playing a subordinate role. The further sensor signal

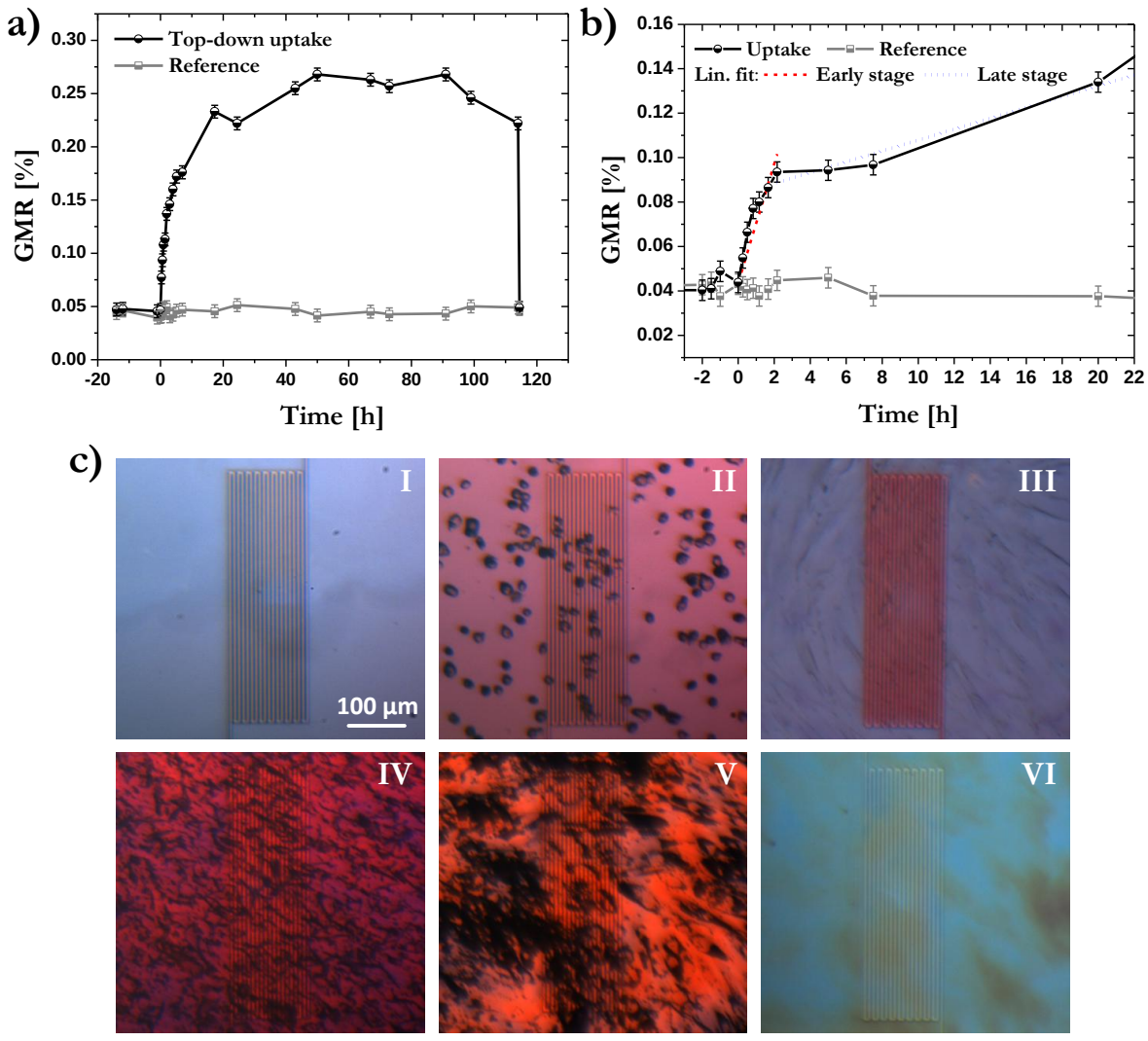

Figure 7.3: a) Time evolution of the GMR-signal throughout the entire phagocytosis experiment at 37 °C. b) Another measurement showing the analysis of the early stage signal behavior. c) Optical microscopy images of the sensor shown in a) taken at different stages: (I) plain sensor, (II) cells as-seeded and (III) confluently grown, (IV) 1 h and (V) 50 h after bead incubation, (VI) after cell removal.

increase beyond the early stage is attributed to bead phagocytosis, which leads to a decrease of the average bead-to-sensor distance. At the end of the experiment, the cells are completely removed by Trypsin-EDTA and several washing steps (replacement). Consequently, the GMR signal drops back to blank level indicated by the last data point of each GMR-trace.

The data of each GMR-trace from t=0 h, excluding the replacement value, is analyzed by an exponential fit function. The fit value reached for $t \to \infty$ denominates the saturation level accounting for 0.229±0.032 %, while the time required to reach 95 % of this level denotes the saturation time of 27.7±14.5 h. The 5 % difference from 100 % signal level corresponds

to the average standard deviation of the GMR values within the time interval of about 20 h to 100 h. The saturation time determines the end of the phagocytosis process. Considering the maximum uptake capacity of 1270 beads per cell (Chapter 5.2.1), the calculated upper limit of the phagocytic uptake rate per cell is about 45 beads per hour, which is by a factor of four smaller compared to phagocyotosis during spreading (Chapter 6.2). The determined average saturation level corresponds to about 87 % of the expected signal level for beads immobilized directly to the sensor surface at 60 % coverage (Figure 4.8). According to the simulated dependence of the GMR-signal on the bead-to-sensor distance (Figure 4.10), an equivalent relative signal drop is obtained when lifting the beads by ~20 nm. This implies a mean vertical intracellular bead position at the lowest possible limit of twice the cells' plasma membrane thickness [Tilney2001].

So far, all experiments have been carried out at physiological conditions (37 °C). In order to better distinguish bead sedimentation and phagocytosis, these experiments are supplemented by studies at 4 °C, where the cells uptake behavior is inhibited. Low temperatures result in a decrease in the metabolism of the cell and the membrane components loose their fluidity [Pratten1979]. Besides other methods such as applying cytoskeletal inhibitors, this is indeed an easy and effective way to actively impair the cell's phagocytic behavior [Berry2004, Olivier2004]. As demonstrated by Pratten and Lloyd, combinations of different inhibitors can completely abolish endocytosis [Pratten1986]. In this study, two complementing types of investigations are carried out. The temperature in the first experiment remains at 4 °C throughout the entire analysis time. In the second experiment, following the uptake monitoring time of 22 h at 4 °C, we again increase the temperature to 37 °C and continue to monitor phagocytosis for another 22 h at physiological conditions. Except of the temperature variations, the sample preparation procedure of both experiment types is identical to the specifications described above. To ensure an appropriate cell growth, the temperature is kept at 37 °C from initial cell seeding until cell confluency is reached. Afterwards, a smooth temperature transition from 37 °C to 4 °C with a constant cooling rate of 0.33 °C/min is applied. As soon as the desired temperature of 4 °C is reached, we keep the cells at 4 °C for another 60 min before incubating the beads (400-450 ml at 65 μg/ml), thus enabling comparability between all types of experiments.

In Figure 7.4 a) and b) the respective GMR-traces of both experiment types are displayed, and looking at their GMR-response within the early stage of up to ~2 h, we again observe a first rapid signal increase due to bead sedimentation. In the subsequent monitoring time period between 2 h and 23 h, the GMR-signal levels off without any further noticeable signal increase or decrease for both experiment types. The reached saturation level of 0.071±0.01 % is clearly lower than the value determined at 37°C (Figure 7.3 a)), which provides evidence of profoundly

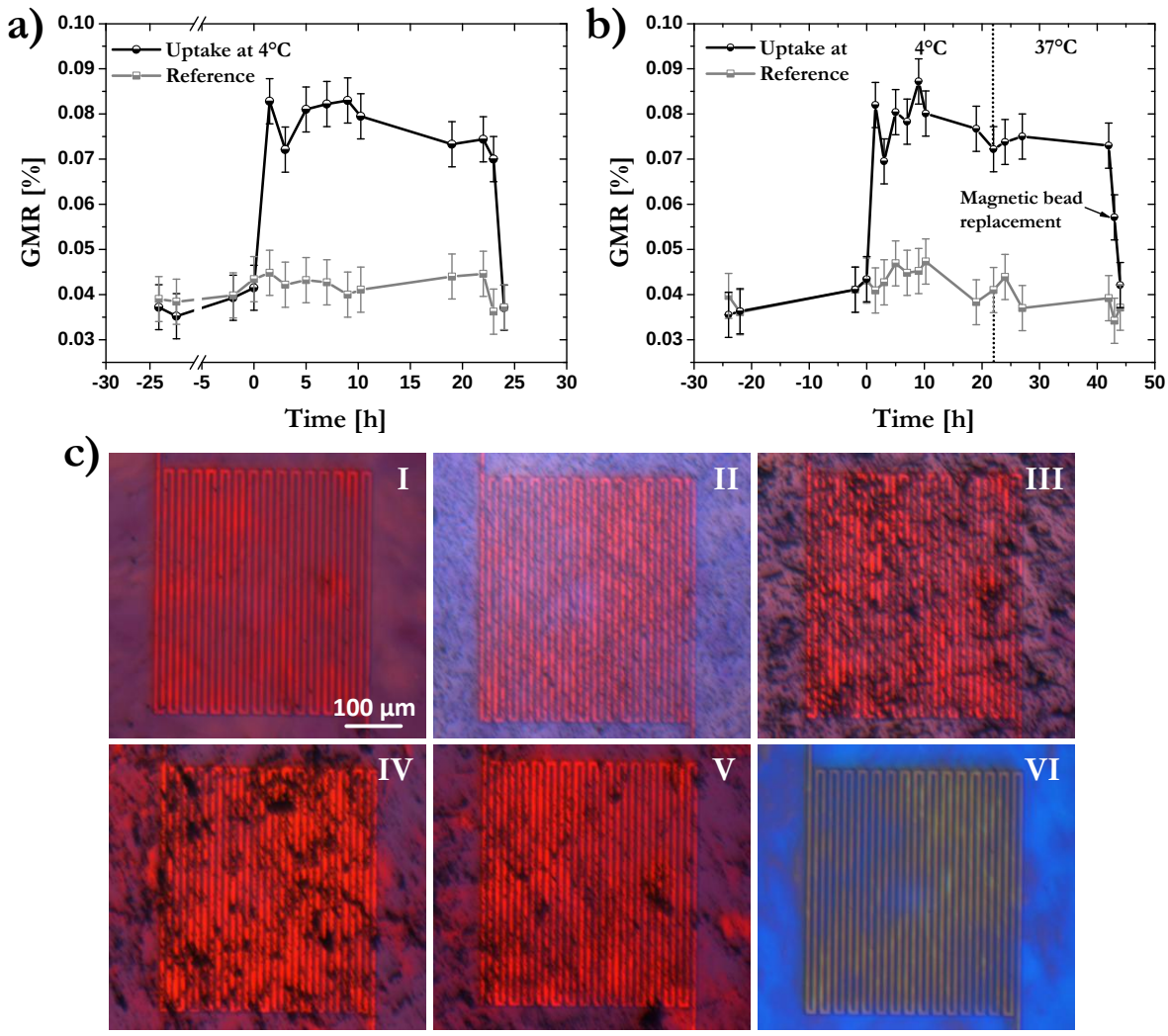

Figure 7.4: a) and b) show the GMR-signal traces for metabolically inhibited phagocytosis experiments. The dashed line in b) indicates the moment of temperature increase to 37 °C. c) Sequence of micrographs showing the sensor measured in b) at different stages: (I) cell confluently, 1 h (II) and 8 h (V) following bead incubation, (IV) 20 h after temperature increase, i.e. taken at t=40 h, (V) after applying the magnet and replacing unbound beads, (VI) cell removal. The stages I-III are similar for both experiment types displayed in a) and b).

inhibited phagocytosis at 4 °C. The mean signal level reached within the early stage of 2.5 h for experiments at 37 °C (0.105±0.014 %) exceeds the level obtained at 4 °C (0.071±0.01 %), supporting our previous assumption that bead phagocytosis and sedimentation take place in parallel at physiological temperatures. The average saturation level for metabolically inhibited experiments corresponds to about 10 % of the measured signal above blank level for beads immobilized directly onto the sensor surface at 60 % coverage (Figure 4.8). Compared to the micromagnetic simulations of the distance dependence (Figure 4.10), this signal drop translates into a mean vertical bead distance to the sensor surface of about 400 nm. TEM

and SEM cross-sectional studies of endothelial and fibroblast cell monolayers revealed the smallest cell thickness of about ~500 nm at the cell-cell connections, which agrees well to the distance derived by our sensor signal analysis [Gimbrone1974, Todaro1964, Schakenraad1989]. Moreover, gaps between the cells due to imperfect or incomplete cell confluency might also contribute to the early stage signal increase by allowing a direct bead sedimentation on top of the sensor surface passing the cell barrier.

Following the temperature increase from 4 °C to 37 °C with a heat-up rate of 5.5 °C/min for the second experiment type (starting point is indicated by the dashed line in Figure 7.4 b)), the GMR signal remains at a constant level for another 22 h. This indicates that the cells do not recover their ability for phagocytosis during this time period. In order to distinguish beads that are partly internalized, superficially bound or simply lying on top of the cell surface monolayer, a cylindrically shaped NbFeB permanent magnet (diameter 3 mm, length 15 mm) is drawn through the DMEM solution at close vicinity to the cell monolayer (~2 mm vertical separation distance). Reference experiments following the same procedure demonstrated the successful removal of unbound beads sedimented on top of an un-functionalized silicon nitride sensor surface (see Chapter 5.2.1, Figure 5.4 d)). In the second type cell experiment, the respective sensor signal drops to 0.060±0.007 % (data point denoted by "magnetic bead replacement"). From this result we conclude that about one half of the beads situated on top of the cell monolayer were weakly bound or even unbound, which further proves that bead phagocytosis of the cells is inhibited under these conditions. The final step in the experiment pertains the complete removal of cells. Consequently, the GMR-signal drops down to the blank level.

As a concluding remark, we compare the uptake rate of NHDF cells at physiological conditions with other cell types. Though drawing a comparison between cell types of widely differing nature interacting with beads of different properties and probably under different conditions has to be treated with caution, they still give an idea on how to bring the uptake behavior observed in our experiments in line with results from the literature. In general, Acanthamoeba or professional phagocytic cells such as macrophages and neutrophils feature a much higher uptake rate than fibroblast cells. For instance, a single amoeba is able to uptake about eight polystyrene latex beads of 1.3 μm [Weisman1967] and up to ten beads of 1.1 μm [Wetzel1969] in diameter per minute, which corresponds to 10-13 fold higher phagocytosis rate. Experiments carried out with murine thio-macrophages have demonstrated their great phagocytic ability of ingesting the equivalent of 48-145 % of their macroscopic plasma surface area (1367 μm^2) within a short time of 30 min [Cox2000]. This membrane area equals the surface area of 145-438 MagSense beads of 1.2 μm in size. In turn, this corresponds to an uptake rate of 4.8-14.6 beads per minute, which is by a factor of 6-19 higher compared

to human fibroblasts. Comparable results have been obtained from micropipette aspiration experiments, where individual neutrophils were incubated with single opsonized polysterene beads in the range of 2-10 μm in diameter [Herant2005, Herant2006]. However, the relatively slow rate of bead internalization observed in our studies compared to professional phagocytes is consistent with literature results obtained in collagen phagocytosis experiments with human fibroblasts [McCulloch1993, Segal2001].

7.2.3. DU145 cells

Figure 7.5 a) and b) display the GMR-signal traces of few selected sensors from two different sets of top-down experiments carried out at 37 °C, while Figure 7.5 c) features a series of optical microscopy images taken at different stages during phagocytosis. The presented results are gained from the exponential fit function trace analysis of 17 sensors from three separate experiments. Following bead incubation at t=0 h, the GMR-signal increases steadily reaching an average saturation level of 0.090±0.023 % after a mean saturation time of 8.94±3.90 h. The saturation time denotes the time required to reach 73 % of the saturation level, while the 27 % threshold value corresponds to the mean standard deviation of the GMR-values within the time interval of 11 h to 50 h (Figure 7.5 a)) and 8 h to 25 h (Figure 7.5 b)). The saturation values are by a factor of 2.5 and 3.1 lower than measured for fibroblasts, respectively. The previously observed kink in the early uptake phase caused by bead sedimentation appeared in only 2 of 17 GMR-traces, thus suggesting a greater DU145 cell-monolayer thickness compared to fibroblasts. The implemented removal of cells including the incorporated beads from the sensor surface terminates each experiment, and as a result, the signal drops down to the blank level.

The GMR-traces shown in Figure 7.5 a) and b) correspond to two different sets of experiments performed under similar conditions. The latter experiment comprises much shorter measuring intervals and focuses on the phagocytic behavior in the first 30 h following bead incubation, a time period well beyond the measured saturation time of about 9 h. Although the optical images taken 30 min after bead incubation proved an homogeneous bead distribution over the whole sensing area, the saturation level reached for individual sensors of the same (Figure 7.5 b)) as well as different chips (Figure 7.5 a)) shows a two-fold higher variation compared to fibroblast experiments, which explains the standard error of 27 %.

As discussed in chapter 5.2.1, phase-contrast optical microscopy imaging revealed an inhibited phagocytosis of DU145 cells for the top-down approach. Beside of some exceptions, the majority of cells was free of any internalized beads. With regard to the sensor calibration (Figure 4.8), a bead-surface coverage of about 60 % with beads directly immobilized onto the sensor surface leads to GMR-signal amplitude of about 0.26 %. As determined in the previous

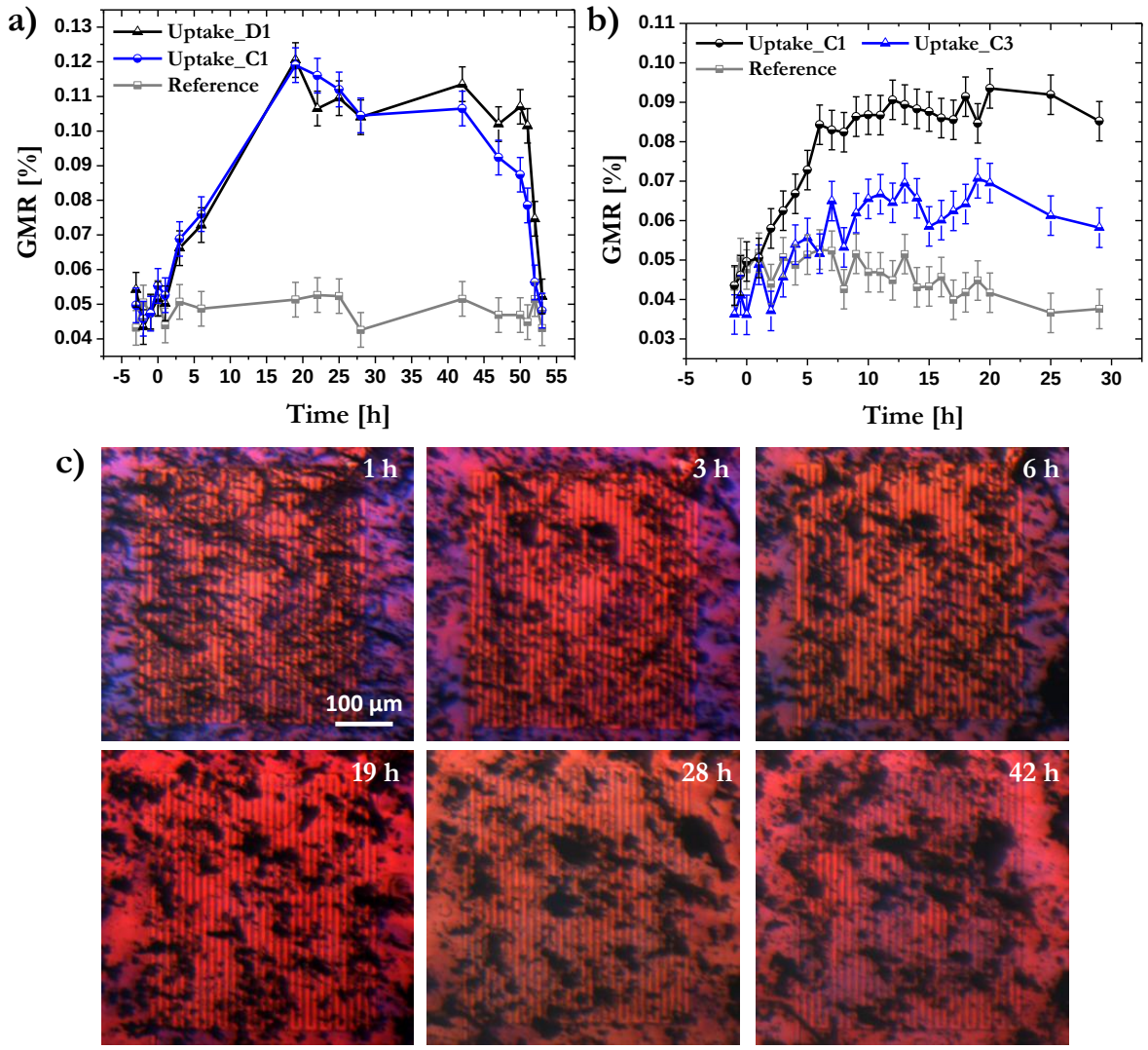

Figure 7.5: a) and b) represent selected GMR-signal traces from two distinct phagocytosis experiments carried out under similar conditions. c) Optical microscopy images taken at different stages during the uptake experiment illustrating the formation of bead-accumulations with elapsing time.

bottom-up approach (Chapter 6), the average bead-to-sensor surface distance of internalized beads is about 46 % larger in cancer cells compared to fibroblasts, i.e. 175 nm and 120 nm, respectively. In the top-down approach, the bead-to-sensor distance for fibroblasts was about 20 nm and, thus, assuming for cancer cells a 46 % higher average bead-to-sensor distance corresponds to 29 nm. Concerning the OOMMF simulation of the top-down approach, lifting beads from their initial position (0 nm) by 29 nm leads to a respective GMR-signal drop of 15 % with respect to the maximum. Accordingly, the initial GMR-amplitude of 0.26 % is expected to decrease to 0.221 %, which is far from the measured mean saturation level of 0.09 %. This leads to the conclusion that only a low amount of incubated beads are phagocy-

tosed, which is in aggreement to the observations made by optical microscopy. On the other hand, a GMR-signal of 0.09 %, by assuming a mean bead-to-sensor distance of 29 nm, corresponds to a sensor surface bead coverage of about 12 %. Considering the maximum spreading area of 790 μm^2, each cancer cell should contain about 80 internalized beads. Since the majority of cells examined by phase-contrast microscopy was free of any beads, this estimated amount of phagocytosed beads is slightly too high. Thus, we assume that the signal increase observed here must have another origin in addition to phagocytosis. One possible source could be the observed island-formation with elapsing time (Figure 7.5 c)). Island formations have been observed in the presence and absence of external magnetic fields. The applied homogeneous magnetic field required to read-out the sensors might additionally amplify the island-formation by temporarily magnetizing the beads. Conglomerations in terms of long bead chains are characteristic only in the early phase of the phagocytosis experiments, where all of the beads are either still suspended in the cell medium solution or sedimented on top of the cell-monolayer. Attached or internalized beads do not follow or orientate themselves along the applied external field. Bead agglomerations on top of the cell monolayer can be considered as one big particle. In order to assess the range of influence of their magnetic dipole field, we calculated the total magnetic field of six particles that are arranged either at the corners of a hexagon (homogeneously distribution) or formed to a bead-island (data not shown). This simple example demonstrated that for certain vertical separation distances the strength of the total magnetic field within the GMR sense layers for agglomerated beads exceeds that of homogeneously distributed ones. It is obvious from the micrographs that with elapsing time, more and more beads agglomerate to bigger islands and as a consequence, the effective magnetic field affecting the sensor becomes larger, thus causing an additional GMR-signal increase without decreasing the bead-to-sensor surface distance. The determined saturation time of about 9 h agrees well with the time required to form the bead islands (Figure 7.5 c)). In addition, fluctuations in the signal after reaching the saturation level with a to standard error of 27 % possibly reflect reconfiguration of particle islands. In conclusion, the GMR-signal increase measured in Figure 7.5 might be attributed to both bead phagocytosis and island-formation.

Another aspect neglected so far concerning bead phagocytosis is the polarity of cells (Chapter 4.1). Cancer cells utilized in this study possess two different surfaces, denoted as apical and basal side. Experiments reported by Gottlieb at al. demonstrated actin-dependent endocytosis for only the apical side [Gottlieb1993]. Actin-filaments along with integrins play an important role in binding and phagocytosis of particles [Segal2001]. Cancer cells grown on a two-dimensional surface form oriented colonies, and due to their non-uniformity in the uptake, only beads presented to the apical surface might attach to the cell surface. With time, this probably manifests in bead-island formations at the apical side as observed in our

experiments. Similar bead accumulations at the cell's outer plasma surface prior to their uptake have been reported with amoeba cells [Korn1967]. The accumulated beads seemed to be covered by an amorphous material and the authors assumed that the amoeba might secrete a substance that serves to bind the particles. The bead concentration was several hundred fold higher compared to their initial concentration in medium solution. However, to gain a detailed insight into this agglomeration phenomenon observed for cancer cells, a method that clearly can distinguish the apical from the basal surface, for instance by staining both sides with different dyes, would be helpful.

7.3. Summary

In vitro phagocytosis of magnetic particles by human fibroblast and cancer DU145 cells has been monitored in real-time by recording the time evolution of the magnetoresistive sensor response throughout the entire experiment. The introduced concept of the top-down approach resembles that of the previously presented bottom-up approach and relies on monitoring the bead-to-sensor surface distance, which changes during the phagocytosis process. In living systems, adherent cells are completely spread within the extracellular matrix and, thus, in the top-down approach the cells were first grown confluently followed by bead incubation. The time required for all beads to sediment is about 80 min. Following bead sedimentation, the phagocytosis of particles was accomplished by the dorsal plasma membrane, excluding the cell spreading process.

Regarding fibroblast cells, the uptake rate is not a linear function with time. During the early uptake phase (up to 2.4 h), a first rapid signal increase is observed, which was attributed to both bead sedimentation and phagocytosis. In the late uptake phase beyond 2.4 h, we measured a 8.5 times slower signal increase due to progressive phagocytosis. The fit function analysis revealed a mean signal saturation level of 0.229 % that was reached after a mean saturation time of 27.7 h. The saturation time determines the end of the phagocytosis process, and the overall uptake rate per cell accounts for 45 beads of 1.2 μm in diameter per hour, which is four times smaller compared to phagocyotosis during spreading (Chapter 6). Compared to professional phagocytes such as macrophages or neutrophils, the uptake rate of fibroblasts is approximately 6-19 times slower. Supplementary investigations carried out at 4 °C clearly demonstrated metabolically inhibited phagocytosis, and we were able to distinguish between cell membrane adherent and internalized beads. Monitoring the regulated entry into the cells demonstrates that our magnetic approach is well suited to detect possible disease-related or environmental impacts leading to a profound inhibition or malfunction in phagocytosis. As an example from the biomedical point of view, by employing collagen-coated beads one could simulate the receptor-mediated phagocytosis processes during collagen degradation, which is an important mechanism for tissue maintenance and homeostasis.

Experiments carried out with cancer cells at physiological conditions revealed that phagocy-

tosis is terminated after a saturation time of about 9 h. Up to the mean saturation level of 0.09 %, the uptake rate is a linear function with time. Compared to fibroblast experiments at 37 °C, cancer cells completed the phagocytosis process three times faster, while the measured saturation level is by a factor of 2.5 lower, corresponding to an about five times lower uptake capacity. Taking into account the observations made by optical (phase-contrast) microscopy, we concluded that the attained GMR-signal increase was due to both bead phagocytosis and agglomerations that lead to island-formations. The saturation time and the time required to successively form bead-islands was comparable. The origin or the driving force of bead-agglomerations is unknown. One possible reason could be the polarity of a cancer cell and the non-uniformity in the uptake between the apical and basal surface. As long as beads are not attached or internalized, island-formations might additionally be amplified by the presence of external magnetic fields required for the sensor read-out.

8. On-chip real-time monitoring of cell migration and detachment

Besides the demonstrated real-time monitoring of dynamic interaction mechanisms such as cell spreading and phagocytosis, we present two more examples of nano-biointerface studies that can be realized by our magnetic lab-on-a-chip. Focus of these investigations are time-dependent processes including cell migration and detachment. Both studies are carried out with fibroblast cells that are labeled with magnetic beads by means of phagocytosis. In case of cell migration, the cell's micro-environment is suddenly enlarged, giving rise to cell movements successively occupying the free space. In the second part, we directly detect cell morphology changes caused by external influences such as enzyme treatments leading to rapid cell detachment.

The detection principle is basically similar to the previously introduced bottom-up and top-down approaches. Apart from schematic illustrations of the underlying detection idea, we give a brief thematic introduction elucidating their biological or biomedical background. Afterwards the sample preparation procedure and the attained results are presented for each topic, starting with the cell migration assay first.

8.1. Chip-based cell migration assay

Since the body of human beings is almost completely covered by the skin, most of the injuries are associated with the disruption of the skin integrity, leading to the so-called cutaneous wounds. Wound healing is a well-regulated process that is basically divided in three intertwined phases, namely inflammation, proliferation and tissue remodeling. In the initial phase, inflammatory reactions are activated that recruit different cell types to the wound side and initiate their migration, proliferation and differentiation. The proliferative phase comprises besides neoangiogenesis and re-epithelialization also the stimulation of fibroblast proliferation and collagen production, resulting in the formation of granulation tissue and extracellular matrix. In the final tissue remodeling phase, a variety of proteinases contribute in the degradation of provisional wound tissue [Schreml2010].

In such organized wound repair mechanisms, abnormal healing processes can lead to chronic wounds, where the anatomic and functional integrity is not restored within a reasonable period of time. A delayed wound healing reflects a less coordinated physiological wound repair, where the healing process is trapped in a self-sustaining inflammation phase. In order to better understand the origin and to improve the therapeutic treatment of such inadequate healing processes, a clear understanding of the individual repair phases is required. Of particular interest is the regulation of the activity of cells involved in the cutaneous wound healing mechanism [Schreml2010].

Another promising strategy, which is not only restricted to cutaneous wound treatment, is tissue engineering. Tissue engineered constructs are implanted either to repair damaged or substitute lost skin tissue. The challenge of developing such artificial constructs is to reach the required biological functionality, and in order to achieve the desired properties, an active control or directed development of the construct is needed. Besides parameters such as the choice of cell source, scaffold design or cell cultivation conditions, the in vitro homogeneous spatial distribution by cell migration plays a key role in the tissue engineering process. One possible reason of non-uniform cell distribution can be transport restrictions due to inhomogeneous cell migration, which influences the overall functionality of the scaffold [Sengers2007].

Several optical- and chip-based techniques have been developed for cell migration monitoring [Sengers2007, Wang2008]. The most prominent and simplest two-dimensional wound healing assay is the so-called in vitro scratch-assay. Here, a section of cells from a confluent monolayer is removed by scraping, thus producing a wound. Then, the migration of cells into the free space reoccupying the area is examined by optical microscopy. Besides monitoring the two cell fronts subsequently closing the wound, commonly also single cells are tracked for several hours and the measured trajectories of a number of cells with initial position close to the cell-front illustrate their migration traces. At the end of the experiment, the time-lapse images taken at different stages of the experiment are compared in order to determine the migration rate. However, the idea behind each cell migration assay remains the same and concerns the monitoring of the migration rate of a cell-front or leading-edge while occupying a free area. Cell population migration is regulated by two parameters, the rate of locomotion that is denoted as migration speed, and the directional persistence that describes the time period over which the leading-edge progressively migrates in about the same direction [Ware1998]. Determining the migration velocity of the cell-front can be interpreted as a combination of these two intertwining processes.

In our magnetic approach, we first grow fibroblast cells to a confluent monolayer in microwells and then feed them - according to the procedure described in Chapter 5.2.1 - with 1.2 μm MagSense beads by adding 2 ml of either 20 or 40 μg/ml bead-DMEM solution. After an over night incubation, all beads are internalized and the magnetically labeled cells are transfered following trysinization to the chip that is mounted with the MagLab-fluidic fixture. The connecting channel is situated directly above the biosensor row and parts of it are protected by an additional PDMS barrier (Figure 8.1 a)). Following cell seeding, only the unprotected biosensor area within the channel is occupied by cells forming a confluent monolayer. The required cell-front is established at direct vicinity to the PDMS barrier, representing the wound edge. After 9 h of confluent cell growth, the PDMS barrier is removed and the migration process of the leading-edge over the free biosensor area is initiated, thus mimicking the wound

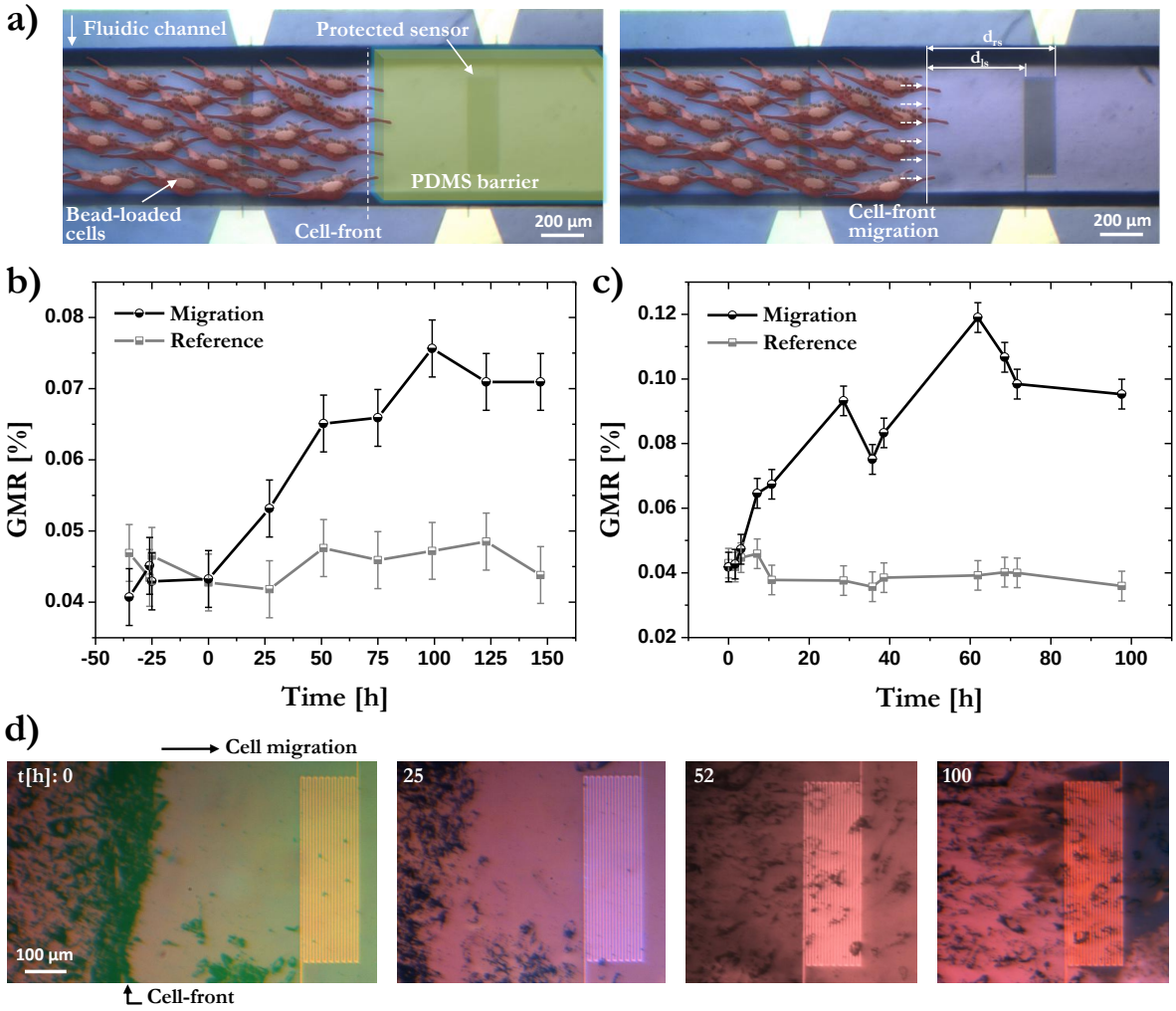

Figure 8.1: a) Concept of the chip-based cell migration assay (true to scale, except of the cell size). Following PDMS barrier removal, the cell-front migrates above the embedded sensor which detects the magnetic stray field of internalized beads. b) and c) display the GMR-traces of two B-type sensors of two distinct migration experiments, while in the latter one a higher bead-loading of cells is chosen. d) Time-lapse images taken during the experiment shown in b) illustration the migration progress.

healing process.

Figure 8.1 b) and c) display the GMR-traces of two different experiments carried out under similar conditions, reflecting the time-dependent signal change during cell migration. For the first (second) experiment shown in Figure 8.1 b) (Figure 8.1 c)), cells incubated with 20 (40) μg/ml bead-solution are used. The time-lapse optical microscopy images taken at the indicated times after PDMS barrier removal correspond to the measurements shown in Figure 8.1 b). In the following, the data of three GMR-traces from two sets of experiments are presented. The time required for the migrating cell-front to reach the left side of the

sensor (t_{ls}) is different, since the distance d_{ls} can vary from experiment to experiment (Figure 8.1 a)). To better visualize the cell migration process and for comparison reasons, the time scale of the GMR-traces is always shifted by the time t_{ls} in a way that the data point at t=0 h indicates the arrival of the cell-front at the left sensor side. Following t=0 h, the sensing area is more and more occupied by migrating cells and, consequently, a steady GMR-signal increase is observed. Once the sensor area is confluently grown by cells, no further significant changes are observed and a certain saturation level is reached.
Each GMR-trace from t=0 h is analyzed by an exponential fit function. The saturation level given by the fit value reached for $t \rightarrow \infty$ accounts for 0.075 % (Figure 8.1 b)) and 0.105 % (Figure 8.1 c)), reflecting the two different bead-labeling densities of cells. The saturation time, which is the time required to reach 94 % of the saturation level, is 59±27 h. The saturation time reflects the time the wound-edge needs to migrate over the sensor area of 142 μm distance, leading to an average migration velocity of 40±23 nm/min.
In the first experiment (Figure 8.1 b)), the distance d_{ls} and the time required for the initial signal increase above blank after PDMS replacement are 370 μm and 34 h, respectively. At early stages of the migration process, the velocity of the cell-front is about 181 nm/min. Taking the required time of 122 h to migrate over the full distance d_{tot}=512 μm, we receive a mean velocity of 70 nm/min. Considering the second experiment (Figure 8.1 b)), where the distance d_{ls} is about zero μm, the measured migration speed is 45 nm/min.

The migration of cell populations can be described as a diffusion process, which is based on random cell movements [Sengers2007]. The direction of moving cells also can be influenced by gradients of dissolved chemoattractants (chemotaxis), gradients in adhesion factors immobilized to growing surfaces (heptotaxis) and by micro- and nano-topography including a variety of groove, pillar and island patterns, leading to directional cell migration. In our experiment, the cell movement in lateral direction is basically confined by the fluidic channel dimensions, but at this large feature sizes the individual cell migration direction remains unaffected [Sengers2007, Berry2004]. After PDMS barrier replacement, the direction of the random cell movement is slightly biased, since the cells can only move to the right direction. Independent of the migration mode, fibroblast migrate at speeds within the range of 100-1000 nm/min [Friedl1998, Lauffenburger1996, Cai2007]. Compared to the mean (maximum) migration speed measured here, the downer limit of 100 nm/min is about 2.5 times (0.6) higher, and the upper limit of 1000 nm/min is about 25-fold (6-fold) higher, respectively. This variations in migration velocity can have several reasons. The migration speed is usually determined by means of cell trajectories following individual cell tracking. As reported by Cai et al., the migration speed of cells initially at the wound-edge and those behind the cell-front can differ by a factor of three [Cai2007]. In most studies, alterations in the physical and chemical surface modification show a strong affect in the cell motility [Berry2004]. Kaiser et

al. demonstrated, that changing the topographic characteristics of the surface leads to velocities around 133±33 nm/min [Kaiser2006], which are comparable to our results. In our study, the cells contain a large amount of beads, which could impair the migration process. On the one hand, the employed MagSense beads have an about twice higher density and in case of a maximum loading of about 1270 beads (Chapter 5.2.1), the cell's weight is about 1.5 times higher compared to reference cells. On the other hand, the driving force in the migration process is the cytoskeleton. Following phagocytosis, the phagosomes remain attached to the cytoskeleton, and during migration both the cell's locomotion as well as the reorganization of beads need to be regulated in parallel. In order to better analyze the affect of bead-loading to the cell motility, a set of additional migration experiments is necessary, where the migration speed of cells with different bead-loadings including reference cells is investigated. This task was not in the frame of this thesis.

8.2. Enzymatic cell detachment

We have discussed in Chapter 2.2.1 the way cells attach at surfaces and link the cell's cytoskeleton to extracellular ligands via adhesion receptors. The adhesion strength is basically determined by receptor clusters, which influences cell growth, differentiation and motility [Ward1994]. In turn, receptor clustering can be affected by altering the chemical and mechanical properties of receptor-ligand bonds by either changing the cell plasma membrane or the substratum characteristics. To better understand the cell-substrate contact, it is essential to investigate the formation of receptor clusters, and one method is based on adhesion and detachment kinetics, while the detachment process can be considered as the reverse process of cell adhesion. There are several methods to achieve and investigate cell detachment such as low-temperature lift-off, mechanical dissociation, fluid flow induced shear stress, acid and enzymatic treatment [Canavan2005, Chesla1998, Decave2002, Abatangelo1982, Cozens-Roberts1990]. As already mentioned in Chapter 5.3, cell detachment leading to its death can also be induced by toxicity [Xing2005]. In our study, the receptor or protein connections are cleaved by utilizing proteolytic and collagenolytic enzymes such as Trypsin-EDTA and Accutase (see Appendix A.2.2). During the detachment process, the cell's morphology transforms from a flat to a spherically shaped state. In case of magnetically labeled cells, the mean bead-to-sensor distance d of internalized beads increases with proceeding stage of detachment and, as a result, a continual signal drop is expected (Figure 8.2 a)).

For all experiments, the chip is mounted with a fluidic fixture consisting of an integrated window sufficient to comprise the entire biosensor row. In a first step, about 6000-8000 NHDF cells are added and confluently grown on top of the sensing area. Thereafter, MagSense 1.2 μm beads dissolved in DMEM cell medium (2 ml of 35 or 75 μg/ml concentration) are incubated

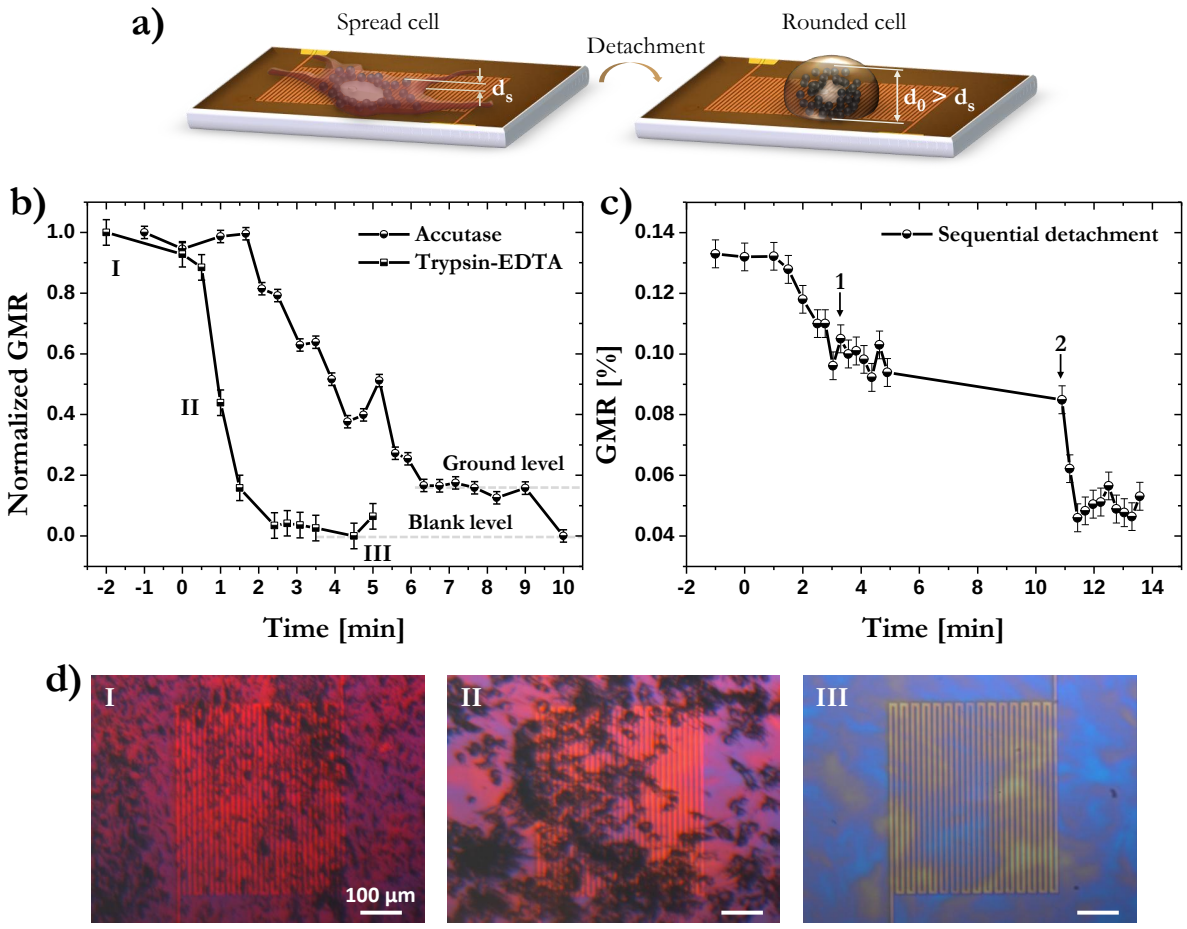

Figure 8.2: a) Shape transformation of bead-loaded cells during the enzymatic detachment process leading to higher bead-to-sensor distances. b) Normalized GMR-traces of two distinct experiments of the first type displaying the detachment process with original GMR-amplitudes of 0.107 % (Trypsin-EDTA) and 0.267 % (Accutase), reflecting the different bead-loading of cells. c) GMR-trace of the second type experiment showing a sequential Accutase and Trypsin-EDTA detachment process. Starting with Accutase, the detachment is temporary terminated by adding cell medium and subsequently continiued by Trypsin-EDTA detachment. d) Time-lapse images taken during the detachment experiment shown in b) at stages including confluent cell growth (I), during cell rounding (II) and after cell replacement (III).

over night. When bead phagocytosis is completed, the cell medium is removed, followed by three times PBS buffer washing. Immediately afterwards, 200 μl of either Trypsin-EDTA or Accutase are added above the cells that are free of cell medium and buffer. The GMR-response is recorded during the entire experiment, allowing real-time monitoring.

Our study includes two types of experiments, which are basically similar up to the stage where the enzymes are added. The procedure of the first type of experiments corresponds to that described above. In the second experiment type, first 200 μl Accutase are added, and

after a reaction time of 2.5 minutes, the detachment progress is stopped by adding 300 μl DMEM medium. About eight minutes later, the Accutase-DMEM mixture is carefully removed, followed by two buffer washing steps. The detachment process is than continued by adding 200 μl of a Trypsin-EDTA solution.

The detachment of cells by enzymes is a standard procedure in cell culturing. Our fibroblast cells are passaged every three days by applying either Trypsin-EDTA or Accutase. The time required to detach the reference cells in culture flasks is about 2-3 minutes and 4-5 minutes for Trypsin-EDTA and Accutase, respectively [Charwat2013, Purtscher2013]. Exactly the same exposure times are also reported for fibroblasts in the literature by applying Trypsin-EDTA [Campisi1983, Halaban1984] and Accutase [Hristov2010, Preynat-Seauve2009, Saretzki2008]. However, fibroblasts show with increasing number of passaging, i.e. cell aging, a tendency to delayed detachment, and for passage beyond number 30, we observe about one to two minutes longer detachment times [Charwat2013, Purtscher2013]. In all experiment, cells with total passage number below 25 are used.

The GMR-traces of both types of experiments displaying the detachment kinetics are shown in Figure 8.2 b) and c), while 8.2 d) features typical images taken at different stages of the first type of experiments. The data analysis comprises in total five experiments, two of them each pertaining the detachment by Accutase and Trypsin-EDTA in the first experiment type and one concerning the second experiment type involving both enzymes. In all experiments, the enzyme is added at t=0 min to initiate the cell detachment. Following t=0 min in the first experiment type, a characteristic lag time of t_l=1.33±0.47 min and t_l=0.75±0.35 min is observed for Accutase and Trypsin, respectively, where no significant signal change is measured, indicating no noticeable detachment. Beyond the lag time, the signal drops linearly, reaching ground level for Accutase and Trypsin within a detachment time of t_D=4.96±1.36 min and t_D=2.86±1.33 min, respectively. The detachment time corresponds to the time required for the signal to drop from its initial amplitude to 6 % obove the ground/blank level, while the 6 % threshold value is given by the standard error of the ground/blank level. Depending on the bead concentration used for cell labelling, i.e. 75 or 35 μg/ml, the ground level reaches a value of 0.0788±0.004 % or it drops completely down to the blank level (Figure 8.2 b)).
The slope of the GMR-signal drop is analyzed by a linear fit function revealing on average a 1.6-fold higher value for Trypsin-EDTA detachment. Here, only the interval of the GMR-trace starting from the last data point of the lag time until reaching the first data point of the ground level is fitted.
In order to determine further kinetic parameters representing a quantitative analysis, we correlate the cell-projection area with the determined detachment time. Magnetically loaded cells possess in a spread state a projection area of A_s=3250 μm^2 (Chapter 6.1) and the con-

tact area of a rounded NHDF cell of radius r_0=10.5 μm, assuming a cup-like adhesion shape as illustrated in Figure 8.2 a), is A_0=346 μm^2. By measured detachment time t_D, we can calculate the detachment kinetics by determining the rate by which the cell-projection area decreases according to $D_a=(A_s\text{-}A_0)/t_D$. Assuming a uniform area decrease with time, the experiments reveal for Accutase and Trypsin-EDTA a kinetic rate of $D_{a,acc}$=10 μm^2/s and $D_{a,tryp}$=17 μm^2/s, respectively.
From analyzing the profile of the GMR-trace, we can conclude that the enzymatic detachment of fibroblast cells is divided in two phases. It commences with a lag phase that is about 1.8 times longer for Accutase than for Trypsin-EDTA. According to the GMR-signal, no significant morphological changes are measured and we assume that the lag phase is required to hydrolyze the peptide bonds of cell-cell connections of the confluent cell monolayer (cell-cell dissociation). In the second phase, i.e. $\Delta t = t_D - t_l$, the fast signal decrease indicates a rapid cell morphology change that corresponds to the time required to cleave the cell-surface receptor connections, which is about 1.5 time higher for Accutase compared to Trypsin-EDTA (cell-surface dissociation). Considering both phases, the total detachment time for Accutase is about 1.7-fold higher compared to Trypsin-EDTA and agrees to the times observed for reference cell detachment in culture flasks.

The investigation of adherent cells such as fibroblasts usually implies the detachment of cells from their culture dish wall and their transfer to the analyzing platform. The detachment step is crucial, especially by applying enzymes which can have adverse effects on the membrane-associated proteins and, thus, irreversibly influence the integrity of the cell plasma membrane. In order to receive intact cell samples for further analysis, the exposure time required to cleave solely the extracellular proteins can be optimized by utilizing real-time monitoring techniques. Moreover, also new detachment approaches which allow a gentle detachment can be studied. For instance, thermoresponsive copolymer surfaces are one method that allows the noninvasive detachment of adherent cells, and their temperature-induced detachment is monitored by using TIRF microscopy (Chapter 3.1.2) [Uhlig2010].

In the second type experiment, the enzymatic inhibition of the DMEM cell medium is investigated. The cell medium is supplemented with calf serum that terminates the enzymatic reaction by binding the Trypsin-EDTA [Yamada1990]. After adding Accutase at t=0 min, the GMR-signal behavior resembles that of the first type experiments starting with a lag time of about 1.5 minutes followed by a rapid signal decrease (Figure 8.2 c)). At time t=3 min, the cell medium is added and the data point measured 15 seconds thereafter is indicated by the number "1" in Figure 8.2 c). Following cell medium incubation, the GMR-signal remains at about the same level (0.097±0.006 %) for the next 8 minutes, suggesting no further morphological changes of the cell and, thus, an immediate termination of the enzymatic reaction.

In order to be able to continue the detachment process, the Accutase-DMEM mixture is carefully removed, the cells are washed with PBS buffer and the sensor response is recorded (data point indicated by number "2"). Directly after adding Trypsin-EDTA (t=10.9 min), the detachment process is continued and, consequently, the GMR-signal drops within 30 seconds to the blank level, suggesting complete cell detachment. Remarkable is the lack of the first detachment phase, supporting the previous suggestion that the lag time represents the time required for the cell-cell dissociation. In this case, the cell-cell connections are cleaved by the first Accutase treatment. In addition, the detachment times including the lag time of 5.4 min and 2.1 min are extrapolated according to the slopes of the first and second signal decrease and agree within the mean standard error with the previously measured values of the first type experiments.

8.3. Summary

We have presented two more examples of nano-biointerface studies focusing on the investigation of time-dependent processes including cell migration and detachment. Both studies were based on magnetic labeling of fibroblast cells by means of phagocytosis and the magnetoresistive detection of the magnetic stray field of internalized particles. In our chip-based cell migration assay, the proliferation phase of the cutaneous wound healing process has been examined. The required cell-front was realized by means of a MagLab fluidic fixture and an additional PDMS barrier, representing the wound edge. The time required to close the cutaneous wound was determined by measuring the average migration velocity of the cell-front that accounts for 40 nm/min, while the maximum velocity measured was 180 nm/min. Independent of the migration mode, i.e. random or directed cell movement, fibroblasts migrate at speeds within the range of 100-1000 nm/min, which compared to the mean (maximum) migrating speed of the cell-front measured here is 2.5-25 (0.6-6) times higher. Another important question in this regard, which has not been addressed yet, is, to what extent the migration behavior is affected by the number of internalized beads. Due to the calculations made, the weight of a cell with maximum bead-loading is about 1.5 time higher compared to a reference cell. Moreover, during migration the cytoskeleton has to coordinate in parallel the cells locomotion and bead-rearrangements inside the cell. However, additional studies are required to clarify whether cell motility is impaired by internalized beads.
In the second study, the enzymatic detachment kinetics was investigated by treating adherent cells with Trypsin-EDTA and Accutase. According to the measured GMR-traces, the detachment process features two phases. It begins with a lag phase that lasts about 1.8 times longer for Accutase than for Trypsin-EDTA. The measured lag time was identified as the time required to dissociate the cell-cell connections of a confluent cell monolayer. In the cell-substrate dissociation phase, a rapid linear signal decrease was measured with a slope value 1.6-fold higher for the Trypsin-EDTA detachment. Taking both phases into account, the

detachment process was completed for Accutase and Trypsin-EDTA after a total detachment time of 5.0 min and 2.9 min, respectively. The determined values agree well to our reference cell detachment times observed in cell passaging and also to values reported in the literature. A quantitative analysis of the cell's projection-area during the detachment process revealed for Accutase and Trypsin-EDTA a kinetic rate of $D_{a,acc}$=10 $\mu m^2/s$ and $D_{a,tryp}$=17 $\mu m^2/s$, respectively. In our sequential detachment experiment using subsequently Accutase, cell medium and Trpysin-EDTA, we could monitor the inhibition effect of cell medium by terminating cell detachment within 15 seconds. After continuing the detachment by adding Trypsin-EDTA, a further signal drop without the typical lag phase was observed, supporting the conclusion that the lag time corresponds to the time required for cell-cell dissociation.

9. Summary and outlook

The fundamental idea behind a lab-on-a-chip system is the integration of single or multiple laboratory operations on a small chip platform that allows to design miniaturized devices with superior analytical performance compared to standard laboratory bench-scale methods. In this thesis, a magnetic lab-on-a-chip (MAGLab) system at the interface of biology, chemistry, and physics is developed that integrates giant magnetoresistive sensors, superparamagnetic particles, and microfluidics. A magnetoresistive-based methodology is developed for real-time monitoring of time dependent interactions between living cells and magnetic particles, which opens up a completely new research and application field that is of high biotechnological and biomedical relevance. By an appropriate microfluidic architecture, it is possible to design microenvironments that mimic the cell's native extracellular matrix and allow to study interactions close to in-vivo conditions. Employing the MAGLab system, a variety of nano-biointerface studies concerning the dynamic interaction of human cells with their extracellular environment is realized, thus representing a multifunctional platform enabling serial on-chip cell analysis.

Chapter 3 presents existing real-time monitoring methods and the magnetoresistive detection principle, which is based on measuring changes of the local magnetic stray field of superparamagnetic particles (beads) within embedded GMR-sensors. These stray field variations are induced by distance changes of the beads relative to the sensor during dynamic cell-bead interactions, thus allowing real-time monitoring.
In Chapter 4, a comprehensive introduction to all components of our MAGLab system has been given. As model cells, human skin fibroblasts from healthy tissue and mutated or epigenetically changed human prostate cancer cells have been used. The beads of choice for all real-time monitoring experiments are completely characterized, including magnetic and all cell-relevant physical and biochemical properties. Besides determining the best operating range, the magnetic properties of the magnetoresistive biosensor in presence of external magnetic fields are discussed by means of energy minimization and micromagnetic simulations. Two different scenarios are simulated which resemble the conditions encountered during the cell experiments. The simulated results contribute to the interpretation of the GMR-response observed in the phagocytosis and spreading experiments. Turning to the magnetic field configuration of the MAGLab setup, a unique feature of using superposed homogeneous and inhomogeneous magnetic fields is the ability to apply both attractive and repulsive forces to magnetic particles within the biochip. The required fields are simulated by finite element methods, and a computer controlled three-dimensional movement of magnetic particles and magnetically labeled cells is experimentally proven. The demonstrated manipulation features could enable integration of multiple laboratory tasks such as the acceleration of molecular recognition reactions by a three-dimensional bead mixing procedure, which illustrates the po-

tential of this MAGLab system to operate at the molecular level and serve as a total analysis system.

In Chapter 5 emphasis has been placed on off-chip investigations concerning basic cell-environment interactions that are essential for the following on-chip monitoring experiments. By varying the modification of the surface and exposing cells to a variety of beads differing in size and surface functionalization, a broad spectrum of interaction possibilities is covered. The uptake capability and capacity strongly depends on the bead coating and size, cell type, and the way beads are exposed to the cells. Fibroblast exhibit similar phagocytic behavior independent of the uptake approach and clearly show a higher uptake capacity compared to cancer cells. The cancer cells feature a significantly inhibited uptake when beads are presented to the dorsal plasma membrane of confluently grown cells (top-down approach). The uptake capacity of both cell types during spreading on bead-immobilized surfaces is assessed and a limiting coverage degree for 100 % bead uptake is determined. Finally, the fluorescent-based viability assay revealed no cytotoxicity of the beads of choice for both cell types.

In Chapter 6, the phagocytic behavior of cells during their spreading process on bead-immobilized (sensor-)surfaces has been investigated by means of standard optical microscopy and by real-time monitoring of the magnetoresistive sensor signal evolution (bottom-up approach). The optical reference measurements on bead-immobilized and bead-free surfaces reveal that simultaneous cell spreading and phagocytosis are competing events that rival the surplus plasma membrane area required for both processes. As a result, the difference in saturation spreading area agrees well to the total membrane area required to envelop the respective number of internalized beads. According to the GMR-based real-time magnetoresistive measurements, the bead uptake rate and, consequently, cell spreading is not a linear function with time. It is higher at early stages and decreases steadily leveling off after a mean saturation time of 97±32 min and 263±85 min for fibroblast and cancer cells, respectively. The optically and magnetically determined saturation times agree within the standard deviation, thus reflecting the cell spreading kinetics. The associated bead uptake rate of fibroblasts accounts for three beads per minute, which is by a factor of eight higher compared to cancer cells. In addition to determining time scales, a unique feature of our magnetic approach is its ability to determine the mean vertical distance of internalized beads from the sensor surface, which accounts for 120 nm and 175 nm for fibroblast and cancer cells, respectively. Long-term monitoring measurements of internalized beads suggest no noticeable bead degradation and exocytosis in fibroblast cells. Our magnetoresistive-based real-time monitoring methodology is reproducible and background-free.

In a living multicellular system such as a human body, adherent cells are found in a complete spread and confluent state anchored at their extracellular microenvironment. In Chapter 7, the phagocytic behavior of confluently grown cells, excluding the spreading process, has been investigated employing a similar magnetoresistive detection methodology (top-down

approach). The uptake rate of fibroblasts is not a linear function with time. The signal increase in the early uptake phase is attributed to both bead sedimentation and phagocytosis. In the late uptake phase, a 8.5 times slower signal increase due to progressive phagocytosis is observed. The phagocytosis process is terminated after a mean saturation time of 27.7 h, and the uptake rate per cell accounts for 45 beads per hour, which is four times smaller compared to phagocytosis during spreading. Investigations carried out at 4 °C clearly demonstrate metabolically inhibited phagocytosis and prove that our magnetic approach is well suited to detect possible disease-related or environmental impacts that lead to a profound malfunction in phagocytosis. The uptake rate of cancer cells under physiological conditions is a linear function with time, and the phagocytosis process is terminated three times faster compared to fibroblast experiments. Analysis of the reached saturation level compared to fibroblasts suggests a five times lower uptake capacity. The measured GMR-signal increase is attributed to both bead phagocytosis and agglomerations, the latter leading to island-formations.
In Chapter 8 two more nano-biointerface studies concerning the migration and detachment of fibroblasts have been presented. A chip-based cell migration assay is developed enabling the investigation of the proliferation phase in the cutaneous wound healing process. The migrating wound edge is mimicked by a magnetically labeled cell-front. The average migration velocity of the cell-front accounts for 40 nm/min. The detachment kinetics has been investigated by treating confluently grown fibroblast cells with two distinct enzymes, namely Trypsin-EDTA and Accutase. The time evolution of the GMR-response features two phases during the detachment process. The first lag phase reflects the dissociation of cell-cell connections, which is followed by a rapid cell-substrate dissociation phase. The detachment process is completed for Accutase and Trypsin-EDTA after a detachment time of 5.0 min and 2.9 min, respectively, which is coherent to reference values. The kinetic rate of the cell's projection-area during the detachment process accounts for $D_{a,acc}$=10 $\mu m^2/s$ and $D_{a,tryp}$=17 $\mu m^2/s$ for Accutase and Trypsin-EDTA, respectively. In a sequential detachment experiment using Accutase, cell medium and Trpysin-EDTA subsequently, the fast inhibition effect of cell medium is demonstrated.
Although GMR-based biosensors or biochips are by now well established in a variety of bioassay technologies for investigating molecular recognition processes, this thesis proved for the first time the successful application of magnetic biochips or lab-on-a-chips in the field of dynamic cell-environmental interactions employing human cells.

Future perspectives

The question how temperature effects influence the uptake behavior has been addressed by the metabolically inhibited experiments. These investigations have raised the issue, how other external influences such as magnetic forces applied to magnetic beads might influence cell-bead interactions. Magnetic forces can be applied either prior or after the phagocytosis process is completed. The bottom-up approach represents a suitable method to study the cytoskeletal forces that prevail during cell spreading and phagocytosis. Prior to cell seeding and subsequent spreading, the immobilized beads can be captured by applying magnetic forces by means of the small coils underneath the biochip. The magnetic force can be gradually increased by sourcing the millicoil with increasing current intensity. Once a threshold force value is exceeded, phagocytosis is expected to terminate, thus suggesting an upper limit of cytoskeletal forces a cell can apply.

The top-down approach enables to distinguish between beads that are inside the cell and those adhering on top of the cell. In biomedical applications, beads are loaded with a variety of distinct drugs that have to be delivered inside the cell. In case the drug-loaded beads are not phagocytosed, directed magnetic forces exerted by the millicoils towards the cell interior could promote their uptake. The bead transfer can be monitored instantaneously by the sensor embedded underneath the cells. A similar approach is utilized in "magnetofection", where magnetic forces are utilized for rapid and efficient delivery of genes associated with beads inside the cell [Plank2003], but no integrated monitoring system has been reported to date. The internalized beads can also be released from the cell by exocytosis, and their secretion could be enhanced/impeded by applying repulsive/attractive magnetic forces, which facilitates the optimization of drug dwell times within cells.

The developed migration assay can be utilized to investigate whether magnetic forces, drugs, gene manipulations or other factors influence the migration velocity of cells. The idea of capturing magnetically labeled cells at predefined area, for instance by means of on-chip integrated flux concentrators, is appealing for a variety of applications, especially for those focusing on single cell analysis.

Moreover, magnetic beads localized inside the cell can also be utilized to induce a heat stress (hyperthermia), which leads to changes in the cell physiology. Possible alterations in the cell viscosity or plasma membrane permeability can be monitored in real-time by guiding the beads using external gradient fields and measuring their transport characteristics inside the cell.

A. Appendix

A.1. Preparation and analytical tools

An overview of all sample preparation and analytical tools used in this thesis is given. Emphasis is put on the parameter settings and device specifications rather than the physics underlying each method. Most of the experimental techniques described pertain the sensor fabrication starting with the deposition of a thin multilayered film. Subsequently, the film is patterned by means of UV lithography, etching and lift-off techniques. Other tools such as SEM are utilized for sample analysis. Finally, the successive process steps of the biosensor fabrication process are illustrated.

A.1.1. Thin film deposition

There are a variety of techniques capable of depositing nanometer thin films such as molecular beam epitaxy, atomic layer deposition, thermal oxidation, evaporation, chemical vapor deposition and sputtering. In this work the last two techniques have been employed.

Sputter deposition

The sputtering was carried out with a customized cluster system from Leybold UNIVEX. Two film deposition chambers are equipped with seven 4" and two 3" DC magnetron sources as well as two 4" RF magnetron sources, allowing the deposition of 11 distinct materials without vacuum break. The sample holder can operate either in a static or dynamic mode, while the latter mode results in an improved film deposition homogeneity. The standard base pressure in both chambers is $1 \cdot 10^{-7}$mbar and the process gas is pure Argon (Ar). All metallic layers have been DC magnetron-sputtered in the static mode at a source voltage of 200-300 V, a gas inlet pressure of 2 μbar, and a power of either 40 W (Cu-layer) or 20 W (others). The first 1.7 nm of the Cu-layer were deposited in a static mode followed by a dynamic mode sputtering, which results in an additional wedge layer of 0.0 to 0.7 nm thickness. The MgO film was RF magnetron-sputtered at a power of 150 W at 5 μbar. During the sputtering, the sample holder was cooled at room temperature.

Plasma enhanced chemical vapor deposition (PECVD)

The Si_3N_4 passivation layer has been chemical-vapor-deposited in an Oxford Instruments Plasmalab 100 PECVD system. A mixture of SiH4 (silane, 700 sccm) and NH_3 (ammoniac, 18 sccm) precursor gases were used at a power of 10 W and a process base pressure of 1 Torr. In order to avoid any thermal induced interlayer diffusions of the GMR-multilayers, a process temperature of 200 °C have been chosen, which is about 100 °C below the standard

Table A.1: UV-Lithography process parameters and chemicals.

Positive resist		Negative resist	
Primer	HDMS or Ti-Prime	Primer	HDMS or Ti-Prime
Spin coating	4000 rpm, 35 sec	Spin coating	4000 rpm, 35 sec
Photo-resist	LOR 3A	Photo-resist	AZ 5214 Image reversal
Soft bake	150 °C, 5 min	Spin coating	8000 rpm, 35 sec
Photo-resist	AZ MIR701	Soft bake	120 °C, 1 min
Spin coating	4000 rpm, 35 sec		
Soft bake	110 °C, 1 min		
Exposure		Exposure	
Time	6 or 7 sec	Time	3 sec
		Post exposure bake	120 °C, 1 min
		Flood exposure	10 sec
Developer	AZ MIF726, 30 or 40 sec	Developer	AZ MIF726, 30

deposition procedure. GMR-multilayer systems annealed for 30 min at temperatures up to 250 °C are considered as thermally stable, while those annealed at 300 °C and higher result in significantly lower GMR amplitudes [Schroeder2011].

A.1.2. Optical UV-lithography

An important patterning technique used in processing continuous films toward functioning sensor elements is ultraviolet (UV) lithography, which was carried out with a Suess MicroTech MJB3 Mask Aligner equipped with a 350 W mercury lamp. UV lithography is suitable for realizing arbitrary geometrical patterns with feature sizes down to about 1 μm, while for the fabrication of nanometer precise patterns e-beam lithography is utilized. The processing steps described in the following remain the same for all types of photoresists used (Table A.1). First of all, the sample surface was cleaned from residual contaminants in an ultrasonic bath by a two minute acetone and isopropanol washing step. Afterwards, a two minute drying step at 120 °C was carried out to evaporate condensed water. In an usual standard process, a primer such as Hexamethyldisiloxan (HMDS) and the respective photoresist were subsequently spin-coated. In other cases, also a modified process consisting of an additional spin-coated photoresist (LOR 3A) between the primer and the selected photoresist has been utilized. The latter approach generates an undercut that facilitates the following lift-off process. After spin-coating, each resist was placed on a hot plate to drive out the solvents and to cross-link its molecules resulting in a resist activation and structural stability. Treating the LOR resist with higher (lower) temperatures leads to a smaller (larger) undercut.
The patterned photo-resist can serve two different purposes, either to deposit or remove material in the regions uncovered by the resist. In a so-called lift-off process, a material is deposited on top of the sample and resist. By dissolving the resist, the material on the resist is lifted off, while the material on the sample remains and creates a structure. The resist can also be used as a hard mask protecting the sample. In a subsequent etching process, only

material of the unprotected regions is removed.

A.1.3. Etching techniques

Wet chemistry

An image reversal photoresist serves as protective mask covering, except for the area above the contact pads, the entire biochip surface. After spin-coating, the resist was UV-exposed using an appropriate mask and developed as previously described. The insulating Si_3N_4 passivation layer above the contact pads has been removed by dipping the biochip for 25 s in buffered hydrofluoric acid (BHF, ammoniumfluoride 875-125 Riedel-de Haén 40207). The remnant resist was subsequently removed in an ultrasonic bath by acetone and isopropanol washing steps.

Ion beam etching (IBE)

The etching of the meander-shaped sensor elements has been accomplished by an Ion Sys500 ion beam milling machine from *Roth&Rau*. The etching system incorporates an Electron Cyclotron Resonance ion source that is additionally equipped with a Hiden Analytical HAL 301 Secondary Ion Mass Spectrometer (SIMS) allowing the real-time monitoring of the as-etched materials. After the Ar gas inlet into the champer, the base pressure of $1 \cdot 10^{-7}$mbar reaches a process pressure of $4 \cdot 10^{-4}$mbar. The etching was carried out in a beam current regulating mode. For it, a beam and acceleration voltage of each 500 V and a power of 300 W were chosen, resulting in a beam current of 45 mA. The angle of incidence of the ion beam relative to the rotating (3 rpm) sample surface is 50° and the time required to etch the entire GMR-multilayer system was 11 min.

A.1.4. Chip fabrication

The individual fabrication steps from a continuous film to meander-shaped sensor elements are illustrated in Figure A.1. Following the sputtering of the GMR-multilayer system, the chip surface was spin-coated with the primer and photo-resists (Figure A.1 a), b)). The solubility of the resist can be altered by UV-light exposure. In order to allow the illumination of only predefined areas, a photo-mask controlled by the mask-aligner was placed between the light source and the chip. In case of a positive photo-resist, the illuminated regions were dissolved by a subsequent development step (Figure A.1 c)). In a next step, a Tantalum (Ta) layer was sputter-deposited on top of the resist and GMR-multilayer (resist-free area), covering the entire chip surface (Figure A.1 d)). As the resist was removed by NMP or accetone, the Ta-layer on the resist was lifted off, resulting in a meander-shaped pattern (Figure A.1 e)). This pattern was transfered to the GMR-multilayer by removing the areas unprotected by Tantalum by means of ion beam milling. The thickness of the Ta-layer (45

nm) was adjusted to the time (11 min) required to etch the GMR-stack. After etching, both the unprotected and the Ta hard mask were removed completely and the remaining structure represents the meander-shaped sensor elements (Figure A.1 f)). To ensure electrical contacting, each sensor element was connected to patterned Ti/Au conducting lines that were produced following similar fabrication steps as described in Figure A.1 b) - e). A 230 nm chemical-vapor-deposited Si_3N_4 passivation layer covering the entire chip surface protects the sensor elements from interactions with biological fluids such as cell medium or buffer (Figure A.1 i)). In a final step, the chip surface was spin coated by a negative photo-resist. After UV-light exposure and development, the contact pads that are unprotected by the resist were removed by dipping the entire chip into a buffered hydrofluoric acid (BHF) for 25 seconds. The remaining resist was finally removed by NMP or acetone.

A.1.5. Scanning electron microscopy

A Zeiss Supra 40 Scanning Electron Microscope (SEM) was utilized to visualize the bead arrangement within fixated NHDF cells. On top of all cell-samples, an additional 100 nm thick Au-layer was sputter-deposited to ensure surface conductivity. The sample was mounted on a x-y-z positioning table that allows sample rotation and tilting in all three dimensions. In a SEM system, electrons are generated by an e-gun in a high vacuum chamber and are accelerated towards the anode. The kinetic energy of the electrons depends on the voltage applied at the e-gun cathode, which was usually in the range of 5 to 20 kV. The images are produced by scanning the sample surface by a focused electron beam that is controlled by means of electromagnetic lenses. The electrons interact with the sample and depending on its composition and surface topography, different signals are generated which can be monitored by respective detectors. With the employed system, either secondary, back-scattered or transmitted electron signals can be monitored. The signal amplitudes at each beam position were displayed as gray values in the image allowing a sub-nanometer resolution.

A.1.6. Zeta potential

We have measured the Zeta potential of our particles with the Zetasizer Nano ZS 90 (Malvern Instr. Ltd.). This device utilizes a combination of two measurement techniques, namely Electrophoresis and Laser Doppler Velocimetry that is also denoted as "Laser Doppler Electrophoresis". This method measures how fast a particle moves in a liquid when an electrical field is applied. As a result both the Zeta potential and the particle size distribution are obtained. The pH of all buffer solutions was measured by a Sartorius PB-11 pH-meter while stirring at 300 rpm with a bar magnet.

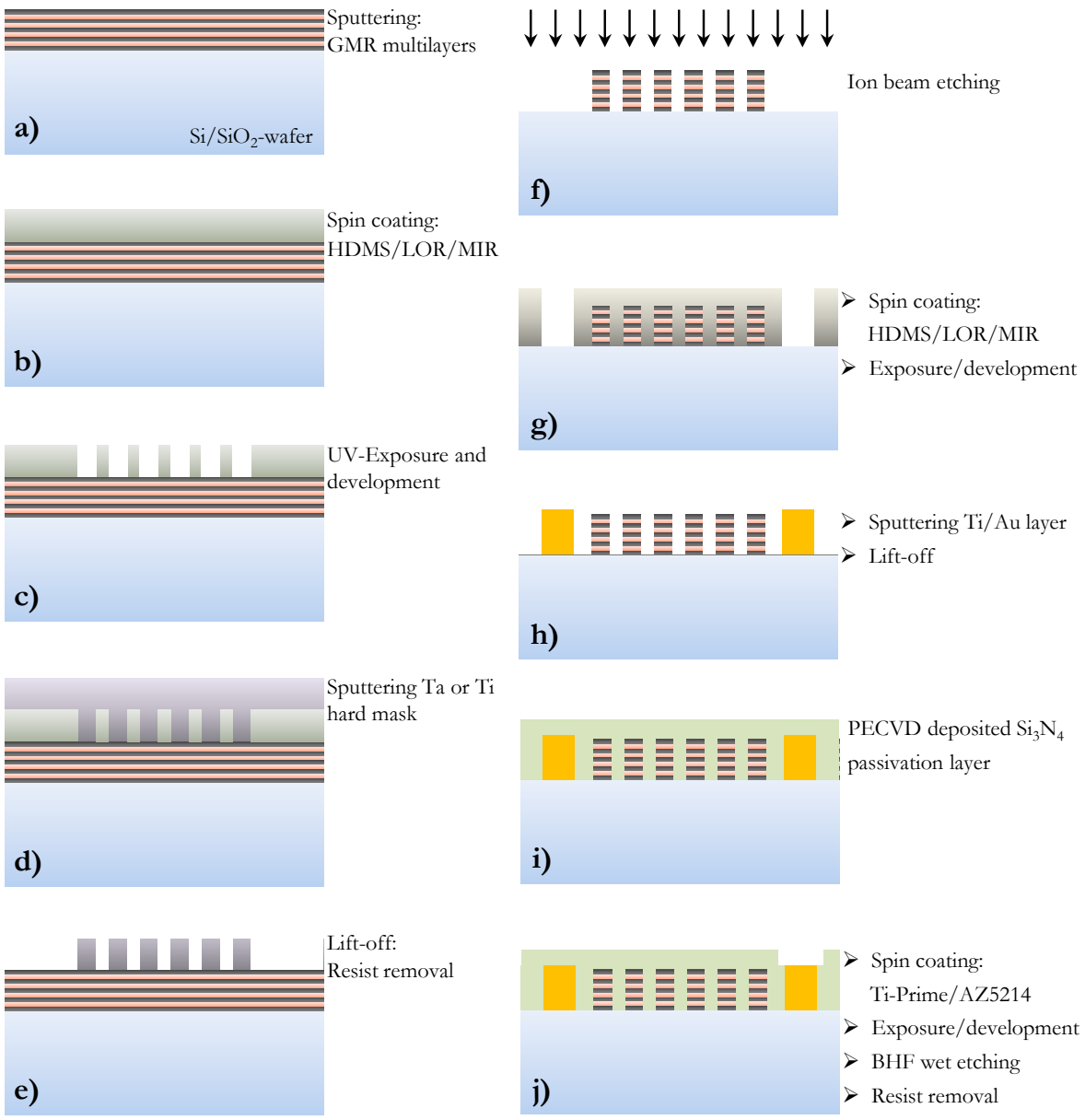

Figure A.1: Illustration of the sensor-chip fabrication process cycle including several sputtering, UV-exposure and etching steps.

A.1.7. Evaluation of the sensor bead-surface coverage

To determine the degree of bead-surface coverage of the sensor, a homemade image analysis program has been used. All pictures were captured by a Leica MZ 16 long-range optical microscope equipped with a Leica DFC 320 CCD camera. The image setting parameters can be adjusted by the image manager (IM50) software from Leica. Beside standard settings (2088 x 1150 pixels, 16(8)bit color(grayscale), tag image file format), also other imaging parameters such as brightness (92 %), amplification (5.0x) and color saturation (1.5x) were kept constant

during image recording. Still, these settings can lead depending on the experimental setup conditions to variation in the image characteristics and serve only as orientation values.
Figure A.2 illustrates exemplarily the evaluation procedure, which starts with the conversion of the original images into grayscale and subsequently into raw data files. The image analysis program scans the raw image and assigns to each pixel a certain gray scale value. According to image A.2 b), the beads could be identified as black dots, whereas the sensor meanders and the background were clearly brighter. Thus, as displayed in the histogram, beads belong to low grayscale values and can easily be discriminated from the rest. In addition to the histogram, another output image file was created (A.2d)), which displays all pixels up to an adjustable threshold grayscale value. Pixels above the threshold are cut off. This image file served as a control and facilitates to find the appropriate threshold grayscale value. As a final step, the pixels below the threshold value were counted and represent the bead surface coverage.

A.2. Cell biology

Basics in working with living cells including the preparation of cell medium, cell viability assays involving fluorescent dyes, and cell passaging are presented. To avoid any bacterial or viral infections, the cells were handled under a laminar flow providing a sterile environment. In addition, all objects (culture flask, mulitwells etc.) transfered inside the laminar flow hood were disinfected by ethanol sprinkling.

A.2.1. Culture medium

Culture media contain a variety of nutrients that guarantee cell survival, growth and proliferation. Depending on the cell type cultured, different variations based on the Eagle's minimal essential medium (EMEM) can be used, which contain amino acids, salts, glucose and vitamins. In case of DU145 cancer cells, the EMEM medium was supplemented with 2 mM L-glutamine, 1 % non-essential amino acids, 1 mM sodium pyruvate, and 10 % fetal bovine serum (FBS). For NHDF cells, the Dulbecco's modified Eagle's medium (DMEM) has been used, which was supplemented with 2 mM L-glutamine, and 10 % fetal bovine serum [CLS]. For all on-chip cell experiments, each cell medium was additionally supplemented with 10 mM HEPES buffer solution and 1 % antibiotika (Gentaminci), remaining the pH for several hours at about 7 and preventing cell contaminations, respectively [CLS]. Before use, the medium was heated up to 37 °C swinging in a water bath. All mentioned medium components were purchased from PAA Laboratories GmbH [PAA] and VWR International [VWR].

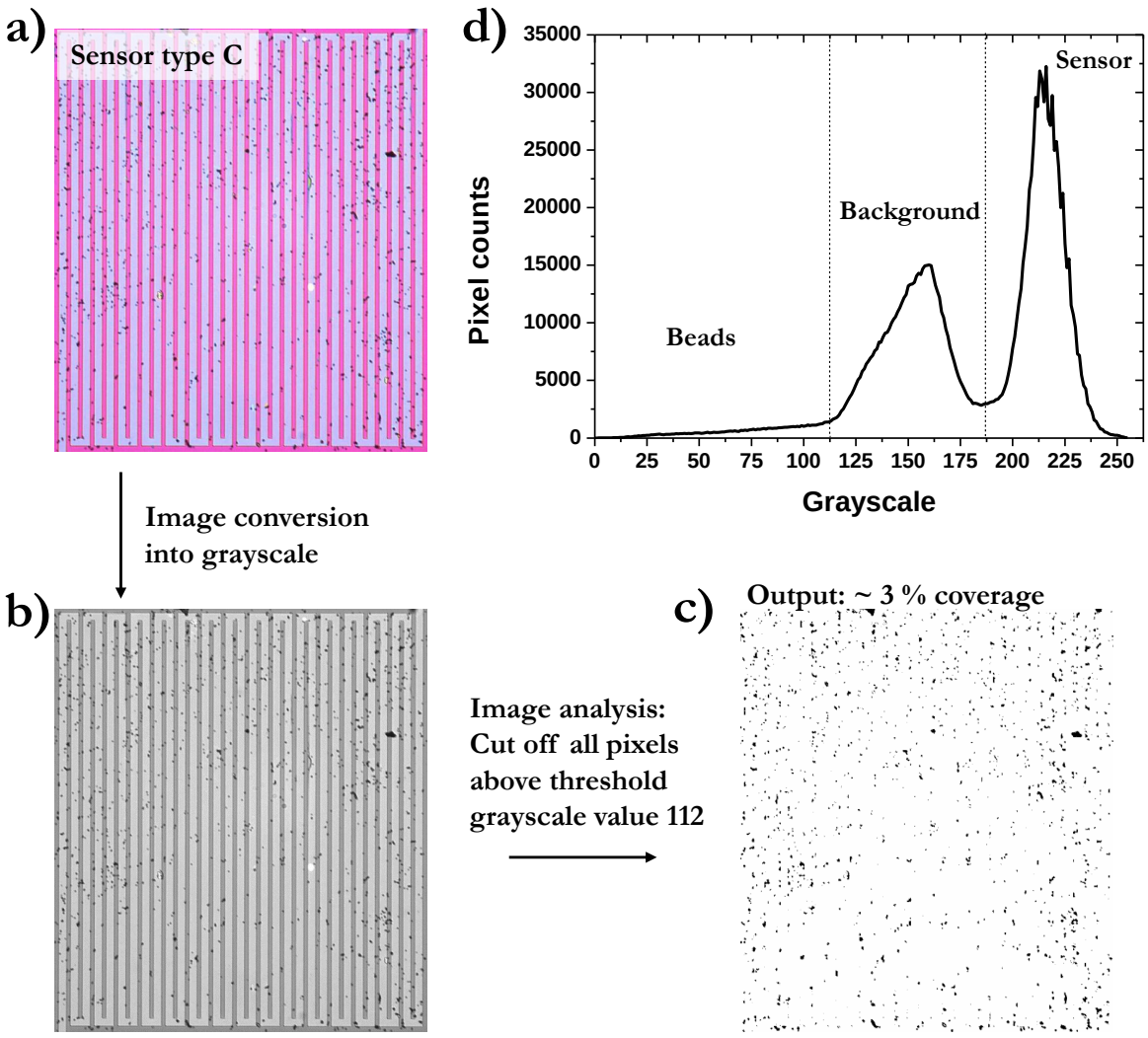

Figure A.2: Exemplary bead-surface coverage evaluation procedure for MagSense 1.2 μm beads. a) original and b) grayscale converted optical microscopy images. c) Output control file according to the threshold graycale value of 112 resulting in a 3 % surface coverage. d) Histogram of the three distinct areas consisting of beads, meander stripes, and background.

A.2.2. Cell passaging

Cells grow on appropriate surfaces until the entire surface is populated forming a two-dimensional cell monolayer of highest cell density (cell confluency). Once reaching a confluent state, the cell start inhibiting each other, known as contact inhibition. To ensure a continued cell growth and doubling, cell passaging is needed. The culture flask including the cell monolayer was transfered from the CO_2 incubator to the laminar flow hood. The cell medium was replaced and the cells were washed three times by PBS buffer. After adding 0.5 ml of either Trypsin-EDTA or Accutase for cell detachment, the cells were placed for about 2-3 min or 4-5 min, respectively, in the CO_2 incubator. The detached cells were suspended in fresh culture

medium and about 50 % of the initial cell number was seeded again in a new culture flask of the same size. This procedure is denoted as cell passaging and ensures the continued cell growth up to a passage of about 50±10, known as the Hayflick-limit [Hayflick1965].
NHDF cells from Promo-Cell [P-C] and DU145 cancer cells from Cell Lines Service GmbH [CLS] are cultured at 37 °C under humidified atmosphere of 5 % CO_2. The cells were grown in 25 cm^2 culture flasks with cell densities at confluency, according to the supplier, of $2 \cdot 10^4$ and $1 - 3 \cdot 10^5$ cells/cm^2 for NHDF and cancer cells, respectively.

A.2.3. Cell viability and staining

A common way to better visualize the cell's cytoplasm or to investigate the cell viability is the use of fluorescent dyes such as Calcein-acetoxymethylester (Calcein-AM). The dye is dissolved in Dimethyl sulfoxide (DMSO) and stored as a 1 mM stock solution at -20 °C. Prior to staining, the cells were transfered to the laminar flow hood, followed by cell medium removal and three times PBS washing. For staining the whole culture flask containing about $3 \cdot 10^6$ confluent grown cells, about 2 ml PBS-dye-solution with a final concentration of 4 μM was used. After an incubation time of about 30 (20) minutes at 37 °C for NHDF (DU145) cells, the PBS-dye solution is removed, followed by three times PBS washing steps. Depending on the current experiment, the cell are either detached and transfered suspended in medium to the chip or immediately incubated with cell medium if their detachment is unnecessary. The excitation and emission of the dye was accomplished by a Nikon, TE2000-S fluorescence microscope, equipped with several filers (TRIC, FITC etc.) allowing the excitation with different wavelengths.

References

[ASCB] The American Society for Cell Biology: http://www.ascb.org. Cell image library, Augsut 2012.

[Abatangelo1982] G. Abatangelo, R. Cortivo, M. Martelli, and P. Vecchia. Cell detachment mediated by hyaluronic acid. *Experimental Cell Research*, 137(1):73 – 78, 1982.

[Abraham2007] Leah C. Abraham, J. Fred Dice, Kyongbum Lee, and David L. Kaplan. Phagocytosis and remodeling of collagen matrices. *Experimental Cell Research*, 313(5):1045 –1055, 2007.

[Aderem1999] Alan Aderem and David M. Underhill. Mechanisms of phagocytosis in macrophages. *Annual Review of Immunology*, 17:593 – 623, 1999.

[Aggeler1982] Judith Aggeler and Zena Werb. Initial events during phagocytosis by macrophages viewed from outside and inside the cell: Membrane-particle interactions and clathrin. *The Journal of Cell Biology*, 94:613–623, 1982.

[Alberts1989] Bruce Alberts, Dennis Bray, Julian Lewis, Martin Raff, Keith Robers, and James D. Watson. *Molecular biology of the cell*. Garland Publishing, 2 edition, 1989.

[Ali-Zade2004] R.A. Ali-Zade. Structure and magnetic properties of polymer microspheres filled with magnetite nanoparticles. *Inorganic Materials*, 40:509–515, 2004.

[Allen1996] Lee-Ann H Allen and Alan Aderem. Mechanisms of phagocytosis. *Current Opinion in Immunology*, 8(1):36 – 40, 1996.

[Ashcroft1976] N.W. Ashcroft and N.D. Mermin. *Solid State Physics*. Saunders College Publishing, Philadelphia, 1976.

[Axelrod1984] Daniel Axelrod. Total internal reflection fluorescence in biological systems. *Journal of Luminescence*, 31&32(0):881 – 884, 1984.

[Babes1999] Lucia Babes, Benoit Denizot, Gisèle Tanguy, Jean Jacques Le Jeune, and Pierre Jallet. Synthesis of iron oxide nanoparticles used as mri contrast agents: A parametric study. *Journal of Colloid and Interface Science*, 212(2):474 – 482, 1999.

[Bae1998] S. Bae, A. Schlensog, W. Mertin, E. Kubalek, and M. Maywald. A new test method for contactless quantitative current measurement via scanning magneto-resistive probe microscopy. *Microelectronics Reliability*, 38(6-8):969 – 974, 1998.

[Baibich1988] M. N. Baibich, J. M. Broto, A. Fert, F. Nguyen van Dau, F. Petroff, P. Etienne, G. Creuzet, A. Friederich, and J. Chazelas. Giant magnetoresistance of (001)Fe/(001)Cr magnetic superlattices. *Physical Review Letters*, 61:2472–2475, November 1988.

[Bardsley1983] W.G. Bardsley and J.D. Aplin. Kinetic analysis of cell spreading. *Journal of Cell Science*, 61(1):365–373, 1983.

[Barnas1990] J. Barnas, A. Fuss, R. E. Camley, P. Grünberg, and W. Zinn. Novel magnetoresistance effect in layered magnetic structures: Theory and experiment. *Phys. Rev. B*, 42:8110–8120, Nov 1990.

[Barnas1992] J. Barnas. Coupling between two ferromagnetic films through a non-magnetic metallic layer. *JMMM*, 111, 3:L215–L219, 1992.

[Baselt1998] D. R. Baselt, G. U. Lee, M. Natesan, S. W. Metzger, P. E. Sheehan, and R. J. Colton. A biosensor based on magnetoresistance technology. *Biosens Bioelectron*, 13(7-8):731–739, 1998.

[Bergmann1992] L. Bergmann and C. Schäfer. *Lehrbuch der Experimentalphysik - Festkörperphysik*. Walter de Gruyter, 1992.

[Berkowitz1992] A.E. Berkowitz, J.R. Mitchell, M.J. Carey, A.P. Young, S. Zhang, F.E. Spada, F.T. Parker, A. Hütten, and G. Thomas. Giant Magnetoresistence in Heterogeneous Cu-Co-alloys. *Phys. Rev. Lett.*, 68:3745–3748, 1992.

[Berry2004] Catherine C Berry, Stuart Charles, Stephen Wells, Matthew J Dalby, and Adam S.G Curtis. The influence of transferrin stabilised magnetic nanoparticles on human dermal fibroblasts in culture. *International Journal of Pharmaceutics*, 269(1):211 – 225, 2004.

[Betz1996] William J Betz, Fei Mao, and Corey B Smith. Imaging exocytosis and endocytosis. *Current Opinion in Neurobiology*, 6(3):365 – 371, 1996.

[Binasch1989] G. Binasch, P. Grünberg, F. Saurenbach, and W. Zinn. Enhanced magnetoresistance in layered magnetic structures with antiferromagnetic interlayer exchange. *Physical Review B. Condensed Matter*, 39(7):4828–4830, Mar 1989.

[Bioclone] Bioclone Inc. http://www.bioclon.com/, October 2012.

[Blazej2006] Robert G. Blazej, Palani Kumaresan, and Richard A. Mathies. Microfabricated bioprocessor for integrated nanoliter-scale sanger dna sequencing. *Proceedings of the National Academy of Sciences*, 103(19):7240–7245, 2006.

[Booth2001] James W Booth, William S Trimble, and Sergio Grinstein. Membrane dynamics in phagocytosis. *Seminars in Immunology*, 13(6):357 – 364, 2001.

[Bosch] Robert Bosch GmbH. http://www.bosch.de, February 2013.

[Bozorth1993] Richard M. Bozorth. *Ferromagnetism*. John Wiley & Sons, Inc., Hoboken, New Jersey, 1993.

[Brasier2006] Owen Green Martin Brasier, Nicola McLoughlin and David Wacey. A fresh look at the fossil evidence for early archaean cellular life. *Philos. Trans. R. Soc. Lond. B Biol. Sci.*, 361 (1470):887–902, 2006.

[Bratosin2005] Daniela Bratosin, Laura Mitrofan, Carmen Palii, Jérome Estaquier, and Jean Montreuil. Novel fluorescence assay using calcein-am for the determination of human erythrocyte viability and aging. *Cytometry Part A*, 66A(1):78–84, 2005.

[Braun2006] Virginie Braun and Florence Niedergang. Linking exocytosis and endocytosis during phagocytosis. *Biology of the Cell*, 98(3):195–201, 2006.

[Bruno1993] P. Bruno. Oscillations of interlayer exchange coupling vs. ferromagnetic-layers thickness. *Europhys. Lett.*, 23:615, 1993.

[Bruno1995] P. Bruno. Theory of interlayer magnetic coupling. *Phys. Rev. B*, 52:411–439, Jul 1995.

[Brzeska2004a] M. Brzeska, M. Panhorst, P.B. Kamp, J. Schotter, G. Reiss, A. Pühler, A. Becker, and H. Brückl. Detection and manipulation of biomolecules by magnetic carriers. *Journal of Biotechnology*, 112:25–33, 2004.

[Buettiker1988] M. Büttiker. Symmetry of electrical conduction. *IBM Journal of Research and Development*, 32:317–334, 1988.

[Burmeister1998] Jeffrey S. Burmeister, Lauri A. Olivier, W.M. Reichert, and George A. Truskey. Application of total internal reflection fluorescence microscopy to study cell adhesion to biomaterials. *Biomaterials*, 19:307 – 325, 1998.

[CLS] CLS Cell lines service GmbH. http://www.cell-lines-service.de.

[Cai2007] Anna Q. Cai, Kerry A. Landman, and Barry D. Hughes. Multi-scale modeling of a wound-healing cell migration assay. *Journal of Theoretical Biology*, 245:576–594, 2007.

[Camley1989] R. E. Camley and J. Barnaś. Theory of giant magnetoresistance effects in magnetic layered structures with antiferromagnetic coupling. *Phys. Rev. Lett.*, 63:664–667, 1989.

[Campisi1983] Judith Campisi and Estela E. Medrano. Cell cycle perturbations in normal and transformed fibroblasts caused by detachment from the substratum. *Journal of Cellular Physiology*, 114(1):53–60, 1983.

[Canavan2005] Heather E. Canavan, Xuanhong Cheng, Daniel J. Graham, Buddy D. Ratner, and David G. Castner. Cell sheet detachment affects the extracellular matrix: A surface science study comparing thermal liftoff, enzymatic, and mechanical methods. *Journal of Biomedical Materials Research Part A*, 75A(1):1–13, 2005.

[Cannon1992] G.J. Cannon and J.A. Swanson. The macrophage capacity for phagocytosis. *Journal of Cell Science*, 101(4):907–913, 1992.

[Cans2001] Ann-Sofie Cans, Fredrik Höök, Oleg Shupliakov, Andrew G. Ewing, Peter S. Eriksson, Lennart Brodin, and Owe Orwar. Measurement of the dynamics of exocytosis and vesicle retrieval at cell populations using a quartz crystal microbalance. *Analytical Chemistry*, 73(24):5805–5811, 2001.

[Cantor2000] Charles R. Cantor. Biotechnology in the 21st century. *Trends in Biotechnology*, 18(1):6 – 7, 2000.

[Carr2007] C. Carr, A.N. Matlachov, H. Sandin, M.A. Espy, and R.H. Kraus. Magnetic sensors for bioassay: Hts squids or gmrs? *Applied Superconductivity, IEEE Transactions on*, 17(2):808 –811, 2007.

[Cavalcanti-Adam2007] Elisabetta Ada Cavalcanti-Adam, Tova Volberg, Alexandre Micoulet, Horst Kessler, Benjamin Geiger, and Joachim Pius Spatz. Cell spreading and focal adhesion dynamics are regulated by spacing of integrin ligands. *Biophysical Journal*, 92(8):2964 – 2974, 2007.

[Cavalier-Smith2004] Thomas Cavalier-Smith. Only six kingdoms of life. *Proc. R. Soc. Lond. B*, 271 (1545):1251–1262, 2004.

[Chamaraux2005] F. Chamaraux, S. Fache, F. Bruckert, and B. Fourcade. Kinetics of cell spreading. *Phys. Rev. Lett.*, 94:158102, Apr 2005.

[Charwat2013] V. Charwat. Personal communication, 2013.

[Chavrier2001] Philippe Chavrier. Molecular basis of phagocytosis. *Seminars in Immunology*, 13(6):337 – 338, 2001.

[Chen2000] Hui Chen, Barbara W Bernstein, and James R Bamburg. Regulating actin-filament dynamics in vivo. *Trends in Biochemical Sciences*, 25(1):19 – 23, 2000.

[Chesla1998] Scott E. Chesla, Periasamy Selvaraj, and Cheng Zhu. Measuring two-dimensional receptor-ligand binding kinetics by micropipette. *Biophysical Journal*, 75:1553–1572, 1998.

[Chithrani2006] B. Devika Chithrani, Arezou A. Ghazani, and Warren C. W. Chan. Determining the size and shape dependence of gold nanoparticle uptake into mammalian cells. *Nano Letters*, 6(4):662–668, 2006.

[Chovan2002] Tibor Chován and András Guttman. Microfabricated devices in biotechnology and biochemical processing. *Trends in Biotechnology*, 20(3):116 –122, 2002.

[Comsol] Comsol Multiphysics. http://www.comsol.de.

[Conner2003] Sean D. Conner and Sandra L. Schmid. Regulated portals of entry into the cell. *Nature*, 422:37–44, 2003.

[Cox2000] Dianne Cox, Donna J. Lee, Benjamin M. Dale, Jero Calafat, and Steven Greenberg. A rab11-containing rapidly recycling compartment in macrophages that promotes phagocytosis. *Proceedings of the National Academy of Sciences*, 97(2):680–685, 2000.

[Cozens-Roberts1990] Cindi Cozens-Roberts, John A. Quinn, and Douglas A. Lauffenburger. Receptor-mediated cell attachment and detachment kinetics: Ii. experimental model studies with the radial-flow detachment assay. *Biophys. J.*, 58:857–872, 1990.

[Craighead2006] Harold Craighead. Future lab-on-a-chip technologies for interrogating individual molecules. *Nature*, 442(7101):387–393, 2006.

[Cretel2010] E Cretel, D Touchard, A M Benoliel, P Bongrand, and A Pierres. Early contacts between t lymphocytes and activating surfaces. *Journal of Physics: Condensed Matter*, 22(19):194107, 2010.

[Curtis1964] A. S. G. Curtis. The mechanisms of adhesion of cells to glass: A study by interference reflection microscopy. *The Journal of Cell Biology*, 20(2):199–215, 1964.

[Curtis2001] Adam Curtis, Chris Wilkinson, Adam Curtis, and Chris Wilkinson. Nanotechniques and approaches in biotechnology. *Materials Today*, 4(3):22 – 28, 2001.

[Cuvelier2007] Damien Cuvelier, Manuel Théry, Yeh-Shiu Chu, Sylvie Dufour, Jean-Paul Thiéry, Michel Bornens, Pierre Nassoy, and L. Mahadevan. The universal dynamics of cell spreading. *Current Biology*, 17(8):694 – 699, 2007.

[Daw2006] Rosamund Daw and Joshua Finkelstein. Lab on a chip. 442 (7101):367, 2006.

[DeMello2006] A.J. DeMello. Control and detection of chemical reactions in microfluidic systems. *Nature*, 442(7101):394–402, 2006.

[Decave2002] Emmanuel Décavé, Daniel Garrivier, Yves Bréchet, Bertrand Fourcade, and Franz Bruckert. Shear flow-induced detachment kinetics of dictyostelium discoideum cells from solid substrate. *Biophysical Journal*, 82(5):2383 – 2395, 2002.

[Desjardins2003] Michel Desjardins and Gareth Griffiths. Phagocytosis: latex leads the way. *Current Opinion in Cell Biology*, 15(4):498 – 503, 2003.

[Dieny1991] B. Dieny, V. S. Speriosu, S. S. P. Parkin, B. A. Gurney, D. R. Wilhoit, and D. Mauri. Giant magnetoresistive in soft ferromagnetic multilayers. *Phys. Rev. B*, 43:1297–1300, Jan 1991.

[Doebereiner2004] Hans-Günther Döbereiner, Benjamin Dubin-Thaler, Gre´gory Giannone, Harry S. Xenias, and Michael P. Sheetz. Dynamic phase transitions in cell spreading. *Physical Review Letters*, 93 (10):1081051–1081054, 2004.

[Doebereiner2005] Hans-Günther Döbereiner, Benjamin J. Dubin-Thaler, Gregory Giannone, and Michael P. Sheetz. Force sensing and generation in cell phases: analyses of complex functions. *J. Appl. Physiol.*, 98:1542–1546, 2005.

[Doebereiner2006] Hans-Günther Döbereiner, Benjamin J. Dubin-Thaler, Jake M. Hofman, Harry S. Xenias, Tasha N. Sims, Gregory Giannone, Michael L. Dustin, Chris H. Wiggins, and Michael P. Sheetz. Lateral membrane waves constitute a universal dynamic pattern of motile cells. *Phys. Rev. Lett.*, 97:038102, 2006.

[Doolittle2000] Russell F Doolittle. Searching for the common ancestor. *Research in Microbiology*, 151(2):85 – 89, 2000.

[Dubin-Thaler2008] Benjamin J. Dubin-Thaler, Jake M. Hofman, Yunfei Cai, Harry Xenias, Ingrid Spielman, Anna V. Shneidman, Lawrence A. David, Hans-Günther Döbereiner, Chris H. Wiggins, and Michael P. Sheetz. Quantification of cell edge velocities and traction forces reveals distinct motility modules during cell spreading. *PLoS ONE*, 3(11):e3735, 11 2008.

[Dynal] Dynal Biotech. http://www.dynalbiotech.com, October 2012.

[Edelstein2000] R. L. Edelstein, C. R. Tamanaha, P. E. Sheehan, M. M. Miller, D. R. Baselt, L. J. Whitman, and R. J. Colton. The BARC biosensor applied to the detection of biological warfare agents. *Biosens Bioelectron*, 14(10-11):805–813, Jan 2000.

[Edwards1991] Edwards, Mathon, Muniz, and Phan. Oscillations of the exchange in magnetic multilayers as an analog of de Haas-van Alphen effect. *Physical Review Letters*, 67(4):493–496, Jul 1991.

[Eggeling2006] Eike Moritz Eggeling. Mischen von dünnen flüssigkeitsfilmen durch manipulation magnetischer micro- und nano-partikel mit magnetischen feldern; hybacc, hybridisierungsbeschleuniger für biochips. Master's thesis, Universität Bielefeld, 2006.

[El-Ali2006] Jamil El-Ali, Peter K. Sorger, and Klavs F. Jensen. Cells on chips. *Nature*, 442(7101):403–411, 2006.

[Evans1993] E. Evans, A. Leung, and D. Zhelev. Synchrony of cell spreading and contraction force as phagocytes engulf large pathogens. *The Journal of Cell Biology*, 122 (6):1295–1300, 1993.

[Franke1978] W. Werner Franke, Erika Schmid, Mary Osborn, and Klaus Weber. Different intermediate-sized filaments distinguished by immunofluorescence microscopy. *Proc. Natl. Acad. Sci.*, 75 (10):5034–5038, 1978.

[Fredriksson1998] C. Fredriksson, S. Khilman, B. Kasemo, and D. M. Steel. In vitro real-time characterization of cell attachment and spreading. *Journal of Materials Science: Materials in Medicine*, 9:785–788, 1998.

[Friedl1998] Peter Friedl, Kurt S. Zänker, and Eva-B. Bröcker. Cell migration strategies in 3-d extracellular matrix: Differences in morphology, cell matrix interactions, and integrin function. *Microscopy Research and Technique*, 43:369–378, 1998.

[Giancotti1999] Filippo G. Giancotti and Erkki Ruoslahti. Integrin signaling. *Science*, 285:1028–1032, 1999.

[Gibbons1991] John H. Gibbons. U.s. congress, office of technology assessment, ota-tct-514 (washington, dc: U.s. government printing office). In *Miniaturization Technologies*, 1991.

[Giebel1999] K.-F. Giebel, C. Bechinger, S. Herminghaus, M. Riedel, P. Leiderer, U. Weiland, and M. Bastmeyer. Imaging of cell/substrate contacts of living cells with surface plasmon resonance microscopy. *Biophysical Journal*, 76(1):509 – 516, 1999.

[Gijs1997] M. A. M. Gijs and G. E. W. Bauer. Perpendicular giant magnetoresistance of magnetic multilayers. *Adv. Phys. 46, 285 (1997)*, 46:285–445, 1997.

[Gilbert2004] T.L. Gilbert. A phenomenological theory of damping in ferromagnetic materials. *Magnetics, IEEE Transactions on*, 40(6):3443 – 3449, nov. 2004.

[Gimbrone1974] Michael A. Gimbrone, Ramzi S. Cotran, and Judah Folkman. Human vascular endothelial cells in culture. *The Journal of Cell Biology*, 60:673–684, 1974.

[Gingell1979] D. Gingell and I. Todd. Interference reflection microscopy. a quantitative theory for image interpretation and its application to cell-substratum separation measurement. *Biophysical Journal*, 26(3):507 – 526, 1979.

[Gottlieb1993] T. A. Gottlieb, I. E. Ivanov, Adesnik M., and D. D. Sabatini. Actin microfilaments play a critical role in endocytosis at the apical but not the basolateral surface of polarized epithelial cells. *J. Cell Biol.*, 120:695–710, 1993.

[Graham2002] D. L. Graham, H. Ferreira, J. Bernardo, P. P. Freitas, and J. M. S. Cabral. Single magnetic microsphere placement and detection on-chip using current line designs with integrated spin valve sensors: Biotechnological applications. *Journal of Applied Physics*, 91(10):7786 –7788, 2002.

[Graham2004] Daniel L. Graham, Hugo A. Ferreira, and Paulo P. Freitas. Magnetoresistive-based biosensors and biochips. *Trends in Biotechnology*, 22(9):455–462, 2004.

[Greenberg2002] Steven Greenberg and Sergio Grinstein. Phagocytosis and innate immunity. *Current Opinion in Immunology*, 14(1):136 – 145, 2002.

[Greiner] Greiner bio one. http://www.greinerbioone.com.

[Griffin1975] F M Griffin, J A Griffin, J E Leider, and S C Silverstein. Studies on the mechanism of phagocytosis. i. requirements for circumferential attachment of particle-bound ligands to specific receptors on the macrophage plasma membrane. *The Journal of Experimental Medicine*, 142(5):1263–1282, 1975.

[Griffiths2007] Gareth Griffiths. Cell evolution and the problem of membrane topology. *Nat Rev Mol Cell Biol.*, 8 (12):1018–1024, 2007.

[Grinnell1994] Frederick Grinnell. Mini-review on the cellular mechanisms of disease: Fibroblasts, myofibroblasts, and wound contraction. *The Journal of Cell Biology*, 124 (4):401–404, 1994.

[Grossman2004] H. L. Grossman, W. R. Myers, V. J. Vreeland, R. Bruehl, M. D. Alper, C. R. Bertozzi, and John Clarke. Detection of bacteria in suspension by using a superconducting quantum interference device. *Proceedings of the National Academy of Sciences*, 101(1):129–134, 2004.

[Groves2008] E. Groves, A. Dart, V. Covarelli, and E. Caron. Molecular mechanisms of phagocytic uptake in mammalian cells. *Cellular and Molecular Life Sciences*, 65:1957–1976, 2008.

[Gruenberg1986] P. Grünberg, R. Schreiber, Y. Pang, M. B. Brodsky, and H. Sowers. Layered magnetic structures: Evidence for antiferromagnetic coupling of fe layers across cr interlayers. *Phys. Rev. Lett.*, 57:2442–2445, 1986.

[Gruenberg1993] P. Grünberg. Magnetische Übergitter: Oszillierende zwischenschichtaustauschkopplungen in magnetischen schichtsystemen. *Phys. Bl.*, 49:27–30, 1993.

[Gruenberg1999] P. Grünberg. *Magnetische Schichtsysteme - Zwischenschichtaustauschkopplung: Phänomenologische Beschreibung, Materialabhängigkeit.* Institut für Festkörperforschung der Forschungszentrum Jülich GmbH, 1999.

[Gruenberg2000] Peter Grünberg. Layered magnetic structures in research and application. *Acta Materialia*, 48(1):239 – 251, 2000.

[Gryte1993] David M. Gryte, Michael D. Ward, and Wei Shou Hu. Real-time measurement of anchorage-dependent cell adhesion using a quartz crystal microbalance. *Biotechnology Progress*, 9(1):105–108, 1993.

[Guilak2000] Farshid Guilak and Van C. Mow. The mechanical environment of the chondrocyte: a biphasic finite element model of cell - matrix interactions in articular cartilage. *Journal of Biomechanics*, 33(12):1663–1673, 2000.

[Gupta2004] Ajay Gupta and Adam Curtis. Surface modified superparamagnetic nanoparticles for drug delivery: Interaction studies with human fibroblasts in culture. *Journal of Materials Science: Materials in Medicine*, 15:493–496, 2004.

[Haeberle2007] Stefan Haeberle and Roland Zengerle. Microfluidic platforms for lab-on-a-chip applications. *Lab Chip*, 7(9):1094–1110, 2007.

[Halaban1984] Ruth Halaban and FrancisD. Alfano. Selective elimination of fibroblasts from cultures of normal human melanocytes. *In Vitro*, 20:447–450, 1984.

[Haldane1929] John B. S. Haldane. The origin of life. *Rationalist Annual*, 148:3–10, 1929.

[Hartwig1980] J. H. Hartwig, H. L. Yin, and T. P. Stossel. *Contractile proteins and the mechanism of phagocytosis in macrophages. In Mononuclear Phagocytes: Functional Aspects.* The Hague: Martinus Nijhoff Publishers, 1980.

[Hayflick1965] L. Hayflick. The limited in vitro lifetime of human diploid cell strains. *Exp. Cell Res.*, 37:614–636, 1965.

[Heer2007] Rudolf Heer, Moritz Eggeling, Jörg Schotter, Christa Nöhammer, Rudolf Pichler, Markus Mansfeld, and Hubert Brückl. Acceleration of incubation processes in dna bio chips by magnetic particles. *Journal of Magnetism and Magnetic Materials*, 311(1):244 – 248, 2007.

[Helou2013] Michael Helou, Mathias Reisbeck, Sandro F. Tedde, Lukas Richter, Ludwig Bar, Jacobus J. Bosch, Roland H. Stauber, Eckhard Quandt, and Oliver Hayden. Time-of-flight magnetic flow cytometry in whole blood with integrated sample preparation. *Lab Chip*, 13(6):1035–1038, 2013.

[Herant2005] Marc Herant, Volkmar Heinrich, and Micah Dembo. Mechanics of neutrophil phagocytosis: behavior of the cortical tension. *Journal of Cell Science*, 118(9):1789–1797, 2005.

[Herant2006] Marc Herant, Volkmar Heinrich, and Micah Dembo. Mechanics of neutrophil phagocytosis: experiments and quantitative models. *Journal of Cell Science*, 119(9):1903–1913, 2006.

[Himmelhaus2009] Michael Himmelhaus and Alexandre Francois. In-vitro sensing of biomechanical forces in live cells by a whispering gallery mode biosensor. *Biosensors and Bioelectronics*, 25(2):418 – 427, 2009.

[Hoeink2008] Volker Höink. *Magnetoresistance and ion bombardment induced magnetic patterning.* PhD thesis, Universität Bielefeld, 2008.

[Holevinsky1998] Kathleen O. Holevinsky and Deborah J. Nelson. Membrane capacitance changes associated with particle uptake during phagocytosis in macrophages. *Biophysical Journal*, 75(5):2577 – 2586, 1998.

[Holody1998] P. Holody, W. C. Chiang, R. Loloee, J. Bass, W. P. Pratt, and P. A. Schroeder. Giant magnetoresistance of copper/permalloy multilayers. *Phys. Rev. B*, 58:12230–12236, 1998.

[Homola1999] Jiri Homola, Sinclair S. Yee, and Günter Gauglitz. Surface plasmon resonance sensors: review. *Sensors and Actuators B: Chemical*, 54:3 – 15, 1999.

[Hristov2010] Mihail Hristov, Denis Gümbel, Esther Lutgens, Alma Zernecke, and Christian Weber. Soluble cd40 ligand impairs the function of peripheral blood angiogenic outgrowth cells and increases neointimal formation after arterial injury. *Circulation*, 121(2):315–324, 2010.

[Huang2011] Jianyong Huang, Xiaoling Peng, Chunyang Xiong, and Jing Fang. Influence of substrate stiffness on cell-substrate interfacial adhesion and spreading: A mechano-chemical coupling model. *Journal of Colloid and Interface Science*, 355(2):503 – 508, 2011.

[Huetten1999] A. Hütten, S. Mrozek, S. Heitmann, T. Hempel, H. Brückl, and G. Reiss. Evolution of the gmr-effect amplitude in copper/permalloy-multilayered thin films. *Acta Materialia*, 47(15-16):4245 – 4252, 1999.

[Huttenlocher1995] Anna Huttenlocher, Rebecca R Sandborg, and Alan F Horwitz. Adhesion in cell migration. *Current Opinion in Cell Biology*, 7(5):697 – 706, 1995.

[Ionescu2010] A. Ionescu, N. J. Darton, K. Vyas, and J. Llandro. Detection of endogenous magnetic nanoparticles with a tunnelling magneto resistance sensor. *Philosophical Transactions of the Royal Society A: Mathematical,Physical and Engineering Sciences*, 368(1927):4371–4387, 2010.

[Jackson1999] John David Jackson. *Klassische Elektrodynamik*. De Gruyter, 1999.

[Janasek2006] Dirk Janasek, Joachim Franzke, and Andreas Manz. Scaling and the design of miniaturized chemical-analysis systems. *Nature*, 442(7101):374–380, 2006.

[Jeng2006] Hueiwang Anna Jeng and James Swanson. Toxicity of metal oxide nanoparticles in mammalian cells. *Journal of Environmental Science and Health, Part A*, 41(12):2699–2711, 2006.

[Justus2003] Maik Justus. *Magnetische Tunnelelemente mit Pulsplasma-oxidierten Barrieren und Elektroden aus Kobalt-Chrom Legierungen*. PhD thesis, Universität Bielefeld, 2003.

[Kaiser2006] Jean-Pierre Kaiser, Andreas Reinmann, and Arie Bruinink. The effect of topographic characteristics on cell migration velocity. *Biomaterials*, 27:5230–5241, 2006.

[Kalluri2006] Raghu Kalluri and Michael Zeisberg. Fibroblasts in cancer. *Nat Rev Cancer*, 6(5):392–401, 2006.

[Kobitski2004] A.Yu Kobitski, C.D Heyes, and G.U Nienhaus. Total internal reflection fluorescence microscopy - a powerful tool to study single quantum dots. *Applied Surface Science*, 234:86 – 92, 2004.

[Korn1967] Edward D. Korn and Robert A. Weisman. Phagocytosis of latex beads by acanthamoeba. *The Journal of Cell Biology*, 34:219–227, 1967.

[Kuswandi2007] Bambang Kuswandi, Nuriman, Jurriaan Huskens, and Willem Verboom. Optical sensing systems for microfluidic devices: A review. *Analytica Chimica Acta*, 601(2):141 – 155, 2007.

[Kvenvolden1970] Keith Kvenvolden, James Lawless, Katherine Pering, Etta Peterson, Jose Flores, Cyril Ponnaperuma, I.R. Kaplan, and Carleton Moore. Evidence for extraterrestrial amino-acids and hydrocarbons in the murchison meteorite. *Nature*, 228(5275):923–926, 1970.

[Lagae2002] L. Lagae, R. Wirix-Speetjens, J. Das, D. Graham, H. Ferreira, P. P. F. Freitas, G. Borghs, and J. De Boeck. On-chip manipulation and magnetization assessment of magnetic bead ensembles by integrated spin-valve sensors. *Journal of Applied Physics*, 91(10):7445 –7447, 2002.

[Landauer1988] R. Landauer. Spatial variation of currents and fields due to localized scatterers in metallic conduction. *IBM Journal of Research and Development*, 32:306–316, 1988.

[Lauffenburger1996] Douglas A. Lauffenburger and Alan F. Horwitz. Cell migration: A physically integrated molecular process. *Cell*, 84:359–369, 1996.

[Le1998] Hue P. Le. Progress and trends in ink-jet printing technology. *The Journal of Imaging Science and Technology*, 42 (1):49–62, 1998.

[Lee2010] Rimi Lee, Pyung Hwan Kim, Joung-Woo Choi, Kwon Oh-Joon, Kyujung Kim, Donghyun Kim, Chae-Ok Yun, and Kyung-Hwa Yoo. Capacitance-based real time monitoring of receptor-mediated endocytosis. *Biosensors and Bioelectronics*, 25(6):1325 – 1332, 2010.

[Levy1990] Peter M. Levy, Shufeng Zhang, and Albert Fert. Electrical conductivity of magnetic multilayered structures. *Phys. Rev. Lett.*, 65:1643–1646, 1990.

[Li2010] Yue Li, Guang-Kui Xu, Bo Li, and Xi-Qiao Feng. A molecular mechanisms-based biophysical model for two-phase cell spreading. *Applied Physics Letters*, 96(4):043703 –043703–3, 2010.

[Lim2006] C.T. Lim, E.H. Zhou, and S.T. Quek. Mechanical models for living cells - a review. *Journal of Biomechanics*, 39(2):195 – 216, 2006.

[Lim2010] Y.C. Lim, A.Z. Kouzani, and W. Duan. Lab-on-a-chip: a component view. *Microsystem Technologies*, 16(12):1995–2015, 2010.

[Lindner2008] Juha Lindner. *Immunologische und epidemiologische Aspekte antigenspezifischer T- und B-Zell-Antworten gegen humanpathogene Parvoviren.* PhD thesis, Universität Regensburg, 2008.

[Lindquist1988] S. Lindquist and E. A. Craig. The heat-shock proteins. *Annual Review of Genetics*, 22:631–677, 1988.

[Linnaeus1735] Carolus Linnaeus. Systemae naturae, sive regna tria naturae, systematics proposita per classes, ordines, genera & species. 1735.

[Llandro2010] J. Llandro, J. Palfreyman, A. Ionescu, and C. Barnes. Magnetic biosensor technologies for medical applications: a review. *Medical and Biological Engineering and Computing*, 48:977–998, 2010.

[Loosli2010] Y. Loosli, R. Luginbuehl, and J. G. Snedeker. Cytoskeleton reorganization of spreading cellsÂ on micro-patterned islands: a functional model. *Philosophical Transactions of the Royal Society A: Mathematical,Physical and Engineering Sciences*, 368(1920):2629–2652, 2010.

[Loureiro2011] J. Loureiro, P. Z. Andrade, S. Cardoso, C. L. da Silva, J. M. Cabral, and P. P. Freitas. Magnetoresistive chip cytometer. *Lab Chip*, 11(13):2255–2261, 2011.

[Lundberg2003] Mathias Lundberg, Sara Wikstrom, and Magnus Johansson. Cell surface adherence and endocytosis of protein transduction domains. *Molecular Therapy*, 8(1):143–150, 2003.

[Luzio2007] J. Paul Luzio, Paul R. Pryor, and Nicholas A. Bright. Lysosomes: fusion and function. *Nat Rev Mol Cell Biol*, 8(8):622–632, 2007.

[MagSense] Inc. MagSense Life Sciences. http://magsenselifesci.com/, October 2012.

[Manteca2011] A. Manteca, M. Mujika, and S. Arana. Gmr sensors: Magnetoresistive behaviour optimization for biological detection by means of superparamagnetic nanoparticles. *Biosensors and Bioelectronics*, 26(8):3705 – 3709, 2011.

[Manz1990a] A. Manz, Y. Miyahara, J. Miura, Y. Watanabe, H. Miyagi, and K. Sato. Design of an open-tubular column liquid chromatograph using silicon chip technology. *Sensors and Actuators B: Chemical*, 1(1-6):249–255, 1990.

[Manz1990b] A. Manz, N. Graber, and H.M. Widmer. Miniaturized total chemical analysis systems: A novel concept for chemical sensing. *Sensors and Actuators B: Chemical*, 1(1-6):244–248, 1990.

[Mark2010] Daniel Mark, Stefan Haeberle, Günter Roth, Felix von Stetten, and Roland Zengerle. Microfluidic lab-on-a-chip platforms: requirements, characteristics and applications. *Chem. Soc. Rev.*, 39:1153–1182, 2010.

[Marx2003] Kenneth A. Marx. Quartz crystal microbalance:a useful tool for studying thin polymer films and complex biomolecular systems at the solution-surface interface. *Biomacromolecules*, 4(5):1099–1120, 2003.

[Marx2005] Kenneth A. Marx, Tiean Zhou, Anne Montrone, Donna McIntosh, and Susan J. Braunhut. Quartz crystal microbalance biosensor study of endothelial cells and their extracellular matrix following cell removal: Evidence for transient cellular stress and viscoelastic changes during detachment and the elastic behavior of the pure matrix. *Analytical Biochemistry*, 343(1):23 – 34, 2005.

[Mathon1991] J Mathon. Exchange interactions and giant magnetoresistance in magnetic multilayers. *Contemporary Physics (USA)*, 32, no. 3:143–156, 1991.

[McCulloch1993] Christopher A. G. McCulloch and Gisele C. Knowles. Deficiencies in collagen phagocytosis by human fibroblasts in vitro: A mechanism for fibrosis? *Journal of Cellular Physiology*, 155(3):461–471, 1993.

[McDonald2000] J. Cooper McDonald, David C. Duffy, Janelle R. Anderson, Daniel T. Chiu, Hongkai Wu, Olivier J.A. Schueller, and George M. Whitesides. Fabrication of microfluidic systems in poly(dimethylsiloxane). *Electrophoresis*, 21:27–40, 2000.

[Meckel] Tobias Meckel. Membrane dynamics in response to cell adhesion: http://www.bio.tu-darmstadt.de, August 2012.

[Medina-Sanchez2012] Mariana Medina-Sanchez, Sandrine Miserere, and Arben Merkoci. Nanomaterials and lab-on-a-chip technologies. *Lab Chip*, 12(11):1932–1943, 2012.

[Megens2005] Mischa Megens and Menno Prins. Magnetic biochips: a new option for sensitive diagnostics. *Journal of Magnetism and Magnetic Materials*, 293(1):702 – 708, 2005.

[Melnik] Eva Melnik. Personal communication, 2013.

[Merkel2000] T. C. Merkel, V. I. Bondar, K. Nagai, B. D. Freeman, and I. Pinnau. Gas sorption, diffusion, and permeation in poly(dimethylsiloxane). *Journal of Polymer Science Part B: Polymer Physics*, 38(3):415–434, 2000.

[Meyer2001] D.E. Meyer, B.C. Shin, G.A. Kong, M.W. Dewhirst, and A. Chilkoti. Drug targeting using thermally responsive polymers and local hyperthermia. *Journal of Controlled Release*, 74(1-3):213 – 224, 2001.

[Microchem] Microchem. http://microchem.com/.

[Micromod] Micromod Partikeltechnologie GmbH. www.micromod.de.

[Miller1997] Stanley L. Miller, J. William Schopf, and Antonio Lazcano. Oparin's "origin of life": Sixty years later. *Journal of Molecular Evolution*, 44:351–353, 1997.

[Miller2001] M.M. Miller, P.E. Sheehan, R.L. Edelstein, C.R. Tamanaha, L. Zhong, L.J. Bounnak, S.and Whitman, and R.J. Colton. A dna array sensor utilizing magnetic microbeads and magnetoresistive detection. *Journal of Magnetism and Magnetic Materials*, 225:138–144, 2001.

[Moloney2004] M. Moloney, L. McDonnell, and H. O'Shea. Atomic force microscopy of bhk-21 cells: an investigation of cell fixation techniques. *Ultramicroscopy*, 100:153 – 161, 2004.

[Morgan2007] Mark R. Morgan, Martin J. Humphries, and Mark D. Bass. Synergistic control of cell adhesion by integrins and syndecans. *Nature Reviews Molecular Cell Biology*, 8:957–969, 2007.

[Mott1964] N. F. Mott. Electrons in transition metals. *Advances in Physics*, 13:325–420, 1964.

[Mrksich2000] Milan Mrksich. A surface chemistry approach to studying cell adhesion. *Chem. Soc. Rev.*, 29:267–273, 2000.

[Mu2010] C.P. Mu, W.W. Wang, B. Zhang, Q.F. Liu, and J.B. Wang. Dynamic micromagnetic simulation of permalloy antidot array film. *Physica B*, 405:1325–1328, 2010.

[Nakagawa2000] Toshiyuki Nakagawa, Hong Zhu, Nobuhiro Morishima, En Li, Jin Xu, Bruce A. Yankner, and Junying Yuan. Caspase-12 mediates endoplasmic-reticulum-specific apoptosis and cytotoxicity by amyloid-[beta]. *Nature*, 403(6765):98–103, 2000.

[Nelder1965] J. A. Nelder and R. Mead. A simplex method for function minimization. *The Computer Journal*, 7(4):308–313, 1965.

[Niedergang2004] Florence Niedergang and Philippe Chavrier. Signaling and membrane dynamics during phagocytosis: many roads lead to the phagos(r)ome. *Current Opinion in Cell Biology*, 16(4):422 – 428, 2004.

[O'Sullivan1999] C.K. O'Sullivan and G.G. Guilbault. Commercial quartz crystal microbalances - theory and applications. *Biosensors and Bioelectronics*, 14:663 – 670, 1999.

[OOMMF2008] National Institute of Standards and Technology. *OOMMF User's Guide*, 2008. Release 1.2a3.

[Olivier2004] V. Olivier, C. Rivière, M. Hindié, J.-L. Duval, G. Bomila-Koradjim, and M.-D. Nagel. Uptake of polystyrene beads bearing functional groups by macrophages and fibroblasts. *Colloids and Surfaces B: Biointerfaces*, 33(1):23 – 31, 2004.

[Oparin1924] Alexander I. Oparin. *Proiskhozhdenie zhizny*. Izd. Moskovski Rabochii, Moscow, 1924.

[Orgel1998] Leslie E. Orgel. The origin of life - a review of facts and speculations. *Trends in Biochemical Sciences*, 23(12):491 – 495, 1998.

[P-C] Promocell. http://www.promocell.com.

[PAA] PAA Laboratories GmbH. http://www.paa.com.

[PTC] Pro/Engineer Parametric Technology Corporation. http://www.ptc.com/, 2001.

[Paguirigan2008] Amy L. Paguirigan and David J. Beebe. Microfluidics meet cell biology: bridging the gap by validation and application of microscale techniques for cell biological assays. *BioEssays*, 30(9):811–821, 2008.

[Pamme2006] Nicole Pamme. Magnetism and microfluidics. *Lab Chip*, 6(1):24–38, 2006.

[Panhorst2005] Michael Panhorst, Paul-Bertram Kamp, Gunter Reiss, and Hubert Brückl. Sensitive bondforce measurements of ligand-receptor pairs with magnetic beads. *Biosensors and Bioelectronics*, 20(8):1685–1689, 2005.

[Panhorst2005a] M. Panhorst. *On-Chip manipuation and positioning of biomolecules with magnetic beads*. Dissertation, Phakultät für Physik, Universtität Bielefeld, 2005.

[Parak2005] Wolfgang J Parak, Teresa Pellegrino, and Christian Plank. Labelling of cells with quantum dots. *Nanotechnology*, 16(2):R9, 2005.

[Parkin1990] S. S. P. Parkin, N. More, and K. P. Roche. Oscillations in exchange coupling and magnetoresistance in metallic superlattice structures: Co/ru, co/cr, and fe/cr. *Phys. Rev. Lett.*, 64:2304–2307, May 1990.

[Parkin1991] S. S. P. Parkin. Systematic variation of the strength and oscillation period of indirect magnetic exchange coupling through the 3 d , 4 d , and 5 d transition metals. *Phys. Rev. Lett.*, 67:3598–3601, 1991.

[Parkin1998] S.S.P. Parkin. The magic of magnetic multilayers. *IBM Journal of Research and Development*, 42 (1):3–6, 1998.

[Piercenet] Pierce Protein Biology Products Thermo Scientific. http://www.piercenet.com.

[Pierres2003] Anne Pierres, Philippe Eymeric, Emmanuelle Baloche, Dominique Touchard, Anne-Marie Benoliel, and Pierre Bongrand. Cell membrane alignment along adhesive surfaces: Contribution of active and passive cell processes. *Biophysical Journal*, 84(3):2058 – 2070, 2003.

[Plank2003] C. Plank, U. Schillinger, F. Scherer, C. Bergemann, J.-S. Rémy, F. Krötz, M. Anton, J. Lausier, and J. Rosenecker. The magnetofection method: Using magnetic force to enhance gene delivery. *Biological Chemistry*, 384 (5):737–747, 2003.

[Plank2010] C. Plank. Meeting: Personal communication, 2010.

[Pratten1979] Margaret K. Pratten and John B. Lloyd. Effects of temperature, metabolic inhibitors and some other factors on fluiid-phase and adsorptive pinocytosis by rat peritoneal macrophages. *Biochemical Journal*, 180:567–571, 1979.

[Pratten1986] Margaret K. Pratten and John B. Lloyd. Pinocytosis and phagocytosis: the effect of size of a particulate substrate on its mode of capture by rat peritoneal macrophages cultured in vitro. *Biochimica et Biophysica Acta (BBA) - General Subjects*, 881(3):307 – 313, 1986.

[Press1988] W.H. Press, B. Flannery, S. Teukolsky, and W. Vetterling. *Numerical Recipes in C*. Camebridge University Press, 1988.

[Press1992] W. H. Press, S. A. Teukolsky, W. T. Vetterling, and B. P. Flannery. *Numerical Recipes in Fortran*. Cambridge University Press, 1992.

[Preynat-Seauve2009] Olivier Preynat-Seauve, Casimir de Rham, Diderik Tirefort, Sylvie Ferrari-Lacraz, Karl-Heinz Krause, and Jean Villard. Neural progenitors derived from human embryonic stem cells are targeted by allogeneic t and natural killer cells. *Journal of Cellular and Molecular Medicine*, 13(9b):3556–3569, 2009.

[Purcell1991] S. T. Purcell, W. Folkerts, M. T. Johnson, N. W. E. McGee, K. Jager, J. aan de Stegge, W. B. Zeper, W. Hoving, and P. Grünberg. Oscillations with a period of two cr monolayers in the antiferromagnetic exchange coupling in a (001) fe/cr/fe sandwich structure. *Phys. Rev. Lett.*, 67:903–906, 1991.

[Purtscher2013] M. Purtscher. Personal communication, 2013.

[RSB] ImageJ: Area Measurements Research Service Branch and Particle Counting. http://rsbweb.nih.gov, 2013.

[Rabinovitch1995] M. Rabinovitch. Professional and non-professional phagocytes: an introduction. *Trends Cell Biol*, 5 (3)(3):85–87, 1995.

[Ralph2008] D.C. Ralph and M.D. Stiles. Spin transfer torques. *Journal of Magnetism and Magnetic Materials*, 320:1190–1216, 2008.

[Reiss2005] Guenter Reiss, Hubert Brueckl, Andreas Huetten, Joerg Schotter, Monika Brzeska, Michael Panhorst, Daniela Sudfeld, Anke Becker, Paul B. Kamp, Alfred Puehler, Klaus Wojczykowski, and Peter Jutzi. Magnetoresistive sensors and magnetic nanoparticles for biotechnology. *Journal of Materials Research*, 20:3294–3302, 11 2005.

[Richter2007] Lukas Richter, Christoph Stepper, Andy Mak, Alessa Reinthaler, Rudolf Heer, Michael Kast, Hubert Bruckl, and Peter Ertl. Development of a microfluidic biochip for online monitoring of fungal biofilm dynamics. *Lab Chip*, 7(12):1723–1731, 2007.

[Richter2011] Lukas Richter, Verena Charwat, Christian Jungreuthmayer, Florian Bellutti, Hubert Brueckl, and Peter Ertl. Monitoring cellular stress responses to nanoparticles using a lab-on-a-chip. *Lab Chip*, 11(15):2551–2560, 2011.

[Ridley2003] Anne J. Ridley, Martin A. Schwartz, Keith Burridge, Richard A. Firtel, Mark H. Ginsberg, Gary Borisy, J. Thomas Parsons, and Alan Rick Horwitz. Cell migration: Integrating signals from front to back. *Science*, 302(5651):1704–1709, 2003.

[Rife2003] J.C. Rife, M.M. Miller, P.E. Sheehan, C.R. Tamanaha, M. Tondra, and L.J. Whitman. Design and performance of gmr sensors for the detection of magnetic microbeads in biosensors. *Sensors and Actuators A: Physical*, 107(3):209 – 218, 2003.

[Rios2012] Ángel Ríos, Mohammed Zougagh, and Mónica Avila. Miniaturization through lab-on-a-chip: Utopia or reality for routine laboratories? a review. *Analytica Chimica Acta*, 740(0):1 – 11, 2012.

[Ryzhkov2010] P. Ryzhkov, M. Prass, M. Gummich, J.-S. Kühn, C. Oettmeier, and H.-G. Döbereiner. Adhesion patterns in early cell spreading. *Journal of Physics: Condensed Matter*, 22:194106, 2010.

[Safarik1999] Ivo Safarik and Mirka Safarikova. Use of magnetic techniques for the isolation of cells. *Journal of Chromatography B*, 722:33–53, 1999.

[Saretzki2008] Gabriele Saretzki, Theresia Walter, Stuart Atkinson, Joao F. Passos, Bettina Bareth, W. Nicol Keith, Rebecca Stewart, Stacey Hoare, Miodrag Stojkovic, Lyle Armstrong, Thomas von Zglinicki, and Majlinda Lako. Downregulation of multiple stress defense mechanisms during differentiation of human embryonic stem cells. *STEM CELLS*, 26(2):455–464, 2008.

[Schakenraad1989] J.M. Schakenraad, J. Arends, H.J. Busscher, F. Dijk, P.B. van Wachem, and C.R.H. Wildevuur. Kinetics of cell spreading on protein precoated substrata: a study of interfacial aspects. *Biomaterials*, 10(1):43–50, 1989.

[Schneckenburger2005] H. Schneckenburger. Total internal reflection fluorescence microscopy: technical innovations and novel applications. *Curr Opin Biotechnol*, 16 (1)(1):13–18, 2005.

[Schotter2004] Jörg Schotter. *Development of a magnetoresistive biosensor for the detection of biomolecules*. PhD thesis, University of Bielefeld, 2004.

[Schotter2004b] J Schotter, P.B Kamp, A Becker, A PÃ¼hler, G Reiss, and H BrÃ¼ckl. Comparison of a prototype magnetoresistive biosensor to standard fluorescent dna detection. *Biosensors and Bioelectronics*, 19(10):1149 – 1156, 2004.

[Schotter2009] Joerg Schotter, Astrit Shoshi, and Hubert Brueckl. Development of a magnetic lab-on-a-chip for point-of-care sepsis diagnosis. *Journal of Magnetism and Magnetic Materials*, 321(10):1671 – 1675, 2009.

[Schreml2010] Stephan Schreml, Rolf-Markus Szeimies, Lukas Prantl, Michael Landthaler, and Philipp Babilas. Wound healing in the 21st century. *Journal of the American Academy of Dermatology*, 63(5):866 – 881, 2010.

[Schroeder2011] Philipp Schroeder. *Realisation and Validation of a Biomimetic Mechanosensor assembled by Nanowires and Giant Magneto Resistive Detection*. PhD thesis, Universität Bielefeld, 2011.

[Segal2001] G. Segal, W. Lee, P.D. Arora, M. McKee, G. Downey, and C.A. McCulloch. Involvement of actin filaments and integrins in the binding step in collagen phagocytosis by human fibroblasts. *Journal of Cell Science*, 114(1):119–129, 2001.

[Sengers2007] B.G. Sengers, M. Taylor, C.P. Please, and R.O. Oreffo. Computational modelling of cell spreading and tissue regeneration in porous scaffolds. *Biomaterials*, 28(10):1926–1940, 2007.

[Shenoy2005] V. B. Shenoy and L. B. Freund. Growth and shape stability of a biological membrane adhesion complex in the diffusion-mediated regime. *Proceedings of the National Academy of Sciences of the United States of America*, 102(9):3213–3218, 2005.

[Shoshi2005] Astrit Shoshi. Suche nach magnetischen führsystemen und gmr-sensoren zur on-chip manipulation und detektion von magnetischen teilchen. Master's thesis, Universität Bielefeld, 2005.

[Shoshi2012a] A. Shoshi, J. Schotter, P. Schroeder, M. Milnera, P. Ertl, V. Charwat, M. Purtscher, R. Heer, M. Eggeling, G. Reiss, and H. Brueckl. Magnetoresistive-based real-time cell phagocytosis monitoring. *Biosensors and Bioelectronics*, 36(1):116 – 122, 2012.

[Shoshi2013] A. Shoshi, J. Schotter, P. Schroeder, M. Milnera, P. Ertl, R. Heer, G. Reiss, and H. Brueckl. Contemporaneous cell spreading and phagocytosis: Magneto-resistive real-time monitoring of membrane competing processes. *Biosensors and Bioelectronics*, 40 (1)(0):82–88, 2013.

[Sigmaaldrich] Sigma Aldrich. http://www.sigmaaldrich.com.

[Sivagnanam2008] V. Sivagnanam, A. Sayah, C. Vandevyver, and M.A.M. Gijs. Micropatterning of protein-functionalized magnetic beads on glass using electrostatic self-assembly. *Sensors and Actuators B: Chemical*, 132(2):361 – 367, 2008.

[Southwick1983] F.S. Southwick and T.P. Stossel. Contractile proteins in leukocyte function. *Semin Hematol*, 20(4):305–321, 1983.

[Stewart1989] M.G. Stewart, E. Moy, G. Chang, W. Zingg, and A.W. Neumann. Thermodynamic model for cell spreading. *Colloids and Surfaces*, 42 (3 - 4):215 – 232, 1989.

[Stiles1993] M.D. Stiles. Exchange coupling in magnetic heterostructures. *Physical Review B: Condensed Matter*, 48(10):7238–7258, 1993.

[Stuart2005] Lynda M. Stuart and R. Alan B. Ezekowitz. Phagocytosis: Elegant complexity. *Immunity*, 22(5):539 – 550, 2005.

[Swanson1995] Joel A. Swanson and Stephen C. Baer. Phagocytosis by zippers and triggers. *Trends in Cell Biology*, 5(3):89 – 93, 1995.

[Swanson2008] Joel A. Swanson. Shaping cups into phagosomes and macropinosomes. *Nat Rev Mol Cell Biol*, 9(8):639 – 649, 2008.

[Tauber2003] Alfred I. Tauber. Metchnikoff and the phagocytosis theory. *Nat Rev Mol Cell Biol*, 4(11):897 – 901, 2003.

[Terry1979] S.C. Terry, J.H. Jerman, and J.B. Angell. A gas chromatographic air analyzer fabricated on a silicon wafer. *Electron Devices, IEEE Transactions on*, 26(12):1880–1886, 1979.

[Thompson1997] Nancy L Thompson and B Christoffer Lagerholm. Total internal reflection fluorescence: applications in cellular biophysics. *Current Opinion in Biotechnology*, 8(1):58 – 64, 1997.

[Tilney2001] Lewis G. Tilney, Omar S. Harb, Patricia S. Connelly, Camenzind G. Robinson, and Craig R. Roy. How the parasitic bacterium legionella pneumophila modifies its phagosome and transforms it into rough er: implications for conversion of plasma membrane to the er membrane. *Journal of Cell Science*, 114:4637–4650, 2001.

[Todaro1964] George J. Todaro, Howard Green, and Burton D. Goldberg. Transformation of properties of an established cell line by sv40 and polyoma virus. *Proc Natl Acad Sci U S A*, 51 (1):66–73, 1964.

[Toepke2006] Michael W. Toepke and David J. Beebe. Pdms absorption of small molecules and consequences in microfluidic applications. *Lab Chip*, 6(12):1484–1486, 2006.

[Tokunaga1997] Makio Tokunaga, Kazuo Kitamura, Kiwamu Saito, Atsuko Hikikoshi Iwane, and Toshio Yanagida. Single molecule imaging of fluorophores and enzymatic reactions achieved by objective -type total internal reflection fluorescence microscopy. *Biochemical and Biophysical Research Communications*, 235(1):47 – 53, 1997.

[Tollis2010] Sylvain Tollis, Anna E Dart, George Tzircotis, and Robert G Endres. The zipper mechanism in phagocytosis: energetic requirements and variability in phagocytic cup shape. *BMC Systems Biology*, 4:149, 2010.

[Toscano1992] S. Toscano, B. Briner, H. Hopster, and M. Landolt. Exchange-coupling between ferromagnets through a non-metallic amorphous spacer-layer. *Journal of Magnetism and Magnetic Materials*, 114:L6–L10, 1992.

[Tsan1971] Min-Fu Tsan and Richard D. Berlin. Effect of phagocytosis on membrane transport of nonelectrolytes. *The Journal of Experimental Medicine*, 134(4):1016–1035, 1971.

[Tsymbal2001] E.Y. Tsymbal and D.G. Pettifor. Perspectives of giant magnetoresistance. *Advances in Research and Applications*, 56:113–237, 2001.

[Uhlig2010] Katja Uhlig, Erik Wischerhoff, Jean-Francois Lutz, Andre Laschewsky, Magnus S. Jaeger, Andreas Lankenau, and Claus Duschl. Monitoring cell detachment on peg-based thermoresponsive surfaces using tirf microscopy. *Soft Matter*, 6(17):4262–4267, 2010.

[VWR] VWR International. https://at.vwr.com/app/home.

[Vaziri2008] Ashkan Vaziri and Arvind Gopinath. Cell and biomolecular mechanics in silico. *Nature Materials*, 7:15–23, 2008.

[Vollmer2008a] Frank Vollmer and Stephen Arnold. Whispering-gallery-mode biosensing: label-free detection down to single molecules. *Nature Methods*, 5(7):591–596, 2008.

[Vollmer2008b] F. Vollmer, S. Arnold, and D. Keng. Single virus detection from the reactive shift of a whispering-gallery mode. *Proceedings of the National Academy of Sciences*, 105(52):20701–20704, 2008.

[Waechtershaeuser1988] Günter Wächtershäuser. Before enzymes and templates: Theory of surface metabolism. *Microbiol Rev.*, 52 (4):452–484, 1988.

[Waechtershaeuser1992] Günter Wächtershäuser. Groundworks for an evolutionary biochemistry: The iron-sulphur world. *Progress in Biophysics and Molecular Biology*, 58(2):85 – 201, 1992.

[Waechtershaeuser2000] Günter Wächtershäuser. Life as we don't know it. *Science*, 289(5483):1307–1308, 2000.

[Wang2008] Lei Wang, Jing Zhu, Cheng Deng, Wan li Xing, and Jing Cheng. An automatic and quantitative on-chip cell migration assay using self-assembled monolayers combined with real-time cellular impedance sensing. *Lab Chip*, 8:872–878, 2008.

[Wang2010] SH Wang, CW Lee, A Chiou, and PK Wei. Size-dependent endocytosis of gold nanoparticles studied by three-dimensional mapping of plasmonic scattering images. *Journal of Nanobiotechnology*, 8:33–, 2010.

[Wang2012] Wei Wang, Shaopeng Wang, Qiang Liu, Jie Wu, and Nongjian Tao. Mapping single cell-substrate interactions by surface plasmon resonance microscopy. *Langmuir*, 28(37):13373–13379, 2012.

[Ward1994] M.D. Ward, M. Dembo, and D.A. Hammer. Kinetics of cell detachment: peeling of discrete receptor clusters. *Biophysical Journal*, 67(6):2522 – 2534, 1994.

[Ware1998] Margaret F. Ware, Alan Wells, and Douglas A. Lauffenburger. Epidermal growth factor alters fibroblast migration speed and directional persistence reciprocally and in a matrix-dependent manner. *Journal of Cell Science*, 111:2423–2432, 1998.

[Weddemann2009] Alexander Weddemann. *A finite element analysis of a microfluidic lab-on-a-chip system employing magnetic carriers for biomedical applications.* PhD thesis, Bielefeld University, 2009.

[Weddemann2010] A. Weddemann, C. Albon, A. Auge, F. Wittbracht, P. Hedwig, D. Akemeier, K. Rott, D. Meißner, P. Jutzi, and A. Hütten. How to design magneto-based total analysis systems for biomedical applications. *Biosensors and Bioelectronics*, 26:1152–1163, 2010.

[Wegener2001] Joachim Wegener, Andreas Janshoff, and Claudia Steinem. The quartz crystal microbalance as a novel means to study cell-substrate interactions in situ. *Cell Biochemistry and Biophysics*, 34:121–151, 2001.

[Weisman1967] Robert A. Weisman and Edward D. Korn. Phagocytosis of latex beads by acanthamoeba. i. biochemical properties. *Biochemistry*, 6(2):485–497, 1967.

[Wells2005] C. M. Wells, T. Ahmed, J. R. W. Masters, and G. E. Jones. Rho family gtpases are activated during hgf-stimulated prostate cancer-cell scattering. *Cell Motility and the Cytoskeleton*, 62(3):180–194, 2005.

[Wetzel1969] Mary G. Wetzel and Edward D. Korn. Phagocytosis of latex beads by acanthamoeba castellani (neff). *The Journal of Cell Biology*, 43:90–104, 1969.

[Whitesides2006] George M. Whitesides. The origins and the future of microfluidics. *Nature*, 442(7101):368–373, 2006.

[Williams1998] I.R. Williams. *In Encyclopedia of Immunology: Fibroblasts.* Academic Press, 2nd edition edition, 1998.

[Woese1977] Carl R. Woese and George E. Fox. Phylogenetic structure of the prokaryotic domain: The primary kingdoms. *Proc. Natl. Acad. Sci.*, 74:5088–5090, 1977.

[Woese1990] Otto Kandler Carl R. Woese and Mark L. Wheelis. Towards a natural system of organisms: Proposal for the domains archaea, bacteria, and eucarya. *Proc. Nati. Acad. Sci.*, 87:4576–4579, 1990.

[Woods1986] A Woods, J R Couchman, S Johansson, and M Höök. Adhesion and cytoskeletal organisation of fibroblasts in response to fibronectin fragments. *EMBO Journal*, 5 (4):665–670, 1986.

[Xing2005] James Zan Xing, Lijun Zhu, Jo Ann Jackson, Stephan Gabos, Xue-Jun Sun, Xiao-bo Wang, and Xiao Xu. Dynamic monitoring of cytotoxicity on microelectronic sensors. *Chemical Research in Toxicology*, 18(2):154–161, 2005.

[Yafet1987] Y. Yafet. Ruderman-kittel-kasuya-yosida range function of a one-dimensional free-electron gas. *Phys. Rev. B*, 36:3948–3949, 1987.

[Yager2006] Paul Yager, Thayne Edwards, Elain Fu, Kristen Helton, Kjell Nelson, Milton R. Tam, and Bernhard H. Weigl. Microfluidic diagnostic technologies for global public health. *Nature*, 442(7101):412–418, 2006.

[Yamada1990] Noriko Yamada, Teruo Okano, Hideaki Sakai, Fumiko Karikusa, Yoshio Sawasaki, and Yasuhisa Sakurai. Thermo-responsive polymeric surfaces; control of attachment and detachment of cultured cells. *Die Makromolekulare Chemie, Rapid Communications*, 11(11):571–576, 1990.

[Yeatman1996] Eric M. Yeatman. Resolution and sensitivity in surface plasmon microscopy and sensing. *Biosensors and Bioelectronics*, 11(6/7):635 – 649, 1996.

[Zemel2010] A Zemel, F Rehfeldt, A E X Brown, D E Discher, and S A Safran. Cell shape, spreading symmetry, and the polarization of stress-fibers in cells. *Journal of Physics: Condensed Matter*, 22(19):194110, 2010.

[Zhang1991] S. Zhang and P. M. Levy. Conductivity perpendicular to the plane of multilayered structures. *J. Appl. Phys.*, 69:4786–4788, 1991.

[Zienkiewicz2005] O.C. Zienkiewicz, R.L. Taylor, and J.Z. Zhu. *The Finite Element Method.* Elsevier Butterworth-Heinemann, 2005.

[Zigmond1996] Sally H Zigmond. Signal transduction and actin filament organization. *Current Opinion in Cell Biology*, 8(1):66 – 73, 1996.

[vanBokhoven2001] Adrie van Bokhoven, Marileila Varella-Garcia, Christopher Korch, Daphne Hessels, and Gary J. Miller. Widely used prostate carcinoma cell lines share common origins. *The Prostate*, 47 (1):36–51, 2001.

Acknowledgments

I would like to express my gratitude to everybody who has contributed in any way to this work.
First of all, I want to thank my supervisor PD Dr. Hubert Brückl for his great support over the years, his prospective idea to focus on cell analysis, and for giving me the opportunity in the last two years as a Junior Scientist to gain experience in scientific topics beyond this thesis.
I would like to address my special thanks to Dr. Jörg Schotter for his great guidance through this thesis, his valuable input in designing the MAGLab-setup, the many helpful discussions regarding new experimental approaches and data interpretation, and for his always patient and friendly manner.
I thank my correspondence advisor Prof. Günter Reiss from the *University of Bielefeld* for giving me the possibility to do a "cooperative dissertation" under his supervision and for valuable suggestions.
A big thanks goes to Alexandra Keller for the prolific teamwork during her Diploma Thesis, and for carrying out most of the experiments concerning the cancer cells.
I'm very thankful for the constructive cooperation with our biology colleagues, and especially with PD Peter Ertl. The discussions with him led to a variety of interesting ideas, including the investigation of phagocytic processes. Many thanks also to Verena Charwat, Michaela Purtscher, Dr. Lukas Richter, Dr. Andy Mak, Dr. Kriemhilt Roppert, and Florian Bellutti for introducing me to the cell culturing, passaging, staining, surface functionalization and for the continual exchange of valuable ideas and impressions.
I want to thank Dr. Philipp Schroeder for optimizing the sputtering parameters for the GMR multilayers, sample supply and measurements, Dr. Thomas Uhrmann for LabView programming and ProE software supply, Dr. Marcus Milnera for producing the MAGLab chips in the final stage of my thesis, Dr. Moritz Eggeling for 3D magnetic bead manipulation and proofreading parts of this work, Dr. Rudolph Heer for contributing to the MAGLab electronics and AFM introduction, Dr. Volker Ennen for providing the amoeba code and OOMMF installation, and Dr. Xenia Descovich for proofreading parts of this thesis.
I'm also grateful to Dr. Thomas Maier, Dr. Christoph Stepper, Dr. Theodore Dimopoulos, Dr. Michael Kast, Dr. Ole Bethge, Leoni Breth, and Dr. Paul Müllner for the introduction to laboratory equipment, proper working in a clean room ambient, and Magix software supply.
A very big thanks goes to all my colleagues of the nano-group for the outstanding atmosphere, especially Raghu, Shweta, Leoni, Rudi, Thomas U., Jörg, Paul, Roman, Kerstin, Giorgio, Stefan, Eva and Max for the good times we had during and beside the work. A special thanks goes to Moritz, Ole and Philipp not only for their scientific and moral support but also for the great fun we shared in the last years.

Së fundi, falënderoj familjen time përzemërsisht për mbështetjen financiare dhe morale gjatë studimeve dhe doktoratës.

Curriculum vitae

Personal Data

Name	Astrit Shoshi
Address	Kölblgasse 12/9, 1030 Vienna, Austria
Date/Place of birth	May 10^{th}, 1979 / Gjakova, Kosova
Nationality	Kosova-Albanian, German

Education

06/2006 - 05/2013	Dr. rer. nat. in Physics, University of Bielefeld, Germany
10/2001 - 12/2005	Diploma in Physics, University of Bielefeld, Germany
08/1997 - 06/2001	High-school diploma and elementary studies in Physics, Oberstufen-Kolleg at the University of Bielefeld, Germany

Professional Experience

03/2011 - 05/2013	Junior Scientist at *Molecular Diagnostics*, Austrian Institute of Technology: Magnetic Lab-on-a-Chip devices for point-of-care analysis of infectious diseases; Integration of TMR-Sensors in CMOS-based biochips. Supervisor: Dr. Jörg Schotter
06/2006 - 03/2011	PhD thesis at *Molecular Diagnostics*, Austrian Institute of Technology and *Thin Films and Physics of Nanostructures*, University of Bielefeld: "Magnetic lab-on-a-chip for cell analysis: Magnetoresistive-based real-time monitoring of dynamic cell-environment interactions". Supervisors: PD Dr. Hubert Brückl, Dr. Jörg Schotter, Prof. Günter Reiss
10/2001 - 12/2005	Diploma thesis in physics, University of Bielefeld:"Suche nach magnetischen Führsystemen und GMR-Sensoren zur on-chip Manipulation und Detektion von magnetischen Teilchen". Supervisor: Prof. Andreas Hütten
11/2000- 01/2001	Internship at the University of Bielefeld, Germany, Supervisors: Dr. Harald Schulz, Prof. Peter Andresen.